3D motion-based high-resolution imaging techniques for automotive radar

Yuan, S.

DOI
10.4233/uuid:24b76740-a92f-4d77-9875-6bda6e7aee1c

Publication date
2024

Document Version
Final published version

Citation (APA)
Yuan, S. (2024). *3D motion-based high-resolution imaging techniques for automotive radar*. [Dissertation (TU Delft), Delft University of Technology]. https://doi.org/10.4233/uuid:24b76740-a92f-4d77-9875-6bda6e7aee1c

3D Motion-based High-resolution Imaging Techniques for Automotive Radar

Sen Yuan

3D MOTION-BASED HIGH-RESOLUTION IMAGING TECHNIQUES FOR AUTOMOTIVE RADAR

Dissertation

for the purpose of obtaining the degree of doctor
at Delft University of Technology
by the authority of the Rector Magnificus, Prof. dr. ir. T.H.J.J. van der Hagen,
chair of the Board for Doctorates
to be defended publicly on
Wednesday 2 October 2024 at 17:30 o'clock

by

Sen YUAN

Master of Science in Information and Communication Engineering,
Beihang University, China
born in Yuncheng, Shanxi province, China

This dissertation has been approved by the promotors.

Composition of the doctoral committee:

Rector Magnificus,	chairperson
Prof. Dsc. A. Yarovoy	Delft University of Technology, promotor
Dr. F. Fioranelli	Delft University of Technology, promotor

Independent members:

Prof. dr. ir. R.F. Hanssen	Delft University of Technology
Prof. dr. D. Gavrila	Delft University of Technology
Prof. dr. K. Doris	Eindhoven University of Technology
Prof. dr. M. Martorella	University of Birmingham
Dr. ir. R.F. Remis	Delft University of Technology

This research was supported by the China Scholarship Council and the EEMCS faculty of Delft University of Technology.

Keywords: High-resolution Imaging, Signal Processing, Automotive Radar, Ego-motion Estimation, Direction of Arrival Estimation, MIMO Techniques.

Printed by: Proefschriftspecialist, 1506RZ Zaandam, The Netherlands.

Front & Back: Design by Sen Yuan.

ISBN/EAN: 978-94-6384-629-5 (Paperback/softback)
ISBN/EAN: 978-94-6384-630-1 (E-book, PDF)

An electronic version of this dissertation is available at
`http://repository.tudelft.nl/`.

Author e-mail: sjiandanx@163.com

To my family and friends, for their support and encouragement

CONTENTS

SUMMARY

Autonomous driving is one of the most popular research topics. Radar technology is used for many applications of ADAS and is considered one of the key technologies for HAD. It has unique advantages compared with other sensors, especially its capabilities during adverse weather conditions and Doppler information extraction. Required by autonomous applications, radar has to change its historical role from a simple detector to an imaging sensor, which requires not only the range and Doppler resolution ability but also a high spatial resolution, i.e., the azimuth and the elevation angle resolution. To address this problem, in this thesis, new signal processing algorithms are proposed, which pave the way to improved performance of the automotive radar sensor.

The FMCW waveform is widely used in current automotive applications due to its low cost and simplicity. MIMO array techniques exploit the spatial diversity of transmit and receive antenna arrays and have been exploited in current automotive radar because of their ability to achieve high angular resolution with a few antennas. Platform movement is one of the main characteristics of automotive radar, which introduces movement uncertainty compared with radars at fixed locations but provides an opportunity to use the movement to boost the angular resolution. Thus, FMCW waveform and MIMO antenna array are the main research subjects in this thesis.

The FMCW signal model, the MIMO geometry and the platform movement are derived and analyzed in Chapter 2, which, for the first time, takes the elevation information into account for 3D imaging at the same time.

In Chapter 3, a robust algorithm using multi-channel FMCW radar sensors to instantly determine the complete 3D motion state of the ego-vehicle (i.e., translational speed and rotational speed) is proposed. The angle information of targets is extracted, and then their phase information from different time instances is used to determine vehicle ego motion through an optimization process. Any pre-processing steps, such as clustering or clutter suppression, are not required. The performance of the algorithm is compared with the state-of-the-art algorithms based on real-world data, and superior performance has been demonstrated. The algorithm proposed can be easily integrated into radar signal processing pipelines for other tasks relevant to autonomous driving.

Subsequently, the concept of motion-enhanced snapshots is proposed to tackle the high-resolution imaging for side-looking regions in a limited number of snapshots context in Chapter 4. Then, a 3D motion-enhanced high-angular resolution algorithm for side-looking radar is proposed using only a 1D radar array for automotive applications in Chapter 5. The formulation of a modified steering vector to compensate for errors due to complex vehicle motion and the approximation in the time tag are developed in both algorithms. Both simulated data from point-like and complex extended targets, as well as experimental data, have been used in the method performance analysis.

The side-looking radar in Chapters 4 & 5 is mainly used for mapping the environment surrounding the radar, while the forward-looking region attracts more interest in

autonomous driving. Doppler beam sharpening is combined with MIMO processing to improve the angular resolution as well as solve the ambiguity problem in a robust movement of the platform and the diverse reflectivity of the different scatterers in Chapter 6. 3D Robust unambiguous Doppler beam sharpening using adaptive threshold (3DRUDAT) in Chapter 7 extends the approach in Chapter 6 to solve the coupling problem between the elevation and azimuth, equipping the method with 3D imaging ability.

The motion information obtained from Chapter 3 is input into the proposed pipeline, combined with the 3D high-resolution imaging algorithms under different installations to solve the 3D motion-based high-resolution imaging problem jointly. First, based on the side-looking geometry, the 3D ego-motion estimation is performed by two optimizations. Second, based on the estimated velocities, the motion-enhanced snapshots are selected and form a larger virtual array. Finally, based on the new array, the 3D imaging is performed in Chapter 8. Also, a different pipeline is proposed for the forward-looking regions, combining the ego-motion estimation and 3DRUDAT.

All the proposed methods in this thesis have been validated comprehensively in simulations, i.e., Monte Carlo tests of point targets and simulated extended targets, but also with experimental data with a real radar board, i.e., the radar installed in a moving platform in an anechoic chamber, the radar installed on real vehicle platform during driving.

SAMENVATTING

Autonoom rijden is een van de meest populaire onderzoeksonderwerpen. Radartechnologie wordt voor veel toepassingen van ADAS gebruikt en wordt beschouwd als een van de sleuteltechnologieën voor HAD. Het heeft unieke voordelen vergeleken met andere sensoren, vooral de mogelijkheid tot functioneren tijdens ongunstige weersomstandigheden en de extractie van Dopplerinformatie. Voor het gebruik in autonome toepassingen moet radar zijn historische rol veranderen van een eenvoudige detector naar een beeldvormende sensor, wat niet alleen afstands- en de Doppler-resolutie vereist, maar ook een hoge ruimtelijke resolutie, dat wil zeggen de azimut- en de elevatiehoekresolutie. Om dit probleem aan te pakken worden in dit proefschrift nieuwe signaalverwerkingsalgoritmen voorgesteld, die de weg vrijmaken voor verbeterde prestaties van de autoradarsensor.

De FMCW-golfvorm wordt veel gebruikt in de huidige autoradartoepassingen vanwege de lage kosten en de eenvoud van de sensor. MIMO-arraytechnieken maken gebruik van de ruimtelijke diversiteit van zend- en ontvangstantenne-arrays en zijn benut in de huidige autoradar vanwege hun vermogen om met een paar antennes een hoge hoekresolutie te bereiken. Platformbeweging is een van de belangrijkste kenmerken van autoradar, die bewegingsonzekerheid introduceert in vergelijking met radars op vaste locaties, maar de mogelijkheid biedt om de beweging te gebruiken om de hoekresolutie te vergroten. Daarom zijn de FMCW-golfvorm en de MIMO-antenne-array de belangrijkste onderzoeksonderwerpen in dit proefschrift.

Het FMCW-signaalmodel, de MIMO-geometrie en de platformbeweging worden afgeleid en geanalyseerd in hoofdstuk 2, waarin voor het eerst tegelijkertijd rekening wordt gehouden met de hoogte-informatie voor 3D-beeldvorming.

In Hoofdstuk 3 wordt een robuust algoritme voorgesteld dat gebruik maakt van meerkanaals FMCW-radarsensoren om onmiddellijk de volledige 3D-bewegingstoestand van het ego-voertuig (d.w.z. translatiesnelheid en rotatiesnelheid) te bepalen. De hoekinformatie van doelen wordt geëxtraheerd en vervolgens wordt hun fase-informatie op verschillende tijdstippen gebruikt om de ego-beweging van het voertuig te bepalen via een optimalisatieproces. Eventuele voorbewerkingsstappen, zoals clustering of onderdrukking van storingsbronnen, zijn niet vereist. De prestaties van het algoritme worden vergeleken met de modernste algoritmen op basis van data uit de praktijk, en superieure prestaties zijn aangetoond. Het voorgestelde algoritme kan eenvoudig worden geïntegreerd in radarsignaalverwerkingspijplijnen voor andere taken die relevant zijn voor autonoom rijden.

Vervolgens wordt in Hoofdstuk 4 het concept van bewegingsverbeterde snapshots voorgesteld om de beeldvorming met hoge resolutie voor zijwaarts gelegen gebieden aan te pakken in een beperkt aantal snapshots. In hoofdstuk 5 wordt voorgesteld om alleen 1D-radararrays te gebruiken voor autoradartoepassingen. De formulering van een aangepaste stuurvector om fouten als gevolg van complexe voertuigbewegingen te com-

penseren en de benadering in het tijdslabel zijn in beide algoritmen ontwikkeld. Zowel gesimuleerde gegevens van puntdoelen en complexe uitgebreide doelen, als experimentele gegevens zijn gebruikt in de prestatieanalyse van de methode.

De zijwaarts gerichte radar in Hoofdstuk 4 & 5 wordt voornamelijk gebruikt om de omgeving rondom de radar in kaart te brengen, terwijl de regio in de bewegingsrichting meer belangstelling trekt voor autonoom rijden. Doppler Beam Sharpening wordt gecombineerd met MIMO-verwerking om de hoekresolutie te verbeteren en het ambiguïteitprobleem op te lossen in een robuuste beweging van het platform en de diverse reflectiviteit van de verschillende verstrooiingspunten in Hoofdstuk 6. 3D Robust Unambiguous Doppler beam sharpening using Adaptive Threshold (3DRUDAT) in Hoofdstuk 7 breidt de aanpak uit Hoofdstuk 6 uit om het koppelingsprobleem tussen de elevatie en azimut op te lossen, en rust daarmee de methode uit met 3D-beeldvormingsmogelijkheden.

De bewegingsinformatie verkregen uit Hoofdstuk 3 wordt ingevoerd in de voorgestelde pijplijn, gecombineerd met de 3D-algoritmen voor beeldvorming met hoge resolutie onder verschillende installaties, om het 3D bewegingsbeeldvormingsprobleem met hoge resolutie gezamenlijk op te lossen. Ten eerste werd, op basis van de zijwaarts gerichte geometrie, de 3D ego-schatting uitgevoerd door twee optimalisaties. Ten tweede werden op basis van de geschatte snelheden de bewegingsverbeterde snapshots geselecteerd en vormden ze een grotere virtuele array. Ten slotte werd op basis van de nieuwe array de 3D-beeldvorming uitgevoerd. Ook werd voor de regio's in de bewegingsrichting een andere pijplijn voorgesteld, waarbij de ego-schatting en 3DRUDAT werden gecombineerd.

Alle voorgestelde methoden in dit proefschrift zijn uitgebreid gevalideerd in simulaties, d.w.z. Monte Carlo-tests van puntdoelen, gesimuleerde uitgebreide doelen, maar ook met experimentele gegevens met een echt radarbord, d.w.z. de radar geïnstalleerd in een bewegend platform in een echoloze kamer alsmede op een voertuigplatform.

List of Acronyms

ACC	Adaptive Cruise Control
ADAS	Advanced Driver Assistance Systems
AI	Artificial Intelligence
BP	Back Projection
CFAR	Constant False Alarm Rate
CNN	Convolutional Neural Network
CPI	Coherent Processing Interval
DAT	Doppler Angle Tensor
DBF	Digital Beamforming
DBS	Doppler Beam Sharpening
DOA	Direction Of Arrival
DoF	Degrees of Freedom
ESPRIT	Estimation of Signal Parameters via Rational Invariance Techniques
E2E	End-to-End
FCA	Forward Collision Avoidance
FFT	Fast Fourier Transform
FMCW	Frequency-Modulated Continuous-Wave
GPS	Global Positioning System
HAD	Highly Automated Driving
IMU	Inertial Measurement Unit
LOS	Line of Sight
MIMO	Multi-Input-Multi-Output
MUSIC	MUltiple SIgnal Classification
MVDR	Minimum Variance Distortionless Response
NDT	Normal Distribution Transform
PRI	Pulse Repetition Interval
RCS	Radar Cross Section
RDS	Range-Doppler Spectrum
RNN	Recurrent Neural Network
ROS	Robot Operating System
SAR	Synthetic Aperture Radar
SIMO	Single-input-multiple-output
SLAM	Simultaneous Localization And Mapping
SNR	Signal-to-Noise Ratio
TDM	Time Division Multiplexing
ULA	Uniformly Distributed Linear Array

1

INTRODUCTION

1

1.1. MOTIVATION OF RESEARCH

The autonomous driving industry is undergoing a remarkable transformation, marked by significant advancements in the realm of ADAS. These systems are designed to enhance driving safety and improve overall driving comfort. Furthermore, the emergence of HAD has become a prominent technological frontier. The effectiveness and dependability of these systems are intricately tied to environmental sensing capabilities [1] and the SLAM functions. Various technologies and approaches have been developed to address these critical requirements. These innovations are driven by the goal of creating robust solutions for a more integrated, smaller, and power-efficient sensor.

Radar technology stands out as an indispensable sensor because it accurately and directly measures multiple targets' range, relative velocity, and angle and a long-range coverage of more than 200 m even in challenging weather or lighting conditions [2]. It has the inherent advantage of achieving velocity sensing in one single sensor. In contrast, other sensing sensors, including vision and laser, need to fuse information with classical navigation sensors such as wheel-based odometry and inertial sensors. Additionally, proprioceptive sensors, like wheel encoders and IMUs, suffer from significant drift among other detrimental effects [3], and may have systematic errors caused by kinematic imperfections, unequal wheel diameters or uncertainties about the exact wheelbase. Furthermore, it is worth noting that current GNSS systems operate within the L band, which limits their bandwidth and subsequently impacts their resolution. In contrast, automotive radar operates in the mm-wave frequencies, resulting in a theoretical resolution difference of up to 40 times. This discrepancy in theoretical resolution translates into significant disparities in ideal localization or mapping accuracy. As a result, there would be a shift in the trajectory of future localization and navigation systems, with a transition from GPS-centric solutions to the increasingly prominent role of automotive radar systems.

In terms of environment sensing, to meet the sensing capabilities requirement of autonomous driving, automotive radars must provide high-resolution information on the vehicle environment in the range-Doppler–azimuth–elevation domains. Mm-wave radar can offer a large operational bandwidth, up to 4G Hz, providing centimetre-level range resolution. Doppler resolution is a function of chirp duration and the number of chirps used for the estimation, so it is limited by the coherent observation time, with better velocity resolution achieved by operating at higher frequency [4]. Angular resolution is contingent upon the antenna aperture and thus is determined by the number and placement of the transmit and receive antenna elements, which are limited by the radar cost and packaging size. Power consumption is another issue when increasing spatial resolution with a larger antenna array. Developing a robust, high-resolution, power-efficient algorithm for automotive radar systems is the first and urgent task.

Although many improvements have been developed [5–7], the sparsity of point clouds provided by traditional automotive radars is still a bottleneck in corresponding research. Due to their small number of points, it is challenging to regress accurate 2D bird's-eye view bounding boxes, especially for smaller objects such as pedestrians. Furthermore, the lack of elevation information (i.e., the height of the points) makes it nearly impossible to infer objects' height and vertical offset, i.e., to regress 3D bounding boxes. The latest improvement in automotive radar technology, 3+1D radars, may help overcome

these limitations. They also tend to provide a denser point cloud. Recent research has demonstrated that 3+1D radar technology, particularly in the form of radar cubes, has substantially enhanced radar-based applications in various domains [8, 9]. Thus, the adoption of 3+1D radar for 3D imaging represents a major and promising future trend in radar technology for automotive applications.

The motivation of this research is to develop 3D high-angular resolution imaging algorithms to tackle the resolution problem of automotive radar and improve the 3D imaging ability for current radar. With a high angular resolution and 3D imaging ability, radar can provide denser point clouds and sharper target contour information for different applications. For automotive radar, the radar will move with the vehicle, providing a potentially larger aperture for an even higher resolution. Thus, utilizing the ego-motion of the vehicle will be a very attractive approach for automotive radar. To avoid errors in the synchronization between different sensors and provide a high localization ability for the self-driving vehicle, approaches for accurate estimation of the 3D ego-motion are researched as well.

1.2. RESEARCH OBJECTIVES

The primary focus of the work lies in the investigation of the capabilities of the FMCW MIMO radar and the development of a high-resolution 3D imaging algorithm for radar. MIMO radar technology exploits the spatial diversity of transmit and receive antenna arrays and has received considerable attention in automotive. Due to its ability to achieve high angular resolution with a few antennas, MIMO has been exploited in current automotive radar for ADAS [5]. However, the practical implementation on vehicles constrains the radar size and limits the number of MIMO antennas. In MIMO radar with a virtual ULA, angle finding can be implemented via DBF [10] by performing computationally efficient FFTs on snapshots taken across the array elements, or using computationally intensive super-resolution methods such as MVDR [11], and subspace-based methods, such as MUSIC [12, 13] and ESPRIT [14]. Despite many high-resolution algorithms being proposed in this field, the actual resolution ability is limited by the physical Rayleigh limit. Synthetic aperture radar achieves a high resolution in cross-range by forming a larger aperture using the radar's trajectory and breaking the limitation of the radar itself. So, the actual movement of the vehicle carrying the radar provides the potential to break the limitations.

The following research questions should be addressed to achieve the aforementioned research objective of increasing angular resolution for 3D radar imaging in the automotive industry.

Q1: How can we increase angular resolution with the current limited antenna aperture size by exploiting the vehicle's motion?

The vehicle's motion will physically move the antenna along its trajectory at different times. The physical moved distance can provide a larger aperture than the original antenna array. Those snapshots collected at different times (equivalent to different positions) are used coherently in this thesis to provide higher angular resolution for radar DOA estimation. However, using motion information of the vehicle puts higher demands on the radar system's velocity estimation.

Q2: How can we use the radar itself to derive the vehicle velocity with a high up-

dated rate without losing accuracy?

Motion information can be obtained either by other sensors, such as the IMU or GPS or by the radar itself. Fusing with other sensors will face the unsynchronization problem, which may introduce extra error and cause degraded performance, especially for high-bandwidth radar. Radar can determine the targets' radial velocity directly by the Doppler effect. For static targets in the radar field of view, such targets' Doppler information is the projection of the vehicle's velocity. This allows the vehicle's velocity to be retrieved with the measured targets' data. The update ratio can be further improved compared with the SOTA algorithm, i.e. one frame, by utilizing this information within a frame of time. However, the algorithm's accuracy depends on the measurement quality and the signal processing techniques.

Q3: How can we extend the high-resolution imaging algorithm to 3D space and beyond 2D assumptions?

3D imaging algorithms for different radar installations will face different challenges. For the forward-looking regions, the algorithms must address the "blind zone" problem, mitigating ambiguities induced by forward motion and the coupling between elevation and azimuth in 3D imaging. For the side-looking regions, the imaging could be achieved by the 2D beamscan with motion-enhanced snapshots. We aim to enhance angular resolution through vehicle motion exploitation.

Q4: How can we use the radar to jointly solve the ego-motion estimation and the high-resolution imaging in one processing system?

Some of the high-resolution imaging algorithms benefit from the platform's natural movement. Those algorithms require an accurate ego-motion estimation algorithm for motion information. The joint problem of ego-motion estimation and the high-resolution imaging can be solved by estimating the ego-motion and imaging the observed region using data from the same radar sensor. Conventional ego-motion estimations are designed based on the radar point cloud, which needs at least one coherent processing time. The extra pre-processing for generating the point cloud will increase processing time, potentially limiting fast update rates. Thus, starting the processing chain directly from the radar raw signal will simultaneously solve the problem and achieve better performances.

The algorithms proposed in this thesis are not only validated at the simulation level but also with experimental data obtained in various conditions. The experimental data consists of corner reflectors in the anechoic chamber and the extended targets during real driving. The waveforms are designed for different applications. A detailed analysis of the method proposed in this thesis is also performed. Limitations and new research challenges also arise when dealing with real driving scenarios with more uncertainty to provide future recommendation work in this research field.

1.3. NOVELTY AND RESULTS

By addressing the aforementioned research questions, some novel contributions and results have been obtained and are presented in the thesis as follows:

- A novel 3D full ego-motion estimation algorithm working with radar raw signal at its input (i.e., the radar base-band signal before FFTs) is proposed by a two-

step optimization. It is demonstrated that 3 DoF ego-motion estimation can be performed with the algorithm proposed, on a smaller timescale than a frame and by using only one multi-channel radar. A detailed analysis of the proposed method performance is provided based on numerical simulations with point targets and realistic scenes reconstructed from the public *RadarScenes* dataset in [15].

- A high angular resolution DOA approach with lower computational load is proposed by combining the vehicle's motion with automotive MIMO radar. The proposed method operates on a limited number of snapshots. It includes the formulation of a modified steering vector to compensate for errors due to complex vehicle motion and the approximation in the time tag. The performance of the proposed method is analyzed in terms of its accuracy and probability of resolution and is shown to outperform alternative approaches from the literature. For the first time in the literature, a detailed analysis of the impact of forward and cross-forward velocity estimation errors on the performance of the DoA method has been performed. Both simulated data from point-like and complex extended targets and experimental data have been used in the method performance analysis.

- A novel 3D imaging algorithm using a 1D MIMO array by introducing motion-enhanced snapshots to achieve high angular resolution for side-looking automotive radar is proposed. The steering vector is used to jointly address the 3D imaging in the azimuth and elevation domain to benefit from the target's elevation diversity, and the motion errors are compensated in the steering vector to improve the method's performance further. Experimental data using multiple sensors during driving are collected and calibrated to verify the proposed methods. The motion-enhanced snapshots increase the degree of freedom for DOA estimation, which can distinguish more targets. Also, the SNR increases as more coherent processing snapshots are used for DOA estimation.

- An unambiguous Doppler-based forward-looking multiple-input multiple-output radar beam sharpening scan (*UDFMBSC*) method is proposed by combining Doppler beam sharpening and MIMO array processing to solve the ambiguity problem of symmetric targets in forward-looking automotive radar. To make the '*UDFMBSC*' suitable for more complicated vehicle movements and cope with the diverse reflectivity of different targets in the scene, a new approach named 'Robust Unambiguous DBS with Adaptive Threshold' (*RUDAT*) is proposed. The problem of ambiguous symmetric targets for non-ideal forward-looking vehicle trajectory is addressed via additional phase shift compensation. Targets with different reflectivity are retrieved by applying an adaptive threshold. The proposed method has been verified for simulated point-like and extended targets, as well as experimental data from a radar sensor, showing that the proposed method achieves better angular estimation than conventional DBS and DBF.

- A 3D imaging using Doppler beam sharpening (3DRUDAT) for achieving high angular resolution is proposed to extend RUDAT into a 3D imaging framework. The ambiguity problem for Doppler beam sharpening in the robust vehicle's trajectory in the forward-looking region is solved by combining the MIMO processing. The

coupling between the elevation and the azimuth in the Doppler beam sharpening is addressed by processing the algorithm in both elevation and azimuth direction. The voxelization accuracy and the image contrast are proposed as metrics to evaluate the general 3D imaging results.

- A joint ego-motion estimation and high-resolution 3D imaging algorithm is proposed for both side-looking and forward-looking automotive radar. A detailed analysis of the method's performance and limitations is performed based on numerical simulations. The proposed method uses raw radar signals without further information to achieve ego-motion estimation and dense point cloud generation, which is challenging but essential for automotive radar. The proposed method does not need prior information on the environment, surroundings, or the targets' positions and numbers, making it insensitive to dynamic environments.

- A fast, high-resolution imaging algorithm that incoherently accumulates the images from multiple frames' data in the radar field of view is proposed. The proposed method, compared with the conventional BP algorithm, is up to three times faster, making its potential implementation possible in real time.

1.4. OUTLINE OF THE THESIS

The rest of the thesis is organized as follows:

Chapter 2 presents some fundamentals related to FMCW MIMO radar. A brief introduction of the FMCW theory, MIMO technology, and the corresponding 3D FMCW MIMO technology signal model is given. The signal model is general for every 3D FMCW multi-channel radar, and all the range-Doppler-azimuth-elevation estimations are based on such signal models.

Chapter 3 investigates a 3D full ego-motion estimation algorithm using general multi-channel radar. It is based on the radar raw signal (i.e., the radar base-band signal before FFTs). After obtaining raw radar data, a 2D FFT is performed for a different group of chirps with different starting times. This is followed by CFAR detection and a proposed optimization process to finally obtain the ego-motion estimation, i.e. the estimation of the rotation and translation velocity components. The algorithm's performance is evaluated using simulated Monte Carlo tests and simulated scenarios.

Chapter 4 demonstrates a 2D high angular resolution DOA estimation for limited snapshot scenarios. The proposed method forms a phased array with a larger aperture size by introducing the time tag, which also helps control the computation load. Velocity components in directions other than the main driving trajectory are compensated for during the DOA process. The method is proposed for 2D imaging, and the performance is analyzed comprehensively with point targets, simulated extended targets and experimental data. The proposed approach outperforms alternative approaches from the literature.

Chapter 5 extends the algorithm in chapter 4 to a 3D imaging algorithm. The conventional automotive radar is equipped with a larger number of antennae for azimuth DOA estimation. The proposed method replaces the conventional azimuthal antenna elements with motion-enhanced snapshots. Thus, the so-called larger azimuthal ULA can

be used for elevation estimation. The proposed method provides higher angular resolution for 3D imaging radar, with improved DoF and increased SNR. The movements in the other two directions are compensated in the steering vector. The performance is analyzed comprehensively with point targets, simulated extended targets and experimental data. The proposed approach outperforms alternative approaches from the literature.

Chapter 6 presents a 2D unambiguous DBS DOA estimation algorithm for forward-looking radar. The method proposed as UDFMBSC combines Doppler beam sharpening and MIMO array processing to solve the ambiguity problem of symmetric targets in forward-looking automotive radar. To make the '*UDFMBSC*' suitable for more complicated vehicle movements and cope with the diverse reflectivity of different targets in the scene, RUDAT is proposed. The problem of ambiguous symmetric targets for non-ideal forward-looking vehicle trajectory is addressed via additional phase shift compensation. Targets with different reflectivity are retrieved by applying an adaptive threshold. The performance is analyzed using point targets, simulated extended targets, and experimental data.

Chapter 7 extends the 2D DBS imaging to 3DRUDAT with adaptive threshold for forward-looking FMCW 3D MIMO radar. The Doppler frequency, when it is projected to the spatial domain for DBS, will face coupling problems in the elevation domain and ambiguity problems in the azimuth domain. The proposed method addresses the problem by combining MIMO processing with DBS in both the elevation and azimuth domains. The proposed method has been verified for simulated point-like and extended targets and experimental data from a radar sensor.

Chapter 8 combines the proposed 3D ego-motion estimation algorithm in chapter 3 with the 3D imaging algorithm in chapter 4 and 5. A joint processing framework is proposed to simultaneously achieve the ego-motion estimation and 3D imaging for both side-looking and forward-looking installation. It is shown that automotive radar imaging achieves much better resolution by introducing motion information through different proposed methods.

Chapter 9 presents the collection of experimental data in realistic driving scenarios in the city of Delft and discusses several practical challenges to be addressed in this regard. Furthermore, a computationally efficient high-resolution imaging algorithm for side-looking automotive radar is proposed. This uses multiple frames and speeds up the processing time three times faster than the conventional BP algorithm, making its potential implementation possible in real time.

Chapter 10 contains the conclusions and gives recommendations for possible future research.

2

SIGNAL MODEL OF DOA FOR AUTOMOTIVE MIMO FMCW RADAR

2.1. FUNDAMENTALS

Important requirements for automotive radar are high resolution in range, Doppler and angle [16], low hardware cost, and small size. With the advent of high-bandwidth and high-frequency FMCW radar, the resolution in range and velocity increased dramatically. Due to its ability to achieve high angular resolution with a few antennas, MIMO has been exploited in current automotive radar [5]. Thus, the MIMO FMCW radar and its signal are considered the main object of this thesis.

2.1.1. FMCW RADAR

Continuous-wave (CW) radar systems transmit the electromagnetic (EM) wave continuously, and the echo reflections from the objects are received and recorded simultaneously and continuously as well. Since the high duty ratio is achieved, it has much higher integrated energy in a short time than the pulse counterpart. The range of the targets will be determined by the EM wave's round-trip delay, and the characteristics of the CW waveforms must be changed to retrieve the range information (e.g., change the wave's frequency or phase over time).

There are many possible modulation patterns, i.e., Sawtooth modulation, also called linear FMCW, triangular modulation, square-wave modulation (simple frequency-shift keying, FSK), stepped modulation (staircase voltage), and sinusoidal modulation. Among these modulations, FMCW has several main advantages, including simultaneous ranges and Doppler velocities estimation, relatively low sampling frequency with de-chirping technique, safety with low transmitted power, low cost, portable size, high reliability and good sensitivity. It is widely used in the automotive radar.

The received chirp signals (FMCW signal) can be processed analogously by the matched filter or de-chirping techniques. The dechirped signal is the instantaneous frequency difference between the transmitted and received chirps, which is called the beat frequency or beat signal. The beat signal contains the range information as well as the Doppler information. However, the Doppler frequency shift within one beat signal is much smaller than that of range and is mostly negligible. Multiple chirps are used to obtain the Doppler information, and Doppler frequency is estimated from the phase shift within multiple beat signals. On the one hand, applying a de-chirping technique instead of the matched filter can reduce the sampling frequency dramatically, which is especially beneficial for real-time applications. On the other hand, the maximum unambiguous velocity and maximum unambiguous range will be influenced simultaneously by the low sampling frequency.

2.1.2. MIMO RADAR

SIMO radar refers to a radar device with single transmit (TX) and multiple receive (RX) antennas. The angle resolution of a SIMO radar depends on the number of RX antennas. Therefore, a direct approach to improving the angle resolution requires increasing the number of RX antennas. This approach has its limits because each additional RX antenna requires a separate RX processing chain on the device (each with an LNA, mixer, IF filter, and ADC).

MIMO refers to a radar with multiple TX and multiple RX antennas. MIMO radar with $M_{\mathbf{t}}$ transmit and $M_{\mathbf{r}}$ receive antennas provides a cost-effective way to improve the

angle resolution of the radar. The signals that are sent must be orthogonal to each other because otherwise, they might start interfering with each other, either constructively or destructively. The orthogonality of the system can be achieved in different ways, for example, by spreading them out in time (Time-Division Multiplexing) or frequency (Orthogonal Frequency Division Multiplexing). When the transmitted signals are orthogonal, we can create a virtual MIMO array that is equivalent to a SIMO radar with $M_{\mathbf{t}}M_{\mathbf{r}}$ RX. This virtual array is the advantage that MIMO has over a normal phased array, as it can have the same performance with fewer actual antenna elements. This leads to a better angular resolution overall.

A coherent MIMO array consists of a set of transmitting and receiving elements that are placed in proximity to each other. According to this configuration and by assuming a far-field target to have the same RCS response to the probing signals coming from the multiple transmitters at the receiver side, the different transmitter-receiver channels can be coherently combined. An array pattern associated with an extended virtual array can then be synthesized, as shown in Fig. 2.1.

Figure 2.1: The MIMO channel array illustration.

2.2. MIMO FMCW SIGNAL

FMCW MIMO 3D radar with N_a virtual ULA for azimuth angle estimation and N_e virtual ULA for elevation angle estimation is considered here. Without losing generality, the omnidirectional antenna pattern is considered for the transmitter and receiver.

The virtual antenna array responses at a particular time interval consisting of data obtained at all virtual receivers and corresponding to the same range-Doppler bin is defined as the array *snapshot* [5]. During one snapshot, assumed to be equivalent to one coherent processing interval, the FMCW chirp is transmitted with chirp duration T_c and PRI T. A normalized single chirp signal with bandwidth B has the form:

$$s_0(t) = \begin{cases} e^{j2\pi(f_0 t + 0.5\mu t^2)} & t \in [0, T_c] \\ s_{settle}(t) & t \in [T_c, T] \end{cases} \tag{2.1}$$

where f_0 denotes the starting frequency, $\mu = \frac{B}{T_c}$ denotes the frequency modulation rate and $s_{settle}(t)$ means the signal during the settle time.

The periodic transmitted signal is decomposed into fast-time domain t' and chirp number domain $l = \lfloor \frac{t}{T} \rfloor$ as $t' = t - lT, t' \in [0, T_c]$, where $l = 0, 1, 2, ..., L_d - 1$ and L_d is the total number of the chirps in one snapshot.

Then, the periodically transmitted signal can be expressed as:

$$s(t) = s(t' + lT) = s(l, t') = s_0(t') \tag{2.2}$$

As shown in Fig. 2.2, the 2-D MIMO array, chosen as an example in this chapter, is placed in the Y-Z plane, with the X-axis pointing towards the illuminated scene. Assume N_s point targets with unknown spatial position $\mathbf{T}_t = [\mathbf{T}_{t1}, \mathbf{T}_{t2}, ..., \mathbf{T}_{tN_s}]$, $\mathbf{T}_{to} = [T_{txo}, T_{tyo}, T_{tzo}]^T$, own motion velocity $\mathbf{V}_t = [\mathbf{V}_{t1}, \mathbf{V}_{t2}, ..., \mathbf{V}_{tN_s}]$, $\mathbf{V}_{to} = [V_{txo}, V_{tyo}, V_{tzo}]^T$, where o is the index of the targets, the subscripts tx, ty, tz mean the x, y, z directions respectively. Correspondingly, their ranges $\mathbf{r}_t = [\mathbf{r}_{t1}, \mathbf{r}_{t2}, ..., \mathbf{r}_{tN_s}]$, azimuth angles $\Theta = [\theta_{t1}, \theta_{t2}, ..., \theta_{tN_s}]^T$, elevation angles $\Phi = [\phi_{t1}, \phi_{t2}, ..., \phi_{tN_s}]^T$ can be expressed as $\mathbf{r}_t = |mathbf T_t|$ where || is to take the norm of each column, and the Doppler velocity $\mathbf{D}_t = \mathbf{A}\mathbf{V}_t$. $\mathbf{A}$ is the transformation matrix

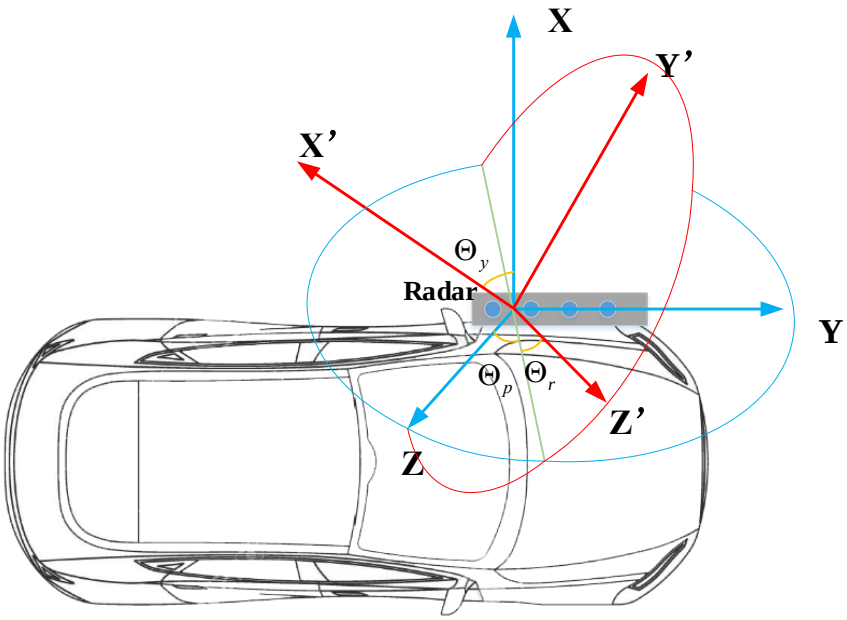

Figure 2.2: The geometry of the rotation of the radar mounted to the side of a vehicle, where Y is the forward direction, X is the cross-forward direction, and Z is the elevation direction, satisfying the left-handed Cartesian coordinates.

$$\mathbf{A} = \begin{bmatrix} \cos\Theta\cos\Phi & \sin\Theta\cos\Phi & \sin\Phi \end{bmatrix} \tag{2.3}$$

The radar is moving by the platform's motion at translational speed $\mathbf{V}_v = [v_{vx}, v_{vy}, v_{vz}]$ and rotation speed $[\omega_{vp}, \omega_{vr}, \omega_{vy}]$. The subscript p, r and y indicate the vehicle's pitch, row and yaw rotation. The azimuth antenna elements are denoted by $p \in [0, N_a]$, and the index of the elevation antenna elements is denoted by $q \in [0, N_e]$. Based on the different geometry of the 2D array, the total received channel might change within $N_a N_e$. The distance between different adjacent antenna elements is d for both azimuth and elevation directions to avoid grating lobe and ambiguity. d is equal to $d = \frac{\lambda}{2}$.

The p-th in azimuth and q-th in elevation antenna's position is denoted by $\mathbf{C}$. During one chirp duration, the position will be the same; it will change according to the slow time index l as $\mathbf{C}(l)$. Then the range between the static scatter o and the p-th azimuth antenna and q-th elevation antenna would be $D_{o,p,q}(l)$ at time l as in (2.4):

$$D_{o,p,q}(l) = |\mathbf{C}(l) - \mathbf{T}_{to}| \tag{2.4}$$

where $|\,|$ means the norm of the vector.

The round trip delay of the reflected signal for the q-th azimuth antenna and p-th elevation antenna of the scatter is

$$\begin{aligned} \tau_o\left(l, t'\right) &= \frac{2\left(D_{o,p,q}(t' + lT) + v_o\left(t' + lT\right)\right)}{c} \\ &\approx \gamma_o + \frac{2v_o(t' + lT)}{c} \end{aligned} \tag{2.5}$$

where c is the speed of light, $\gamma_o = \frac{2D_{o,p,q}(t'+lT)}{c} \ll T_c$, $v_o = \mathbf{A}(\mathbf{V}_{to} - \mathbf{V}_v)$ is the radial velocity between the radar and scatter.

The corresponding received signal can be written as:

$$\begin{aligned} r_o(l, t', p, q) &= \alpha_o e^{j\rho(o,p,q,l)} s(t' + lT - \tau_o(l, t')) \\ &= \alpha_o e^{\rho(o,p,q,l)} e^{j2\pi\Phi_o(l,t')} \\ with\ t' &\in [\gamma_o, T_c] \end{aligned} \tag{2.6}$$

where α_o is the constant complex amplitude of the scatter, $e^{j\rho(o,p,q,l)}$ denotes the phase delay of scatter o with the p-th antenna in azimuth direction and q-th receive antenna in elevation direction at time l. According to (2.2), the term $\Phi_o(l, t')$ has the form:

$$\begin{aligned} &\Phi_o(l, t') = f_0(t' - \tau_o(l, t')) + 0.5\mu(t' - \tau_o(l, t'))^2, \\ &with\ t' \in [\gamma_o, T_c] \end{aligned} \tag{2.7}$$

From the phase of the received signal, the instantaneous frequency of the received signal is extracted as:

$$\begin{aligned} f_o(l, t') &= \frac{\partial\Phi_o(l, t')}{\partial t'} = (f_0 + \mu(t' - \tau_o(l, t')))(1 - \frac{\partial\tau_o(l, t')}{\partial t'}) \\ &\approx f_0 + \mu t' \end{aligned} \tag{2.8}$$

A property of the virtual uniform linear array is that the range difference between scatters and different receiver antenna pairs will be approximately equal to a constant with respect to the direction of arrival. The range differences are shown as in (2.9,2.10)

$$D_{o,(p+1),q}(t) - D_{o,p,q}(t) \approx d\sin\theta_o\cos\phi_o \tag{2.9}$$

$$D_{o,p,(q+1)}(t) - D_{o,p,q}(t) \approx d\sin\phi_o \tag{2.10}$$

Then, the phase delay of the different antenna pairs relative to the 1st antenna elements in the 2D array is obtained by

$$\rho(o,p,q,l) = 2\pi f_o(l,t') \frac{pd\sin\theta_o(l)\cos\phi_o(l) + qd\sin\phi_o(l)}{c} \tag{2.11}$$

In this thesis, the signal is a narrow band signal, thus $f_o(l,t') \approx f_0$; the targets are located in the far-field, and the observation time in one CPI is very short. Thus, the angles of the target are assumed to be constant during one chirp. Also, the velocity of different antennas due to the rotation will not influence the Doppler velocity (otherwise, the antennas will lose their coherency), and these differences are negligible because the rotating radial distance between them is only half wavelength. Hence, the change in angle is due to the vehicle's rotation in pitch, roll, and yaw directions, $[\Theta_p, \Theta_r, \Theta_y]$, which can be calculated at a given time as the following:

$$\begin{aligned} &A_{xyz}(\Theta_p,\Theta_r,\Theta_y) = A_x(\Theta_p)A_y(\Theta_r)A_z(\Theta_y) = \\ &\begin{bmatrix} 1 & 0 & 0 \\ 0 & \cos(\Theta_p) & -\sin(\Theta_p) \\ 0 & \sin(\Theta_p) & \cos(\Theta_p) \end{bmatrix} \begin{bmatrix} \cos(\Theta_r) & 0 & \sin(\Theta_r) \\ 0 & 1 & 0 \\ -\sin(\Theta_r) & 0 & \cos(\Theta_r) \end{bmatrix} \\ &\begin{bmatrix} \cos(\Theta_y) & -\sin(\Theta_y) & 0 \\ \sin(\Theta_y) & \cos(\Theta_y) & 0 \\ 0 & 0 & 1 \end{bmatrix} \end{aligned} \tag{2.12}$$

Based on the different geometries of the radar mounted on the vehicle, the relationship between the angle and the movement might change. One side-looking radar is given here as an example. The position in the coordinates of the target **o** can be calculated for the radar with rotation speed $[\omega_p, \omega_r, \omega_y]$ as (2.13):

$$\begin{aligned} &\begin{bmatrix} R_o\cos(\theta_o(l))\cos(\phi_o(l)) \\ R_o\sin(\theta_o(l))\cos(\phi_o(l)) \\ R_o\sin(\phi_o(l)) \end{bmatrix} = \\ &A_{xyz}(\omega_p l, \omega_r l, \omega_y l) \begin{bmatrix} R_o\cos(\theta_o(0))\cos(\phi_o(0)) \\ R_o\sin(\theta_o(0))\cos(\phi_o(0)) \\ R_o\sin(\phi_o(0)) \end{bmatrix} \end{aligned} \tag{2.13}$$

The received signal is then correlated with the conjugate copy of the transmitted signal to get the de-chirped signal. Considering that automotive radars work in narrowband conditions, the signal of the **o**-th scatterer received by the l-th element can be written as in the following equation, where, for simplicity, it still indicated the complex amplitude of the de-chirped signal:

$$
\begin{aligned}
z_{(o)}(l,t',p,q) &= r_o(l,t',p,q) \times s^*(l,t') \\
&= \alpha_o \exp[j\rho(o,p,q,l)] \\
&\times \exp[-j2\pi(f_0\frac{2v}{c}Tl+\mu\gamma_o t')] \\
&\times \exp[-j2\pi\mu\frac{2v}{c}Tlt']
\end{aligned}
\tag{2.14}
$$

After the de-chirping, the data in (2.14) is sampled with respect to fast-time with frequency f_s and the discretized data $\hat{z}_o^{i,j}$ in the time domain is obtained as

$$
\hat{z}_o(l,b,p,q) \approx \alpha_o \exp[j\rho(o,p,q,l) - j2\pi(f_{d,o}Tl+\mu\gamma_o\frac{b}{f_s})] \tag{2.15}
$$

where $f_{d,o} = \frac{2v_o f_0}{c}$ represents the Doppler frequency of the **o**-th scatter. The coupling terms between slow and fast times represent range migration terms, which can be neglected because the automotive radar typically works with the narrow bandwidth assumption and the frame time is a small time duration.

When there are N_s scatterer points in the field of view, the signal would be as follows based on the superposition of the contributions of each scatterer:

$$
\hat{z}(l,b,p,q) = \sum_{o}^{N_s} \hat{z}_o(l,b,p,q) \tag{2.16}
$$

In the 2D radar signal, the elevation domain will not be considered. Equation (2.16) will be changed to

$$
\hat{z}(l,b,p) = \sum_{o}^{N_s} \hat{z}_o(l,b,p) \tag{2.17}
$$

where $\hat{z}_o(l,b,p) \approx \alpha_o \exp[j\rho(o,p,l) - j2\pi(f_{d,o}Tl+\mu\gamma_o\frac{b}{f_s})]$, $\rho(o,p) = 2\pi f_o(l,t')\frac{pd\sin\theta}{c}$, which is similar by assume the targets' elevation angles equal to 0, namely flatten earth model.

2.3. DOA ALGORITHM

As for transferring the role from a detector sensor to an imaging sensor, the DOA algorithm is essential for radar processing. Different algorithms can extract the angle profile of the targets from the phase delay between different receivers. The sub-space-based algorithms are summarized here, as they are well-known and easily implemented in processing.

After FFT on the fast time domain of the signal in (2.16), the targets will appear as a peak in the range profile. The signal will become:

$$\begin{aligned}\hat{z_r}(p,q,l,r) = \sum_{o}^{k_s} \alpha_o \pi T_c f_s \text{sinc}(\frac{(r T_c f_s + \mu \gamma_o T_c)}{2}) \\ \times \exp[j(\rho(o,p,q,l) + 2\pi f_0 \frac{2v_o}{c} T l)] \\ \times \exp[-j\pi(m T_c f_s + \mu \gamma_o T_c)]\end{aligned} \tag{2.18}$$

Then, each element is extracted to form a new Doppler Angle Tensor (DAT), which is used for elevation DOA estimation. By doing DOA estimation throughout every range bin, the image results can be obtained. Take targets at a certain range bin $r = r_0 \in [0, r_{un}]$ for demonstration, where r_{un} is the unambiguous range. Its corresponding 3D DAT $\mathbf{Z}(r) \in \mathbb{C}^{N_a \times N_e \times L_d}$ will be obtained for joint elevation and azimuth DOA estimation, 3D imaging, where N_a and N_e stands for azimuth and elevation antenna numbers, and L_d is Doppler data used for obtaining the subspace. All the below descriptions are for the targets in the r_0 for demonstration.

$$\mathbf{Z} = \hat{z_r}(p,q,l,r_0) \tag{2.19}$$

Since the range is already estimated, a 2D sub-space-based algorithm can be implemented for the joint two-dimensional parameters, namely the azimuth and elevation angle estimation. The data have to be reshaped from 3-dimensional tensor form to the 2-dimensional matrix form $Y \in \mathbb{C}^{N_a N_e \times L_d}$ by stacking azimuth and elevation dimensions together as

$$\mathbf{Y}(qN_e + p, l) = \mathbf{Z}(p,q,l) \tag{2.20}$$

The DAT can be modelled as a tensor with the azimuth n elevation i and the slow time index l:

The corresponding signal model will be:

$$\mathbf{Y} = \sum_{m=1}^{M} \mathbf{a}_{\theta_m} \circ \mathbf{a}_{\phi_m} \mathbf{S}_t + \mathbf{N} \in \mathbb{C}^{N_a N_e \times L_d} \tag{2.21}$$

where $\circ$ is the outer production, $\mathbf{S}_t$ is the point scatterer reflection coefficient with dimensions $N_a N_e \times L_d$, M is the number of scatters in the range bin r_0, $\mathbf{N}$ is the noise component. The steering vectors for motion enhanced and elevation are defined as:

$$\begin{aligned}\mathbf{a}_{\theta_\mathbf{m}} &= [1, e^{-j2\pi\omega_a(1,m)}, ..., e^{-j2\pi\omega_a(p,m)} ... e^{-j2\pi\omega_a(N_a-1,m)}]^T \\ \mathbf{a}_{\phi_\mathbf{m}} &= [1, e^{-j2\pi\omega_e(1,m)}, ..., e^{-j2\pi\omega_e(q,m)} ... e^{-j2\pi\omega_e(N_e-1,m)}]^T \\ \omega_a(p,m) &= \frac{d\, p \sin\theta_m \cos\phi_m}{\lambda} \\ \omega_e(q,m) &= \frac{d\, q \sin\phi_m}{\lambda}\end{aligned} \tag{2.22}$$

The matched steering vector $\alpha(\theta_m, \phi_m) \in \mathbb{C}^{N_a N_e}$ for the azimuth angle θ_m and the angle ϕ_m is formulated as:

$$\alpha(\theta_m, \phi_m) = \mathbf{a}_{\theta_\mathbf{m}} \otimes \mathbf{a}_{\phi_\mathbf{m}} \tag{2.23}$$

where $\otimes$ is the Kronecker product.

The sub-spaced methods, including DBF, MVDR, and MUSIC, can be implemented based on the steering vector for DOA estimation. The DBF algorithm does not need any information about the environment and is robust to the environment. Its weight vector $\mathbf{w}_{DBF}$ that maximizes the output signal power of the array antenna is given by [17]:

$$\mathbf{w}_{DBF} = \frac{\alpha(\theta_m, \phi_m)}{\sqrt{\alpha^H(\theta_m, \phi_m)\alpha(\theta_m, \phi_m)}} \tag{2.24}$$

The power of the weighted output is:

$$\begin{aligned} P_{DBF}(\theta_m, \phi_m) &= E[\left|\mathbf{w}_{DBF}^H \mathbf{X}\right|^2] \\ &= \frac{\alpha^H(\theta_m, \phi_m) R_{\mathbf{XX}} \alpha(\theta_m, \phi_m)}{\alpha^H(\theta_m, \phi_m)\alpha(\theta_m, \phi_m)} \end{aligned} \tag{2.25}$$

where $R_{\mathbf{XX}} = E\left[\mathbf{X}^H\mathbf{X}\right]$ is the autocorrelation matrix of $\mathbf{X}$, and the $[\bullet]^H$ denotes the operation of conjugate transpose.

The MVDR [11] based algorithm uses part of the freedom to form a beam on the scatter's DOA, while the remaining freedom to form 'zero' in other directions. It can only give a better result on the incoherent signal, but with limited snapshots, the signals are easier to coherent. The weight vector of $\mathbf{w}_{MVDR}$ that maximizes the output signal power of the array antenna is given by

$$\mathbf{w}_{MVDR} = \frac{R_{\mathbf{XX}}^{-1}\alpha(\theta_m, \phi_m)}{\alpha^H(\theta_m, \phi_m) R_{\mathbf{XX}}^{-1} \alpha(\theta_m, \phi_m)} \tag{2.26}$$

And the spatial profile for MVDR is

$$P_{MVDR}(\theta_m, \phi_m) = \frac{1}{\alpha^H(\theta_m, \phi_m) R_{\mathbf{XX}}^{-1} \alpha(\theta_m, \phi_m)} \tag{2.27}$$

The subspace [11] based algorithms, MUSIC, requires an estimate of the array covariance matrix, which is obtained based on multiple snapshots. The output of MUSIC is

$$P_{MUSIC}(\theta_m, \phi_m) = \frac{1}{\alpha^H(\theta_m, \phi_m)\mathbf{U}_n\mathbf{U}_n^H\alpha(\theta_m, \phi_m)} \tag{2.28}$$

where $\mathbf{U}_n$ is the noise subspace of $R_{\mathbf{XX}}$.

The calculated value from DBF, MVDR or MUSIC is basically the scattered field intensity backpropagated to the scattering point which is located at the cell with coordinates $[r_0, \theta_m, \phi_m]$. After searching all the cells in the space, the total imaging results in $P(r, \theta, \phi)$ can be obtained.

Different from the aforementioned 2D DOA algorithm, 1D DOA refers to either estimating the azimuth angle or elevation angle by 1D ULA. The other angle will be assumed as 0, i.e., the elevation angle equal to 0 for azimuth estimation.

2.4. CONCLUSIONS

This chapter describes the fundamental concepts of MIMO FMCW radar, the signal model of FMCW MIMO radar and the DOA algorithms, which will be used in the following chapters. Unlike the state-of-the-art FMCW MIMO radar, the presented signal model is extended to 3D radar, a major future automotive radar trend. Also, the signal model for 2D radar is given by assuming the flattened earth model. Despite the MIMO technology, the angle resolution still needs to be improved for good automotive imaging sensors. Several high-resolution algorithms have been proposed and explored in both 2D and 3D imaging, which are introduced in the following chapters.

3

3D EGO-MOTION ESTIMATION ALGORITHM FOR MULTICHANNEL RADAR

The problem of estimating the 3D ego-motion velocity using MIMO FMCW radar sensors has been studied. For the first time, the problem of ego-motion estimation is treated using radar raw signals. A robust algorithm is proposed using MIMO FMCW radar sensors to instantly determine the complete 3D motion state of the ego-vehicle (i.e., translational speed and rotational speed). The angle information of targets is extracted, and then their phase information from different time instances is used to determine vehicle ego motion through an optimization process. By iteratively discarding those moving targets, the performance of the ego-motion estimation is further improved. Any pre-processing steps, such as clustering or clutter suppression, are not required. The algorithm's performance is compared with the state-of-the-art algorithms based on real-world data, and superior performance has been demonstrated. The algorithm proposed can be easily integrated into radar signal processing pipelines for other tasks relevant to autonomous driving.

Parts of this chapter have been published in: S. Yuan, S. Zhu, F. Fioranelli and A. G. Yarovoy, "3-D Ego-Motion Estimation Using Multi-Channel FMCW Radar," in IEEE Transactions on Radar Systems, vol. 1, pp. 368-381, 2023; S. Yuan, D. Wang, F. Fioranelli, and A. Yarovoy, "Improved Accuracy for 3D Ego-motion Estimation using Automotive FMCW MIMO radar." 2024 IEEE radar conference (RadarConf'24), Denver, Colorado, the USA, 2024.

3.1. INTRODUCTION

Robust ego-motion estimation plays an important role in various real-world applications, ranging from indoor robotics to automotive scenarios, and remains a challenging task. Various technologies and approaches have been developed to investigate robust solutions, aiming at more integrated, smaller, and power-efficient sensors.

Radar technology has some unique advantages compared to other sensors, including vision, laser, and classical navigation sensors like wheel-based odometry and inertial sensors, namely the accurate and direct measurements of the range, relative velocity, and angle of multiple targets, as well as a long-range coverage of more than 200 m even in challenging weather or light conditions [2]. While extremely fast and high-resolution, lidar is sensitive to weather conditions, especially rain and fog [18]. Vision systems are versatile and cheap but easily impaired by scene changes, like poor lighting or the sudden presence of snow [19]. Both these sensors only yield dependable results for relatively short-range measurements. A typical GPS guarantees, at best, meter-level accuracy and may experience reception difficulties near obstructions and rely on external infrastructure [20]. Additionally, proprioceptive sensors, like wheel encoders and IMUs, suffer from significant drift among other detrimental effects [3], and may have systematic errors caused by kinematic imperfections, unequal wheel diameters or uncertainties about the exact wheelbase.

When addressing the problem of ego-motion estimation, a current trend in automotive is information fusion from different sensors. Milli-RIO algorithm with data fusion coming from a single-chip low-cost radar and an inertial measurement unit sensor with an unscented Kalman filter and RNN to estimate the six-degrees-of-freedom ego-motion of a moving radar is proposed in [21]. A comparison of the automotive SAR measurement of a static object and the representation of the static object from the digital map database to get an accurate localization is proposed in [22]. A millimetre-wave radar SLAM algorithm assisted by the RCS feature of the target and IMU is suggested in [23]. A sliding window on radar measurements to extract Doppler velocity and IMU measurements to constrain the change in velocity between radar measurements, jointly estimating the 3D translational velocity, is suggested in [24]. Fusion of the radar's ego-motion estimation results with monocular Visual Inertial Odometry or monocular Thermal Inertial Odometry to improve the robustness in challenging conditions is described in [25]. Finally, a fusion of the IMU data with radar data to correct the error in the estimation is proposed in [26].

Significant efforts have been made to use only information from multichannel radar systems to perform ego-motion estimation. The state-of-the-art methods can be mainly divided into model-based and AI approaches. Based on the vehicle's mechanical model, the sinusoidal relation between the measured Doppler velocities and the azimuth angles is used in [27] to estimate the ego-motion. This work, which determined an ego-velocity vector of 2 DoF, was extended to the case of multiple distributed radars to deal with the full 2D vehicle motion state, i.e., 3 DoF [28]. A probabilistic model incorporating spatial registrations of radar scans was also proposed in [29], where joint spatial and Doppler-based estimation operates without lever-arm offsets or motion assumptions but involves high computational costs. In subsequent research [30], the NDT model was utilized for faster spatial alignment, and the complexity was further reduced by deriving a sparse

probabilistic representation [31]. A hybrid approach [32] was proposed to decouple translational and rotational motion by combining benefits from scan matching and instantaneous approaches. The ego-motion velocities can also be calculated by the cross-correlation of different Tx-Rx pairs [33, 34]. A Gaussian Mixture Model for two consecutive point sets, achieving robust estimation results with a probabilistic strategy, is used in [35]. A new, unsupervised ego-velocity estimation method for a low-cost Doppler radar to obtain accurate ego-velocity estimation is presented in [36]. Ego-motion can also be generated using SLAM from radar data [37]. Although most of the newest algorithms for SLAM in ego-motion estimation [35, 38, 39] can provide a good performance by transferring the technique from Lidar or Odometry, they suffer from poor updating rate as they generally require a full frame to perform the ego-motion estimation. Moreover, the density of the radar point cloud is much sparser than that of a Lidar one, reducing the performance of these techniques. The AI-based algorithm [40] proposes an end-to-end (E2E) complex-valued neural network architecture using a complex-valued channel attention module that directly handles raw radar data to provide the ego-motion estimation. An ego-velocity prediction model using an LSTM network as a microscopic and non-parametric approach to applying to the various urban driving conditions is proposed in [41].

However, all the aforementioned algorithms for ego-motion estimation are based on radar point clouds, which are generated after several data processing steps. At least one coherent processing interval, i.e. one frame, is required to create such data clouds, which limits the possible update rate. Moreover, point clouds may not necessarily be coherent from frame to frame due to the scintillating scattering behaviour of extended targets at mm-wave frequencies, and their generation process can include artefacts coming from clutter and interference. Performing ego-motion estimation starting from the lower signal level (i.e., the radar base-band signal before range-doppler processing) can benefit automotive scenarios. Firstly, the ego-motion estimation can be performed quickly, within one frame or from chirp to chirp. Secondly, using the algorithms implemented directly on the signal level, it will be easier to combine them with other high-resolution algorithms [42] or automotive SAR algorithms [43] to improve performances for other tasks, such as ACC [44], FCA [45], lane-change assistance [46], evasion assistance [47] or mapping generation[48]. To the best of our knowledge, only a few papers have been published to tackle ego-motion estimation from the radar raw signal. For example, the resolution autocorrelation in the range is used in [34] to estimate the ego-motion, but that algorithm operates at an intermediate frequency. The proposed method estimates the targets' positions and then uses their phase information from different time instances to determine vehicle ego-motion through an optimization process.

The main contributions of this chapter are summarized as follows:

1. A novel 3D full ego-motion estimation algorithm working with radar raw signal at its input (i.e., the radar base-band signal before FFTs) is proposed by a two-step optimization.

2. A threshold has been set for iteratively discarding those moving targets. The performance is improved by only using the information of those static targets.

3. It is demonstrated that using the algorithm proposed, 3 DoF ego-motion estimation can be performed on a smaller timescale than a frame and by using only one multichannel radar.

4. A detailed analysis of the proposed method performance is provided based on numerical simulations with point targets and with realistic scenes reconstructed from the public *RadarScenes* dataset in [15].

The rest of the chapter is organized as follows. In Section 3.2, the fundamentals of how to estimate the ego-motion velocity via the proposed optimization approach are demonstrated in Section 3.3. The method is further improved by introducing iteration considering the existence of the moving target provided in Section 3.4. The simulation results for ideal point targets and complex, realistic scenarios extracted from the *RadarScenes* dataset [15] are provided in Section 3.5. Finally, conclusions are drawn in Section 3.6.

3.2. 3D EGO-MOTION ESTIMATION

3.2.1. SIGNAL MODEL

The signal model of the 3D automotive MIMO FMCW radar in (2.16) will be further explored and processed for the 3D ego-motion estimation. One can obtain the RDS for each antenna by performing the 2-dimensional FFT of the de-chirped signal in the fast and slow time dimensions.

For the signal received by one antenna, it is important to note that a group of chirps in the whole frame will be chosen for further processing, i.e., $\hat{z}(u : u+N_L-1, k)$, with $u \in \mathbb{N}, u+N_L < L_d$. u is the starting slow time index for the selected group of chirps, as shown in Fig. 3.1. Compared to alternative point cloud-based methods for ego-velocity estimation, the updating rate of this and the following steps can be significantly improved from frame to chirp rate by allowing overlap between the selected groups of chirps. After 2D FFT, the signal for the selected group of chirps in (2.16) will become:

$$\begin{aligned}\hat{z}^{p,q}(m,n,u) = \sum_{o}^{k} \alpha_o \pi^2 T_c f_s N_L \operatorname{sinc}\left(\frac{(mT_c f_s + \mu\gamma_o T_c)}{2}\right)\times \\ \operatorname{sinc}\left(\frac{(n+f_{d,o}T)N_L}{2}\right) \times \exp[j\rho(o,p,q,l)] \\ \times \exp[-j\pi((mT_c f_s + \mu\gamma_o T_c) \\ + (n+f_{d,o}T)(2u+N_L))]\end{aligned} \tag{3.1}$$

where m and n are the indices of the frequency in range and Doppler domain, respectively; ρ is the function of phase difference as equation (2.11). Because of the sinc function in the expression, the amplitude peak will change according to the Doppler velocity and range of targets, which is at the basis of the subsequent detection processing.

3.2.2. STEPS FOR THE PROPOSED EGO-MOTION ESTIMATION

Range and Doppler detection can be performed using thresholding-based methods applied to the 2D RDS, such as the CFAR detector [49]. There are many versions of CFAR,

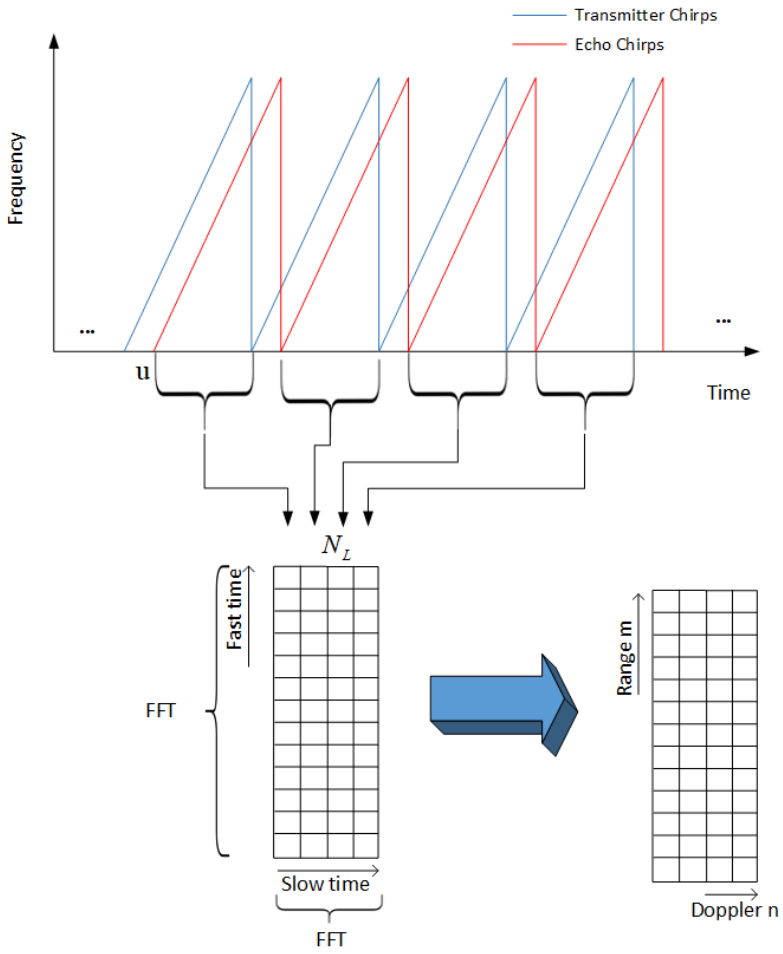

Figure 3.1: The generation of RDS, where u is the index controlling the starting time of the group of chirps within one frame that is selected for further processing.

but the core theory is to estimate the background power and achieve a constant false alarm rate in detection. Also, AI-based detectors have been proposed recently, but they are focused on a specific type of target's detection, e.g., ships [50] or underground targets [51]. In this work, a conventional cell-averaging CFAR algorithm is applied [52]. The radar is installed on the side of the vehicle, which can effectively avoid the Doppler ambiguity problem encountered in forward-looking radar and help distinguish the targets' contribution over the whole Doppler spectrum. Via the 2D FFT, the targets can be separated into the range and Doppler domains. The detections are based on the amplitude information of the RDSs, which are independent of the antenna and the starting slow time index, as in (3.1). It should also be noted that each detected bin may contain the contribution of multiple physical targets or scatter points. However, the algorithm

can regard these as a single "synthetic target" for a detected bin. In other words, no explicit assumption exists that one detected range-Doppler bin would correspond to one specific physical target. It is also assumed that this will not change much in the short duration of one CPI/frame over which the algorithm operates.

After CFAR detection, N_k range-Doppler cells are obtained for every RDS, denoted by $[(m_1, n_1); (m_2, n_2); ...; (m_{N_k}, n_{N_k})]$. These cells will be used to select the corresponding vectors along the antenna/channel dimension of the radar cube for subsequent processing. With FFTs and detections, the proposed ego-motion estimation approach uses raw data from different chirps of the radar cube as its input rather than discrete points from a point cloud after detection. In the following subsections, the estimation of the rotational and translational velocities are presented.

ROTATIONAL MOTION

The phase differences between different antennas for the detected range-Doppler cell will only depend on the angular information of those targets belonging to this cell, i.e., their position in terms of elevation angle and azimuth angle in (2.11). From this, we can extract the angle information of these detected cells, i.e. the angle information of this synthetic target.

By stacking all the RDS at a time u for the detected (m_k, n_k) range-Doppler indices, the target data for each cell is written in the matrix format $\mathbf{Z}(m_k, n_k, u)$ as:

$$\mathbf{Z}(m_k, n_k, u) = \begin{bmatrix} \hat{z}^{1,1}(m_k, n_k, u) & ... & \hat{z}^{1,N_e}(m_k, n_k, u) \\ ... & \hat{z}^{p,q}(m_k, n_k, u) & ... \\ \hat{z}^{N_a,1}(m_k, n_k, u) & ... & \hat{z}^{N_a,N_e}(m_k, n_k, u)) \end{bmatrix} \tag{3.2}$$

Here, the k-th detected RDS is assumed to belong to the k-th 'synthetic target', whose phase information will follow:

$$\exp[j\rho(k, p, q, l)] = \sum_{k_i=1}^{k_n} \exp[j\rho(k_i, p, q, l)] \tag{3.3}$$

where k_i the index of the targets in k-th bin, k_n is the total number of targets in k-th bin. As discussed here, a 'synthetic target' occupying one bin does not necessarily relate to a single physical object.

We then take this target as an example, $Z^{p,q}(m_k, n_k, u) \in \mathbb{C}^{N_a \times N_e}$, where N_a, N_e are the total number of antennas in azimuth and elevation. By applying equation (3.1), each element $\hat{z}^{q,p}(m_k, n_k, u)$ will be written as:

$$\hat{z}^{p,q}(m_k, n_k, u) = \beta \hat{z}^{1,1}(m_k, n_k, u) \exp[j\rho(k, p, q, u)] \tag{3.4}$$

where β is the complex coefficient containing the information about the amplitudes, and $\hat{z}^{1,1}(m_k, n_k, u)$ is the received signal from the reference antenna element.

Two RDSs starting from different slow time values are needed to estimate the rotational motion, u_0 and u_1. The range and Doppler indices for a detected target at time u_0 will also be used for the next RDS at time u_1, as it is assumed that they remain the

same during a few chirps. These can be written in the matrix format as $\mathbf{Z}(m_k, n_k, u_0)$ and $\mathbf{Z}(m_k, n_k, u_1)$.

From the phase differences in (3.4), the angle of the 'synthetic target' at a time u_1 is derived as discussed later in Section 3.2.3, i.e. $\mathbf{Z}(m_k, n_k, u_0) \Rightarrow [\hat{\theta}_k(u_0), \hat{\phi}_k(u_0)]$ and $\mathbf{Z}(m_k, n_k, u_1) \Rightarrow [\hat{\theta}_k(u_1), \hat{\phi}_k(u_1)]$.

With radar, the targets' range information $\hat{r}_k(u)$ can be easily estimated. Then, for k detected targets, a matrix $\mathbf{T_c}(u) \in \mathbb{C}^{N_k \times 3}$ can be formed, which contains their different position information, namely range, azimuth, elevation:

$$\mathbf{T_c}(u) = \begin{bmatrix} \hat{r}_1(u) & \dots & \hat{r}_k(u) \\ \hat{\theta}_1(u) & \dots & \hat{\theta}_k(u) \\ \hat{\phi}_1(u) & \dots & \hat{\phi}_k(u) \end{bmatrix} \tag{3.5}$$

At this stage, three operations are implemented to estimate the rotational velocities: first, the projection to Cartesian coordinates; second, the Kabsch algorithm [53, 54] as shown in Algorithm. 5 to estimate the rotation matrix; finally, the estimation of the rotational velocities based on the rotation matrix. These steps are summarized in Section 3.2.4.

TRANSLATIONAL MOTION

The phase differences between different starting slow time indices for the detected cell will depend on the 'synthetic target' Doppler information, which can be seen in (3.1). To estimate the translational motion from these phase differences, the same process can be applied as the one performed for the angle extraction in the aforementioned rotation estimation.

The Doppler velocity V_d only contains the components of the vehicle and the targets' relative speed in the radial direction. Here, most of the Doppler components come from the radar's speed. This is true especially for side-looking radars, as most targets in the radar field of view are static, like landmarks, road curbs, and buildings. Only the vehicle's movement is considered for simplicity in this derivation. Also, the detected Doppler velocity is combined with all the Doppler components from every target in the given cell. The ego-motion estimation of the radar can be derived from the phase differences.

Once again, let us take the detected k-th target as an example. The radar is moving with velocity $v_r(u) = [v_{rx}(u), v_{ry}(u), v_{rz}(u)]$. Assuming that during the short period $u_1 - u_0$, the relative speed between targets and radar remains constant. Also, the targets within one detected bin will be in the same position. The phase difference $\Gamma(\mathbf{k}, u_1, u_0)$ can be written as:

$$\Gamma(k, u_1, u_0) = 4\pi \frac{dr_k f_0}{c} T \tag{3.6}$$

$$\begin{aligned} dr_k = & V_d * (u_1 - u_0) = v_{rx}(u_0) * (u_1 - u_0) \cos\theta_k \cos\phi_k \\ & + v_{ry}(u_0) * (u_1 - u_0) \sin\theta_k \cos\phi_k \\ & + v_{rz}(u_0) * (u_1 - u_0) \sin\phi_k \end{aligned} \tag{3.7}$$

By stacking all the detected range-Doppler cells at a certain time u, the matrix for translational motion can be formed as $\mathbf{T_t}(u) \in \mathbb{C}^{N_a * N_e \times N_k}$:

$$\mathbf{T_t}(u) = \begin{bmatrix} \hat{z}^{1,1}(m_1, n_1, u) & \dots & \hat{z}^{1,1}(m_{N_k}, n_{N_k}, u) \\ \dots & \dots & \dots \\ \hat{z}^{N_a,N_e}(m_1, n_1, u) & \dots & \hat{z}^{N_a,N_e}(m_{N_k}, n_{N_k}, u) \end{bmatrix} \tag{3.8}$$

with the two matrices $\mathbf{T_t}(u_0), \mathbf{T_t}(u_1)$ related to time u_0, u_1. An element of these matrices can be written as in (3.9):

$$Z^{p,q}(m_k, n_k, u_1) = \beta Z^{p,q}(m_k, n_k, u_0) \exp[j\Gamma(k, u_1, u_0)] \tag{3.9}$$

From the phase differences in (3.9), the translational movement of the radar is derived as discussed in the following Section 3.2.3, i.e. $[\mathbf{T_t}(u_0), \mathbf{T_t}(u_1) \Rightarrow [\hat{v_{rx}}, \hat{v_{ry}}, \hat{v_{rz}}]$.

3.2.3. DETAILS OF THE OPTIMIZATION APPROACH

Both equations (3.9) and (3.4) have the same format, only with different phase information. Here, the problem can be formulated as to how to estimate the desired parameters, i.e., the target's angular position and the translational velocity, from the phase information in the presence of noise.

From the equation (3.4), the measured data in a matrix form $X \in \mathbb{C}^{N_a \times N_e}$ can be obtained:

$$X = \frac{\hat{z}^{p,q}(m_k, n_k, u)}{\hat{z}^{1,1}(m_k, n_k, u)} + N_x \tag{3.10}$$

where $N_x \in \mathbb{C}^{N_a \times N_e}$ is the noise matrix.

The signal model $Y \in \mathbb{C}^{N_a \times N_e}$ was designed for subsequent optimization as:

$$Y(\hat{\theta}_k, \hat{\phi}_k) = \exp\left(j2\pi f_0 \left(\frac{pd}{c}\sin\hat{\theta}_k\cos\hat{\phi}_k + \frac{qd}{c}\sin\hat{\phi}_k\right)\right) \tag{3.11}$$

where $i \in [0, N_a]$ and $j \in [0, N_e]$ are the indices of the matrix, respectively, and the d_i and d_j have been defined in (5.2).

The problem then becomes an optimization problem, with the objective defined as:

$$\arg\min_{\hat{\theta}_k, \hat{\phi}_k} f(\hat{\theta}_k, \hat{\phi}_k) \tag{3.12}$$

where $f(\hat{\theta}_k, \hat{\phi}_k) = [Y - X]^H [Y - X]$, with $X, Y \in \mathbb{C}^{N_a \times N_e}$.

Different optimization algorithms can be used here, e.g., genetic algorithm [55] or simulated annealing [56]. Pattern search [57] is used for solving this optimization problem. In this way, one can obtain the estimated $\hat{\theta}_k$ and $\hat{\phi}_k$ for different detected targets. The advantage of this method is that it can be extremely simple to formulate and implement, as it does not require an explicit estimate of the derivative of the function or Taylor's series. Furthermore, it is globally convergent [58].

Similarly, from the equation (3.9), the measured data can be obtained and written as a matrix $P \in \mathbb{C}^{N_k \times N_e N_a}$

$$P = \frac{\hat{z}^{p,q}(m_k, n_k, u_1)}{\hat{z}^{p,q}(m_k, n_k, u_0)} + N_p \tag{3.13}$$

where $N_p \in \mathbb{C}^{N_k \times N_e N_a}$ is the noise matrix.

We can design the signal model $Q \in \mathbb{C}^{N_k \times N_e N_a}$ as:

$$\begin{aligned} &Q(\hat{v}_{rx}, \hat{v}_{ry}, \hat{v}_{rz}) \\ &= \exp(j4\pi T(v_{rx}(u_0) * (u_1 - u_0)\cos\hat{\theta}_k \cos\hat{\phi}_k \\ &+ v_{ry}(u_0) * (u_1 - u_0)\sin\hat{\theta}_k \cos\hat{\phi}_k \\ &+ v_{rz}(u_0) * (u_1 - u_0)\sin\hat{\phi}_k) f_0/c) \\ &\times ones(1, N_e N_a) \end{aligned} \tag{3.14}$$

where $\hat{\theta}_k$ and $\hat{\phi}_k$ are the estimated azimuth and elevation angle of detected targets in (3.12).

This problem becomes another optimization problem, with the objective defined as:

$$\arg \min_{\hat{v}_{rx}, \hat{v}_{ry}, \hat{v}_{rz}} f(\hat{v}_{rx}, \hat{v}_{ry}, \hat{v}_{rz}) \tag{3.15}$$

where $f(\hat{v}_{rx}, \hat{v}_{ry}, \hat{v}_{rz}) = [Q - P]^H [Q - P]$, with $Q, P \in \mathbb{C}^{N_k \times N_e N_a}$.

This problem is also solved with pattern search [57] to estimate $\hat{v}_{rx}, \hat{v}_{ry}, \hat{v}_{rz}$.

The proposed method mainly depends on the two optimization steps. Hence, the computation complexity depends on these two steps, i.e., the number of iterations required for each optimization. The optimization in (3.12) is implemented for each detected range-Doppler cell to obtain all the targets' angle information. Thus, the computation complexity of the first optimization step mainly comes from the number of range-Doppler cells with detected targets. The number of iterations depends on the convergence threshold set; specifically, for the setting in this thesis, an average of 80 times per optimization was performed.

3.2.4. SUMMARY OF THE PROPOSED ALGORITHM

Based on the fundamentals described in the previous subsections, ego-motion estimation can be performed by optimizations starting from the received radar signal. To summarize, the steps of the proposed approach are described as follows.

Step 1: *Detection based on the RDS.*

After 2D FFT on fast time and slow time, the radar raw signal will be converted into RDS data. Using 2D cell-averaging CFAR detection [52], the detected targets' indices in range and Doppler domain will be obtained.

Step 2: *Optimization of two consecutive RDS's angle information.*

By stacking all the RDS starting from time u_0 for each detected target, as in equation (3.4), the optimization can be performed as described in (3.12) to obtain the azimuth $\hat{\theta}_{u_1}$ and elevation angle $\hat{\phi}_{u_1}$ for the detected targets at time u_1.

Step 3: *Estimation of the rotational speed.*

For the time u_1, we can obtain the matrix $\mathbf{T_c}(u)$ containing ranges, azimuths angles and elevation angles for each detected target as shown in (3.5). By performing the projection (3.16), the locations of the targets are converted into a Cartesian coordinates system. The matrix in (3.5) can be converted as $\mathbf{T_p}(u)$. The locations of all the detected targets at two different times are stacked separately in the same order to form two matrices $\mathbf{T_p}(u_0)$ and $\mathbf{T_p}(u_1)$.

$$\begin{bmatrix} \hat{x}_k(u) \\ \hat{y}_k(u) \\ \hat{z}_k(u) \end{bmatrix} = \begin{bmatrix} \hat{r}_k(u)\cos(\hat{\theta}_k(u))\cos(\hat{\phi}_k(u)) \\ \hat{r}_k(u)\sin(\hat{\theta}_k(u))\cos(\hat{\phi}_k(u)) \\ \hat{r}_k(u)\sin(\hat{\phi}_k(u)) \end{bmatrix} \tag{3.16}$$

Kabsch algorithm [53, 54] as shown in Algorithm. 1 is then used here to obtain the rotation matrix $R \in \mathbb{C}^{3\times3}$ between two datasets.

Algorithm 1: Kabsch algorithm

Get the position matrix of point clouds from two datasets $\mathbf{T_p}(u_0)$ and $\mathbf{T_p}(u_1)$, where p_i and p'_i are the coordinate values of each point, respectively.
Calculate the centroid of each point cloud:
$p = \frac{1}{n}\sum_{i=1}^{N_k} p_i$
$p' = \frac{1}{n}\sum_{i=1}^{N_k} p'_i$
The displacement vector of each point relative to the centroid is defined as:
$q_i = p_i - p$
$q'_i = p'_i - p'$
Calculate the covariance matrix of those points:
$H = \sum_{i=1}^{N_k} q q'^T$
Perform the SVD decomposition:
$H = U \wedge V^T$
$R = VU^T$
The rotational matrix R can be obtained.

Then, the rotation angle for each axis can be calculated by the elements in the obtained rotational matrix R:

$$\begin{bmatrix} \Theta_p \\ \Theta_r \\ \Theta_y \end{bmatrix} = \begin{bmatrix} \tan^{-1}(\frac{R_{3,2}}{R_{3,3}}) \\ \tan^{-1}(\frac{-R_{3,1}}{\sqrt{R_{1,1}^2+R_{2,1}^2}}) \\ \tan^{-1}(\frac{R_{2,1}}{R_{1,1}}) \end{bmatrix} \tag{3.17}$$

Hence, each component of the rotational speed will be:

$$\begin{bmatrix} \omega_p \\ \omega_r \\ \omega_y \end{bmatrix} = \begin{bmatrix} \frac{\Theta_p}{T(u_1-u_0)} \\ \frac{\Theta_r}{T(u_1-u_0)} \\ \frac{\Theta_y}{T(u_1-u_0)} \end{bmatrix} \tag{3.18}$$

where T is the chirp duration time.
Step 4: *Estimation of the translational speed.*

Start by stacking the two antenna elements vector starting from time u_0 and time u_1 for each detected target (m_{Nk}, n_{Nk}), as in equation (3.9). The optimization can then be performed as described in (3.15) to obtain the translational speed of the radar $\hat{v}_{rx}, \hat{v}_{ry}, \hat{v}_{rz}$.

The proposed algorithm is summarized in the pseudocode shown in Algorithm 2, and the corresponding block diagram was drawn in Fig.3.2.

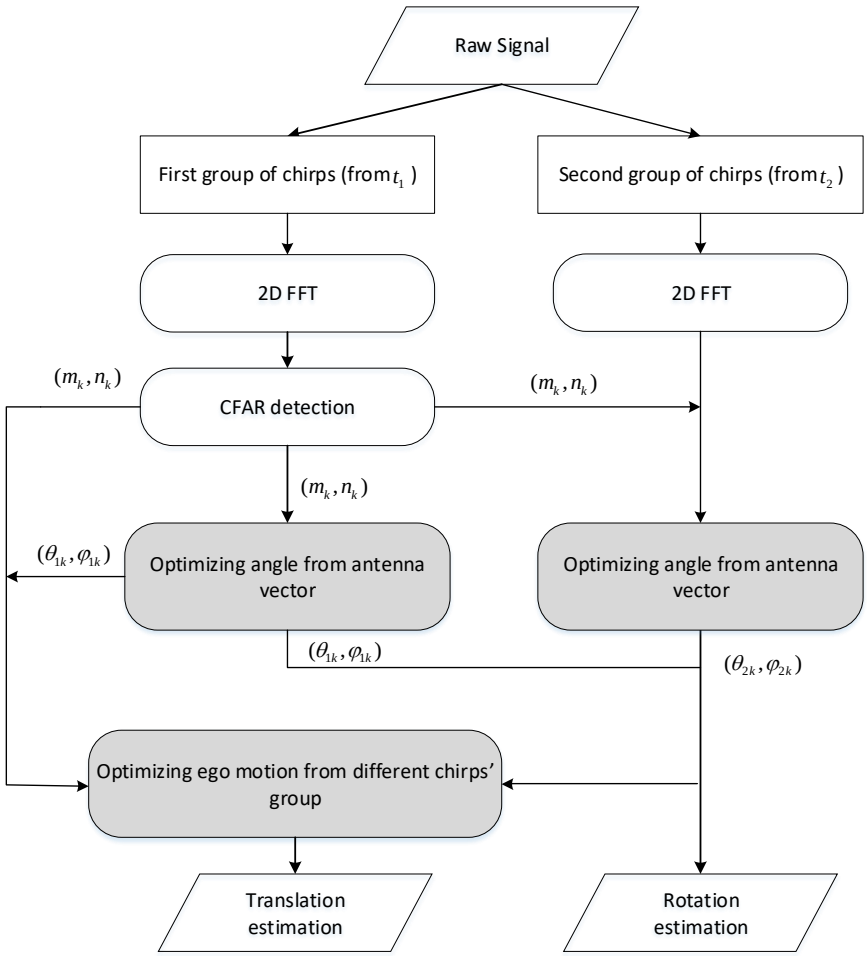

Figure 3.2: The block diagram of the proposed method, where after obtaining raw radar data, a 2D FFT is performed for a different group of chirps with different starting times t_1 and t_2. This is followed by CFAR detection and a proposed optimization process to finally obtain the ego-motion estimation, i.e. the estimation of the rotation and translation velocity components.

3.2.5. LIMITATIONS

A detailed discussion of the results is shown in the following section, where some limitations of the current formulation of the algorithm are reported.

Algorithm 2: 3D ego-motion estimation

Perform 2D FFT on fast time and slow time for the groups of chirps starting from time u_0 and u_1 in a frame to obtain the RDSs $\hat{z}^{p,q}(m,n,u_0)$ and $\hat{z}^{p,q}(m,n,u_1)$ as in (3.1)
Perform 2D cell-averaging CFAR detection [52] on RDS $\hat{z}^{1,1}(m,n,u_0)$ to get the targets' range-Doppler cells $[(m_1,n_1);(m_2,n_2);...;(m_{Nk},n_{Nk})]$.
Stack all the detected RDSs at time u_0 and u_1 to get $\mathbf{Z}(m_k,n_k,u_0)$ and $\mathbf{Z}(m_k,n_k,u_1)$
Form the measure data X as in (3.10) and build the model data Y as in (3.11).
Use pattern search for solving the optimization problem (3.12) to estimate the azimuth and elevation angle $[\hat{\theta}_k(u_0),\hat{\phi}_k(u_0)]$ and $[\hat{\theta}_k(u_1),\hat{\phi}_k(u_1)]$.
Extract the range information $\hat{r}_{o_1}(u)$ from the detection of the range-Doppler matrix.
Project the detected targets from polar coordinates to the cartesian coordinates, as in (3.16).
Perform the Kabsch algorithm as shown in Algorithm 1.
Calculate the rotational angle of each axis as in (3.17).
Calculate the rotational speed as in (3.18).
Stack all the detected RDSs at time, u_0 and u_1 to get $\mathbf{T_t}(u_0)$ and $\mathbf{T_t}(u_1)$ as in (3.8)
Form the measure data P as in (3.13), and build the model data Q as in (3.14).
Use pattern search for solving the optimization problem (3.15) to estimate the translational speed, i.e. $[\hat{v}_{rx},\hat{v}_{ry},\hat{v}_{rz}]$
The 3D ego-motion estimation can finally be obtained.

On the one hand, it is noted that the ego-velocity estimation quality depends on the number of detected targets in the scene. These cannot be distributed in every range and Doppler cell, which means that too many targets will degrade the performances of the proposed method (see Table 3.3 in the following section). On the other hand, too few targets will lead to higher errors in the ego-motion estimation because of the residual uncertainty.

Also, the second optimization step relies on the Doppler information. Thus, the maximum estimated velocity for the algorithm should be less than the maximum unambiguous velocity V_{max}. The current generation of MIMO automotive radar often applies TDM to achieve orthogonal transmit signals. Thus, the maximum unambiguous velocity can be expressed as:

$$V_{max} = \frac{\lambda}{4T_c * N_{ta} * N_{te}} \tag{3.19}$$

where N_{ta} and N_{te} are the number of transmitters for azimuth and elevation directions, respectively. The result with the radar parameters used in the simulation and listed in Table 3.1 is approximately 80 km/h. It should also be noted that working with Code Division Multiplexing or Frequency Division Multiplexing rather than TDM means that the unambiguous velocity range can be further extended.

3.3. 3D ITERATIVE EGO-MOTION ESTIMATION FOR DYNAMIC SCENARIOS

The moving targets will introduce extra Doppler velocities when calculating the ego-motion estimations. Combining the estimated velocities with the target's positions, one can derivate the ego-motion-induced Doppler for each detected target. The real Doppler estimation of the detected targets can be obtained from the radar Doppler processing as well. If the differences between the two values are larger, the target will have its motion. Thus, the following iterative method is proposed to distinguish the moving and static targets.

Moving targets in the scene will introduce additional Doppler components so that the velocity V_d in our signal model (3.7) will be the combination of the vehicle ego-motion and the targets' motion. Most Doppler-based algorithms in automotive, such as Doppler beam sharpening and SLAM and SAR implementations, will be affected by this. Also, the ego-motion estimation presented in the previous section will be affected, and the model for dr_k in equation (3.7) will face the mismatch problem and degrade the estimation results. Given the diversity of moving target classes and their motion models in automotive, reducing their effect in the ego-motion estimation process will be challenging.

3.3.1. PROPOSED METHOD

To reduce the moving targets' influence, a feedback loop is added to the flow chart of the proposed iterative method, as shown in Fig. 3.4. The Doppler/velocity estimation $V_{dd}(m_k, n_k)$ will be obtained from the range-Doppler spectrum detections. The iteration will be at first initialized with the first rough estimation from (3.9), i.e., the Doppler/velocity estimation $V_{dd}(m_k, n_k)$. During each iteration, all the detected targets will be iteratively divided into virtual static and virtual moving targets groups. Only the static targets will be processed to derive more accurate ego-velocity estimation results. Specifically, the proposed method contains two important steps: the updating of the static targets' group and the breaking point to end the iterations.

UPDATING OF THE STATIC TARGETS' GROUP

The vector $[v_x^i, v_y^i, v_z^i]$ is the velocity estimation from the $i-th$ iteration. Knowing each target's position $[\theta_k, \phi_k]$, the target's ego-motion induced Doppler/velocity can be calculated as:

$$V_{ed}^{i+1}(m_k, n_k) = v_x^i \cos\theta_k \cos\phi_k + v_y^i \sin\theta_k \cos\phi_k + v_z^i \sin\phi_k \tag{3.20}$$

An example of the motion-induced velocity results and the detected velocity are drawn in Fig. 3.3, where differences between these two values due to the movement of targets are visible. The velocity difference $D_V^i(m_k, n_k) = V_{ed}^i(m_k, n_k) - V_{dd}(m_k, n_k)$ is defined as the difference between the ego-motion induced velocity V_{ed} and the velocity obtained from the spectrum V_{dd}. Suppose the difference between the ego-motion-induced velocity and the velocity obtained from the spectrum is higher than a certain threshold. In that case, the target will be marked as a moving target. This label is obtained from the last iteration and shown as follows:

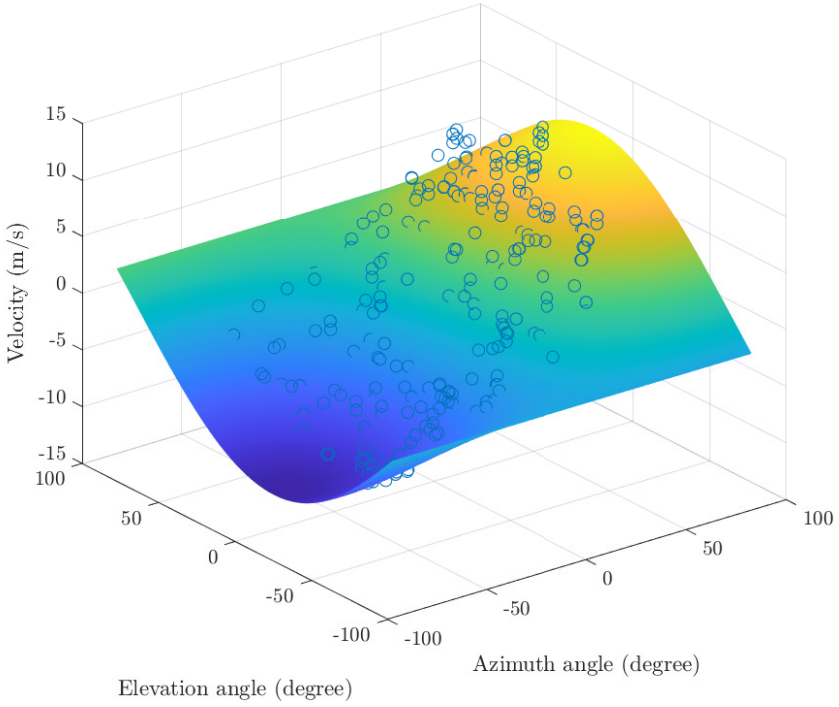

Figure 3.3: An example of estimated velocity surface plot with the detections and calculated motion-induced velocity values. The blue points denote the detection results, while the surface plot shows the motion-induced velocity value in each azimuth estimation position.

$$Label(m_k, n_k) = \begin{cases} static & |D_V^{i+1}(m_k, n_k)| \leq D_c E(|D_V^i|) \\ moving & |D_V^{i+1}(m_k, n_k)| > D_c E(|D_V^i|) \end{cases} \tag{3.21}$$

The static targets will be stacked together to form the matrix for translational motion $\mathbf{T_t}^{i+1}(u) \in \mathbb{C}^{N_a * N_e \times N_k}$ according to equation (3.8), and an optimization algorithm will be implemented to derive the new estimation $[v_x^{i+1}, v_y^{i+1}, v_z^{i+1}]$.

BREAKING POINT TO END THE ITERATION

To ensure the number of iterations is enough to provide accurate estimation, different criteria are proposed here to define the threshold, namely Averaging-based-threshold (ABT), Ordered Statistics threshold (OST), and Ordered Statistics Averaging based threshold (OS-ABT),

Averaging based threshold (ABT):

$$E(abs(D_V^{i+1}(m_k, n_k))) - E(abs(D_V^i(m_k, n_k))) < \epsilon \tag{3.22}$$

where ϵ is the tolerant distance of moving targets, E is the operation of expectation.

Ordered Statistics threshold (OST): The velocity differences D_V^* will be sorted according to their amplitude. A new sequence of the variables is defined as:

$$D_V^*(1) \leq D_V^*(2) \leq ... \leq D_V^*(K) \tag{3.23}$$

The iterations will then stop when:

$$D_V^{i+1}(k_{os}) - D_V^i(k_{os}) < \epsilon \tag{3.24}$$

Ordered Statistics Averaging based threshold (OS-ABT): The velocity differences D_V^* will be sorted to get the new sequence. To avoid some extreme case errors, the average is calculated after sorting. The iterations will then stop when:

$$E(D_V^{i+1}(1:k_{os})) - E(D_V^i(1:k_{os})) < \epsilon \tag{3.25}$$

where $(1:k_{os})$ denotes the values from the first to k_{os}.

The algorithm is summarized in the pseudocode shown in Algorithm 3, and the corresponding block diagram is drawn in Fig. (3.4). Summarizing, after obtaining raw radar data, a 2D FFT is performed, followed by 2D-CA-CFAR [52]. The initial ego-motion estimation is performed with the obtained information, and the motion-induced velocity is calculated and compared with the detected velocity. The detected points will be labelled, and the static targets will be sent to the iterative algorithm. These steps will be performed until the threshold is met and the final ego-motion estimation results are obtained.

Algorithm 3: Proposed iterative method

Initialization.
Obtain the velocity estimation for the detected targets $V_{dd}(m_k, n_k)$ and the initial estimation of translation speed $[v_x^1, v_y^1, v_z^1]$ with all the detected targets.
Iteration i.
Calculate the ego-motion induced velocity as in (3.20).
Distinguish static targets based on the threshold as in (3.21).
Form the new matrix for translation speed estimation $\mathbf{T_t}^{i+1}$
Implement the ego-motion estimation Algorithm 2.
    $i = i + 1$
Break the iteration when the threshold is met.
Obtain estimated results V_{ab} when using (3.22)
Obtain estimated results V_{os} when using (3.24)
Obtain estimated results V_{os-ab} when using (3.25)

3.4. 3D EGO-MOTION ESTIMATION RESULTS

To show the effectiveness of the 3D ego-motion estimation, several results based on groups of simulated point targets and realistic scenarios derived from the automotive radar datasets *RadarScenes* [15] are presented in this section.

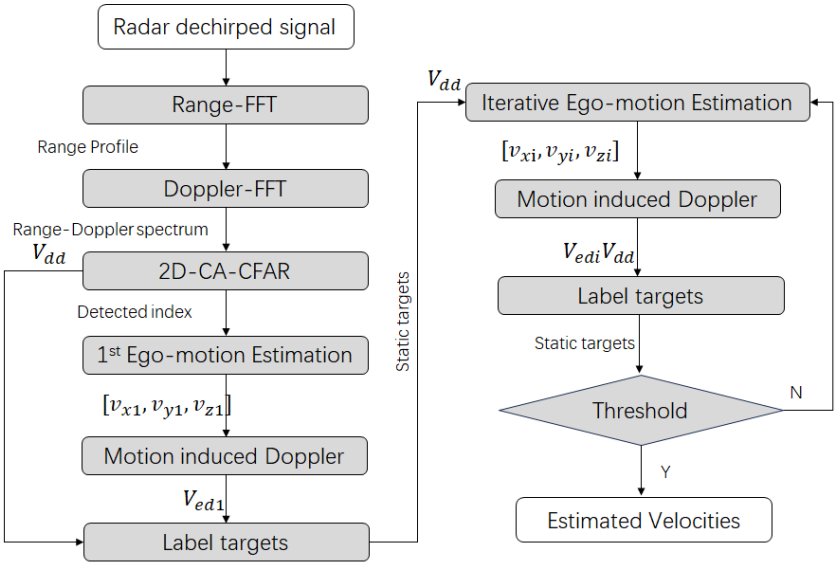

Figure 3.4: Block diagram of the proposed method for ego-motion estimation.

3.4.1. SIMULATED POINT TARGETS

We used a simulated 8×8 2D uniform linear array on the side-looking radar to evaluate the performance of the approach. To avoid ambiguity, the distances between different antennas are constant, $\frac{\lambda}{2}$. The radar parameters are listed in Table 3.1.

Table 3.1: The radar parameters for the verification of the method

Parameters	Value
Central Frequency (GHz)	77
Slope (MHz/us)	62.5
Sampling Rate (Msps)	32
Bandwidth (GHz)	1
PRI (us)	20
Number of chirps per frame	256

Fifty random targets are generated in the radar field of view, i.e. at random range values in the interval [0 m, 35 m], elevation in the interval $[0, 60°]$, and azimuth in the interval $[-30°, 30°]$ with random RCS. The vehicle is moving with random speed selected from a uniform distribution in all three coordinates where $V_x = \mathcal{U}(-10.8 \text{ km/h}, 10.8 \text{ km/h})$, $V_y = \mathcal{U}(32.4 \text{ km/h}, 50.4 \text{ km/h}) = \mathcal{U}(9m/s, 14m/s)$, $V_z = \mathcal{U}(-10.8 \text{ km/h}, 10.8 \text{ km/h})$ $= \mathcal{U}(-3 \text{ m/s}, 3 \text{ m/s})$, and $w_p, w_r, w_y = \mathcal{U}(-15°/s, 15°/s)$. The corresponding value of the three translational velocity components in m/s is $V_x = \mathcal{U}(-3m/s, 3m/s)$, $V_y = \mathcal{U}(9 \text{ m/s},$ $14 \text{ m/s})$, $V_z = \mathcal{U}(-3 \text{ m/s}, 3 \text{ m/s})$. All the targets are set to be static for this first simulation.

As this work is the first to implement 3 DoF ego-motion estimation using low-level

data from only one radar to provide a state-of-the-art reference, the work in [27] is modified by performing the proposed angle extraction in the rotation motion estimation shown in Section. 3.2.2 after detection on range-Doppler spectra, to further improve the angular resolution ability of the original method in that work by introducing Doppler information. Using 3+1D radar, the elevation and azimuth DOA results can be obtained and sent to the algorithm of [27] to get a 3 DoF estimation. This approach will be referred to as the '*modified DOA*' method in the rest of the chapter and used for comparison. All other state-of-the-art algorithms cannot be implemented without using consecutive frame data, so only the modified DOA algorithm and the proposed algorithm will be compared in this section.

A Hundred Monte Carlo tests were performed, and the error for the 3-dimensional velocity estimation is shown in Fig. 3.5, and the evaluation results are shown in Table 3.2. As no alternative method can provide the rotational speed estimation based on only one frame, the results of the proposed method are shown in Fig. 3.6 without comparison.

Table 3.2: The evaluation results for the translational ego-velocity estimation using simulated point targets

Velocity	**Parameter**	Proposed	Modified DOA
X direction	Mean (mm/s)	1.5	46
	Variance (10^{-4})	0.088	34.0
Y direction	Mean (mm/s)	4.0	51.2
	Variance (10^{-4})	0.573	43.0
Z direction	Mean (mm/s)	4.2	64.8
	Variance (10^{-4})	0.581	67.0

Regarding the estimation of the translational velocity, the proposed curve shown in Fig. 3.5 is closer to 0 with less fluctuation compared with the Modified DOA method. Also, the proposed method achieves the best performance for every velocity component, with smaller mean error and variance, demonstrating a robust estimation as in Table. 3.2. Regarding the estimation of the rotation velocity in Fig. 3.6, the error for pitch is 0.0348 rad/s, 0.0609 rad/s for roll and 0.0515 rad/s for yaw. The variance of the error in pitch is 0.002, 0.006 in roll, and 0.0045 in yaw, which is acceptable considering the small values of radar rotation velocity in the ground truth for the simulated scenario.

The performance of the ego-motion estimation will be influenced by the total number of targets in the scene, the ratio of moving targets concerning the total, and the size of the antenna array. A Hundred additional Monte Carlo tests were performed with respect to each of these parameters to assess their effect while keeping the radar parameters as listed in Table 3.1.

In this new simulation, five hundred targets are placed randomly in the radar field of view. The radar is moving in three directions with random velocity values. The moving targets' radial velocity follows the uniform distribution $V_r = \mathscr{U}(0\text{ km/h}, 10.8\text{ km/h}) = \mathscr{U}(0\text{ m/s}, 3\text{ m/s})$, with varying ratios of moving vs static targets. The SNR is set constant at 20dB. As shown in Table 3.3, the proposed method achieves the best estimation result in all three directions with respect to the mean value and variance of the estimation error. It is expected that with the increase of the moving targets' ratio, the performance

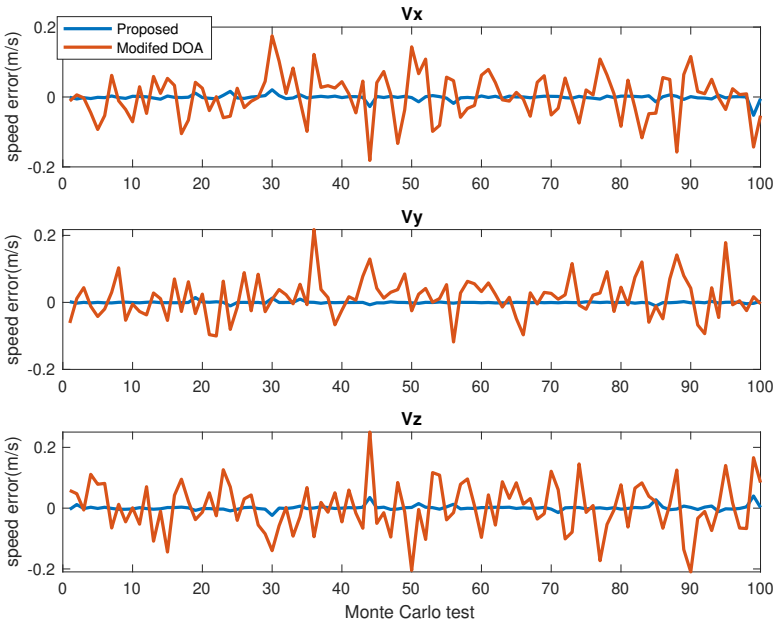

Figure 3.5: Performance comparison in terms of velocity error [m/s] for 3D translational velocity estimation for simulated targets. (a) Velocity in the X direction. (b) Velocity in the Y direction. (c) Velocity in the Z direction. The proposed method (blue) is compared with the modification of the method (red) in [27].

drops in all three directions. This is reasonable, as the targets' extra movement will introduce extra Doppler components, and the optimization step in (3.15) will suffer from this. However, the proposed method is generally less sensitive to this problem than the alternative method ('modified DOA'). The 'modified DOA' method performs estimation with detected range-Doppler-angle values instead of exploiting the phase domain, meaning that the extra Doppler velocity induced by the targets' random movement will introduce more errors than the proposed approach. The proposed method uses the least squares solution for solving the optimization problem so that those extra Doppler components will not influence the final result, as most targets are still static. As the ratio of moving to static targets increases (e.g., in a dense urban scene with many moving objects), the ego-velocity estimation accuracy decreases. The solution to this limitation is to separate moving and static targets and to utilize only those static targets for estimation to avoid the Doppler errors introduced by the targets' motion,as proposed in Section. 3.3.

To test the influence of the array size, another simulation was performed. Five hundred static targets are generated. The radar is moving with random velocities in the three directions. The results are shown in Fig. 3.7. The $Mean_p$ and $Mean_d$ denote the mean error value of the proposed method and the modified DOA method, respectively, while Var_p and Var_d are the error variances of the proposed method and the modified DOA method, respectively. The performance of the proposed methods is marginally improved with a larger array size, as the optimization (3.15) will highly rely on more data. In contrast, the performances of the modified DOA method remain almost the same with slight

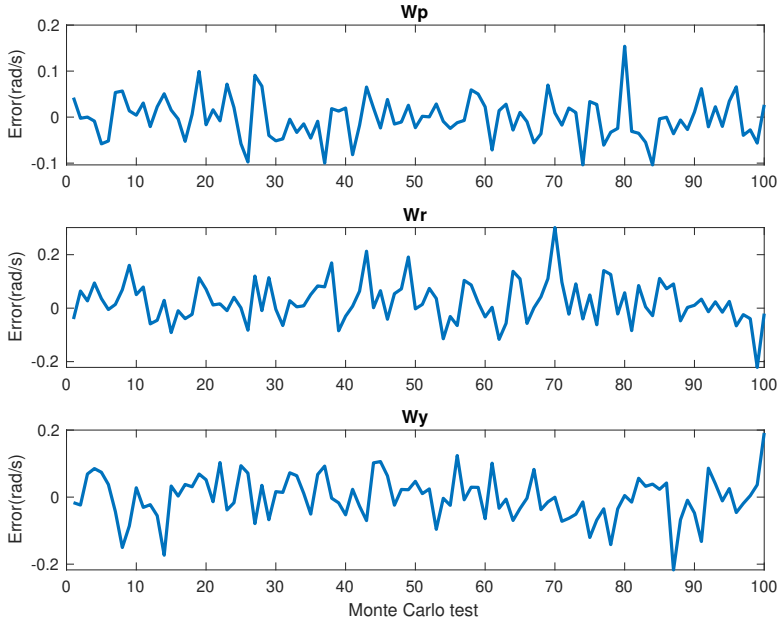

Figure 3.6: Performance of the proposed approach in terms of estimation error [rad/s] for 3D rotational velocity for simulated targets. (a) Pitch rotation speed. (b) Roll rotation speed. (c) Yaw rotation speed.

improvement. The angle information can be estimated with small array sizes because during the detection stage, the targets are separated in the RDS, and the different antenna vectors only provide the information of the differences.

As mentioned in Section. 3.2.5, the number of targets in the scene will influence the detection, and thus the angle estimation within the optimization in (3.12). On the other hand, if fewer targets are detected, the error will also increase because of the uncertainty. Another Monte Carlo simulation is performed with SNR equal to 20 dB to investigate this aspect with a different overall number of targets in the scene. All the targets are static with the same radar parameters listed in Table 3.1; only the ego-vehicle is moving at random speeds in the three directions. The results are shown in the bar plots of Fig. 3.8. The proposed method performs consistently better than the modified DOA method. The performance improves at first when more targets are present and then drops, which is visible for both methods as expected. Moreover, one extreme case where 10000 targets are distributed randomly in the scene with the vehicle speed equal to [18 km/h, 54 km/h, 7.2 km/h] was tested. The estimation achieves 0.17 km/h error in the x-direction, 0.97 km/h in the y-direction and 1.15 km/h in the z-direction, which is a relatively small proportion compared to the actual speed. This proves that with the algorithm's current formulation, the ego-velocity estimation will be impacted by the presence of many targets. However, it will still provide acceptable performances without failing.

To test the influence of the SNR, another Monte Carlo simulation was performed with values ranging within $[-5, 20]$ dB. There are no obvious differences between the different

Table 3.3: The evaluation results for the ego-velocity estimation's errors (mean and variance value in X Y Z direction) using the simulated point targets as a function of the ratio of moving targets

Parameters	Methods	Ratio of moving targets					
		10%	20%	30%	40%	50%	60%
Velocity in X direction							
Mean(m/s)	Modified DOA	0.1366	0.9086	1.2309	1.4939	1.6131	1.6763
	Proposed	0.0118	0.7721	1.1016	1.3706	1.4860	1.5486
Variance (10^{-3})	Modified DOA	1.6	281.5	310.9	423.7	338.0	343.7
	Proposed	0.1	249.3	281.8	400.8	306.8	306.4
Velocity in Y direction							
Mean(m/s)	Modified DOA	0.0494	0.6841	1.1074	1.4148	1.5805	1.7585
	Proposed	0.0181	0.6733	1.0972	1.4078	1.5794	1.7612
Variance (10^{-3})	Modified DOA	1.8	296.6	436.6	364.6	306.9	275.8
	Proposed	0.3	292.8	424.5	342.8	292.9	261.5
Velocity in Z direction							
Mean(m/s)	Modified DOA	0.0612	0.6861	0.7235	0.8307	0.9579	1.0586
	Proposed	0.0234	0.6705	0.7102	0.8153	0.9436	1.0407
Variance (10^{-3})	Modified DOA	2.4	565.4	340.6	360.4	412.2	551.5
	Proposed	0.3	538.3	343.2	332.4	389.7	529.6

SNR conditions in terms of estimation results. Hence, they are not reported here. This is related to the fact that the proposed algorithm does not require a certain number of targets detected, but a few static strong targets detected will be sufficient to apply the algorithm. CFAR detection considers the background noise level during its process, so the influence of SNR can be partly compensated. This proves that the algorithm is quite robust to the noise.

It is expected from the formulation in Section III that if the platform moves faster, the targets will separate more in the range-Doppler spectrum so that their angle estimation will be more accurate. So, this subsection has not reported the effect of this parameter (platform ego-velocity). It should also be noted that the velocity components are estimated within one frame with a high update ratio. Nevertheless, the estimation performance could be improved with the temporal information from past or future frames.

3.4.2. SIMULATED REALISTIC SCENARIOS

To test the proposed algorithm with more realistic data, two automotive scenarios are generated from the experimental data of the *RadarScenes* [15] dataset. To generate a scenario with denser targets, all four radars' data from the dataset [15] are used as the source of point scatterers for the simulation. The four radar sensors have a maximum range detection of 100 m and a field of view of about -60° to +60°. The range and radial velocity resolution are reported to be 0.15 m and 0.1 km/h, respectively. At the boresight direction, the angular resolution is about 0.5° and degrades to 2° at the outer parts of the field of view.

Two scenes are selected to represent two typical automotive scenarios, namely a European city street and a campus road. Two examples of images from the two selected

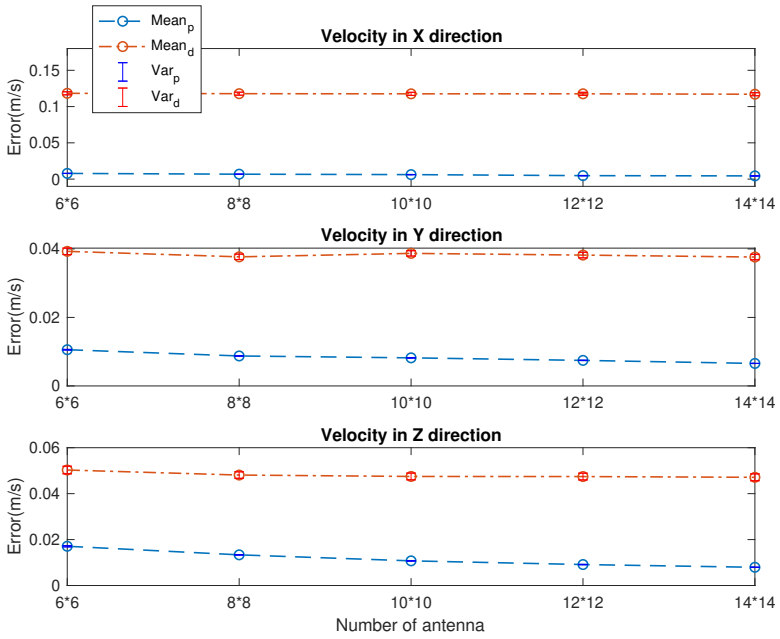

Figure 3.7: The error of the velocity estimation in [m/s] with different array sizes. The blue curves refer to the proposed method, whereas the red curves refer to the modified DOA method derived from [27].

scenes are shown in Fig. 3.9. As the RadarScenes dataset provides only processed radar point clouds for four radars orientated in different directions, we have used this radar point cloud to synthesize raw data for a single side-looking MIMO radar with a 2D uniform antenna array 8×8. The flowchart of the synthesize procedure is shown in Fig. 3.10. These newly generated raw data have been used for all ego-motion estimation algorithms.

To simulate a scene, all the scatter points extracted from the experimental dataset are converted into the world coordinates pre-defined in the dataset. As the dataset does not provide height information, all the targets have been set for simplicity at a fixed height of 3 m for this simulation. The velocity in the Z direction and the rotation in the X and Y direction are set to 0, as no ground truth is provided for those either. Based on the signal model described in Chapter 2, the corresponding radar signals are generated from the superposition of these scatter points in each frame. Subsequently, the proposed estimation algorithm is used to estimate the ego-velocity.

Two different evaluation metrics are defined to compare different ego-motion estimation algorithms using the simulated realistic data [59]. These are:

Absolute pose error (APE):

$$\epsilon_{APE} = \sqrt{\frac{1}{m}\sum_{i=1}^{m} \|P_{est}(i) - P_{gro}(i)\|^2} \tag{3.26}$$

where i is the frame index, m is the total number of frames, P_{est} and P_{gro} are the esti-

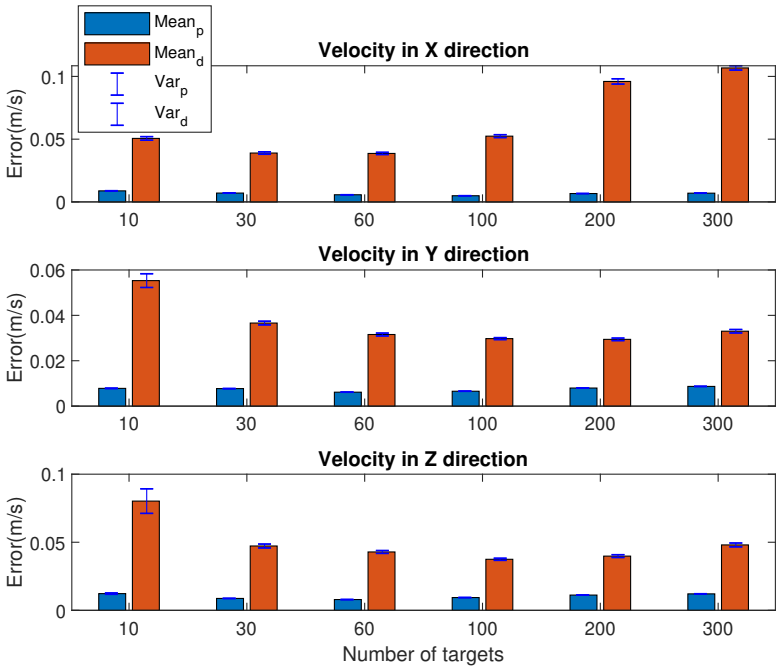

Figure 3.8: The velocity estimation error in [m/s] with different numbers of static targets. The blue bars refer to the proposed method, whereas the red bars refer to the modified DOA method derived from [27].

mated pose parameters and ground truth poses, respectively.

Relative trajectory error (RTE): The equation is given in (3.27), where T_{est} and T_{gro} are the estimated trajectory parameters and ground truth trajectory, respectively. N is a relatively short period to evaluate the metric, which is set as 100 and 300 frames in this chapter, equivalent to 1.85 s and 5.55 s, respectively. RTE is the average trajectory root-mean-square error (RMSE) over time segments with a length of 100 and 300 frames over which errors can accumulate.

Different ego-motion estimation algorithms have been implemented and compared for these tests, namely the one by *Kellner* [27], which is the first paper to tackle the ego-motion estimation problem using only radar and achieving a decent and robust performance; the *NDT-based* algorithm in [31] which uses probability and transformation to address the ego-motion estimation problem; the *Modified DOA* algorithm which is the updated version of Kellner's methods as previously explained in this section; and finally the proposed algorithm. For Kellner's method, the number of anchor points is chosen as 100, the probability of inlier ratio is 0.99, and the resulting number of iterations per scan is 10. Regarding implementing the selected NDT method, two important hyperparameters of the DBSCAN clustering algorithm [60], the maximum distance and the minimum number of samples, are selected as 2m and 5m, respectively.

The resulting vehicle trajectories from these algorithms are shown in Fig.3.11. All the methods maintain the basic shape of the ground truth trajectory. However, it is clearly

(a)

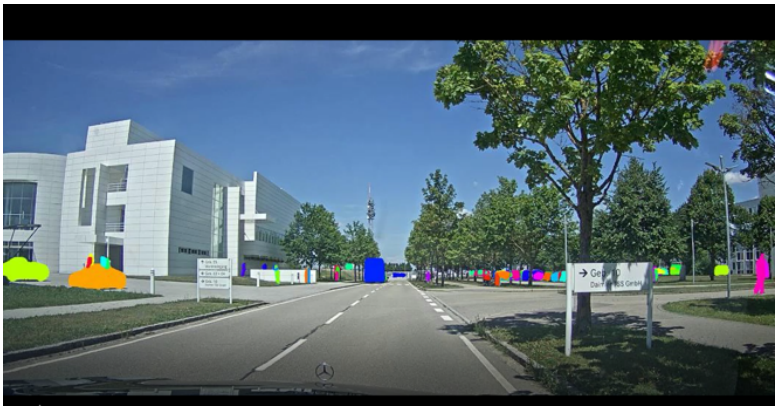

(b)

Figure 3.9: Pictures of the two experimental automotive scenarios from the dataset (a) Scene1, (b) Scene2.

shown that the proposed method and the modified DOA method generate estimated trajectories that follow the ground truth almost for the whole duration, while the other two drift or shift to other directions at some points. The proposed method and the modified DOA method provide better estimations than other alternative methods, based on the evaluation metrics shown in Table 3.4. The proposed algorithm provides the smallest error compared with other methods.

3.5. 3D ITERATIVE EGO-MOTION ESTIMATION RESULTS

To show the effectiveness of the proposed method, several results based on groups of simulated point targets are initially presented and analyzed. The same uniform square array of the side-looking radar for testing 3D ego-motion estimation is used here with the same parameters. The ϵ in equation (3.22), (3.24) and (3.25) is set in the following simulations as 0.2.

Four hundred targets are generated in the radar field of view at random range val-

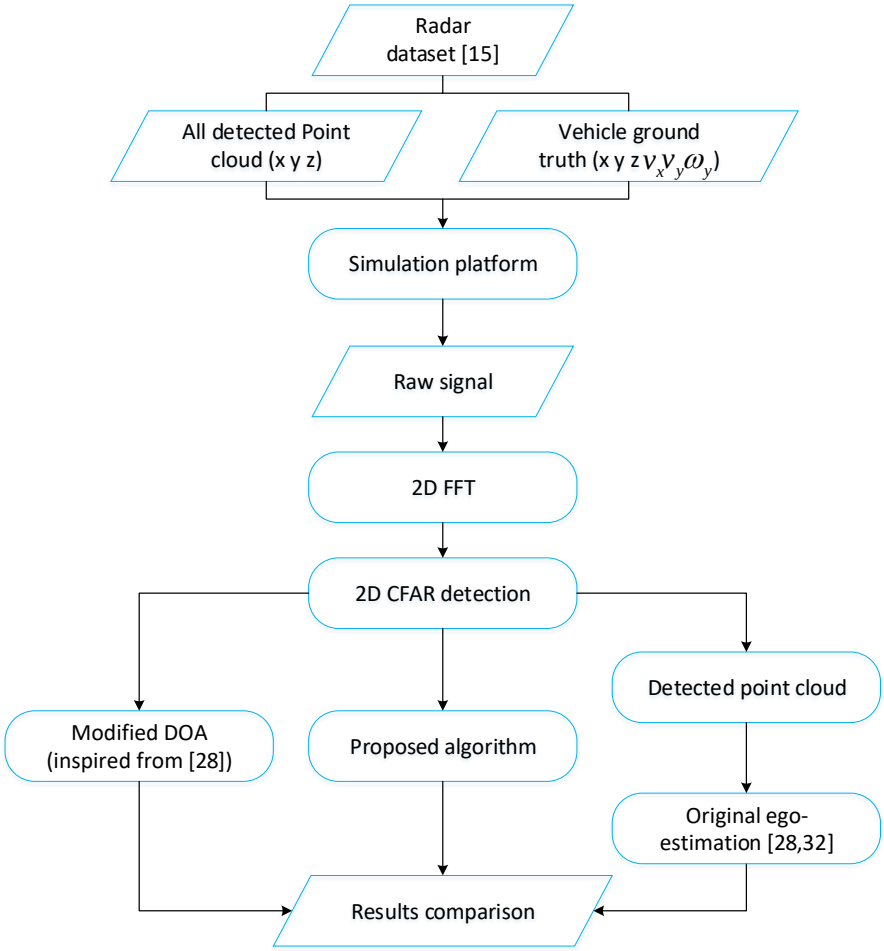

Figure 3.10: The comparison flowchart for the proposed method and the modified DOA method implemented on data from the simulated realistic scenarios generated from [15].

ues in the interval [0 m, 35 m], elevation in the interval $[-30°, 30°]$, and azimuth in the interval $[-60°, 60°]$. The amplitude of all scatterers is drawn from the uniform distribution $\alpha_{\mathbf{o}} = \mathscr{U}(0, 300)$. According to the Swerling model III, the amplitude can be seen as constant during one coherent processing interval. The scatterers are also assumed to be isotropic and provide constant amplitude and phase of the scattered field during the processing period, as in [61]. The vehicle is moving with random speed selected from a uniform distribution in all three coordinates where $V_x = \mathscr{U}(-10.8 \text{ km/h}, 10.8 \text{ km/h})$, $V_y = \mathscr{U}(14.4 \text{ km/h}, 46.8 \text{ km/h})$, $V_z = \mathscr{U}(-10.8 \text{ km/h}, 10.8 \text{ km/h})$.

One example of the velocity plot cut at $\phi = 0$ is extracted from the velocity surface

$$\epsilon_{RTE} = \sqrt{\frac{1}{m-N}\sum_{i=1}^{m-N}(\|T_{est}(i+N) - T_{est}(i)\| - \|T_{gro}(i+N) - T_{gro}(i)\|)^2} \tag{3.27}$$

Table 3.4: The evaluation results for the trajectory estimation (APE, RTE) using the realistic data from two scenes of [15]

Evaluation metrics		Methods			
		Modified DOA	Proposed	Kellner [28]	NDT [32]
		Scene 1			
APE(m/s)	Velocity in X direction	0.09	0.08	0.52	2.26
	Velocity in Y direction	0.06	0.05	1.89	2.02
RTE(m)	100frames	0.05	0.04	0.44	341.53
	300frames	0.11	0.10	0.70	1.02e3
		Scene 2			
APE(m/s)	Velocity in X direction	0.15	0.11	0.64	1.52
	Velocity in Y direction	0.10	0.10	1.49	1.87
RTE(m)	100frames	0.10	0.07	0.59	176.56
	300frames	0.26	0.21	3.43	604

in Fig. 3.3. As shown in Fig. 3.12, the estimated ego-velocity results after three iterations of the proposed method are closer to the ground truth than the estimation without iteration.

To test performances under different ratios of moving targets, 100 Monte Carlo tests are performed. The moving targets' radial speeds are selected from a uniform distribution $v_r = \mathcal{U}(-21.6\ \text{km/h}, 21.6\ \text{km/h})$. The ratio of total moving targets ranges from 10% to 50%, as in common automotive scenarios, many scatter points are often from static targets or clutter. The results for different threshold calculations, ABT, OST, and OS-ABT, are compared in Figure 3.13. With the proposed iterative method, the ego-motion estimation performances are improved compared with the conventional algorithm (blue line in the figure). The smaller the ratio of moving targets, the better improvement can be achieved. This is reasonable because outliers will show significant differences when the moving targets' ratio is lower. Thus, the iterative method can easily discard those outliers. However, as the moving targets' ratio increases, the differences become negligible because of high bias, reducing performances. Notably, as a combination of advantages from ABT and OST, the OS-ABT approach achieves the best results in almost every ratio and direction. Only when the ratio of moving targets is small, i.e. 10%, the ABT approach already achieves good performance. The OS might introduce more bias by setting a fixed order, slightly decreasing performance.

Another Monte Carlo test is performed, where 30% of targets in the field of view are simulated with random speeds. The radial speeds are chosen randomly in the range $[0 : v_r]$, with $v_r \in [3\ \text{m/s}, 6\ \text{m/s}, 9\ \text{m/s}]$. The results are shown in Fig. 3.14. As expected, the performance drops in all cases with increasing speeds because of the larger error

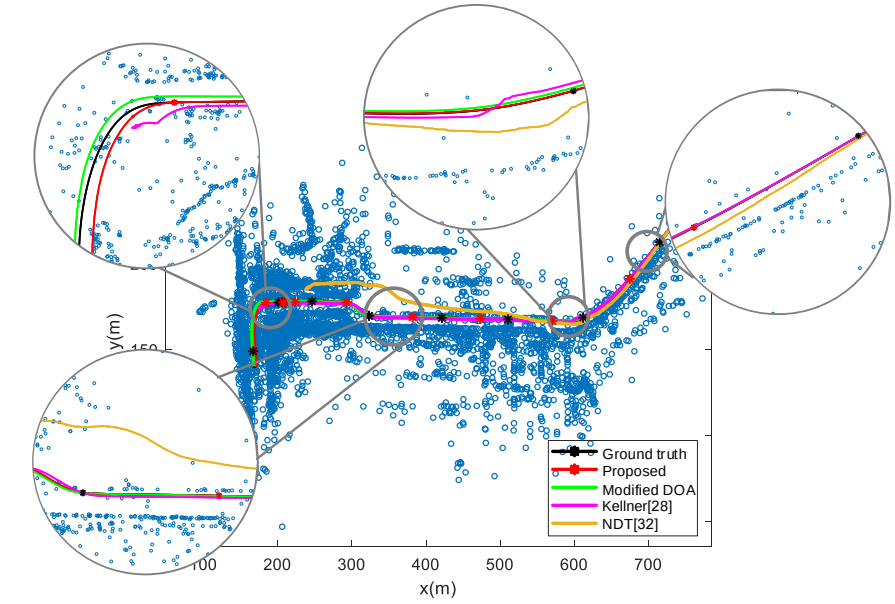

(a)

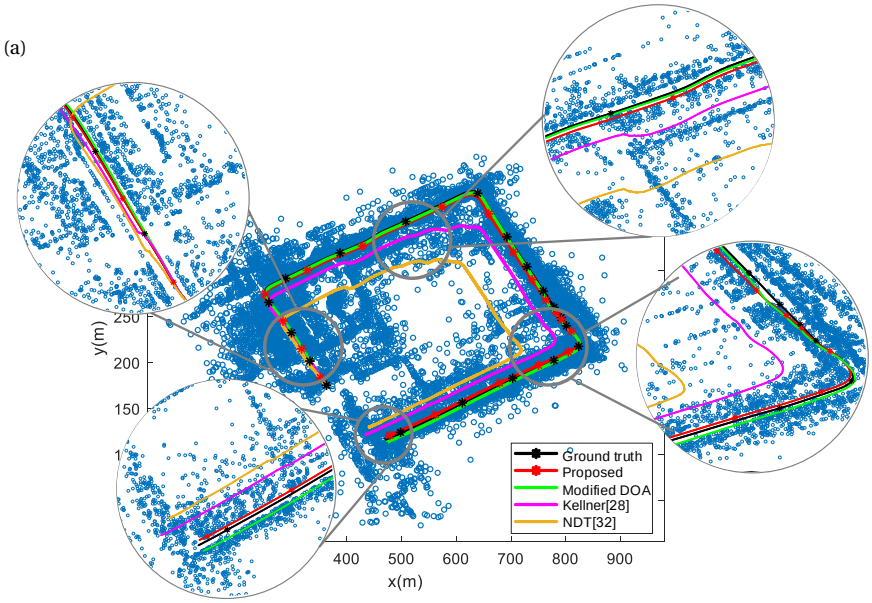

(b)

Figure 3.11: Estimated trajectory using realistic data from two scenes of [15] with different algorithms (a) Scene1, (b) Scene2.

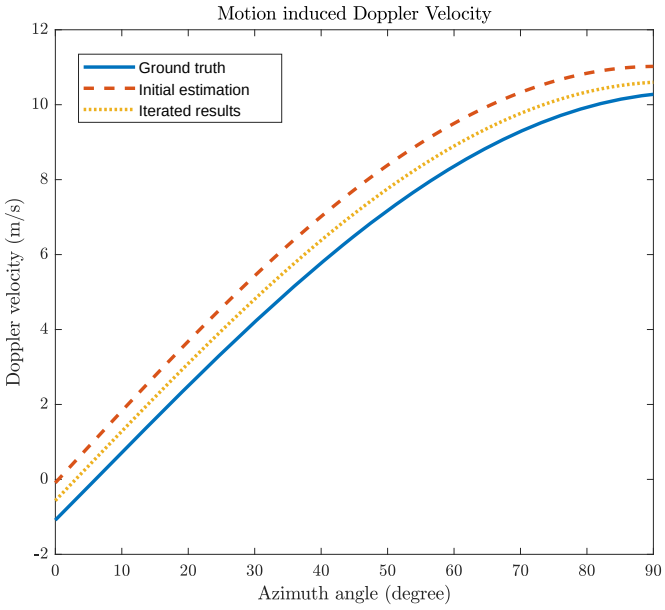

Figure 3.12: Comparisons of estimated velocity without iteration and iterative method, compared to the ground truth when 40% targets are moving in [0 m/s, 6 m/s] .

introduced in the ego-motion estimation. Still, all the iterative algorithms reduce the estimated error of the ego-motion estimation. OS-ABT achieves the best results in all directions and at all different speed ranges compared to the other two variants.

After testing different scenarios, i.e. different speeds of the targets and different ratios of moving targets, the parameters in the iterative algorithm are also tested. D_c in equation (3.21) is tested with different values, namely $[0.5, 1, 1.5, 2, 2.5]$. D_c is used to determine the boundary between the static targets and the moving targets. If the value is too small, the constraint will be too strict, and the algorithm will highly rely on the initial estimation and stop easily at an inaccurate separation of targets. On the other hand, if the value is too large, more moving targets will be used for the final estimation, leading to a drop in the estimation accuracy. The results are shown in Fig. 3.15. The red boxes are the proposed method without iteration, which does not depend on D_c. We can see that ABT and OS-ABT obtain better results than OST. The outliers for OS-ABT are less than ABT, providing a lower variance estimation. The performances first improve from $D_c = 0.5$ to $D_c = 1.5$ by relaxing the strict constraint, but then the errors increase again with higher D_c values.

The ϵ and k parameters in the OST & OS-ABT are also tested with different values, and with moving targets' ratio equal to 30% and targets' speed range equal to 3m/s. The results show that for $k >= 3$, the algorithm's performance remains broadly constant since the outliers are discarded in the iterations and only the static targets are selected.

As shown in Fig. 3.16, several extended targets in random shapes are also simulated

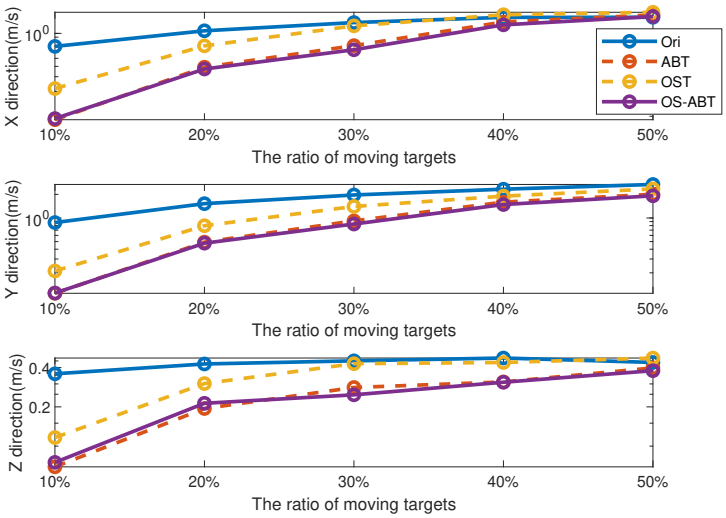

Figure 3.13: Ego-motion estimation error in three directions, with different ratios of moving targets present in the scene and different termination thresholds approaches (ABT, OST, OS-ABT).

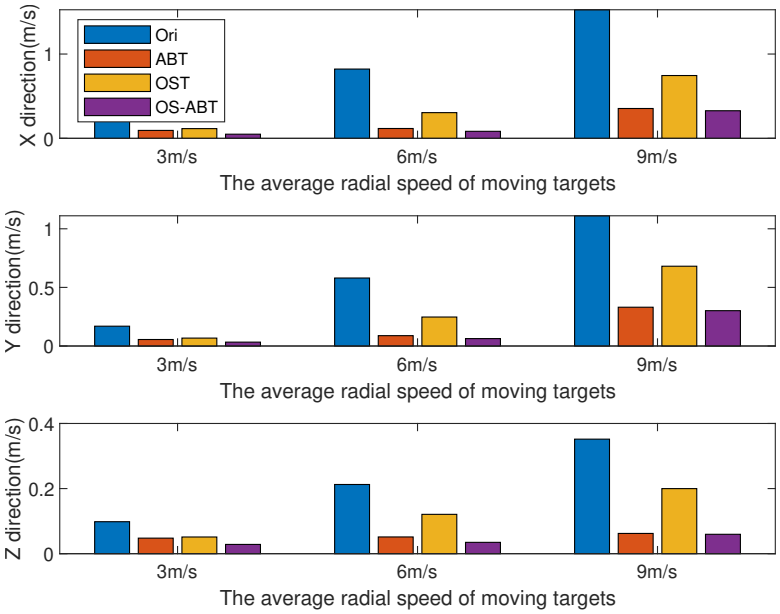

Figure 3.14: Ego-motion estimation in three directions, with targets in the scene moving at different average speeds; different termination thresholds approaches compared (ABT, OST, OS-ABT).

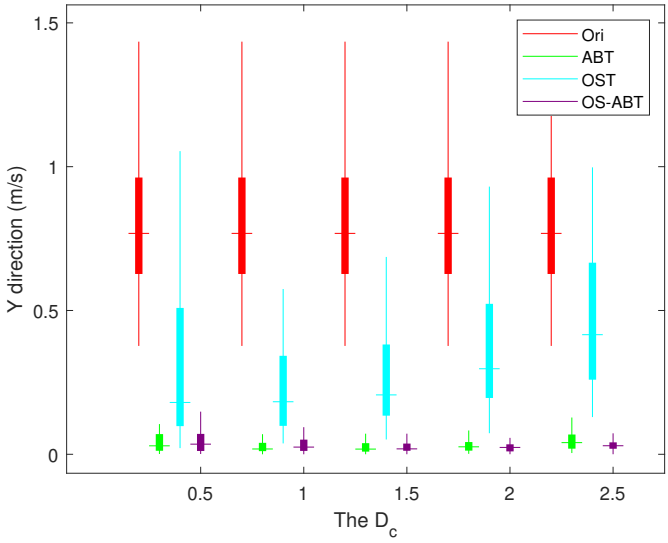

Figure 3.15: Ego-motion estimation in three directions with different values of the parameter D_c for different termination thresholds approaches (ABT, OST, OS-ABT).

as the targets in the radar's field of view. The signal generation will consider all the targets within the maximum range of 100m for this simulation. Based on the signal model described in Chapter 2, the corresponding radar signals are generated from each frame's superposition of the scatter points. The ground truth trajectory and estimated trajectories are compared in Fig. 3.16 to evaluate the algorithm performance in a continuous, more realistic sequence of frames. The estimated trajectory moves closer to the ground truth with the proposed iterative approach. APE for the original algorithm is 1.4046 m/s, with the proposed algorithm 1.1154 m/s and the alternative method in [27] 54.29 m/s. ATE for the original algorithm is 79.1799 m, with the proposed algorithm 29.0577 m and the method in [27] 778 m. RTE calculated with ten frames for the original algorithm is 2.4695 m, with the proposed algorithm 2.3209 m and the method in [27] 20.1m. All these evaluations prove that the iterative method improves the performance of the original algorithm.

3.6. CONCLUSIONS

This chapter proposes a novel algorithm for 3D ego-motion estimation, which can operate using only one multi-channel FMCW radar. The proposed algorithm uses the radar raw signals as input and estimates the 3 DoF velocity by estimating first the targets' position and then using their phase information from different times instances. The proposed approach achieves at least four times better results in terms of errors compared with algorithms operating on radar point clouds. Starting from raw signals provides opportunities to implement additional radar signal processing tasks, broadening the limits

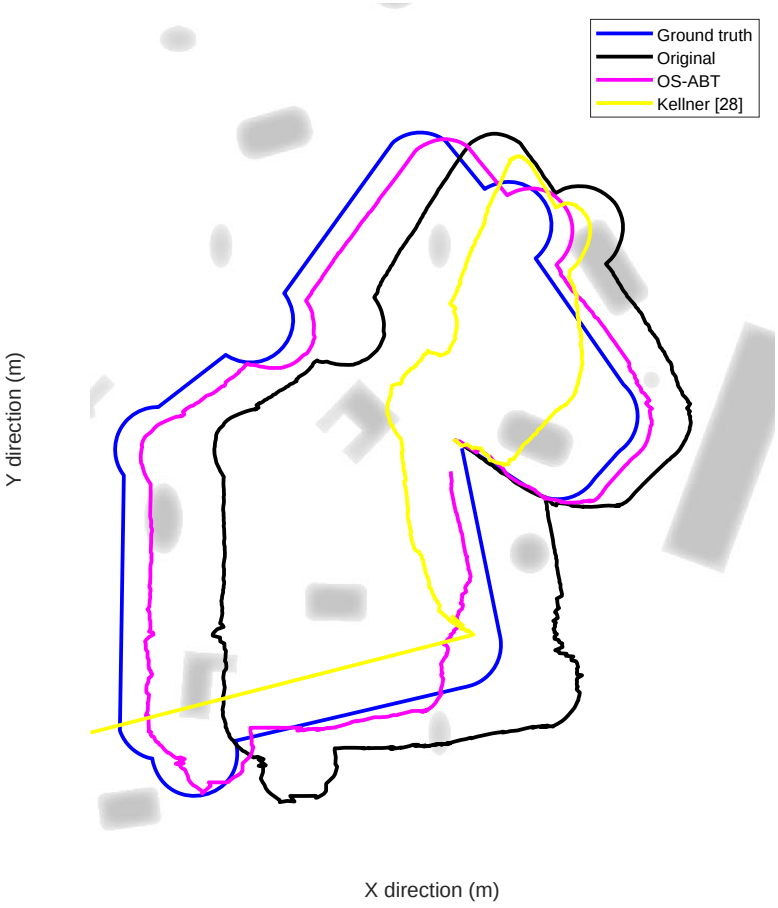

Figure 3.16: Estimated trajectory using simulated data with different methods.

of alternative SLAM approaches that operate only after several other processing steps to generate point cloud data.

Besides, to address the performance degradation with an increasing ratio of moving to static targets, an iterative solution is proposed by introducing a threshold to distinguish moving vs static targets and only using the static targets' information for ego-velocity estimation.

We verified both proposed algorithms with and without iteration by performing simulations with point-like and realistic scenarios generated from the *RadarScenes* dataset using one side-looking multi-channel FMCW radar. The superior performance of the algorithm in comparison with the state-of-the-art methods is demonstrated. The proposed approach provides very robust results in different scenarios.

4

2D MOTION ENHANCED IMAGING ALGORITHM FOR SIDE-LOOKING RADAR

The problem of high-resolution DOA estimation for imaging in automotive side-looking MIMO radar has been studied. A computationally efficient approach for side-looking arrays is developed, combining the generation of motion-enhanced snapshots and MIMO technology, thus exploiting the vehicle's movement and the spatial diversity of the transmit and receive antennas. Due to motion, a larger virtual aperture for azimuth estimation will be obtained, and the angular resolution for azimuth is boosted. With a better estimation in azimuth, the elevation estimation will be more accurate with generated motion-enhanced snapshots for elevation channels. The proposed method achieves the separation of targets that the traditional MIMO approach cannot discriminate, as well as better results than with other single snapshot DOA estimation techniques. Algorithm performance has been studied in simulations, and possible limitations have been discussed. In addition, the method has been verified experimentally with point-like and extended targets, and good agreement between simulations and experimental results has been observed.

Parts of this chapter have been published in:

S. Yuan, F. Fioranelli and A. Yarovoy, "An Approach for High-Angular Resolution Implementation in Moving Automotive MIMO Radar," 2021 18th European Radar Conference (EuRAD), London, United Kingdom, 2022, pp. 449-452.

S. Yuan, F. Fioranelli and A. G. Yarovoy, "Vehicular-Motion-Based DOA Estimation With a Limited Amount of Snapshots for Automotive MIMO Radar," in IEEE Transactions on Aerospace and Electronic Systems, vol. 59, no. 6, pp. 7611-7625, Dec. 2023.

4.1. INTRODUCTION

Autonomous driving requires high-resolution sensing capabilities, and thus, automotive radars must provide high-resolution information on the vehicle environment in the range-Doppler–azimuth–elevation domains. The side-looking region will help the self-driving vehicle to localize and map the surrounding environments; thus, side-looking radar is one of the important sensors for autonomous driving.

To obtain *high angular resolution*, large-aperture antenna arrays are created either via phased array [62], or SAR [63], or MIMO array techniques [64]. Phased arrays typically use numerous half-wavelength spaced antennas to form a large aperture with a narrow beamwidth. However, they are not an economical option for civilian applications. SAR techniques form a large effective (i.e., virtual) aperture array by moving a small antenna or array that reduces the number of physical antennas required for imaging. This provides a cost-effective solution for high-resolution imaging applications but cannot be used efficiently in the forward direction. MIMO radar technology exploits the spatial diversity of transmit and receive antenna arrays and has received considerable attention in automotive. Due to its ability to achieve high angular resolution with a few antennas, MIMO has been exploited in current automotive radar for ADAS [5]. However, the practical implementation on vehicles constrains the radar size and limits the number of MIMO antennas.

This chapter proposes a novel approach to enhance the DOA estimation with the radar's motion for sidelooking regions. Specifically, this article proposes a high angular resolution approach based on generating 'motion-enhanced snapshots within a single frame', suitable for automotive side-looking or corner-placed radar. The velocity of the radar can be derived from the motion of the ego vehicle, which can be obtained with the algorithm proposed in Chapter 3 or other sensors, i.e., GPS. By combining the movement of the radar with the spatial diversity of the transmit/receive antennas, larger coherent virtual apertures can be formed and provide enhanced angular resolution. In this chapter, the method is proposed to work with a limited amount of snapshots and deal with the vehicle's cross-forward motion via a modified steering vector. Furthermore, the proposed method does not need any prior information on the characteristics of the environment or the targets in the scene, making it suitable for practical automotive applications.

Extending the array aperture with radar movement has been researched in automotive applications. An approach forming a synthetic aperture for automotive MIMO radar has been explored in [65, 66]. However, the methods in these studies can only enhance the resolution in their region of interest, i.e., the range of angles where targets have already been detected. Therefore, an additional processing step is needed to first detect the targets and estimate their related DOA values, followed by the step of enhancing the angular resolution. The proposed method can directly image the targets in the radar field of view and use motion-enhanced snapshots coherently to reduce the computational cost of the DOA estimation. Other studies propose using the vehicle's trajectory to image the scenarios with the SAR approach. A two-radar approach is proposed in [67]: while one radar determines the vehicle trajectory, another radar utilizes SAR on the known trajectory. This method uses back projection, an imaging algorithm with high computational load and less practical use. In contrast, the proposed method uses a digital beam scan and compensates for the extra vehicle movements with the modified steering vec-

tor. The work in [68] uses residual motion compensation to improve the SAR image quality for automotive, but it still relies on snapshots across multiple frames. Doppler beam sharpening methods are proposed for automotive radar in [43, 69]. The velocity information was used for wideband DOA estimation with compensation of range migration and the presence of Doppler ambiguity [70], and for high angular resolution imaging [71]. Studies using neural networks have been proposed [72–75], but despite their good results, the question of their generalization capabilities to unseen scenarios remains.

Other methods aim to perform *DOA estimation with a limited number of snapshots*, which is specifically attractive in automotive radar. Some snapshots may be distorted by interference and thus should not be used for DOA estimation, while others may contain strong clutter and should also be avoided [76]. Furthermore, functionalities such as adaptive cruise control and emergency brake initiation require a fast, online estimation of targets' relative distances, speeds, and DOA. Hence, it is not uncommon to use only a few usable snapshots for DOA estimation [5]. For example, the modified MUSIC in [77] uses the Hankel matrix to form the autocorrelation matrix for a single snapshot case. 2D CNN has been proposed in [78] to achieve super-resolution with a single snapshot, but with results only verified in simulations. Sparse sensing-based methods [79, 80] and IAA [81–83] are potentially applicable to a single snapshot or a limited number of snapshots. However, they both assume targets' sparsity and have high computational costs. Also, the Fourier interpolation methods proposed in [84] require the targets' sparsity to maintain acceptable performances. The reduced signal covariance matrix proposed in [85] operates on a limited amount of snapshots with an unknown nonuniform noise but is affected by the rank deficiency problem and requires the prior number of targets. A purpose-designed array such as the massive uniform linear arrays in [86] focus on improving DOA estimation with a few snapshots but are designed for communication applications rather than automotive. As in [87], Sparse MIMO radar arrays use genetic algorithms to interpolate the missing antennas in sparse arrays, but this is computationally intensive. The aforementioned algorithms either need heavy computational load or a priori information, such as the number of targets in the scene or do not consider a variable time interval between the data acquisition periods. Alternatively, some ideas on creating a large virtual aperture (i.e., the sum co-array and the array aperture extension) using sensor motion under very simplistic scenarios have been discussed in [88, 89]. This chapter proposes a novel formulation of the antenna array aperture extension due to platform motion. This includes a novel expression for the steering vectors to compensate for the error from the complex motion of the vehicle, a formulation with lower computational load via an approximation in the time tag, and a signal model accounting for the variable time interval for the data acquisition periods. To the best of our knowledge, this approach has allowed for the first-ever imaging of extended targets with a priori unknown number of scatterers by using the proposed aperture extension, target imaging with arbitrary movements of the radar platform, and experimental demonstration with a commercial radar with an arbitrary reset time between frames.

Summarizing, the main contributions of this chapter are:

1. A high angular resolution DOA approach with low computational load is proposed by combining the vehicle's motion with automotive MIMO radar. The proposed method operates on a limited number of snapshots and includes the formulation

of a modified steering vector to compensate for errors due to complex vehicle motion and the approximation in the time tag.

2. The performance of the proposed method is analyzed in terms of its accuracy and probability of resolution and is shown to outperform alternative approaches from the literature. For the first time in the literature, a detailed analysis of the impact of forward and cross-forward velocity estimation errors on the performance of the DoA method has been performed. Both simulated data from point-like and complex extended targets, as well as experimental data, have been used in the method performance analysis.

The rest of the chapter is organized as follows. Section 4.2 provides the fundamental for DOA estimation based on a moving FMCW MIMO radar. The problem formulation, proposed method, and modified steering vector for the proposed method are demonstrated in Section 4.3. Simulation results for ideal point targets, complex extended targets, and the experimental tests, are provided in Section 4.4. Finally, conclusions are drawn in Section 4.5.

4.2. FUNDAMENTAL FOR DOA ESTIMATION BASED ON MOVING FMCW MIMO RADAR

4.2.1. GEOMETRY MODEL FOR THE RADAR MOVEMENT

A generic 1-D MIMO array placed in the y direction is considered, with the x-axis pointing toward the illuminated scene and assuming no movement in the z-axis as shown in Fig.4.1. The platform where the radar is installed is moving along the y-axis at speed $v(t) = [0, v_y(t), 0]$, with static objects located in the far field of the MIMO array. Using a two transmit and two receive antenna MIMO array as an example, as shown in Fig.4.1 with a solid line. Here, o refers to a target, and θ_o is its azimuth angle. All the targets' elevation angles are assumed to be 0. Thus the equation (2.10) will change from $D_{o,q,p}(t)$ to $D_{o,p}(t)$.

$$D_{o,p}(t) - D_{o,(p+1)}(t) \approx d \sin\theta_o \tag{4.1}$$

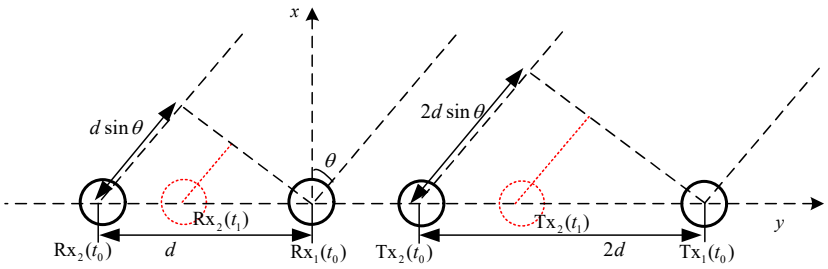

Figure 4.1: The geometrical configuration of the MIMO approach, where the solid black line shows the MIMO antennas at time t_0, and the red dotted line shows the antennas at time t_1 after the movement of the vehicle.

Inspired by SAR approaches, finer angular resolution can be obtained by exploiting the vehicle's movement to expand the MIMO virtual aperture. For example, in Fig. 4.1, after moving in a short time from t_0 to t_1, the target will remain in the same position, while the transmit and receive antenna in the black solid line marked with $\mathbf{R}x_2$ and $\mathbf{T}x_2$ will arrive at the positions marked with the red dotted lines.

When the vehicle moves with velocity v_y, each antenna will move by a range equal to $v_y|t_1 - t_0|$ along the antenna direction-y. Because of the two-way propagation, the difference in range between the target o and the a-th antenna moving position from time t_0 to t_1 will be calculated as in equation (4.2). Essentially, this equation is similar to equation (4.1), but with the difference in range to the target calculated between the same antenna a moving with the vehicle's velocity at two-time steps rather than between two separate antennas at the same time step.

$$D_{o,p}(t_0) - D_{o,p}(t_1) = v_y \frac{|t_1 - t_0|}{2} \sin\theta_o \tag{4.2}$$

4.3. THE PROPOSED DOA ESTIMATION BASED ON A LIMITED AMOUNT OF SNAPSHOTS

4.3.1. FUNDAMENTALS OF THE PROPOSED APPROACH

The array response at a specific time instance with data obtained at all the virtual receivers and corresponding to the same range-Doppler bin is defined as the *array snapshot* [5].

For side-looking radar on a vehicle, the target Doppler velocity is mainly related to the vehicle's movement; hence, the target Doppler cell will remain the same within one frame. However, to maintain the DOA coherency, i.e. ensuring that targets remain in their range bins during processing, only a limited number of snapshots N_L can be used for DOA estimation. This number is determined by the relative speed and the range resolution as:

$$N_L = \frac{\frac{c}{2B}}{T|v_r|} \tag{4.3}$$

where v_r is the radial target velocity caused by the vehicle's speed. It should be noted that for MIMO automotive radar working with time division multiple access (TDMA) mode, the PRI T in (4.3) will be multiplied by the number of transmitters, making N_L smaller. For this limited amount of snapshots N_L, the 3D data tensor (shown in Fig. 4.2) can be expressed as in (2.17). The first dimension is related to the angle estimation, the second to the velocity estimation, and the third to the range estimation.

As well known, only a coherent virtual aperture can improve angular resolution. This means that extra virtual antennas generated from the vehicle's movement are only usable for DOA estimation when the phase differences caused by such movement are the same as those between adjacent MIMO virtual ULA elements.

Here, for simplicity, we use the 2×2 MIMO in Fig.4.1 for demonstration. This means that t_1 and t_0 must satisfy the following equation to make the formed aperture coherent:

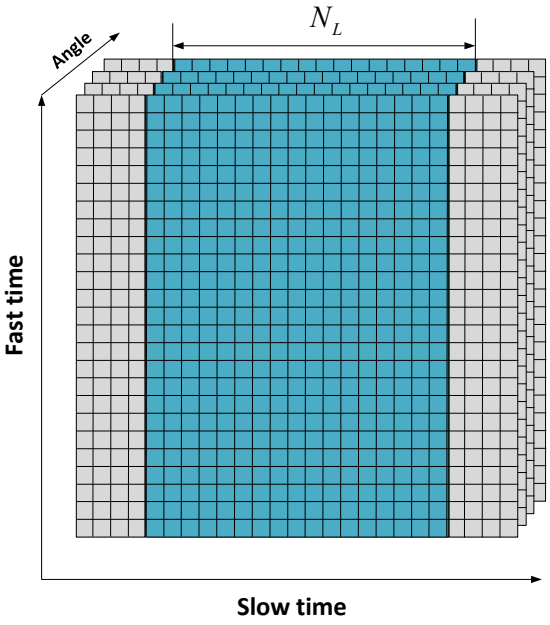

Figure 4.2: Sketch of the '*limited amount of snapshots*', with the 3D tensor with slow time, fast time and angle axes. The whole tensor depicts one frame, where the blue region includes the snapshots used for DOA estimation.

$$2v_r(t_1 - t_0) = d\sin\theta_o \tag{4.4}$$

This equation shows that the coherency relation depends on the position of the target o, i.e., on θ_o. However, considering only the Y component of the velocity, assuming that the effect of the other components is compensated (as described in the next section), then $v_r = v_y \sin\theta_o$. This removes the dependence on θ from (4.4).

Also, when the aperture is extended with the proposed method, then (4.4) becomes:

$$t_i = t_0 + iT_{ind}, i \in \mathbb{Z} \tag{4.5}$$

where $T_{ind} = \lfloor \frac{d}{2v_y T} \rfloor T$ is the approximate time tag interval for a coherent aperture extension. To satisfy the constraint of an integer slow time index, the $\lfloor\rfloor$ rounding operation is implemented here, thus introducing an approximation error.

If the time step satisfies (4.5), equation (4.2) for the 2 × 2 MIMO taken as an example will become:

$$D_{o,p}(t_0) - D_{o,p}(t_1) = d\sin\theta_o \tag{4.6}$$

This relation linking the range difference between the same antenna position moving from time t_0 to t_1 and DOA angle θ_o is the same as the range difference between adjacent Tx-Rx pairs, as shown in (4.1).

The vehicle's movement can be exploited to coherently extend the original MIMO virtual array by calculating a suitable time tag as in (5.4).

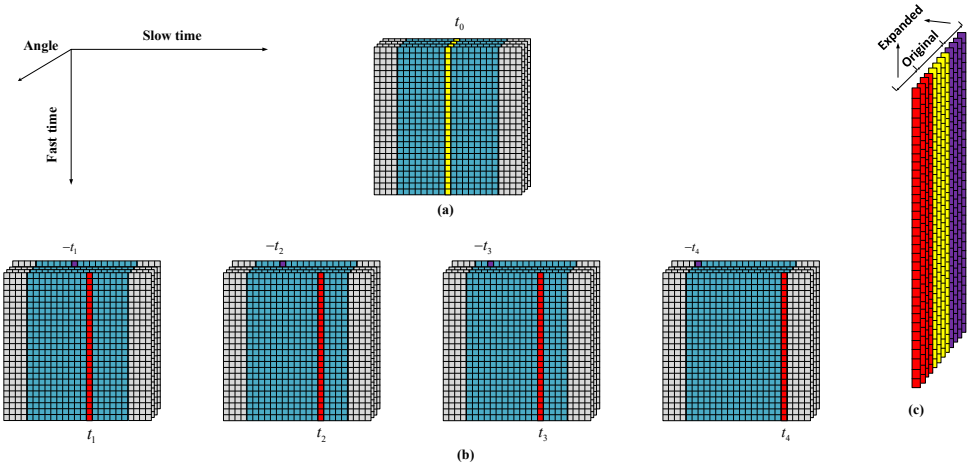

Figure 4.3: The principle of the proposed method: (a) 'Original snapshot' (OS, in yellow colour) taken from the middle of the group of snapshots usable for DOA also shown in Fig. 4.2. (b) 'Motion-enhanced snapshots' (MS, in red and purple colours) derived from the same group of snapshots in a frame. (c) The new 'DOA snapshot' formed by combining OS and different MSs according to the proposed method.

A graphical representation of the proposed approach is shown in Fig. 4.3. One snapshot (marked by yellow) is chosen in the middle of the N_L received snapshots usable for DOA estimation. This initial snapshot $\hat{S}(t_0)$ is named 'original snapshot (OS)' and is defined starting from (2.17) as:

$$\hat{S}(t_0) = \hat{z}(:, t_0, :) \tag{4.7}$$

As shown in Fig. 4.3(a), this choice provides the largest space for generating 'motion-enhanced snapshots (MS)' to coherently expand the OS $\hat{S}(t_0)$. Essentially, as shown in Fig. 4.3(b), the MS in red color $\hat{S}(t_i)$ is generated from the first transmitter and receiver with a positive time tag. In contrast, the MS in purple color $\hat{S}(t_{-i})$ is generated from the last transmitter and receiver with a negative time tag. These motion-enhanced snapshots (MS) are expressed as:

$$\begin{aligned} \hat{S}(t_i) &= \hat{z}(1, t_i, :) \\ \hat{S}(t_{-i}) &= \hat{z}(M_t M_r, t_{-i}, :) \end{aligned} \tag{4.8}$$

After generating multiple MSs, a new range-angle matrix $\mathbf{S}(t)$ can be formed, as shown in Fig. 4.3(c). The OS is located in the middle of the matrix with a length of $M_{\mathbf{t}}M_{\mathbf{r}}$in the dimension associated to the angle/DOA, while the MS is located to the left and right part with a total length of N_{ex}. Therefore, the new, extended range-angle matrix will have a length of $M_{\mathbf{t}}M_{\mathbf{r}} + N_{ex}$ in the dimension associated with the angle/DOA, which is essentially equivalent to having additional, multiple channels for DOA estimation. The matrix

$\mathbf{S}(t)$ can be written as in equation (4.9), with its rows corresponding to angle vectors over which DOA estimation can be performed.

$$\mathbf{S}(t) = \underbrace{[\hat{S}(t_{-\frac{N_{ex}}{2}}), ...\hat{S}(t_{-i}), ..., \hat{S}(t_0), ..., \hat{S}(t_i), ..., \hat{S}(t_{-\frac{N_{ex}}{2}})]}_{M_{\mathbf{t}}M_{\mathbf{r}}+N_{ex}} \tag{4.9}$$

where N_{ex} is the number of additional channels in the aperture formed with the proposed method. This larger aperture improves the resulting angular resolution.

4.3.2. THE MODIFIED STEERING VECTOR

The signal model in Section.2.3 is derived for 2D DOA algorithm. This chapter considers only the DOA algorithm in azimuth direction. Thus, the signal model and steering vector are modified correspondingly.

The signal model $\mathbf{Y}$ in equation (2.21) becomes:

$$\mathbf{X} = \sum_{m=1}^{M} a(\theta_m)s_m(t) + n(t) = \mathbf{A}\mathbf{S}_t + \mathbf{N} \in \mathbb{C}^{(M_{\mathbf{t}}M_{\mathbf{r}}+N_{ex})\times 1} \tag{4.10}$$

With the proposed method, for our generated array with motion enhancement, the steering vector is given by:

$$a(\theta_m) = [1, e^{-j2\pi d \sin\theta_m/\lambda}, ..., e^{-j2\pi(M_tM_r+N_{ex}-1)d\sin\theta_m/\lambda}]^T \tag{4.11}$$

However, in our proposed method, in order to obtain an integer slow time tag, the rounding operation is implemented in equation (4.5), thus introducing an extra time delay as:

$$t_e(i) = \frac{d}{2v_y} - (t_i - t_0) \tag{4.12}$$

This time delay will cause an error equivalent to an extra movement in the forward direction, thus leading to a phase error. For each MS formed with the proposed method, the resulting phase error can be written as:

$$w_{ea}(\theta_m, i) = e^{-j2\pi 2v_y \times t_e(i)\sin\theta_m/\lambda} \tag{4.13}$$

where i is the index in the calculation of the time tag defined in (4.5).

Furthermore, the vehicle's motion will be more complex than linear motion in one direction, i.e., there can be cross-forward movements during driving. This extra velocity component v_x will introduce an additional phase shift as:

$$w_{ev}(\theta_m, i) = e^{-j2\pi v_x \times (t_i - t_0)\cos\theta_m/\lambda} \tag{4.14}$$

Combining the two aforementioned sources of error, a compensation factor for the original steering vector in equation (4.11) can be written as:

$$w_e(\theta_m, i) = w_{ea}(\theta_m, i)\, w_{ev}(\theta_m, i) \tag{4.15}$$

It should be noted that this compensation is only needed for the additional MSs generated by the vehicle's movement but not for the original snapshot (OS).

Finally, the modified new steering vector will be expressed as:

$$\begin{aligned}\mathbf{a}_w(\theta_m) = \mathbf{a}(\theta_m) \odot [w_e(\theta_m, -\frac{N_{ex}}{2}), ..., w_e(\theta_m, -i), ..., \\ \mathbf{w}_e(\theta_m, 0), ..., w_e(\theta_m, i), ..., w_e(\theta_m, \frac{N_{ex}}{2})]^T\end{aligned} \tag{4.16}$$

where $\odot$ is the Hadamard product. $\mathbf{w}_e(\theta_m, 0)$ is the unit vector with length $M_t M_r$, recalling that the OS does not need any compensation. After concatenating the vector with the other scalars derived from equation (25), the total length would be $M_t M_r + N_{ex}$, the same as the range-angle matrix in (4.9).

4

Algorithm 4: Proposed DOA estimation algorithm

Calculate the time tag t_i as in (4.5).
Expand the number of snapshots for DOA estimation, generating the range-angle matrix $\mathbf{S}$ as shown in (4.9).
for θ in $[-90°, 90°]$ do
  Compute the modified steering vector $\mathbf{a}_\mathbf{w}(\theta)$ as in (4.16).
  Compute the angle column vector $\mathbf{X}$ for the range of a detected target.
  $R_{\mathbf{XX}} = E\left[\mathbf{X}\mathbf{X}^H\right]$
  $P_{DBF}(\theta) = \frac{\mathbf{w}_w^H(\theta) R_{\mathbf{XX}} \mathbf{w}_w(\theta)}{\mathbf{w}_w^H(\theta)\mathbf{w}_w(\theta)}$
endfor

4.3.3. SUMMARY OF THE PROPOSED ALGORITHM

Step 1: Expand the amount of snapshots for DOA estimation based on the vehicle's movement.

As discussed in Section 4.3.1, those snapshots (MSs) coherent with respect to the original MIMO virtual ULA are selected as in equation (4.5). Then, the new group of snapshots for DOA estimation $\mathbf{S}$ can be obtained by concatenating OS and MSs in a range-angle matrix, as in equation (4.9).

Step 2: Compensate the phase error in the steering vector.

As discussed in Section 4.3.2, the approximation error in calculating an integer time tag and the error due to additional cross-range velocity components need compensation. Those errors will translate to the phase domain, and the compensation is performed by the term (4.15). Hence, the final modified steering vector $\mathbf{w}_w(\theta)$ is formed as in (4.16).

Step 3: DOA estimation based on the new formed range-angle matrix $\mathbf{S}$ and modified steering vector $\mathbf{w}_w(\theta)$.

$\mathbf{S} \in \mathbb{C}^{K_d \times (M_\mathbf{t} M_\mathbf{r} + N_{ex})}$ defined in (4.9) is a range-angle matrix with K_d rows corresponding to fast time samples and $M_t M_r + N_{ex}$ columns corresponding to the equivalent number of channels to perform DOA estimation. After performing FFT along the fast-time for

range estimation, each matrix row containing detected targets can be considered an angle column vector to perform DOA estimation as in equation (6.1). For a given range index with detected targets, the DBF algorithm can perform the DOA estimation on the corresponding angle column vector **X** defined in (6.1).
The algorithm is summarized in 'Algorithm 4'.

4.3.4. POSSIBLE LIMITATIONS

Possible limitations can come from the memory size of the radar, its transmission rate, or the snapshot number in (4.3). They will influence the snapshot size in the Doppler dimension, which limits the maximum number of MS N_m we can form:

$$N_m = \left\lfloor \frac{min(L_d, N_L)}{\lfloor \frac{d}{2v_y T_p} \rfloor} \right\rfloor \tag{4.17}$$

where L_d is the total number of chirps in one snapshot, d is the distance between different receivers, T_p is the PRT.

The proposed method also requires enough movement to expand the aperture during the snapshots' period. This is highly related to the vehicle speed and the radar chirp duration in (4.5). The requirement for the vehicle speed is:

$$V_v \in [\frac{d}{4min(L_d, N_L)T_c}, \frac{d}{2T_c}] \tag{4.18}$$

Typical values of the speed for vehicles are in the range of approximately $[0.1, 117] km/h$. According to the 77GHz automotive radar parameters in [90, 91], for a normal speed in urban areas of $40 km/h$, the maximum amount of MS will be 40. To obtain a useful aperture size, the cross-range speed should satisfy $v_x \ll v_y tan(\theta)$, where θ is the target azimuth angle. The acceleration of vehicles is not expected to have a large impact as the frame's duration is relatively small. According to [92], the maximum acceleration of vehicles is 2.87 m/s^2, which will lead to 0.01 m/s in velocity difference within a snapshot.

4.4. RESULTS AND DISCUSSION

This section presents results based on simulated ideal point targets, simulated complex extended targets, and experimental data to show the proposed method's effectiveness. It is shown that targets overlapped in the angular domain are successfully separated by our method based on a limited amount of snapshots.

4.4.1. IDEAL POINT TARGETS

We used a simulated 2 × 4 MIMO radar for azimuth DOA estimation, comparable to commercial mm-wave modules operating at 77 GHz. The specifications of the radar parameters are listed as follows: the starting frequency of the FMCW chirp f_0 is 77 GHz, the chirp bandwidth B is 1 GHz, the chirp duration T_c is 30 μs, the sampling rate f_s is 34 Msps, and L = 256 chirps are processed in each frame. The MIMO antenna on the side-looking radar was located at the coordinate centre.

The Cramér-Rao Lower Bound (CRLB) on the accuracy of the DOA estimation in white noise has already been derived in the literature [93] as:

$$CRLB(\theta) = \frac{\sigma}{2}\{Re[\mathbf{X}^H(\theta)\mathbf{D}^H(\theta) \\ [\mathbf{I} - \mathbf{a}(\theta)(\mathbf{a}^H(\theta)\mathbf{a}(\theta))^{-1}\mathbf{a}^H(\theta)]\mathbf{D}(\theta)\mathbf{X}(\theta)]\}^{-1} \tag{4.19}$$

where σ is the noise power obtained from a given SNR, $\mathbf{a}(\theta)$ is the steering vector, $\mathbf{D}(\theta) = d\mathbf{a}(\theta)/d\theta$, and $\mathbf{X}(\theta)$ is a diagonal matrix whose diagonal elements describe the ground truth of the simulated targets.

A comparison between the MSEs of the five considered beamformers, namely original beamscan, proposed method, IAA-APES [82], single snapshot MUSIC[77], and compressed sensing [79] using CVX tools [94] for a limited amount of snapshots (i.e., 128 snapshots) is shown in Fig. 4.4 with the CRLB. Here, only one target is considered at a random position, and the number of independent Monte Carlo trials to generate this figure was 10^3. The MSE figure demonstrates the different beamformers' DOA performance in terms of their accuracy. As expected, the performance of all beamformers drops with increasing SNR, but the proposed method outperforms the other approaches in the literature. Furthermore, a comparison between the CRLB and the proposed DOA method at SNR equal to 6dB with different values of the expanding number N_{ex} is shown in Fig. 4.5, as well as the CRLB of the original array. The CRLB corresponds to the ULA with a size equal to the virtual aperture formed by exploiting the movement of the vehicle with the proposed method. One can observe that with N_{ex} equal to 9, the proposed method reaches the CRLB level of the original array. The MSs formed by the proposed method give the ability to approach and even break the CRLB for the current number of antennas.

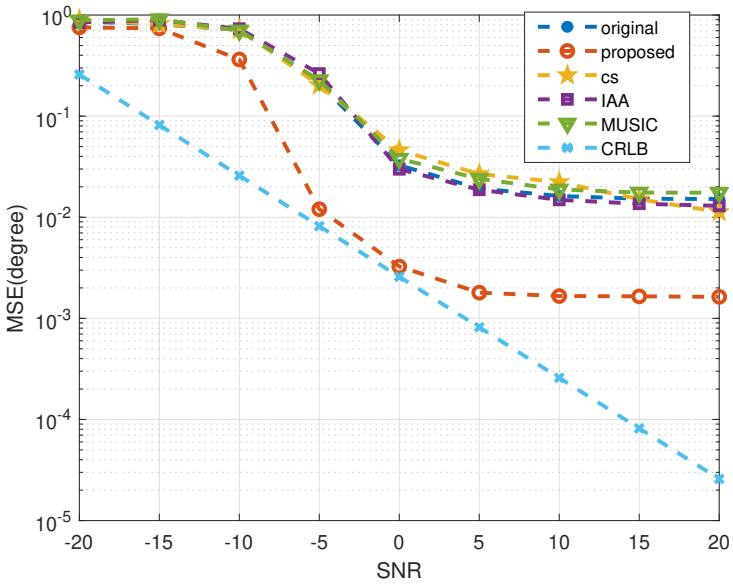

Figure 4.4: The MSE and CRLB for the DOA estimation of different algorithms in different SNR conditions.

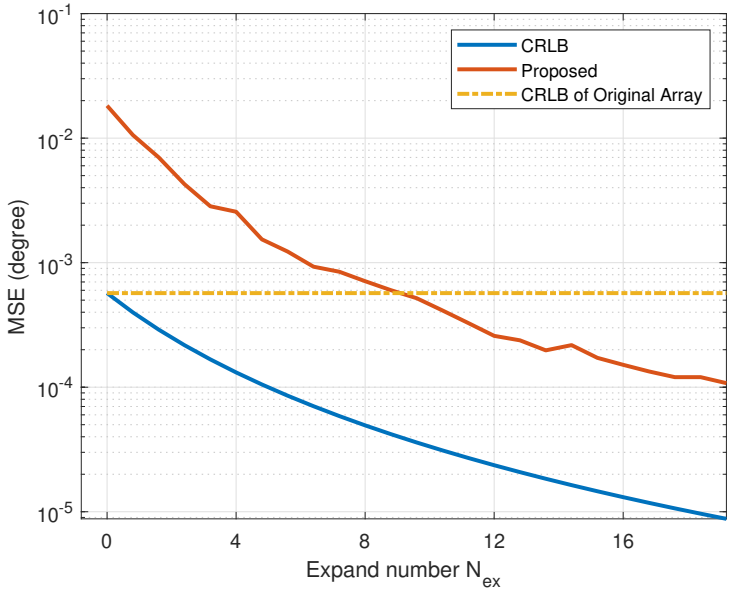

Figure 4.5: CRLB and MSE of the DOA estimation with the proposed method with a different limited amount of snapshots for different aperture sizes.

Additionally, the probability of resolution for the different DOA algorithms at different SNR values is shown in Fig. 4.6. The simulations are performed following this procedure: two targets are placed randomly in the range $[-40°, 40°]$; the number of independent Monte Carlo trials is 500; only those simulations that can separate two targets successfully will be added to the probabilities' numerator. The figure shows that the proposed method achieves the best resolution ability in different SNR conditions, while the single snapshot MUSIC is the worst. It should be noted that DOA estimation algorithms are, in general, applied in relatively high SNR conditions [65]; for example, commercial radar units such as those by Bosch or Conti are both evaluated on SNR = 20 dB. This is reasonable for automotive radar scenarios because it is more important to separate in angle closer targets (hence with higher SNR values) than targets further away (hence detected at lower SNR). So, under high SNR, the probability of resolution almost reaches the value of 90% with the proposed method.

To further compare the performances of different methods, a case where two targets are located at 10° and 16° is shown in Fig.4.7. The MIMO array on the side-looking radar is located at the coordinate centre, with targets placed at the same range bin of 10 meters to meet the Fraunhofer distance requirement [95] and ensure that they are in the far-field of the array. The radar moves with velocity $v_y = 10m/s$, and the SNR is set to 20 dB. From Fig. 4.7, one can observe that in this specific case, the proposed and the CS-based methods separate both targets successfully, while other methods fail to do so. Also, the proposed method provides DoA estimations equal to 10.6°and 15.8°, while the CS-based method estimates the target DoA less accurately: 8.3° and 17.2°.

The above results demonstrate that the proposed algorithm provides the best esti-

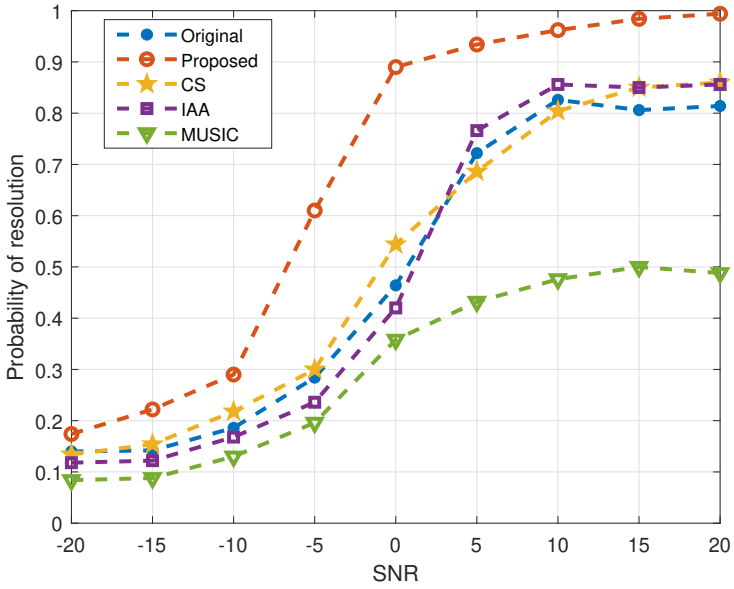

Figure 4.6: The probability of resolution of different algorithms in different SNR conditions.

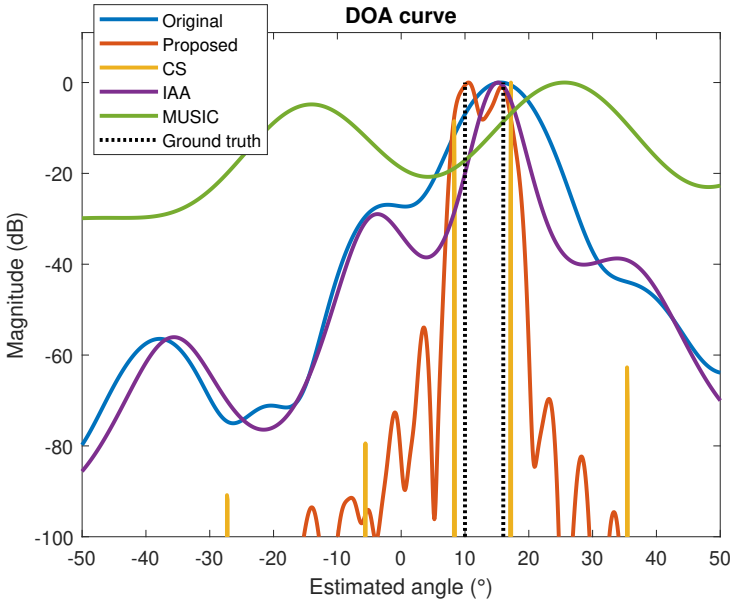

Figure 4.7: Simulated performance comparison of different methods for two targets scenario when 2 point targets are located at 10° and 16°.

mate of the targets' angles with a limited amount of snapshots in terms of accuracy and resolution capability. It is important to mention that no prior information about the tar-

gets is needed for the proposed method compared to compressed-sensing-based methods.

In terms of *computational complexity*, a Monte Carlo test and a theoretical analysis have been reported here. The expressions of the computational complexity for the proposed method is $O((m^2+2m)N)$, for the MUSIC method is $O(m^3+(2mn+m)N+m(log_2 m))$, and for the CS method based on CVX is $O(m^{3.5}ln(\epsilon))$, where m is the number of snapshots used, N is the number of the antennas, n is the number of targets which is required for MUSIC, ϵ is the duality gap defined in the primal-dual interior-point algorithm of the CVX formulation [96]. Thus, the computational complexity of the method proposed grows much slower with the number of snapshots than for the reference methods, and – contrary to MUSIC – the computational complexity is independent of the number of targets. Also, Monte Carlo tests were performed with random positions of two targets located in the same range bin for each test to estimate the average time taken to compute one 1D DOA for each algorithm. Specifically, 500 repetitions are considered for implementation in MATLAB on a standard desktop computer, which is common to all the considered algorithms. In terms of computation time, the original MIMO beamscan takes 10 ms, the compressed sensing-based algorithm takes 1014 ms, the single-snapshot MUSIC takes 323 ms, and the IAA-based takes 2072 ms, whereas the proposed method with $N_{ex}=48$ only needs $56ms$ to generate the DOA results. Compared with other algorithms in the literature, the proposed approach is the fastest to achieve the DOA estimation. The computational time increases if an increasing number of snapshots is used but with very good performances. For example, while using the proposed method with $N_{ex}=48$ increased the computational time, this is only about 5 times larger than the original MIMO beamscan (56 ms vs 10 ms); however, the performance in terms of both resolution and accuracy is significantly improved, as shown in Figures 4.4, 4.6.

To test the impact of the parameter N_{ex}, the same scenario is analysed in which the two targets are located at 10° and 15°. When the radar moves with velocity $v_y=5$ m/s, the results of the proposed approach with $N_{ex}=6$, $N_{ex}=24$, and $N_{ex}=48$ are compared with the original beamscan method. From Fig. 4.8, we can see that the proposed approach starts separating the two targets, and when increasing the aperture with higher expand numbers, the beam becomes narrower, and the DOA estimation is more accurate. In contrast, the original beamscan method cannot separate the targets and only estimates one single target approximately in the middle of the ground truth locations. In order to test the resolution ability more comprehensively, a Monte Carlo simulation for two close targets located at random positions is performed, and the data are processed for different expand number N_{ex} with results shown in Fig. 4.9. There is more error spread and outliers with smaller values of N_{ex}. As larger apertures are generated with higher N_{ex}, the mean value of the error for the DOA estimation of the two targets decreases.

As discussed in the preliminary results in [42], the performance of the proposed method will yield a better estimation with lower speed and shorter chirp duration but is more sensitive to speed fluctuation or chirp duration uncertainty. For the simulated setting in this chapter (the nominal vehicle velocity is equal to 5 m/s), the analysis in (4.20) shows that if the actual velocity is within this interval, $v_y \in [4.69\text{ m/s}, 5.73\text{ m/s}]$, then the

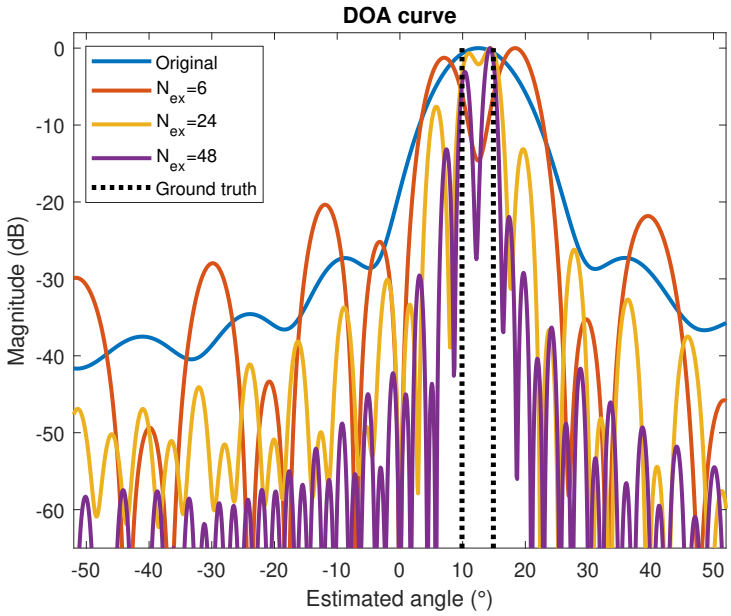

Figure 4.8: Simulated performance comparison of the proposed limited amount of snapshots' method vs original beamscan method, with different aperture sizes. The two point targets are located at 10° and 15°.

time index in (4.5) will be the same, providing the correct DOA estimation. Similarly, if the nominal radar speed becomes $9 m/s$, the tolerance interval to maintain reliable DOA estimation will become $v_y \in [7.4, 10.3] m/s$.

$$\begin{aligned} v_{min} &= \lfloor \frac{d}{2(T_{ind}+0.5)T} \rfloor T \\ v_{max} &= \lfloor \frac{d}{2(T_{ind}-0.5)T} \rfloor T \end{aligned} \tag{4.20}$$

The platform motion in automotive is usually more complicated than a simple one-dimensional translational movement. The error due to this complex motion can be further compensated in the steering vector for our proposed method, as discussed in section 4.3.2. For example, the comparison results using simulated point targets located at 10° and 15° are given in Fig. 4.10, with the same simulation settings used for the other results in this section. The DOA is accurately estimated as 10.2° and 15° after full compensation with the proposed modified steering vector. This includes the compensation of the approximation error due to the rounding operation in (5.4) and the error due to the presence of a velocity component in the cross-forward direction. It can also be seen that compensating for only the former error (denoted by a_{ea}) has a larger impact than compensating for only the latter error (denoted by a_{ev}).

When compensating for the effects of the presence of a cross-forward velocity component, the measurement error in the resulting phase might be significant, especially

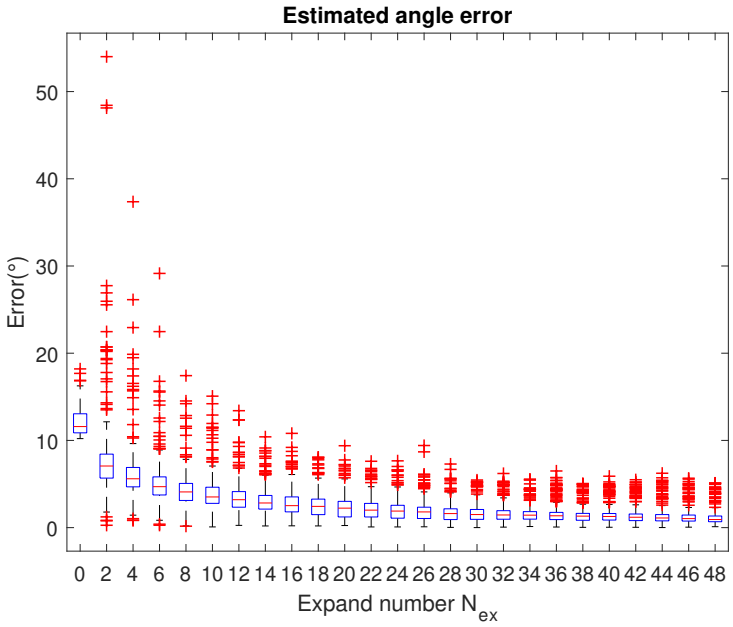

Figure 4.9: Box-plot for DOA estimation error from a 500-repetitions Monte Carlo test with different aperture sizes (parameter N_{ex} described in section III). The central mark in the blue box indicates the median, and the bottom and top edges of the box indicate the 25th and 75th percentiles, respectively. The whiskers extend to the most extreme data points considered as outliers, and the outliers are plotted individually using the '+' marker symbol.

when operating at mm-wave as in automotive radar. To analyse the impact of this velocity component and inaccuracies of this velocity component estimation, velocity measurement errors of different magnitudes have been considered in a Monte Carlo simulation. Their effect on calculating the time tag and subsequent compensation of the steering vector is then checked. Specifically, 500 simulations under SNR equal to 20 dB are performed with the radar moving at 10 m/s in the forward direction-y and at nominal 2 m/s in the cross-forward direction-x. The DOA MSE performance as a function of different magnitudes of the measurement error for the compensated velocity is compared in Fig. 4.11. As expected, not compensating at all with the proposed steering vector yields the highest MSE (plot denoted by 'WC'), whereas the ideal compensation, i.e. compensation that has no added velocity measurement error, yields the lowest MSE (plot denoted by 'CWT'). Notably, even when there are velocity measurement errors, there is an advantage in applying the proposed compensation based on the modified steering vector, as the resulting MSE is lower than the case of not compensating at all (three plots denoted by 'CW'). This shows the advantage of applying the proposed approach, even in the presence of a measurement error that would prevent reaching the ideal, error-free result.

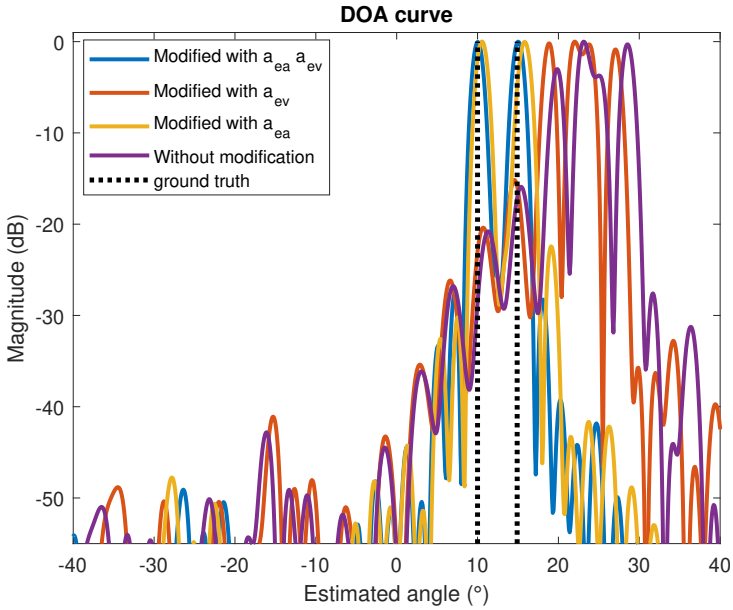

Figure 4.10: The modified steering vectors' influence on error compensation on the DOA estimation. The black lines indicate ground-truth target positions.

4.4.2. COMPLEX EXTENDED TARGETS

To demonstrate the imaging capabilities of the proposed method beyond ideal point targets, simulated models of vehicles perceived as extended targets are used. Each car model is represented by 273 point scatterers, which are generated randomly from the edges of the car as shown in Fig. 4.12.

Despite being placed around the positions of strong physical scatterers on the vehicle's body, these point scatterers are not meant to mimic precise electromagnetic scattering from a car. According to [97], the possible multipath propagation of electromagnetic waves due to reflection from the road is not considered to simplify the subsequent analysis but without restricting the generality of the proposed imaging approach. The multipath propagation of electromagnetic waves due to reflections from the road will influence the received signal, which may result in the appearance of additional points in the image when the specular reflection from the road surface is sufficiently strong (e.g., very smooth road surface, water layer above the road). Furthermore, phenomena of mutual occlusion of scatterers (i.e. one scatter point occluding another located behind it with respect to the radar line of sight) are not modelled for simplicity.

In this work, the amplitude of all scatterers is drawn from the uniform distribution, $\alpha_o = \mathcal{U}(0.5, 1)$. According to the Swerling model III [98], during a limited amount of snapshots (essentially one coherent processing interval), the amplitude can be seen as a constant. These scatterers are also assumed to be isotropic and provide constant amplitude and phase of the scattered field during the processing period, as in [61]. The two cars are the same size, with a width of $2m$ and a length of $4.8m$. According to the traffic

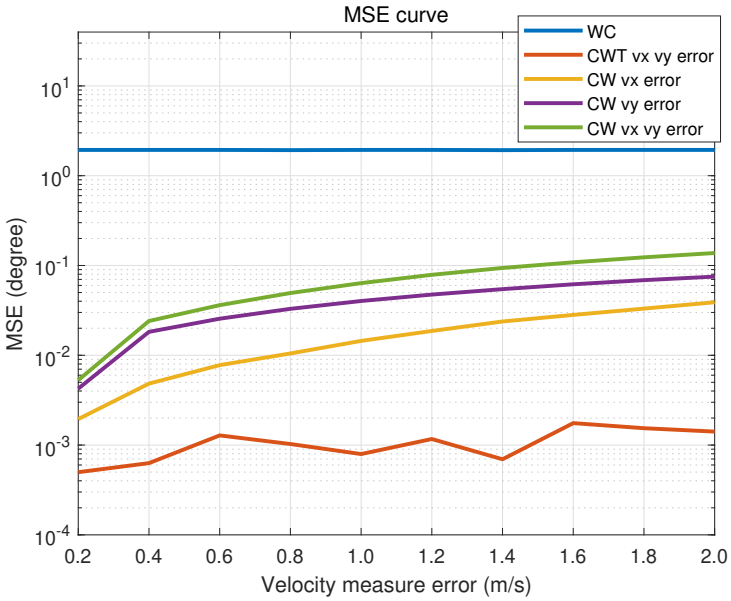

Figure 4.11: The MSE for the DOA estimation with or without compensation based on the modified steering vector with respect to different velocity measure errors. *WC* refers to the estimation without any compensation based on the modified steering vector; *CWT* refers to the estimation with compensation based on the modified steering vector but without velocity measure errors; *CW* refers to the estimation with compensation based on the modified steering vector in the presence of velocity measure errors.

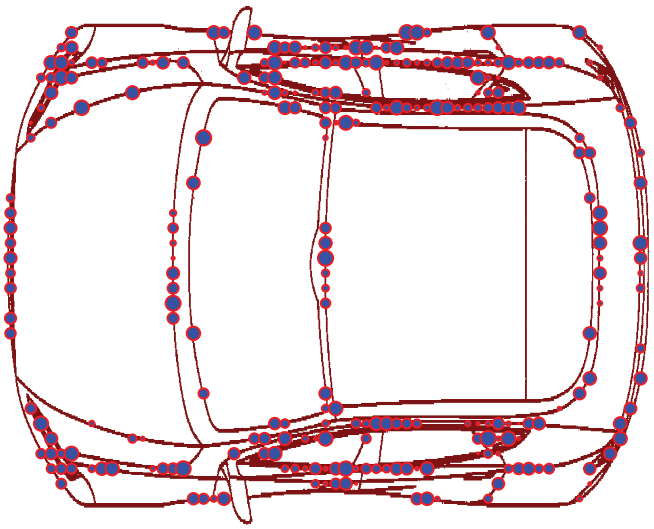

Figure 4.12: Extended target model of a car with 273 point scatterers.

rules, the spatial separation between them is $1m$. Both cars are located at $20m$ distance from the radar, and the angle is approximately 0 deg at the broadside. Using (2.17) for 1D MIMO radar, we can simulate the de-chirped signal for the car's scatterers, essentially treated as two extended targets. The results of the range-angle map with different DOA estimation methods are shown in Fig. 4.13, comparing the proposed method with the traditional beamscan and IAA-APES. As the compressed sensing-based method typically requires knowing the Doppler information of each target a priori, it is unsuitable for our extended targets simulation. Empirically, the capability of the proposed method to separate the two extended targets in the angular domain can be seen.

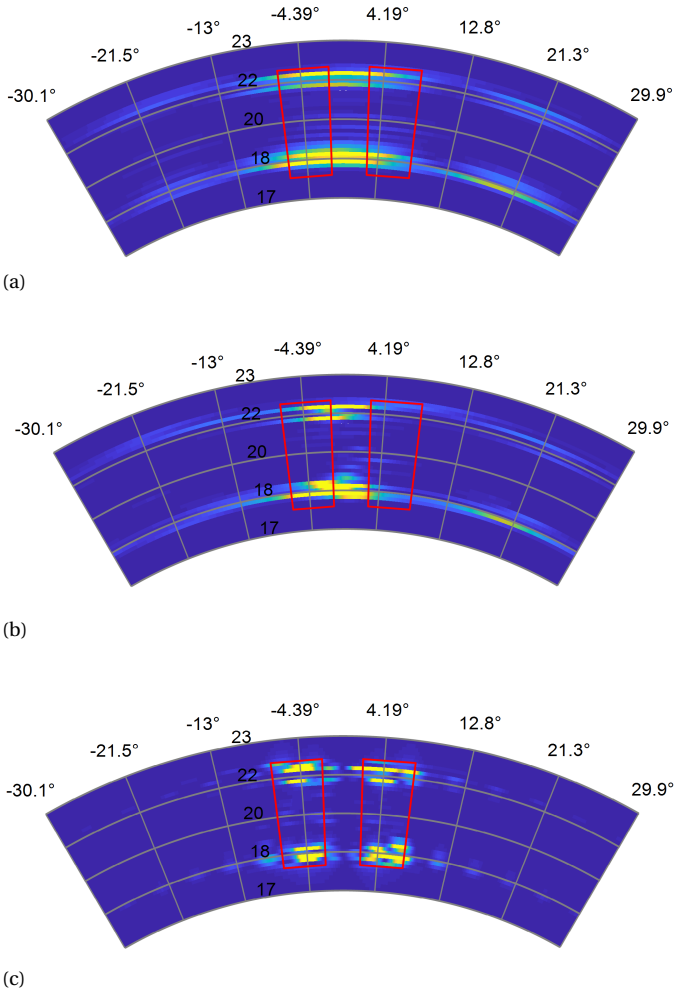

Figure 4.13: Simulated performance comparison of extended targets, where the red region is the ground truth of the vehicle. (a) Original beamscan method. (b) IAA-APES method. (c) The proposed method with the expanded aperture size equal to 56.

For performance evaluation, because of the relatively poor angular resolution, the extended targets cannot be imaged in fine detail as done for lidar or camera systems, which invalidates the usage of performance metrics such as branching factor, missing factor, and quality percentage [99]. It is also not straightforward to compare the result directly with ground truth, as done for point targets occupying only one single range-angle cell, or in evaluating precise range and Doppler estimation methods via the MSE metric [100].

For a quantitative comparison, the image contrast metric is introduced in this work to demonstrate the separation ability of the proposed method. Image contrast shows the differences in the intensity of each pixel of the image, which is used to evaluate the sidelobe suppression on SAR images [101, 102]. Suppose the two extended targets are better separated because of the improved angular resolution. In that case, the intensity values in the interval between them will be lower, leading to an increased image contrast value. The image contrast C is defined as:

$$C = \frac{\sqrt{E\left\{\left[I^2(i,j) - E\left(I^2(i,j)\right)\right]^2\right\}}}{E\left(I^2(i,j)\right)} \tag{4.21}$$

where $I^2(i,j)$ is the pixel intensity of (i,j); $E[\bullet]$ is the mean operation.

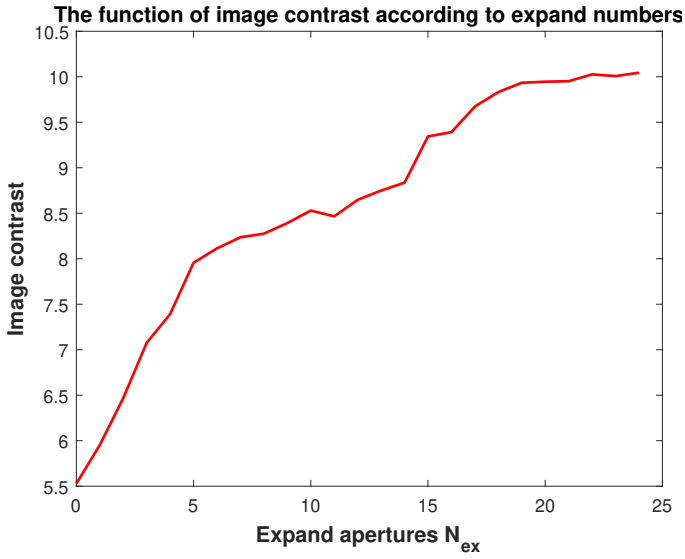

Figure 4.14: The image contrast metric as a function of different aperture sizes formed in the proposed method (parameter N_{ex} described in section III).

The image contrast is calculated with 50 Monte Carlo repetitions of two car models in different locations within the radar's view. The average results of different scenarios from the range angle map of the cars in the scene for different MSs formed are shown in Fig. 4.14. It is shown that the higher the number of apertures formed, the higher the

value of the image contrast metric, meaning the better the separation capability for the considered extended targets.

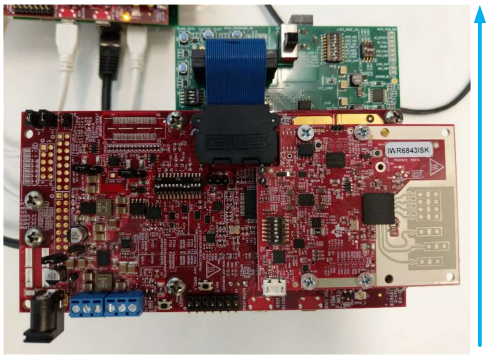

Figure 4.15: Radar with the DSP and data capturing boards for experimental verification, where the blue arrow shows the direction of movement.

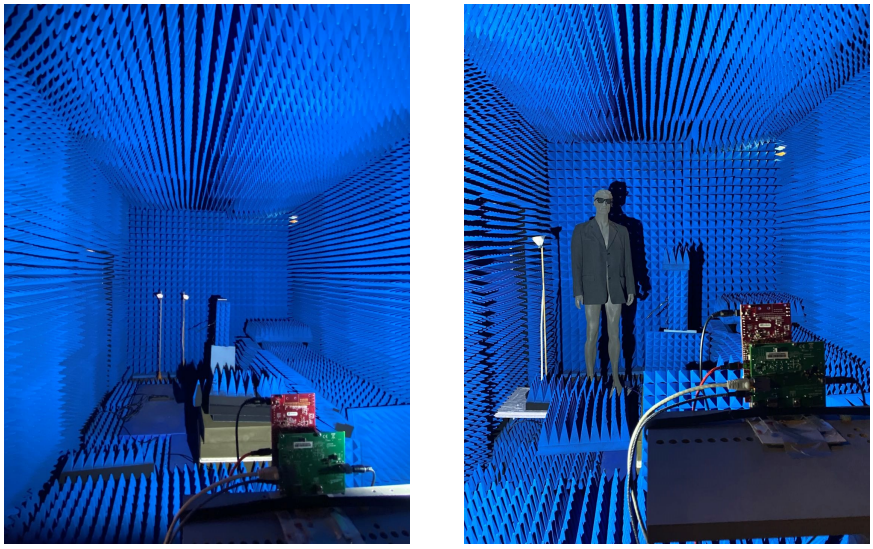

(a) (b)

Figure 4.16: The experimental scene in the MS3 group's anechoic chamber. (a) With two corner reflectors. (b) With a human model and a corner reflector.

4.4.3. EXPERIMENTAL TESTS AND RESULTS

The proposed approach is verified by experimental data. The radar used is the TI IWR6843ISK radar, shown in Fig. 4.15. The parameters of this radar system are shown in Table. 4.1. Two transmit and four receive antennas are used for azimuth angle estimation during the

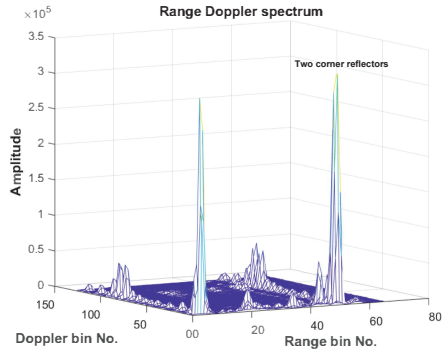

(a)

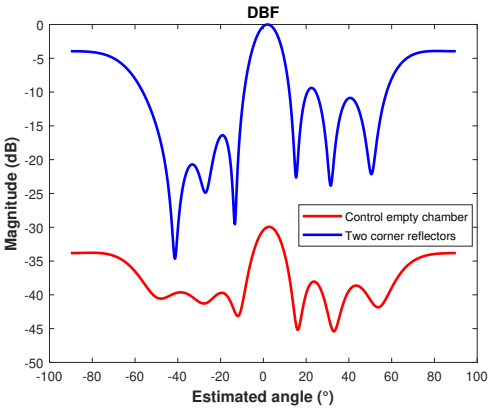

(b)

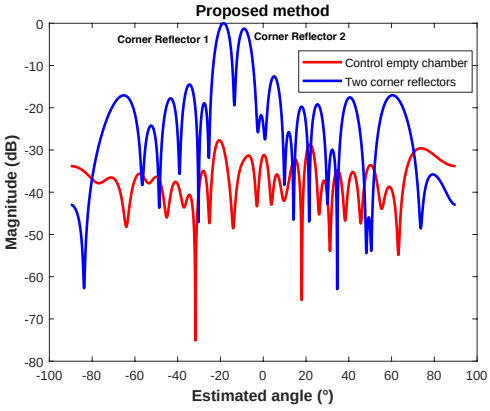

(c)

Figure 4.17: The experimental results for two corner reflectors. (a) Range Doppler spectrum. (b) DOA curve based on original beamscan method. (c) DOA curve based on the proposed method with expanded aperture size equal to 26.

Table 4.1: The radar parameters for the experimental verification

Parameters	Value
Central Frequency (GHz)	60
Slope (MHz/us)	40
Sampling Rate (Msps)	2.95
Bandwidth (GHz)	3
Number of chirps in snapshot	128
PRI(us)	100

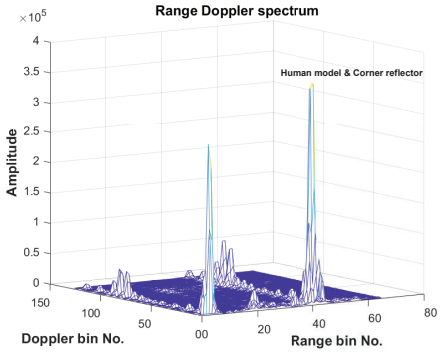

(a)

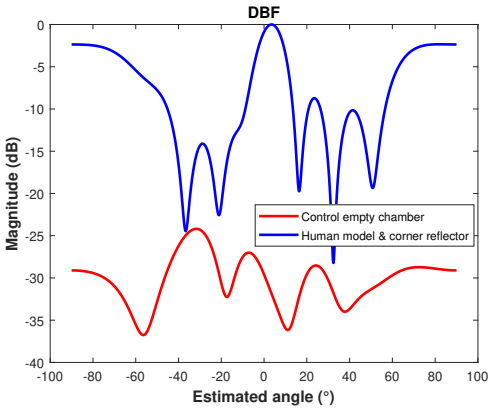

(b)

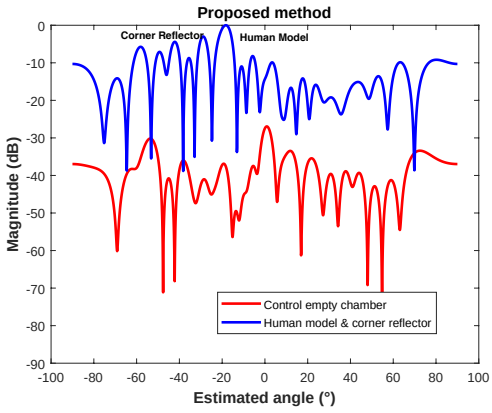

(c)

Figure 4.18: The experimental results for human model and corner reflector. (a) Range Doppler spectrum. (b) DOA curve based on original beamscan method. (c) DOA curve based on the proposed method with expanded aperture size equal to 26.

measurement, and the spacing between adjacent receive antennas is half of the wavelength. The radar is installed on a moving platform, and the experimental measurement campaign was performed in the anechoic chamber at TU Delft. The experimental scene is shown in Fig. 4.16.

Because of the limitations of the moving platform in the chamber, the radar speed is set as $v_y = 0.5m/s$, which meets the condition in (4.18). The experimental results for the two corner reflectors and the corresponding control experiment, i.e., the empty chamber, are shown in Fig. 4.17. With 18 MS formed in the proposed method, the total number of virtual apertures is equivalent to 26 channels, and the two targets can be well separated, and their DOA is estimated at $-8.9°$ and $-18.5°$. The same results are also shown in Fig. 4.18 for the human model and corner reflector, which provide the estima-

tion result as −18.9° and −28.9°. The control empty chamber line shows no significant artefacts from the method, as there are already some minor reflections in the chamber. The two cases' control empty chamber angle responses are different because the background objects and absorbing materials have been partially moved to move the human model without damaging the absorbing materials. Also, the two responses are extracted from different range bins. As also shown in 4.4.1 and 4.4.2, the larger the aperture size is generated, the better angular resolution we can have.

An experiment for the human model and corner reflector with a cross-forward direction velocity of $v_x = 0.1 m/s$ was also performed. After compensating the velocity with the modified steering vector, the azimuthal profile is shown in Fig. 4.19. One can observe that the proposed method can also separate the human model and reflector successfully, given the estimation of −18.0° and −26.5°, which is the same as the results without cross-forward movement.

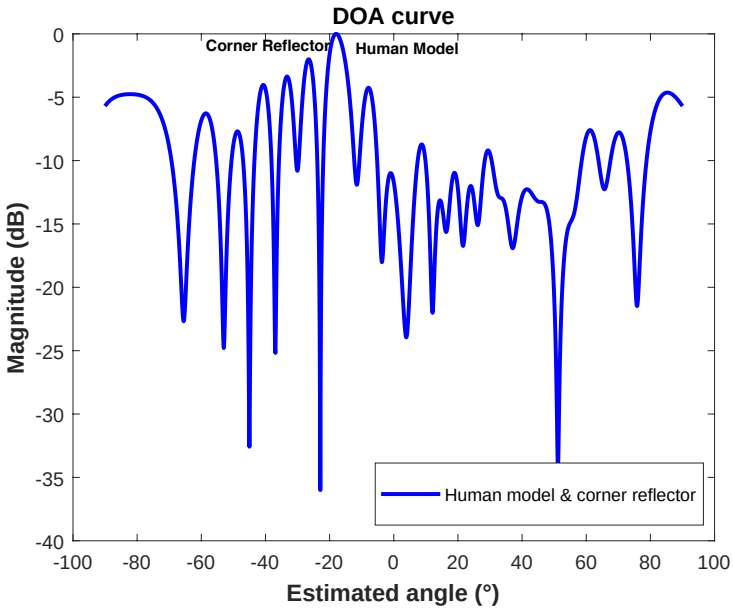

Figure 4.19: DOA curve of human model and corner reflector based on the proposed method with expanded aperture size equal to 26 when the radar moves in both directions.

4.5. CONCLUSION

In this chapter, we have proposed a high-resolution DOA approach using MIMO azimuthal processing in combination with vehicle motion along the array aperture. Azimuthal resolution improvement of approximately three times compared to existing methods has been demonstrated. The targets can be separated and estimated successfully with limited snapshots, which other existing methods cannot achieve. Considering the motion-enhanced apertures formed, the modified steering vector is also proposed to compensate for the approximation and the transverse velocity errors. The limitation of

applicability and tolerance to the velocity error is also investigated.

We verified the proposed method experimentally by performing measurements with point-like and extended targets using a MIMO radar. A good agreement between the simulation and experimental results is demonstrated. It is worth noting that the proposed approach does not need any prior information about the environment, the number of targets, or their approximate position. The proposed approach is easy to apply in automotive applications due to its low computational time and excellent robustness in varying scenarios.

5

3D MOTION ENHANCED IMAGING ALGORITHM FOR SIDE-LOOKING RADAR

The problem of high-resolution DOA estimation for 3D imaging in automotive side-looking MIMO radar has been studied. A novel high-resolution 3D imaging algorithm achieves by using only a 1D MIMO array oriented in the elevation direction. The proposed algorithm leverages motion-enhanced snapshots to achieve high angular resolution in the azimuth direction. A formulation of the steering vector is proposed to address the 3D imaging problem jointly in azimuth & elevation and to compensate motion artefacts from the irregular movement of the ego-vehicle. The performance of the proposed method is thoroughly analyzed for ideal point targets, extended targets in simulations and experimental data.

Parts of this chapter are supposed to be published in: S. Yuan, F. Fioranelli and A. Yarovoy, "3D high-resolution imaging algorithm using 1D MIMO array for autonomous driving application," IEEE Transactions on Radar System. (Submitted)

5.1. INTRODUCTION

As discussed in the previous chapter, motion-enhanced snapshots for 2D high-resolution imaging in azimuth dimension have been proposed. Newly-developed automotive imaging radars can provide information in three spatial dimensions (range, azimuth, and elevation) plus the Doppler information as the fourth one, thus providing more accurate azimuth and elevation estimations for 3D imaging, which also contributes to a denser point clouds benefit for later processing [8, 103]. The quality of 3D imaging will highly rely on the radar's resolution, specifically, the range and spatial resolutions. Spatial resolutions, also called angular resolution, in both azimuth and elevation, are contingent upon the antenna aperture and thus are determined by the number and layout of the transmit and receive antenna elements, limited by the radar cost and packaging size.

The number of antennas is always limited because of the power consumption and the size of the radar, so there is always a trade-off between the elements used for elevation and azimuth estimation. This chapter proposed a novel 3D imaging algorithm to achieve better sensing ability in both azimuth and elevation compared with the state-of-the-art algorithm using a one-dimensional MIMO array in the elevation domain. This is a significant advancement, as it can enable the minimization of the array size while maintaining high-quality imaging capabilities for side-looking automotive radar. Reducing the array size can help mitigate several challenges associated with large arrays, including (1) high complexity in physical design, (2) difficulties in achieving signal orthogonality in larger arrays, and (3) thermal management challenges as the number of RF channels increases. Motion-enhanced snapshots are introduced to generate a larger aperture in the azimuth dimension. The robustness of the vehicle's movement is considered with compensation in the steering vector. The degree of freedom and the SNR increase with the proposed method.

1. A novel 3D imaging algorithm using only a 1D MIMO array oriented in the elevation direction is formulated and demonstrated. The proposed algorithm leverages motion-enhanced snapshots to achieve high angular resolution in the azimuth direction, which is beneficial for side-looking automotive radar applications such as mapping and parking assistance.

2. A formulation of the steering vector is proposed to address the 3D imaging problem jointly in azimuth & elevation and to compensate motion artefacts from the irregular movement of the ego-vehicle on which the radar is mounted.

3. The proposed algorithm is comprehensively validated with simulated data, as well as experimental data collected by multiple sensors in realistic driving scenarios. It is shown that the use of motion-enhanced snapshots with the proposed algorithm increases the SNR and the degrees of freedom for DOA estimation, thus enabling the distinction of more targets and solving the rank deficiency problem of MUSIC.

The rest of this chapter is organized as follows. In Section 5.2, the problem formulation for 3D+1 FMCW MIMO radar is provided. The proposed method is demonstrated in Section 5.3. The results for simulated ideal point targets, simulated complex extended targets and experimental data are provided in Section 5.4. Then, a detailed discussion

about the proposed method using simulation and numerical analysis is given in 5.5. Finally, Section 5.6 concludes the chapter.

5.2. PROBLEM FORMULATIONS

A FMCW MIMO radar 1D uniform linear array with N_e array elements is considered here. The 1D array is installed on the vehicle in the elevation direction to perform DOA estimation in the elevation. An omnidirectional array element pattern is considered for both transmitter and receiver, without losing generality. The radar is installed on the side-looking position, with the y-axis referring to the direction of movement of the radar, as shown in Fig. 5.1.

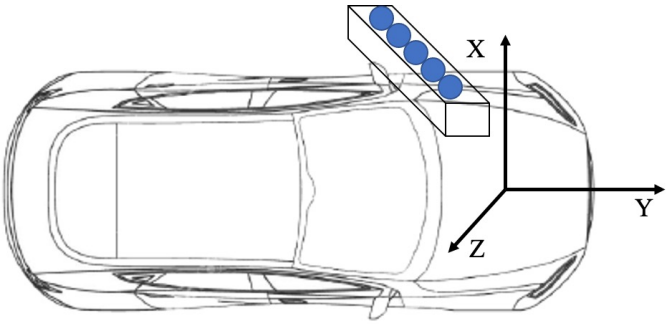

Figure 5.1: The geometry of the side-looking automotive radar along the Z direction. Y is the forward direction, X is the cross-forward direction, and Z is the elevation direction satisfying the left-handed Cartesian coordinates.

The number of antennae is always limited because of the power consumption and the size of the radar, so there is always a trade-off between the elements used for elevation and azimuth estimation. It is necessary but challenging to provide a high angular resolution algorithm for 3D imaging using a limited number of antennae. The movement information of the radar will become the key parameter, and it is the fundamental information for the SAR algorithm, contributing to the high spatial resolution for SAR processing. Utilizing motion information can be a big supplement to automotive imaging radar. It can potentially solve the challenge problem by using the least antenna for 3D imaging algorithms.

5.3. PROPOSED METHOD

In this section, the proposed approach to enable 3D imaging capabilities while keeping the number of antenna elements limited to a 1D array in the elevation direction is described. It shows how the key step of the approach is the exploitation of the movement of the vehicle by motion-enhanced snapshots, but this limits the computational complexity and the duration of the accumulated radar data.

5.3.1. PROPOSED METHOD

The processing chain of the proposed algorithm includes three blocks, namely, the generation of motion-enhanced snapshots, the compensated steering vector, and the 3D beamscan imaging.

MOTION-ENHANCED SNAPSHOTS

As a 1D array in elevation is considered here, the signal in equation (2.18) will be modified containing only elevation information omitting the dependence on the azimuth index p as:

$$\begin{aligned}\hat{z}(q,l,r) = \sum_{o}^{k_s} \alpha_o \pi T_c f_s \text{sinc}(\frac{(r T_c f_s + \mu \gamma_o T_c)}{2}) \\ \times \exp[j(\Phi_e(\phi_o, q) + 2\pi f_0 \frac{2v_o}{c} T l)] \\ \times \exp[-j\pi(m T_c f_s + \mu \gamma_o T_c)]\end{aligned} \tag{5.1}$$

where r is the index of the range bins after range-FFT on the fast time domain. It should be noted that the algorithm is implemented for all the range bins, and no detection algorithm is needed for the method. The second term in the equation is related to the antenna elements for spatial and Doppler/phase information.

If azimuth antenna elements were present, the phase differences of p-th elements and the reference one would be:

$$\Phi_a(\theta_o, \phi_o, p) \approx 2\pi f_0 \frac{pd}{c} \sin\theta_o \cos\phi_o \tag{5.2}$$

where θ_o is the azimuth angle of target o.

It should be noted that if the slow time index satisfies the following relation in equation (5.3), then snapshots at different slow time indices can be used to provide azimuth information coherently. By using only those snapshots spaced at half-wavelength during the movement, a smaller covariance matrix is constructed for DOA estimation, providing computational benefits (i.e., a smaller covariance matrix since not all snapshots in the measurements are used).

$$2\pi f_0 \frac{2v_o}{c} T(l_1 - l_0) = \Phi_a(\theta_o, \phi_o, p+1) - \Phi_a(\theta_o, \phi_o, p) \tag{5.3}$$

Similar to the derivation for equation (4.5) in Section 4.3, the motion-enhanced snapshots for the selected antenna vector at time l_0 will be defined as the group of snapshots whose slow time index follows the following equation:

$$l_n = l_0 + n T_{ind}, n \in \mathbb{Z} \tag{5.4}$$

where $T_{ind} = \lfloor \frac{d}{2v_y T} \rfloor T$ is the approximate time tag interval for a coherent aperture extension.

The radar signal in equation (2.18) can be reshaped according to the time tag as shown in Fig. 5.2. As this reshaping operation of the entire 4D tensor would not be

easy to visualize, the case of a specific range bin is shown here, whereby the initial signal in the 2D elevation and slow-time domain is reshaped by using each motion-enhanced snapshot to add the third dimension and therefore obtain a 3D cube or Doppler Angle Tensor (DAT), which is denoted by $\mathbf{Z}$. The DAT of targets in a given range bin is used in the following derivation for simplicity, i.e., $\mathbf{Z} \in \mathbb{C}^{N_{ex} \times N_e \times L_s}$:

$$\mathbf{Z} = [\mathbf{z}_1 \quad \mathbf{z}_1 \quad \mathbf{z}_2 \quad \mathbf{z}_3 \quad \dots \quad \mathbf{z}_{N_{ex}}] \tag{5.5}$$

where $\mathbf{z}_n = \hat{z}(:, l_n : l_n + L_s)$. Here, l_n is the time tag calculated in equation (5.4), and indicating the same as the index in equation (5.6), N_{ex} is the number of the motion-enhanced snapshots generated for DOA estimation, N_e is the number of antennas in elevation, and L_s is the number of Doppler indices used for constructing the observations in the covariance matrix to decompose into orthogonal signal and noise subspace for DOA estimation. This has the same format as the equation 2.19 in Section. 2.3.

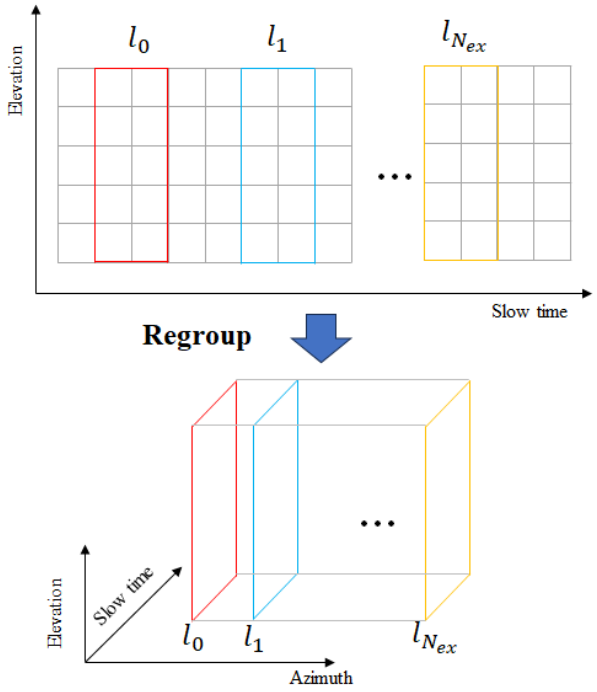

Figure 5.2: The reshaping process to form a 3D data cube in elevation, azimuth, and slow-time domain from 2D data.

At the time l_0, the positions of the MIMO antenna in the elevation direction would be the one in the black rectangle shown in Fig. 5.3. The angular resolution is determined by the aperture size of the array, and only the coherent channels contribute to its improvement. After moving to a different time tag according to equation (5.4), the MIMO antennas move physically to positions suitable to expand the aperture coherently.

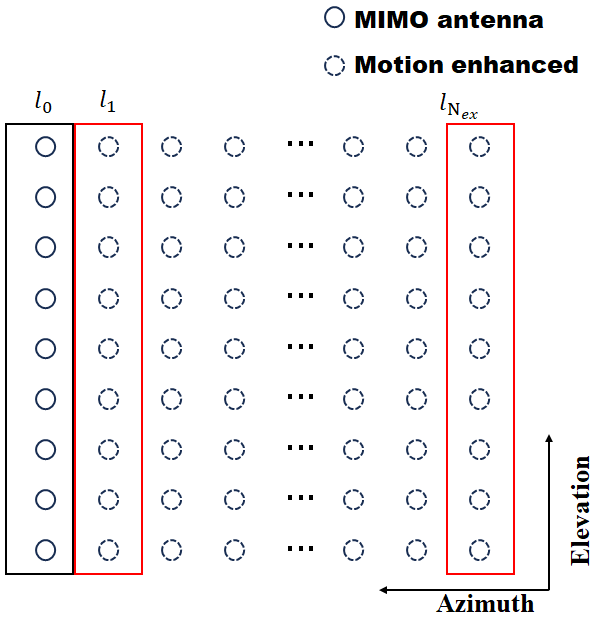

Figure 5.3: The complete imaging array formed by combining the MIMO virtual array & the motion-enhanced 2D arrays. The black solid line rectangle indicates the MIMO antenna positions at time t_0, while the dashed circles within the red rectangles indicate the motion-enhanced antennas, which are formed by the physical movement of the MIMO antenna at different time tags. The final larger array for DOA is formed by combining those together.

The maximum number N_m of motion-enhanced snapshots is the same as equation(4.17).

COMPENSATED STEERING VECTOR

The movement of the vehicle in the Y direction shown in Fig. 5.1 contributes to the generation of motion-enhanced aperture for azimuth sensing. However, there are two approximations in the formation of the motion-enhanced snapshots, as shown in equation (5.4). Because of the fixed chirp duration, the positions of the antenna at each starting time of the chirp are not the same as the coherent positions, leading to extra phase errors. Moreover, movement in other, non-forward directions will introduce extra phase shifts, which may lead to defocus effects. Therefore, a compensated steering vector is proposed as follows.

The error from the approximation of coherent position within a chirp duration can be compensated using the calculated time tag in equation (5.4), as:

$$l_e(n) = \frac{d}{2v_y} - (l_n - l_0) \tag{5.6}$$

where n is the index in the calculation of the time tag defined in (5.4).

This time delay causes an error equivalent to an extra movement in the forward moving direction, thus leading to a phase error. For each motion-enhanced snapshot formed with the proposed method, the resulting phase error is written as:

$$w_{ea}(\theta_m, \phi_m, n) = 2v_y \times l_e(n) \sin\theta_m \cos\phi_m / \lambda \tag{5.7}$$

where m is the index of the targets, θ_m and ϕ_m are the azimuth and elevation angles from the array boresight, respectively.

The movement in the other two non-forward directions will lead to another phase error, which can be written as:

$$w_{ev}(\theta_m, \phi_m, n) = (l_n - t_0)(v_x \cos\theta_m \cos\phi_m + v_z \sin\phi_m)/\lambda \tag{5.8}$$

Combining the two aforementioned sources of error, a compensation factor for the original steering vector can be written as:

$$w_{er}(n, m) = w_{ea}(\theta_m, \phi_m, n) + w_{ev}(\theta_m, \phi_m, n) \tag{5.9}$$

3D HIGH RESOLUTION IMAGING

After getting the DAT $\mathbf{Z}$ a given range bin as in equation (5.5), a 3D high-resolution imaging algorithm can be implemented as in Section. 2.3. The equation (2.22) will add the compensated term and become as:

$$\begin{aligned}
\mathbf{a}_{\theta_\mathbf{m}} &= [1, e^{-j2\pi\omega_a(1,m)}, ..., e^{-j2\pi\omega_a(p,m)} ... e^{-j2\pi\omega_a(N_{ex},m)}]^T \\
\mathbf{a}_{\phi_\mathbf{m}} &= [1, e^{-j2\pi\omega_e(1,m)}, ..., e^{-j2\pi\omega_e(q,m)} ... e^{-j2\pi\omega_e(N_e-1,m)}]^T \\
\omega_a(p,m) &= \frac{dp\sin\theta_m\cos\phi_m}{\lambda} + w_{er}(p,m) \\
\omega_e(q,m) &= \frac{dq\sin\phi_m}{\lambda}
\end{aligned} \tag{5.10}$$

where w_{er} is the compensation factor in equation (5.9), with $d = \frac{\lambda}{2}$.

The matched steering vector $\alpha(\theta_m, \phi_m) \in \mathbb{C}^{N_a N_e}$ for the azimuth angle θ_m and the angle ϕ_m is formulated as:

$$\alpha(\theta_m, \phi_m) = \mathbf{a}_{\theta_\mathbf{m}} \otimes \mathbf{a}_{\phi_\mathbf{m}} \tag{5.11}$$

where $\otimes$ is the Kronecker product.

5.3.2. SUMMARY OF THE PROPOSED ALGORITHM

Step 1: Generate motion-enhanced snapshots.

As discussed in Section 5.3.1, the signal after range-FFT is analyzed. Snapshots coherent with respect to the original MIMO virtual array are selected based on the index in equation (5.4). These so-called motion-enhanced snapshots will form a new, larger aperture for 3D imaging.

Step 2: Compensate phase errors in the steering vector.

The approximation error in the calculation of an integer time tag and the error due to the presence of velocity components in the non-forward directions need compensation. Both errors are related to each index of the motion-enhanced snapshots and are translated into the phase domain for further compensation. This is done via the compensation factor for the steering vector calculated as in equation (5.9).

Step 3: 3D imaging based on the new extended tensor $\mathbf{Z}$ and the compensated steering vector $\alpha(\theta_m, \phi_m)$.

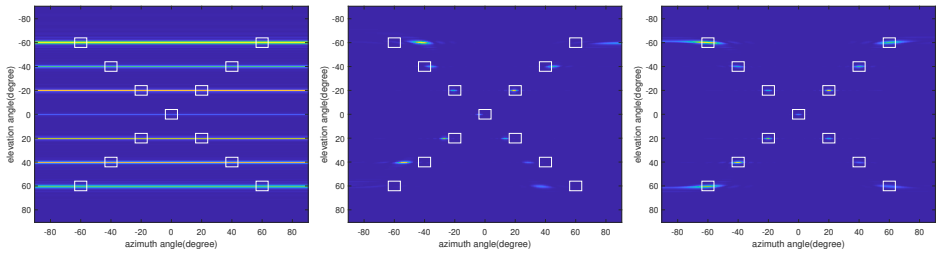

(a) (b) (c)

Figure 5.4: The results of simulated 13-point targets under different methods. The sub-figures (a), (b), and (c) show images of a 1D MIMO array, the proposed method without a compensated steering vector, and the proposed methods with a compensated steering vector, respectively. The white rectangles indicate the ground truth positions of the targets.

After performing FFT along the fast-time, the tensor $\mathbf{Z}$ of each range bin will be formed by grouping the motion-enhanced snapshots with the original antenna tensor. Then, the tensor is reshaped to a 2-dimensional matrix $\mathbf{X}$ according to Section 5.3.1, and the final modified steering vector $\alpha(\theta_m, \phi_m)$ is formed with the compensation factor calculated in the previous steps.

Finally, the DBF is applied to derive the energy distribution in the azimuth-elevation domain for each range bin, thus forming the expected 3D imaging results. After searching all the cells in the space, the total imaging results in $P_{DBF}(r, \theta, \phi)$ can be obtained. The proposed algorithm is summarized in 'Algorithm 5'.

5.4. RESULTS

In this section, the effectiveness of the proposed method is showcased through the use of simulated ideal point targets, simulated complex extended targets, and experimental data.

5.4.1. NUMERICAL SIMULATIONS

We employed a simulated 1D array in the elevation direction with 86 antenna elements, comparable to the Texas Instrument MMWCAS-RF-EVM cascade radar board AWR2243. The radar parameters are specified as follows: the starting frequency of the FMCW chirp f_0 is 77 GHz, the chirp bandwidth B is 1 GHz, the chirp duration T_c is 16 μs, the sampling rate f_s is 32 Msps, and L = 512 chirps are processed in each frame.

Algorithm 5: Proposed 3D imaging algorithm

Perform FFT on the fast time domain and obtain the range indices r.
Calculate the maximum number of motion-enhanced snapshots and their indexes l_n as in (5.4).
Compute the compensated phase term for each motion-enhanced snapshot $w_{er}(n,m)$ as in (5.9).
for r in $[0, r_{un}]$ do
Expand the amount of snapshots for 3D imaging, generate the Doppler-angle tensor $\mathbf{Z}$, and reshape the tensor to matrix $\mathbf{X}$.
  for θ in $[-90°, 90°]$ do
    for ϕ in $[-90°, 90°]$ do
     Compute the compensated steering vector $\alpha(\theta,\phi)$ as in (5.11) based on (5.10)
    $R_{\mathbf{XX}} = E\left[\mathbf{X}\mathbf{X}^H\right]$
    $P_{DBF}(r,\theta,\phi) = \frac{\mathbf{w}_{DBF}^H R_{\mathbf{XX}} \mathbf{w}_{DBF}}{\mathbf{w}_{DBF}^H \mathbf{w}_{DBF}}$
    endfor
  endfor
endfor

First, 13 ideal point targets distributed in a triangle geometry in elevation and azimuth plane are simulated. The vehicle is moving at [-1,15,2] m/s in all directions. The results from the 1D array and proposed method formed array are compared in Fig. 5.4. The ground truth positions of the simulated targets are marked in white rectangle boxes in the images. It can be seen that the original 1D array cannot provide any resolution ability in the azimuth direction. The proposed method without compensation for movements in non-forward directions will lead to wrongly focused positions, while the proposed method with the compensated steering vector enables the focus of the targets in the right positions.

Simulated models of various 3D objects are then utilized as extended targets to verify the 3D imaging ability of the proposed method. These 3D objects are generated from CAD models, including a pedestrian and buildings (i.e., bungalows) as two examples of typical targets for automotive applications, as shown in Fig. 5.5. All the points comprising the surface of each CAD model are used as radar scatterers within the radar field of view. To mimic realistic targets, the scatterers are resampled to ensure a uniform spatial distribution. Also, a denser sampling frequency is implemented to increase the similarity between the models and the real targets. The bungalow contains 23k scattering points, and the pedestrian contains 12k scattering points for radar simulation. It is important to note that the scatterers in the CAD models do not aim to precisely mimic electromagnetic scattering behaviour from the actual objects. Rather, they serve as a representation of the object's body shape and extent.

To simplify the subsequent analysis, certain propagation factors are not considered, such as the multipath propagation due to reflections from the road and the mutual occlusion of scatterers. These simplifications do not restrict the generality of the proposed imaging approach [97].

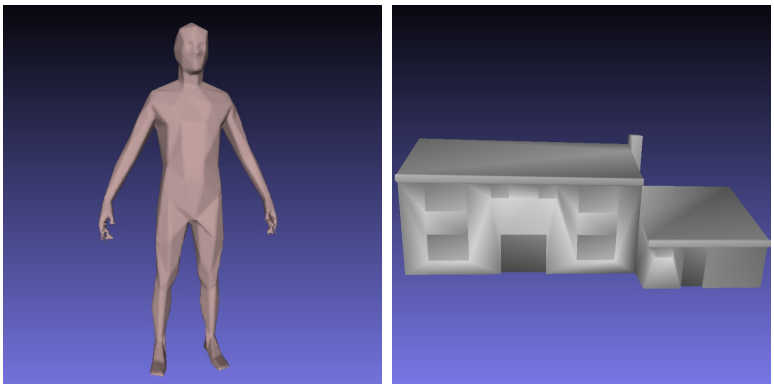

(a) (b)

Figure 5.5: The objects derived from CAD models for the extended targets' simulation: (a) standing pedestrian, (b) bungalow buildings.

The amplitudes of all scatterers are drawn from a uniform distribution, $\alpha_o \sim \mathscr{U}(0.5,1)$, satisfying the Swerling model III, same as the complex car model of Fig. 4.12 in Section 4.4. By employing equation (2.16), the de-chirped signal for the scatterers representing the objects, treated as extended targets, can be simulated manually.

In this simulation, a simulated 86 MIMO radar array was employed for DOA estimation, where no elements were used for azimuth direction, and 86 elements were used for elevation directions to generate the 3D images under MIMO processing for comparison. This setting is comparable to the experimental MMWCAS-RF-EVM Texas Instrument radar board AWR2243. The radar parameters are the same as for the point targets simulation. For representation, the 3D imaging results with the three considered methods use mean and var quantization at first and then are presented with the same spatial view perspective; the radar images are projected onto the Cartesian coordinates using Cubic interpolation for comparison instead of applying another frequency algorithm to avoid creating non-existent points.

The results for the pedestrian are shown in Fig. 5.6. The first column shows the original point scatterers with their respective densities, which can be considered the 'ground truth' of these simulations, with denser scatterers located in the areas with yellow colour. The second and third columns are the 3D images generated with MIMO processing and the proposed methods. As the results in the Y and Z directions are largely impacted by the range and elevation resolution, which are the same during the processing, the results in these planes are omitted. One can easily observe that the results with the proposed method obtain higher similarity with the ground truth, with a more detailed shape of the target, whereas the conventional MIMO provides rather poor results in azimuth as no resolution is available in this domain. It should be noted that the slight difference in the X direction is due to the projection from the sphere coordinate to the Cartesian coordinate.

In a further simulation, two bungalows with a separation of 3 meters are simulated

to mimic the driving scenario of a small road between two buildings, common in many European cities. The results are shown in Fig. 5.7 with the same layout used for the pedestrian. The road between the two bungalows is visible using the proposed method as an area of lower reflectivity, whereas the result for conventional MIMO processing provides no useful information on the shape of the objects.

These observations are based on a simple visual inspection of the images generated from the 3D objects. To further evaluate the performance, two additional quantitative evaluation metrics are introduced: voxelization accuracy and image contrast [104].

The cells in each range-elevation-azimuth above 20 dB are detected to provide the target position information. The space is divided into a discrete grid, and the grid cells which intersect the detected targets are marked as occupied, which is called voxelization [105]. F-score [106] is used here to evaluate the voxelization results, i.e., accuracy, sensitivity, and specificity. 'True' and 'False' are defined as the cells occupied or not by the ground truth-target model, while 'positive' and 'negative' are defined as the cells occupied or not by the imaging results. The results are compared to the ground truth positions to derive the quantitative accuracy metrics shown in Table 5.1. The number of detected cells in both ground truth and imaging results is considered as tp, while fn is the number of cells not detected by ground truth and imaging results. fp is the number of cells detected by imaging results but not ground truth, while tn is the number of cells detected by ground truth but not imaging results. **Accuracy** approximates how effective the algorithm is by showing the probability of the true value of the class label; in other words, it assesses the overall effectiveness of the algorithm; **precision** estimates the predictive value of a label, either positive or negative, depending on the class for which it is calculated; in other words, it assesses the predictive power of the algorithm; **sensitivity (specificity)** approximates the probability of the positive (negative) label being true; in other words, it assesses the effectiveness of the algorithm on a single class; **AUC** shows a relation between the sensitivity and the specificity of the algorithm. **F-score** is a composite measure which benefits algorithms with higher sensitivity and challenges algorithms with higher specificity.

$$
\begin{aligned}
Accuracy &= \frac{tp+tn}{tp+tn+fp+fn} \\
Precision &= \frac{tp}{tp+fp} \\
Sensitivity &= \frac{tp}{tp+fn} \\
Specificity &= \frac{tn}{fp+tn} \\
AUC &= \frac{Sensitivity+Specificity}{2} \\
F-score &= \frac{2*Precision*Sensitivity}{Precision+Sensitivity}
\end{aligned}
\tag{5.12}
$$

The proposed method is considered a better imaging approach with its higher F-score. This achieves significant improvement in precision and accuracy. However, the

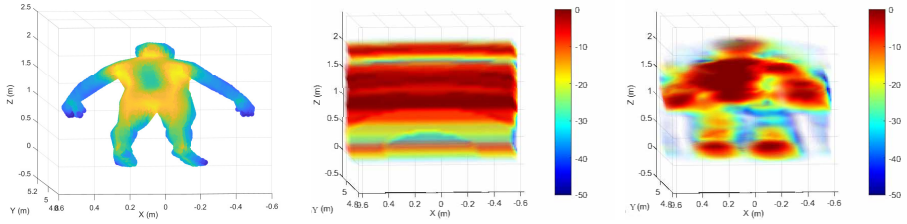

(a) (b) (c)

Figure 5.6: 3D imaging results for the CAD model of a pedestrian. The sub-figures (a), (b), and (c) show images of ground truth, conventional MIMO processing, and the proposed method, respectively.

AUC values for conventional MIMO are slightly better for the bungalow target, which is reasonable because the total number of detected points for the proposed method is much smaller than that for the MIMO processing, leading to lower sensitivity results. Overall, the proposed method has better quantitative metrics than the MIMO, in addition to the qualitative higher resolution already discussed when visually comparing images.

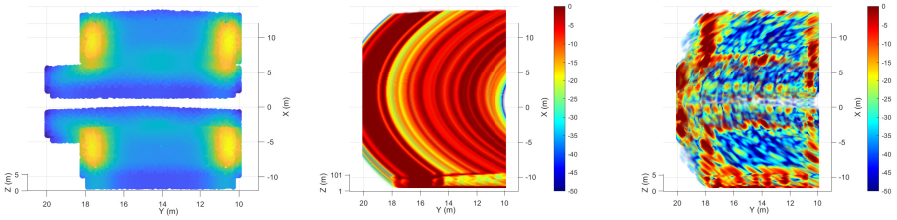

(a) (b) (c)

Figure 5.7: 3D imaging results for the CAD model of bungalow buildings. The sub-figures (a), (b), and (c) show images of ground truth, conventional MIMO processing, and the proposed method, respectively.

Table 5.1: Quantitative evaluation metrics after the voxelization for extended targets

Evaluation metric	Target Type	MIMO	Proposed
Accuracy	Human	22.76	91.04
	Bungalows	59.56	92.92
Precision	Human	0.86	9.14
	Bungalows	2.69	12.77
AUC	Human	25.73	40.01
	Bungalows	47.77	46.95
F-score	Human	1.68	14.30
	Bungalows	4.78	14.02

The image contrast metric shows the differences in the intensity of each pixel of the image or signal. Each slice generated from the 3D radar images projected onto one of the 2D planes, i.e., the azimuth-elevation, the range-azimuth, and the range-elevation plane, is evaluated by calculating the mean value of each slice image contrast as in equation (4.21). The results are shown in Table 5.2. The proposed method obtains around twice a higher image contrast in almost every slice of the 3D imaging for all different objects.

Table 5.2: Evaluation results for the image contrast metric for different extended targets in different planes

Target Types	Method	Image type	Image contrast
Human	MIMO	Range-azimuth	2.3371
		Range-elevation	2.8386
		Azimuth-elevation	1.2335
	Proposed	Range-azimuth	3.3318
		Range-elevation	3.6728
		Azimuth-elevation	2.1603
Bungalows	MIMO	Range-azimuth	1.2953
		Range-elevation	1.3294
		Azimuth-elevation	1.1384
	Proposed	Range-azimuth	3.8339
		Range-elevation	3.3602
		Azimuth-elevation	3.6446

In this work, the *dynamic range ratio*, defined as the ratio between the dynamic range of each image generated by implementing different methods, is also employed for comparison. It should be noted that the dynamic range is calculated as the difference between the maximum value and the minimum value of each image. It is shown that with the proposed method, the dynamic range ratio also increases thanks to the larger amount of coherent data that is accumulated. The ratio of the bungalow equals 7.9537; the ratio of the human is 15.4465.

To test the imaging performance of the proposed method in the presence of velocity errors, the signal from the pedestrian model in Fig. 5.5 is imaged with different velocity errors. The errors in both forward and cross-forward directions, i.e., the two main velocity components in the considered geometry, do not appear to visually influence the imaging results even when reaching 15% (amounting to 2.25m/s error in the forward direction at a speed of 15m/s). The results with 15% velocity errors in both directions are shown in Fig. 5.8.

The evaluation metrics, image contrast and F-score for different velocity errors are shown in table 5.3. There are no significant differences in performance with the different velocity errors thanks to the compensated steering vector used in the proposed method. From the image contrast, one can observe that all the formed images are better than conventional MIMO processing. The velocity error may cause different effects on different image types, i.e., the image contrast value of the range-elevation image increases with the negative velocity error, whereas the image contrast of range-azimuth and azimuth-elevation decreases with the negative velocity error. The F-score shows the

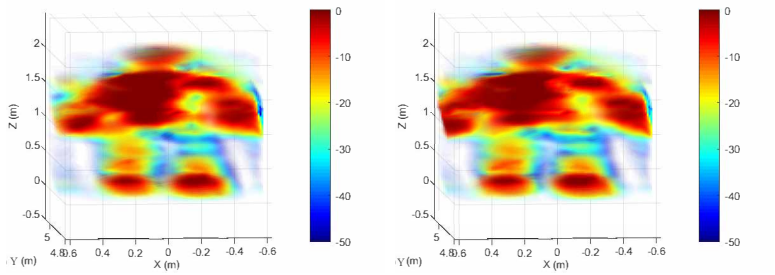

Figure 5.8: The imaging results of the pedestrian under 15% velocity error for (a) velocity in cross-forward direction, (b) velocity in the forward direction.

similarity between the images and the real target's model. The resulting F-score in the case without velocity errors gives as expected the highest score, but the degradation with the considered velocity errors is rather small.

Table 5.3: Evaluation results image contrast (IC) and F-score for the pedestrian for different velocity errors in the forward direction

Evaluation metric		Velocity error						
		-15%	-10%	-5%	0%	5%	10%	15%
IC	Range-azimuth	3.1301	3.1358	3.1474	**3.3318**	3.1785	3.2057	3.2270
	Range-elevation	3.8569	3.8107	3.7705	**3.6728**	3.7083	3.7457	3.7461
	Azimuth-elevation	2.0601	2.1034	2.1489	**2.1603**	2.2269	2.2728	2.3101
F-Score		13.55	13.70	13.86	**14.30**	13.92	13.81	13.96

To demonstrate the effectiveness of the proposed imaging algorithm, we compare the imaging results by the proposed algorithm with those obtained by two different 2D arrays. The first array is an L-shaped array with 86 elements in elevation and 32 in azimuth, identical in both dimensions to the virtual array in the proposed method. The second array is a 2D full array with a total of 32×86 elements In both arrays, all antenna elements are transmitters and receivers. No synthesis of the aperture with L-shaped and 2D arrays due to platform movement has been performed. However, the radial velocity of scatterers due to platform movement has been taken into account. Except for the array structure and number of chirps used for the radial velocity of scatterers estimation, all the parameters in the simulation remain the same, i.e., the moving speed, the targets' model, and the waveform. It also should be noted that the channel signals are already separated from each other; so no transmission scheme (e.g.,TDMA,CDMA or other modes) is considered in this simulation.

The imaging results, in Fig. 5.9, show that the proposed method outperforms the L-shaped array in maintaining the contour and characteristics of the target model and achieves similar results with a 2D full 32×86 array. This result confirms that the pro-

posed method while using 1D moving array produces the images comparable to those generated by a 32 × 86 full array, offering more spatial sampling positions than the L-shaped array. The performance is also quantitatively evaluated based on image contrast and voxelization accuracy, as shown in Table. IV. The L-shaped array exhibits the poorest performance in image contrast and voxelisation accuracy, while the 2D 32 × 86 full array performs similarly in both evaluation matrices, which is consistent with the qualitative, visual assessment of the images

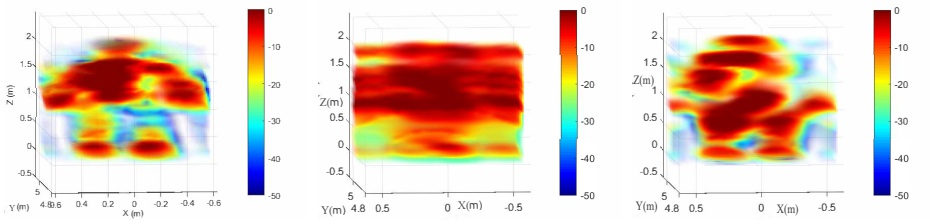

(a) (b) (c)

Figure 5.9: 3D imaging results for the CAD model of a pedestrian with different array structures. The sub-figure (a) uses the proposed method, (b) uses an L-shaped array with 32 elements in azimuth and 86 elements in elevation, equivalent to the size of the array with the motion-enhanced snapshots, and (c) uses a 2D full array with 32 × 86 elements.

Table 5.4: Evaluation results for the pedestrian using different array structures

Evaluation metric		Array structure		
		L-shaped array	2D full array	Proposed method
Image contrast	Range-azimuth	2.3296	3.1271	3.3318
	Range-elevation	2.5323	3.12685	3.6728
	Azimuth-elevation	0.9327	2.2498	2.1603
F-Score		1.54	15.72	14.30

To evaluate the performance of the proposed algorithm under different waveform settings, we simulated and compared the results using various numbers of transmitters in a TDMA configuration, as illustrated in Fig. 5.10. The velocity of the radar and other parameters remain the same as in the simulation for Fig. 5.6. The number of transmitters affects the pulse repetition interval during processing, which subsequently influences the formed virtual array topology and the imaging results. Incidentally, it can noted that the original imaging results in Fig. 5.9 (a), i.e., with no multiple TDMA transmitters being used, can be also considered equivalent to using CDMA waveforms with ideal orthogonality, i.e., with absent or very low level of sidelobes from the code used. It should also be noted that a larger number of repetitions leads to a longer pulse repetition interval. As a result, the position of the antenna at each sampling position due to the platform's movement will begin to lose coherence, even with compensation in the steering vector, which can introduce more grating lobes.

Our findings indicate that a larger pulse repetition interval, resulting from the use of more TDMA transmitters, affects the calculation of the time tag and introduces significant errors because of the non-ideal coherence by the compensation processing at a given speed. This leads to a degradation in imaging quality, as shown in Fig. 5.10 (c) compared to (a), and even worse compared to the original result in Fig. 5.9 (a). Performance was assessed quantitatively using image contrast and voxelization accuracy, as presented in Table. 5.5. Compared with the images generated from conventional MIMO processing, the proposed method achieves improvements in the image contrast metric with different numbers of transmitters. The image contrast remains consistent with different transmitters across the three images, suggesting that the resolution is unaffected, given that the number of motion-enhanced snapshots remains the same. Imaging results from one transmitter achieve the worst image contrast; this might be because the evaluation is only based on the targets' existing area, where the energy will be focused on almost all cells. Using additional transmitters will generate some grating lobes in this region, contributing to high contrast, which can be seen empirically from the visualized images as well. Moreover, a drop in the F-score is observed, especially with a large number of transmitters, indicating that the energy of the target is incorrectly focused, leading to the grating lobes and errors accumulating in the steering vector, which aligns well with the visualized images.

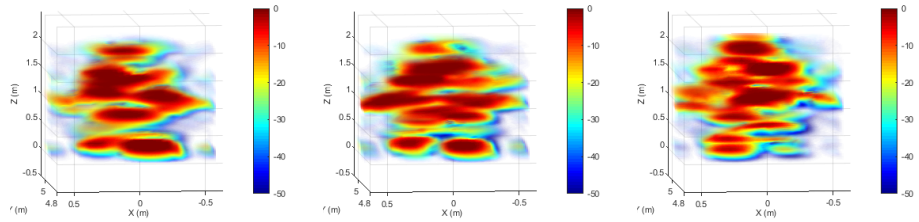

Figure 5.10: 3D imaging results for the CAD model of a pedestrian with different waveform settings in TDMA mode using proposed method. The sub-figures (a) uses 4 transmitters, (b) uses 8 transmitters, and (c) uses 12 transmitters.

5.4.2. EXPERIMENTAL RESULTS

The proposed approach is verified using experimental data collected with the Texas Instrument MMWCAS-RF-EVM cascade radar AWR2243, shown in Fig. 5.11. GPS, IMU, Lidar and GoPro cameras are also installed on the vehicle. The radar is installed next to the GoPro, while the Lidar is on the top middle of the car as shown in Fig. 5.12. The parameters of the radar system are shown in Table 5.6. The radar is rotated in order to use its longer antenna aperture in the elevation domain, whereas DOA in the azimuth domain is performed using the method proposed in this chapter. The radar includes 12 transmitters and 16 receivers. As the radar is working with time-division multiple access (TDMA) modulation, the movement of the car during the different transmit times will cause an extra error, whose correction is beyond the scope of the chapter; thus, for

Table 5.5: Evaluation results for the pedestrian for different numbers of transmitters in TDMA

Evaluation metric			Numbers of transmitters			
			4	8	12	1 (equivalent CDMA)
IC	MIMO	Range-azimuth	2.3198	2.1883	2.1443	2.3351
		Range-elevation	2.7503	2.4686	2.4452	2.8701
		Azimuth-elevation	1.2192	1.2548	1.2266	1.2665
	Proposed	Range-azimuth	3.5966	3.5093	3.4696	3.3318
		Range-elevation	4.1191	4.0562	3.7856	3.6728
		Azimuth-elevation	2.1459	2.4267	2.3639	2.1603
F-Score			14.01	10.45	5.44	14.30

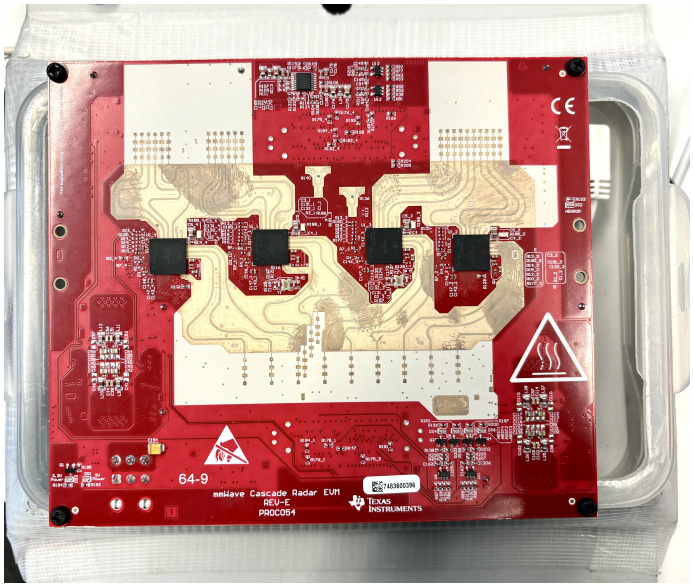

Figure 5.11: The cascade radar board used for radar data collection.

demonstration purposes, only the data from one transmitter are used.

The optical image for an experimental scene considered in this work is shown in Fig. 5.13, with the corresponding image results of different sensors shown in Fig. 5.14. The dashed line in Fig. 5.14(a) is the field of view (FoV) of the radar in sub-figure (b) overlapped with the Lidar data. The distances between targets with high electromagnetic reflectivity (e.g., metal objects) in FoV and radar are measured by the Lidar and also shown in Fig. 5.14(a). With the proposed method, the targets appear to be well-focused on the radar image (sub-figure b) and located at the right positions. The radar image is generated with a 1D elevation array with 16 antenna elements and 64 motion-enhanced snapshots for azimuth sensing. The ground reflection is high, so in the middle, a large energy signature appears.

Figure 5.12: The experimental setup on the vehicle with multiple sensors.

Table 5.6: Radar parameters for the experimental verification

Parameters	Value
Central Frequency (GHz)	78.5
Slope (MHz/us)	30
Sampling Rate (Msps)	6
Bandwidth (GHz)	1.2
Number of chirps in snapshot	128
PRI(us)	75
Modulation	TDMA

The results for the same scene when using different aperture sizes and in different views are shown in Fig. 5.15. From the first row, it is noted that the original result does not have any azimuth sensing ability, whereas, with the proposed method, the azimuth sensing capability is demonstrated. From the comparison between sub-figures (b) and (c), the larger aperture formed, the better resolution obtained. In the second row, the elevation resolution is the same with the same aperture size, and the 3D results are shown in the front view starting from $y = 3m$, where the company slogan side and gate 1 are located. It should be noted that the objects of interest, such as the company slogan sign, are indicated in Fig. 5.14(a). The result in (d) does not resolve targets in azimuth, whereas in (e) and (f), the 3D imaging ability is proved. In (f), one can see that the company slogan sign is around 1m higher than the radar, while gate 1 is 0.5m, and the parking car is around 0m, matching the ground truth of the targets. In the bottom area, the ground reflection can also be observed.

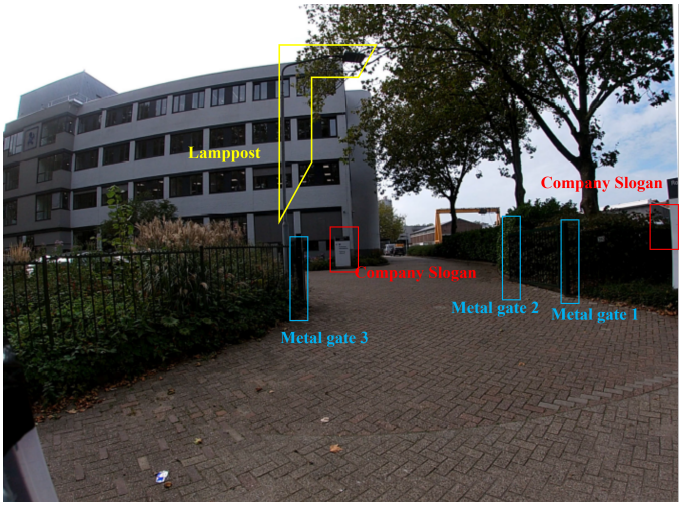

Figure 5.13: The optical image of the measured scene in the experimental data as captured by the GoPro camera.

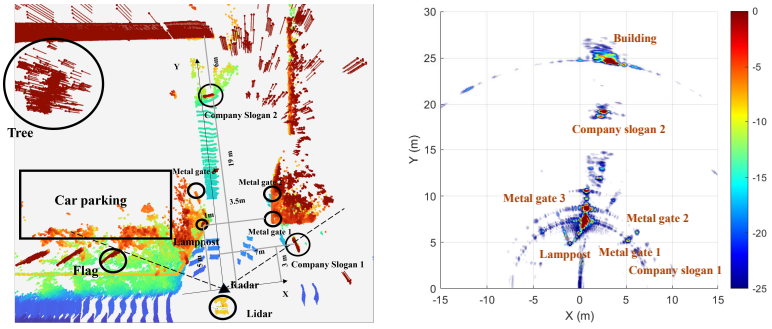

(a) (b)

Figure 5.14: Experimental results of the same scene using different sensors while driving. (a) The Lidar point cloud, where the overlaid dashed line is the radar field of view, and the added contours are the targets linked to the radar images. (b) The radar image using the proposed method with the marked targets' names.

5.5. DISCUSSION

5.5.1. DEGREES OF FREEDOM FOR DOA ESTIMATION

Vertically oriented 1D MIMO array has no degrees of freedom for DOA in the azimuth dimension. With the proposed method, 3D imaging ability is enabled by introducing motion-enhanced snapshots. The azimuth estimation is then achieved, increasing the degrees of freedom from 0 to 1.

To numerically evaluate the improvement, instead of using a 1D large MIMO array, we selected a 4 + 8 MIMO radar to provide a comparison. The + notation here means

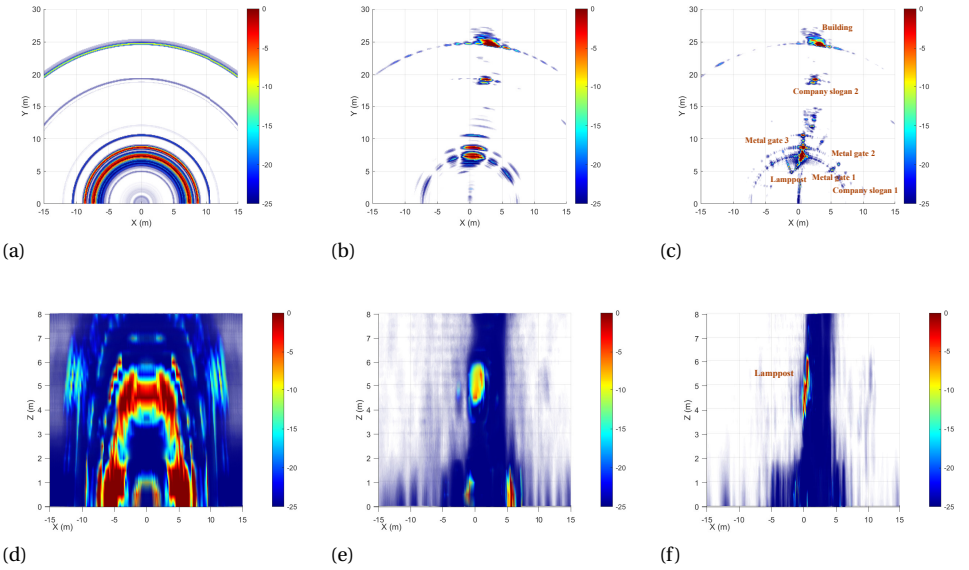

(a) (b) (c)

(d) (e) (f)

Figure 5.15: Experimental results of the same scene while driving using different formed aperture sizes; the objects of interest in the scene were indicated in Fig. 5.14. (a) The results using the original 1D array in elevation direction with BEV. (b) The results using 6 motion-enhanced snapshots with BEV. (c) The results using 64 motion-enhanced snapshots with BEV with marked targets' names. (d) The results using the original 1D array in elevation direction in forward view for the lamppost. (e) The results using 6 motion-enhanced snapshots in forward view for the lamppost. (f) The results using 64 motion-enhanced snapshots in forward view for the lamppost.

the usage of an L-shaped antenna, which contains four elements for elevation and eight elements for azimuth estimation, with a similar setting as the typical automotive radar. By introducing the motion-enhanced snapshots, the aperture size of the radar in the azimuth domain increases, thus increasing the number of targets whose DOA can be estimated. The radar is moving at velocity $[-1, 15, -2] m/s$.

To test the performance of the proposed idea, $32 * 8$ motion-enhanced snapshots are selected. The MIMO antenna on the side-looking radar was located at the coordinate centre, with 12 targets placed at the same range bin of 10 meters to meet the Fraunhofer distance [95]. The targets are distributed uniformly in the azimuth dimension from $[-50° : 60°]$, with a fixed elevation angle of 15°. The MUSIC algorithm highly relies on the rank of the sub-space matrix formed by the antenna elements, which is affected by the known rank deficiency problem. The rank is determined by the available degrees of freedom. After performing MUSIC on a conventional MIMO array and the proposed array, we can easily see that the 12 targets are distinguished well using the proposed method, while this fails with MIMO, as shown in Fig. 5.16. The MUSIC algorithm can only perform well when the number of targets in a certain range bin is known and less than the number of virtual array channels.

The number of motion-enhanced snapshots is calculated as in equation (4.17); thus,

the degrees of freedom are increased by the same factor, i.e., N_m.

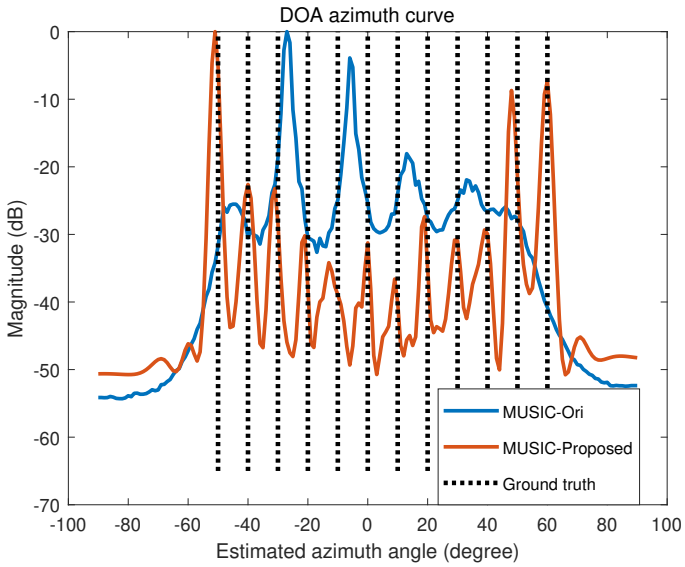

Figure 5.16: The simulation of 12 targets using MUSIC with application of the proposed method ('MUSIC-Proposed') and without it, i.e., with original MIMO array ('MUSIC-Ori').

5.5.2. IMPROVEMENT OF SNR

The coherent combination of motion-enhanced snapshots is expected to increase useful signal power while the noise floor remains the same; hence, the overall SNR is expected to be improved. Specifically, with N motion-enhanced snapshots, the SNR will increase $\sqrt{N}$ times.

To verify the SNR improvement provided by the proposed method, an 86 MIMO radar comparable to the Texas Instrument MMWCAS-RF-EVM radar is implemented. The radar setting and the speed are the same as in the previous section. $32 * 2$ motion-enhanced snapshots are selected for azimuth DOA. The target is placed at the 10 m range, and azimuth & elevation angle 0 degrees. The elevation profile is shown in Fig. 5.17, where the SNR has increased as expected.

5.5.3. ANGULAR RESOLUTION IMPROVEMENT

The spatial difference between adjacent sampling points is $\lambda/2$. If there are two targets located at $\theta + \Delta\theta$ and θ, to resolve them the angle resolution $\Delta\theta$ should satisfy:

$$\begin{aligned} &\frac{2\pi d}{\lambda}(\sin(\theta+\Delta\theta)-\sin(\theta)) > \frac{2\pi}{N_a} \\ &\Rightarrow \Delta\theta_a > \frac{\lambda}{Nd\cos(\theta)} \end{aligned} \tag{5.13}$$

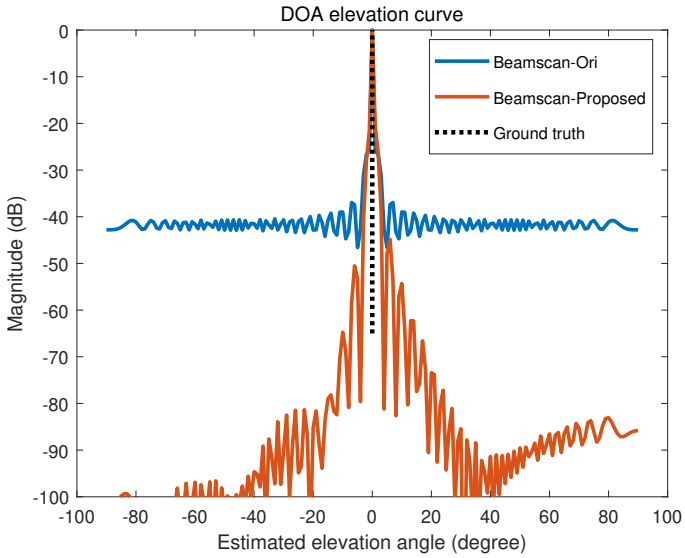

Figure 5.17: The simulation of SNR improvement in the elevation profile comparing the original beamscan beamformer ('Beamscan-Ori') and the beamscan with proposed motion-enhanced snapshots ('Beamscan-Proposed').

where N_a is the number of spatial sampling points. It is noted that the resolution ability depends on the effective aperture size Nd. As no physical movement is present in the elevation dimension, the angular resolution will remain the same as before. The resolution improvement in the azimuth domain is instead equal to $N_{ex}+1$.

5.6. CONCLUSION

In this chapter, a novel high-resolution 3D imaging algorithm using only a 1D MIMO array in elevation dimension is proposed for side-looking automotive radar. The compensated steering vector is proposed for jointly addressing the 3D imaging in the azimuth and elevation domain to benefit from the target's elevation diversity, and the motion errors are compensated to improve the performance of the method further.

Good angular resolution improvement in azimuth and significant improvement in SNR, as well as the freedom of frequency, is demonstrated compared to alternative methods. Specifically, the proposed method has been validated with simulated point-like and extended targets, as well as experimental data collected by the joint team of the MS3 and Intelligent Vehicles (IV) groups of TU Delft.

It is worth noting that the proposed approach does not need any prior information on the environment, the number, and the approximate position of targets. It can also be easily combined with other high-angular resolution algorithms, such as MVDR, MUSIC, etc. One potential limitation is that the movement of the targets in the scene might be unfocused and need to be addressed in the future.

6

2D Robust Doppler Beam Sharpening Algorithm for Forward-looking MIMO Radar

The ambiguity problem of targets in Doppler beam sharpening with forward-looking radar is considered. While Doppler beam sharpening was proposed earlier to improve the angular resolution of the radar while keeping the antenna aperture size limited, such a solution suffers from ambiguities in the case of targets positioned symmetrically concerning the platform movement. To address this problem, an approach named 'Unambiguous Doppler-based forward-looking multiple-input multiple-output radar beam sharpening scan' (UDFMBSC) is proposed, based on the combination of MIMO processing and Doppler beam sharpening. To make it robust to non-ideal movements of the vehicle and fluctuations in the targets' reflectivity, a new approach named 'Robust Unambiguous DBS with Adaptive Threshold' (RUDAT) is developed. The performance has been studied in simulations, and possible limitations have been discussed. In addition, the method has been verified experimentally with point-like and extended targets to show the robustness of the whole processing flowchart. The proposed method's performance is compared to existing approaches using simulated data with point-like and extended targets. The method is successfully verified using experimental data.

Parts of this chapter have been published in:

S. Yuan, P. Aubry, F. Fioranelli and A. G. Yarovoy, "A Novel Approach to Unambiguous Doppler Beam Sharpening for Forward-Looking MIMO Radar," in IEEE Sensors Journal, vol. 22, no. 23, pp. 23494-23506, 1 Dec.1, 2022.

S. Yuan, F. Fioranelli and A. Yarovoy, "An adaptive threshold-based unambiguous robust Doppler beam sharpening algorithm for forward-looking MIMO Radar," 2023 20th European Radar Conference (EuRAD), Berlin, Germany, 2023, pp. 65-68.

6.1. INTRODUCTION

As discussed in Chapter 4, high-resolution imaging for the side-looking regions is developed. Meanwhile, the forward-looking region is especially of interest for autonomous vehicles. Many algorithms have been proposed to provide decent sensing capabilities for this region. DBS is an alternative way to achieve fine angular resolution for targets close to each other in automotive radar[107]. SAR [63] was first named as Doppler beam sharpening when designed, [108]. It utilizes the variations in the relative Doppler frequency shift of scatterers at different look-angles with respect to the trajectory of radar. In this way, it forms a large effective (i.e., virtual) aperture array by moving a small antenna or array. This reduces the number of physical antennas required for imaging, thus providing a cost-effective solution for high-resolution imaging applications. Several researchers have investigated the use of DBS for imaging. Daniel et al. [107] investigated the application of DBS for the angular resolution refinement of low-Terahertz radar sensing. Mao et al. [109] combined DBS with the fast iterative adaptive approach to achieve high azimuth resolution in the forward-squint region. Using this approach in the forward-looking direction is challenging, which is especially of interest for autonomous vehicles because of two challenging problems. Firstly, this approach has no or poor angular resolution for look angles equal or close to zero degrees, i.e.$[-\epsilon, \epsilon]$, where ϵ indicates the angular extension of the blind zone near the forward-looking direction. According to the literature, the extension of the blind zone and the Doppler bandwidth are inversely proportional. As the Doppler bandwidth increases by exploiting the movement of the vehicle, the extension of the blind zone is reduced. This has typical value of $\epsilon = 5^\circ$ [110, 111]. Secondly, the symmetric targets on both sides of the trajectory have the same Doppler history, which leads to ambiguity, i.e. in the angular region $[-\frac{\pi}{2}, -\epsilon] \cup [\epsilon, \frac{\pi}{2}]$.

This chapter focuses on solving the ambiguity problem in the forward-looking direction but outside the blind zone. Several algorithms have been proposed in forward-looking SAR to tackle this problem. Bistatic SAR [112, 113], for example, uses another transmitter located at a different position from the receiver; in this way, the designed geometry can provide additional information to address the ambiguity problem. Frequency diverse array[114] was designed by performing transmit beamforming after range compensation, and the echo from the desired range region can be extracted from ambiguous echoes, thus providing unambiguous imaging. A multi-beam DBS approach was proposed in [115] based on the DBF using a scanning imaging system to provide high cross-range resolution. Multi-channel radar in [116] uses the back-projection (BP) algorithm plus MIMO information to solve the ambiguity problem. At the same time, a curved motion trajectory can be used to improve the poor resolution in the region where look angles are equal or close to zero degrees. However, this algorithm is rather time-consuming, limiting its use in real time. Forward-looking MIMO-SAR and sparse MIMO arrays with decimated back projection (Dec-BP)[117] were proposed in [118] to solve the ambiguity and achieve imaging. However, these two algorithms are rather time-consuming, limiting their use in real-time. An incoherent integration method from the MIMO and Doppler Integral was proposed for automotive applications in [69]. It increases cross-range resolution across the radar's field of view while suppressing side lobe errors. However, this method has a specific requirement for vehicle movement, as it necessitates movement in the boresight direction of the radar. Differently from the

above studies, this chapter proposes an unambiguous Doppler-based forward-looking multiple-input multiple-output radar beam sharpening scan (named in short as '*UDFMBSC*') method. This combines the Doppler beam sharpening with MIMO array processing and jointly provides high angular resolution without ambiguity.

The movement of the vehicle is exploited in this algorithm and characterized in this work. This concept of using the vehicle's movement to improve angular resolution has been proposed in the literature on automotive radar. The motion information of the platform to form a synthetic virtual aperture on automotive MIMO radar to obtain high angular resolution is used in [65, 66]. A two-radars approach is proposed in [67]: while one radar is used to determine the vehicle trajectory, another radar utilizes SAR on the known trajectory. The work in [68] uses the residual motion compensation to improve the SAR image quality for automobiles. The velocity information was also used for wide-band DOA estimation with compensation of range migration and the presence of Doppler ambiguity in [71] and for high angular resolution imaging in [42, 70].

However, all the aforementioned algorithms [42, 65–68, 70, 71] do not consider the ambiguity problem in case of the forward-looking radar. To our knowledge, compared with [107, 109], this article is the first to solve the ambiguity in Doppler beam sharpening for forward-looking MIMO radar. The proposed method does not require any prior information on the environment, the number of targets and their locations. The method is computationally very efficient, which means it can be implemented easily in current radar sensors.

The main contributions of this chapter are:

1. An unambiguous Doppler-based forward-looking multiple-input multiple-output radar beam sharpening scan (*UDFMBSC*) method is proposed by combining Doppler beam sharpening and MIMO array processing to solve the ambiguity problem of symmetric targets in forward-looking automotive radar.

2. To make the '*UDFMBSC*' suitable for more complicated vehicle movements and cope with the diverse reflectivity of different targets in the scene, a new approach named 'Robust Unambiguous DBS with Adaptive Threshold' (*RUDAT*) is proposed.

3. The proposed method has been verified for simulated point-like and extended targets, as well as experimental data from a radar sensor, showing that *UDFMBSC* achieves better angular estimation than conventional DBS and Digital Beam Forming (DBF).

The rest of the chapter is organized as follows. In Section 6.2, the signal model and the fundamentals of Doppler beam sharpening are analyzed. The problem formulation and the proposed method are demonstrated in Section 6.3. The simulation results and evaluations of ideal point targets and complex extended targets, as well as the experimental results, are provided in Section 6.4. Finally, conclusions are drawn in Section 6.5.

6.2. FUNDAMENTALS

The signal model in Section.2.3 is derived for side-looking geometry, and the DOA algorithm is designed accordingly in Section.2.3. This chapter considers the forward-looking

geometry and only the DOA algorithm in azimuth direction. Thus, the signal model and steering vector are modified correspondingly.

The signal model $\mathbf{Y}$ in equation (2.21) becomes:

$$\mathbf{X} = \sum_{m=1}^{M} \mathbf{a}_{\theta_m} \mathbf{S}_t + \mathbf{N} \in \mathbb{C}^{N_a \times L_d} \tag{6.1}$$

The steering vector is given by:

$$\begin{aligned} \mathbf{a}_a(\theta) = \mathbf{a}_{\theta_\mathbf{m}} = [1, e^{-j2\pi\omega_a(1,m)}, ..., e^{-j2\pi\omega_a(p,m)} ... e^{-j2\pi\omega_a(N_a,m)}]^T \\ \omega_a(p,m) = \frac{d\,p \sin\theta_m}{\lambda} \end{aligned} \tag{6.2}$$

The DBF algorithm can handle the DOA estimation robustly and is selected here:

$$\mathbf{w}_{DBF} = \frac{\mathbf{a}_\mathbf{a}(\theta)}{\sqrt{\mathbf{a}_\mathbf{a}{}^H(\theta)\mathbf{a}_\mathbf{a}(\theta)}} \tag{6.3}$$

The power of the weighted output is calculated as in (2.25).

Assuming that all the targets are static in the radar field of view, the maximum Doppler will be no larger than the one corresponding to the vehicle's speed v_0.

The signal model in equation (6.1) is:

$$\mathbf{X}^H = \sum_{m=1}^{M} \mathbf{a}_{d_m} \mathbf{S}_t + \mathbf{N} \in \mathbb{C}^{L_d \times N_a} \tag{6.4}$$

So, for Doppler beam sharpening, we introduce the steering of the Doppler vector:

$$\mathbf{a}_\mathbf{d}(\theta) = \mathbf{a}_{\mathbf{d_m}} = [1, e^{-j2\pi 2 v_0 T \cos\theta_m/\lambda}, ..., e^{-j2\pi(L_d-1)2 v_0 T \cos\theta_m/\lambda}]^T \tag{6.5}$$

The DBS algorithm can also provide the DOA estimation and the weight vector $\mathbf{w}_{DBS}$ has the same form as:

$$\mathbf{w}_{DBS} = \frac{\mathbf{a}_\mathbf{d}(\theta)}{\sqrt{\mathbf{a}_\mathbf{d}{}^H(\theta)\mathbf{a}_\mathbf{d}(\theta)}} \tag{6.6}$$

The power of the weighted output of DBS is:

$$\begin{aligned} P_{DBS}(\theta) &= E[\left|\mathbf{w}_{DBS}^H \mathbf{X}^\mathbf{H}\right|^2] \\ &= \frac{\mathbf{a}_\mathbf{d}{}^H(\theta) R_{\mathbf{X}^\mathbf{H}\mathbf{X}^\mathbf{H}} \mathbf{a}_\mathbf{d}(\theta)}{\mathbf{a}_\mathbf{d}{}^H(\theta)\mathbf{a}_\mathbf{d}(\theta)} \end{aligned} \tag{6.7}$$

$R_{\mathbf{X}^\mathbf{H}\mathbf{X}^\mathbf{H}} = E\left[\mathbf{X}\mathbf{X}^H\right]$ is the autocorrelation matrix of $\mathbf{X}^\mathbf{H}$.

6.2.1. THE DERIVATION OF ANGULAR RESOLUTION

MIMO ARRAY

To satisfy no ambiguity within the field of view $[-90°, 90°]$, the spatial difference between adjacent sampling points (i.e., MIMO antennas) should be $\lambda/2$.

Under such circumstances, let us assume that two targets are located at $\theta + \Delta\theta$ and θ. To resolve the two targets, the angle resolution $\Delta\theta$ should satisfy:

$$\begin{aligned} &\frac{2\pi d}{\lambda}(\sin(\theta+\Delta\theta)-\sin(\theta)) > \frac{2\pi}{N_a} \\ &\Rightarrow \Delta\theta_a > \frac{\lambda}{Nd\cos(\theta)} \end{aligned} \tag{6.8}$$

where N_a is the number of spatial sampling points.

DOPPLER BEAM SHARPENING

For a forward-looking radar borne on a vehicle moving at speed v_0 in the forward direction, the instantaneous Doppler of a static target located at θ will be:

$$f_d = \frac{2v_0 f_0}{c}\cos(\theta) \tag{6.9}$$

Then, to resolve two closed targets using Doppler beam sharpening, the following equation should be satisfied:

$$\begin{aligned} &\frac{2\pi 2v_0 f_0 T}{c}(\cos(\theta+\Delta\theta)-\cos(\theta)) > \frac{2\pi}{N_d} \\ &\Rightarrow \Delta\theta_d > \frac{\lambda}{2N_d T v_0 \sin(\theta)} \end{aligned} \tag{6.10}$$

where N_d is the number of chirps used for Doppler estimation, which is limited by the coherent processing time. Also, it is clear that where $\theta \in [-\epsilon, \epsilon]$, the resolution will tend to infinity, causing the blind zone problem.

Compared with the two resolution equations (6.8) and (6.10), one can easily see that the angular resolution of the MIMO array decreases when the look angle of the region becomes larger, while the Doppler has an inverse behaviour. With typical values in current automotive radar, specifically, the chirp duration of $100us$ and 256 chirps for Doppler estimation, even if influenced by the impact of the angle θ, most of the time, the Doppler can still provide better resolution capability if the ego-vehicle moves faster than $0.5m/s$. The amplification term from Doppler is defined here.

$$n = \frac{\Delta\theta_a}{\Delta\theta_d} = \frac{2N_d T v_0}{N_a d}\tan(\theta) \tag{6.11}$$

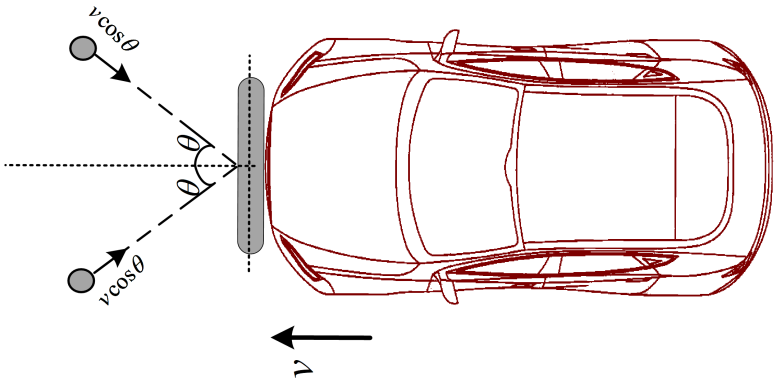

Figure 6.1: The schematic of the Doppler ambiguity arising for two symmetric targets in forward-looking radar.

6.3. THE PROBLEM FORMULATION AND THE PROPOSED ALGORITHM

6.3.1. PROBLEM FORMULATION

The Doppler ambiguity comes from the inherent geometry of the forward-looking radar. As shown in Fig. 6.1, when the vehicle is moving toward the two static targets, both of them will appear symmetric with respect to the boresight of the radar, and they will experience the same Doppler velocity because of the movement of the vehicle. This makes them indistinguishable using Doppler beam sharpening.

Equation (6.5) shows that the weights of the right- and left-hand positions at the same angle will be the same. Furthermore, the targets will have the same Doppler history, making the conventional DBS-based algorithm ambiguous when used in the forward-looking direction. Hence, it will be hard to decide whether one or two targets are in that direction. Moreover, for the targets shown in Fig. 6.2 (a), the generated response will be the same using the DBS-based method as that of the targets shown in Fig. 6.2 (b). This will cause ghost targets to appear when using the conventional DBS approach.

The DBS approach uses the Doppler information to achieve better angular separation. As the target's movement will introduce an additional Doppler component, the DBS approach suggested cannot focus on the target accurately, and the performance of the method will degrade.

6.3.2. THE MODIFIED STEERING DOPPLER VECTOR BASED ON DIFFERENT VEHICLE MOVEMENTS

The DOA estimation algorithm is discussed in section 6.2. The most important part is the steering vector, from which the time delay patterns of different antennas can be extracted to estimate the targets' angle. For the steering Doppler vector, as the movement of the vehicle will not always be in the forward-looking direction as assumed in 6.2.1, the cross-forward movement also needs to be taken into account. The cross-forward velocity component of the movement will also influence the resulting phase. The error due to

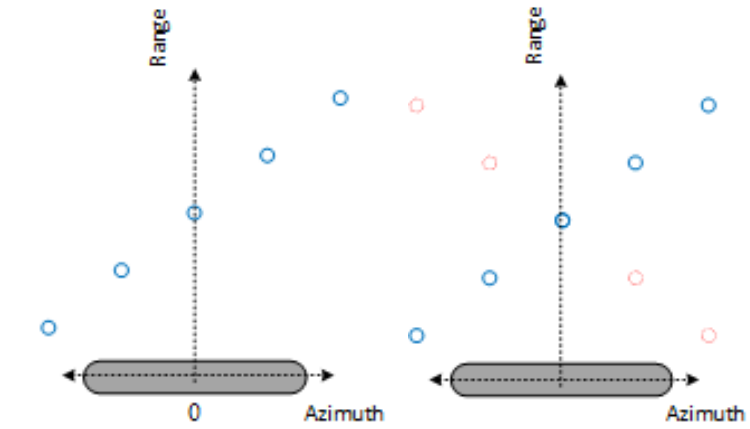

(a) (b)

Figure 6.2: The schematic of the real scene and the ambiguous view of Doppler Beam Sharpening. (a) shows the targets in the real scene, while (b) shows the targets when Doppler Beam Sharpening is applied with a red dash marking the ghost targets.

this effect is calculated for each Doppler element as follows:

$$\mathbf{a_c}(\theta) = [1, e^{-j2\pi 2vT\sin\theta/\lambda}, ..., e^{-j2\pi(l-1)2vT\sin\theta/\lambda}]^T \tag{6.12}$$

where v is the speed of the vehicle in the cross-forward direction. With the compensation factor of the original steering Doppler vector, the new steering vector is given by:

$$a_{dc}(\theta) = a_d(\theta) \odot a_c(\theta) \tag{6.13}$$

where $\odot$ is Hadamard product.

6.3.3. 'UDFMBSC' METHOD

Generally, one can only detect one target within one range-Doppler resolution cells without any high-resolution finding approach. Hence, the FFT will be applied to the angle vector when extracting the antenna vector from a certain range and Doppler cell to get its spatial frequency. The peaks of the auto-convolution of the spatial frequency spectrum were used here to discriminate between the left-right hand positions in the field of view. If only one target is present in the radar of view, even under the Doppler ambiguity condition, the auto-convolution of the spatial frequency spectrum will peak at $f = \frac{2d\sin\theta}{\lambda}$. The deduction of this is shown as follows:

If there is only one target in a certain range-Doppler cell, the angle vector will be

$$s(l) = \begin{cases} e^{j2\pi\frac{ld\sin\theta}{\lambda}} & l \in [0, N_a] \\ 0 & others \end{cases} \tag{6.14}$$

The spatial frequency spectrum after FFT on this angle vector will be:

$$X(f) = \pi N_a \text{sinc}(\frac{N_a(f + \frac{d\sin\theta}{\lambda})}{2}) e^{j\pi N_a(f+\frac{d\sin\theta}{\lambda})} \tag{6.15}$$

where $\text{sinc}(x) = \frac{sin\pi x}{\pi x}$.

According to the convolution theorem, the Fourier transform of the convolution is given by the product of the Fourier transforms of the signal itself.

The Fourier transforms of (6.15) is as follows:

$$s(f') = \begin{cases} 2\pi e^{(d\sin\theta f')} & |f' - \frac{\pi N_a}{2}| < \frac{\pi N_a}{2} \\ 0 & others \end{cases} \tag{6.16}$$

The convolution of (6.15) will be the

$$\begin{aligned} &\chi(\Omega) = \int_{-\infty}^{\infty} X(f)X(\Omega - f)df = \pi^2 N_a \\ &\text{sinc}(\frac{N_a(-\Omega + \frac{2d\sin\theta}{\lambda})}{4}) \exp[j\frac{\pi N_a}{2}(-\Omega + \frac{2d\sin\theta}{\lambda})] \end{aligned} \tag{6.17}$$

So, the peak value will depend on the target's position term $2d\sin\theta/\lambda$.

If two targets appear in this range-Doppler cell, they must be symmetric to each other. Otherwise, they cannot be projected into the same range-Doppler cell. Hence, the auto-convolution of the two targets' spatial frequency spectrum's peak will be in the middle, with the deduction given as follows: If there is more than one target in the range-Doppler cell, because of the Doppler symmetric geometry, the targets must be symmetric, so the angle vector will be

$$s(l) = \begin{cases} e^{j2\pi\frac{ld\sin\theta}{\lambda}} + e^{j2\pi\frac{ld\sin(-\theta)}{\lambda}} & l \in [0, N_a] \\ 0 & others \end{cases} \tag{6.18}$$

The Fourier transform of (6.18) will be:

$$\begin{aligned} X(f) &= \pi N_a \\ &(\text{sinc}(\frac{N_a(f + \frac{d\sin\theta}{\lambda})}{2}) \exp[j\pi N_a(f + \frac{d\sin\theta}{\lambda})] + \\ &\text{sinc}(\frac{N_a(f + \frac{d\sin(-\theta)}{\lambda})}{2}) \exp[j\pi N_a(f + \frac{d\sin(-\theta)}{\lambda})]) \end{aligned} \tag{6.19}$$

In order to get the auto-convolution functions, the Fourier transform of (6.19) is calculated as:

$$s(f') = \begin{cases} 2\pi(e^{(d\sin\theta f')} + e^{(-d\sin\theta f')}) & |f' - \frac{\pi N_a}{2}| < \frac{\pi N_a}{2} \\ 0 & others \end{cases} \tag{6.20}$$

Then the product of two equations (6.20) will be:

$$s(f') = \begin{cases} 4\pi^2(e^{2d\sin\theta f'} + e^{-2d\sin\theta f'} + 2) & |f' - \frac{\pi N_a}{2}| < \frac{\pi N_a}{2} \\ 0 & others \end{cases} \tag{6.21}$$

The auto-convolution function is as follows.

$$\begin{aligned}&\chi(\Omega) = \\ &\pi^2 N_a(\mathrm{sinc}(\frac{N_a(\Omega+\frac{2d\sin\theta}{\lambda})}{4})\exp[j\frac{\pi N_a}{2}(\Omega+\frac{2d\sin\theta}{\lambda})] \\ &+\mathrm{sinc}(\frac{N_a(\Omega-\frac{2d\sin\theta}{\lambda})}{4})\exp[j\frac{\pi N_a}{2}(\Omega-\frac{2d\sin\theta}{\lambda})])+ \\ &2\pi^2 N_a\mathrm{sinc}(\frac{N_a(\Omega)}{4})\exp[j\frac{\pi N_a}{2}(\Omega)]\end{aligned} \tag{6.22}$$

So, the peak will be in the middle of the signal.

As discussed before, the position of the peak in the equation (6.17,6.22) will provide information on whether there is one target or two. If the peak is in the middle of the function, this will mean that two targets are present in this Doppler-range index. Only one target will present if the peak is not in the middlent. If there is only one target, we can use the DBF results to decide which region the target is located in, i.e., the left-hand or the right-hand one. If there are two targets, there should be two symmetric targets in the radar field of view. One exception to be mentioned is when the target's angle is zero; in this case, the peak will be in the middle even with only one target.

To summarize, the steps of the proposed DOA estimation are described as follows.

Step 1: FFT of signal in fast time.

The range estimation of the targets $\hat{r}$ can be determined by the position of the point corresponding to the targets after FFT.

Step 2: DOA estimation of targets using MIMO array and Doppler beam sharpening.

Extract the DAM of the targets' range, then use (2.25) and (6.7) to generate the MIMO angle profile $P_{DBF}(\theta)$ and the Doppler beam sharpening angle profile $P_{DBS}(\theta)$.

Step 3: The proposed UDFMBSC method.

For each searching angle, $\phi \in [-\frac{\pi}{2}, -\epsilon] \cup [\epsilon, \frac{\pi}{2}]$, after finding its corresponding Doppler index named l_ϕ and doing the FFT on the $X(i, l_\phi)$, the spatial frequency spectrum $X(f)$ will be obtained as in equation (6.15) in Appendix. Then, the auto-convolution of $X(f)$ is computed to obtain $\chi(\Omega)$.

If the peak of the $\chi(\Omega)$ is in the middle, then there are two targets, and the UDFMBSC angle profile will be:

$$P(\phi) = P_{DBF}(\phi)/\max(P_{DBF}(\phi)) \times P_{DBS}(\phi) \tag{6.23}$$

If the peak of the $\chi(\Omega)$ is not in the middle, there is one target.

The sign of the single target's angle, i.e., negative or positive, can be decided by comparing the two values in the MIMO angle profile $P_{DBF}(\theta)$.

$$\mathrm{sign}(\phi) = \begin{cases} 1 & P_{DBF}(\phi) > P_{DBF}(-\phi) \\ 0 & P_{DBF}(\phi) < P_{DBF}(-\phi) \end{cases} \tag{6.24}$$

Then, the UDFMBSC angle profile will be:

$$P(\phi) = \mathrm{sign}(\phi)P_{DBF}(\phi)/\max(P_{DBF}(\phi)) \times P_{DBS}(\phi) \tag{6.25}$$

Algorithm 6: Proposed UDFMBSC method

Obtain the range estimation after FFT on fast time.
Get the steering vector of MIMO array and compensated steering for Doppler vector $a_a(\theta)$ and $a_{dc}(\theta)$
Perform the DOA estimation on $\hat{r}$ DAM to get the angle profile $P_{DBF}(\theta)$ and $P_{DBS}(\theta)$ as in equations (2.25) and (6.7)
for ϕ in $[-\frac{\pi}{2}, -\epsilon] \cup [\epsilon, \frac{\pi}{2}]$do
$l_\phi = (2v\cos\phi N_d Tc)/\lambda$
$X(f) = \sum_{i=-M_\Omega/2}^{M_\Omega/2} X(i, l_\phi)\exp(-j2\pi f i)$
$\chi(\Omega) = \sum X(f)X(\Omega - f)$
if $\chi^{-1}(\max(\chi(\Omega))) = \frac{M_\Omega}{2}$
$P(\phi) = P_{DBF}(\phi)/\max(P_{DBF}(\phi) \times P_{DBS}(\phi)$
else
$P(\phi) = \text{sign}(\phi)P_{DBF}(\phi)/\max(P_{DBF}(\phi)) \times P_{DBS}(\phi)$
where sign(ϕ) is shown in equation (6.24)
end
endfor
The unambiguous angle profile can be obtained.

6

The algorithm is summarized in the pseudocode shown in Algorithm 6.

The UDFMBSC method will be implemented over all range bins to get the 2D azimuth-range map.

6.3.4. 'RUDAT' METHOD

First, the target will be detected in the range dimension. Its corresponding Doppler cell will be calculated by $\sqrt{v_x^2 + v_y^2}\cos(\theta - \phi)$. The targets in the same detected range-Doppler cells will be ambiguous after Doppler beam sharpening, i.e., targets at azimuth angle $(\theta - \phi)$ and $(-\theta - \phi)$. Then, the angle vector of this cell will be extracted for further processing.

If there is only one target in the azimuth angle $(\theta - \phi)$, then the Fourier transform $X(f,\theta)$ of the angle vector can be expressed as:

$$\begin{aligned} X(f,\theta) &= s_i(f, \beta(\theta)) \\ &= a_i \pi N_a \text{sinc}(\frac{N_a(f + \beta(\theta))}{2}) e^{j\pi N_a(f+\beta(\theta))} \end{aligned} \tag{6.26}$$

where a_i is the reflection coefficient of the target i, and $\beta(\theta) = \frac{d\sin(\theta-\phi)}{\lambda}$.

If another target is located at the ambiguous position $(-\theta - \phi)$, two targets will be in the detected range-Doppler cell. Similarly, the Fourier transform of the angle vector $X(f,\theta)$ will be by superposition:

$$X(f,\theta) = s_1(f, \beta(\theta)) + s_2(f, \beta(-\theta)) \tag{6.27}$$

The peak searching approach described in [43] comes from the odd function $\sin(-\theta)$, noticing that:

$$\delta(\theta) = -\delta(-\theta) = \beta(\theta) + \frac{d\cos\theta\sin\phi}{\lambda} = \frac{d\sin\theta\cos\phi}{\lambda} \tag{6.28}$$

Here, the extra frequency shift $\delta(\theta)-\beta(\theta)$ is implemented on the Fourier transform of the angle vector $X(f,\theta)$ as compensation to maintain the odd-function property. After this, the auto-convolution will be calculated on the Fourier transform to obtain $\chi(\Omega,\theta)$. The auto-convolution for the one target case $\chi_1(\Omega,\theta)$ is expressed as:

$$\begin{aligned}\chi_1(\Omega,\theta) = S_i(\Omega,\delta(\theta)) = \exp[j\frac{\pi N_a}{2}(-\Omega+2\delta(\theta))] \\ \text{sinc}(\frac{N_a(-\Omega+2\delta(\theta))}{4})a_i^2\pi^2 N_a\end{aligned} \tag{6.29}$$

Correspondingly, the auto-convolution $\chi_2(\Omega,\theta)$ for the two targets' case will be:

$$\begin{aligned}\chi_2(\Omega,\theta) = S_1(\Omega,\delta(\theta)) + S_2(\Omega,\delta(-\theta)) \\ +2a_1a_2\pi^2 N_a\text{sinc}(\frac{N_a(\Omega)}{4})\exp[j\frac{\pi N_a}{2}(\Omega)]\end{aligned} \tag{6.30}$$

For both cases, $\chi^{-1}(\max(\chi(\Omega))$ will be $2\delta(-\theta)$, $2\delta(\theta)$, or $\frac{M_\Omega}{2}$ depending on the reflectivity of the targets, with each value being proportional to $\pi^2 N_a a_1^2$, $\pi^2 N_a a_2^2$ or $2a_1a_2\pi^2 N_a$, respectively. $\frac{M_\Omega}{2}$ denotes the middle position index of the frequency. Note that the two targets' case always satisfies the following equation:

$$\chi_2(\frac{M_\Omega}{2}) >= \sqrt{\chi_2(\Omega_m) * \chi_2(M_\Omega-\Omega_m)} \tag{6.31}$$

On the contrary, the one target case will follow:

$$\chi_1(\frac{M_\Omega}{2}) < \sqrt{\chi_1(\Omega_m) * \chi_1(M_\Omega-\Omega_m)} \tag{6.32}$$

This will be set as the adaptive threshold-based criterion for the ambiguity detector. The adaptive threshold-based criterion for distinguishing one or two targets is only based on the radar signal data itself, which makes the proposed method robust to the diversity of the movement and the reflectivity.

Based on the theoretical analysis above, the algorithm is summarized in the pseudocode shown in Algorithm 7.

The RUDAT method will be implemented over all range bins to get the 2D azimuth-range map.

Algorithm 7: Proposed *RUDAT* method

Obtain the range estimation after 2D FFT on fast time & slow time. Select the angle-Doppler matrix $\mathbf{X}(i,l)$
Perform the DOA estimation on $\hat{r}$ DAM to get the angle profile $P_{DBF}(\theta)$ and $P_{DBS}(\theta)$ as in equations (2.25) and (6.7)
for Φ in $[-\frac{\pi}{2},\frac{\pi}{2}]$do
$l_\Phi = (2(v_x \sin\Phi v_y \cos\Phi N_d Tc)/\lambda$
$X(f) = \sum_{i=-M_\Omega/2}^{M_\Omega/2} \mathbf{X}(i,l_\phi)\exp(-j2\pi f i)$
$\chi(\Omega) = \sum X(f+\delta(\theta)-\beta(\theta))X(\Omega-(f+\delta(\theta)-\beta(\theta)))$
if $\chi(\frac{M_\Omega}{2}) < \sqrt{\chi(\Omega_m) * \chi(M_\Omega - \Omega_m)}$
$P(\Phi) = P_{DBF}(\Phi)/\max(P_{DBF}(\Phi) \times P_{DBS}(\Phi)$
else
$\text{sign}(\Phi) = \begin{cases} 1 & P_{DBF}(\Phi) > P_{DBF}(2\phi - \Phi) \\ 0 & P_{DBF}(\Phi) < P_{DBF}(2\phi - \Phi) \end{cases}$
$P(\Phi) = \text{sign}(\Phi) P_{DBF}(\Phi)/\max(P_{DBF}(\Phi)) \times P_{DBS}(\Phi)$
end
endfor
The unambiguous angle profile can be obtained.

6

6.4. RESULTS AND DISCUSSION

To show the effectiveness of the proposed method, several results based on simulated ideal point targets and complex extended targets are presented in this section, as well as experimental data. The results are presented using the 'UDFMBSC' method first, followed by a comparison with the updated 'RUDAT'. It is worth mentioning that as the proposed algorithm only focused on the ambiguity problem of forward-looking Doppler beam sharpening, i.e. in the angular region $[-\frac{\pi}{2},-\epsilon]\&[\epsilon,\frac{\pi}{2}]$, the blind zone problem is not considered here meaning that the DBS will lose its resolution within $[-\epsilon,\epsilon]$ [110, 111]. It is shown that targets overlapped in angles when using conventional MIMO array DOA estimation are successfully separated using Doppler sharpening. Also, the ambiguity of the Doppler sharpening is solved effectively by the proposed methods.

6.4.1. IDEAL POINT TARGETS-'UDFMBSC' METHOD

A simulated 2×4 MIMO radar was used to demonstrate the proposed UDFMBSC DOA estimation. This simulation assumes that eight channels can be used for DOA estimation in azimuth out of the 12 available in total in commercial 77 GHz automotive radar. The specifications of the radar parameters are listed in table 6.1.

The MIMO antenna on the forward-looking radar was located at the coordinate centre, with targets placed at the same range bin of 10m to meet the Fraunhofer distance [95] and ensure that targets are in the far-field. The two targets are at an azimuth angle of 40° and 50°. When the radar moves with velocity $v_y = 10m/s$, the proposed approach is compared with the traditional DBF and DBS methods. From Fig. 6.3, we can see that the proposed approach can separate the two targets without ambiguity and estimate the position of the two targets at 40.6° and 49.6°, respectively. In contrast, the traditional DBF-

Table 6.1: The chosen radar parameters for the simulation

Parameters	Value
Central Frequency (GHz)	77
Slope (MHz/us)	62.5
Sampling Rate (Msps)	32
Bandwidth (GHz)	1
PRI (us)	100

based method cannot separate the two targets, and the traditional DBS-based method is ambiguous.

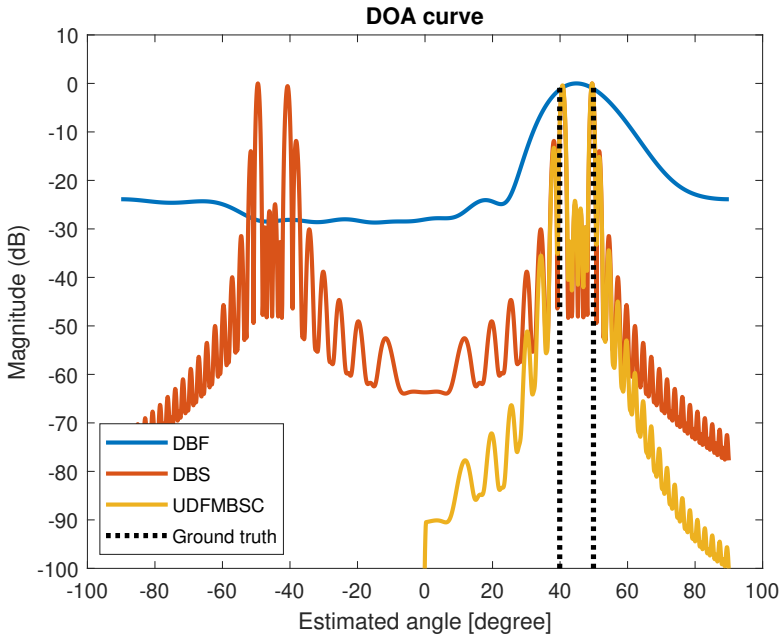

Figure 6.3: Simulated performance comparison with the conventional DBF, DBS and proposed UDFMBSC method. The two point targets are located at 40° and 50° as per ground truth lines.

To prove the capability of the proposed method of determining the left and right azimuth quadrants where the targets are located, another simulation is presented in Fig. 6.4, where the two targets are located at $-40°$ and $50°$. It is shown that the proposed approach estimates the position of the two targets as -40.6° and 49.6°, proving the algorithm's effectiveness. Also, to show that the proposed UDFMBSC can determine well whether there is one target or two, the two targets are symmetrically located at $40°$ and $-40°$ in another simulation. The result is shown in Fig.6.5 where the proposed method can solve the ambiguity and identify the two actual targets.

Finally, what follows is a brief analysis of the computational complexity of the pro-

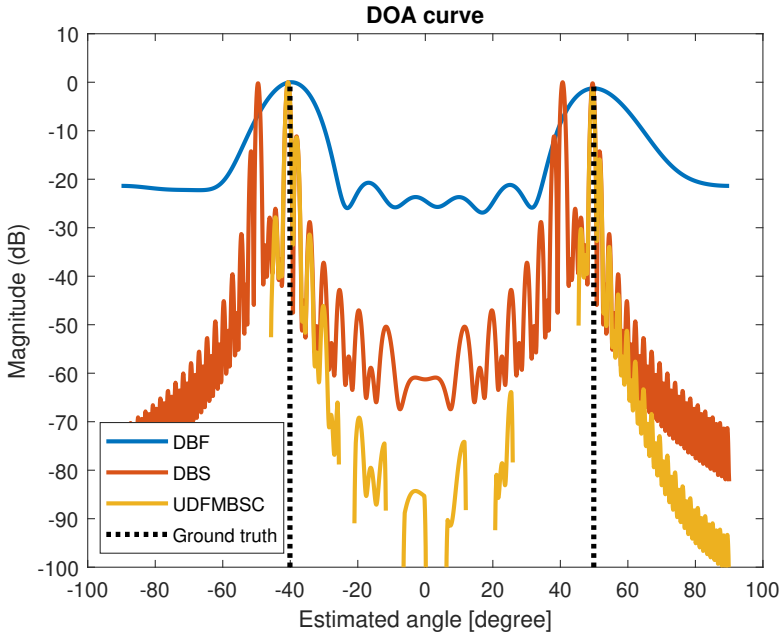

Figure 6.4: Simulated performance comparison with the conventional DBF, DBS and proposed UDFMBSC method. The two point targets are at -40° and 50° per ground truth lines.

posed approach, where N_a is the number of virtual antennas for DBF and N_d is the number of chirps used for DBS. Satisfactory performance can be obtained by implementing both the DBF-based method and the DBS-based method in Algorithm 6, hence the computational complexity is related to only an array consisting of $N_a + N_d$ elements in the digital beamforming stage, plus an auto-convolution computation. The computational requirements are only $N_a + N_d + N_d^2$ multiplications and $N_a + N_d^2$ additions. It should be noted that after the rough estimate of the targets of interest, only a small angular section should be searched to find the peaks. Thus, the computational complexity is about $O(N_a + N_d + N_d^2)$.

6.4.2. IDEAL POINT TARGETS-'RUDAT' METHOD

The MIMO antenna on the forward-looking radar was located at the coordinate centre, with targets placed at the same range bin of 10 m to ensure that targets are in the far field (Fraunhofer distance [95]). When the radar moves with velocity $[0, 15] m/s$, the Doppler symmetric line will be at $\theta = 0$. Two symmetric targets at azimuth angles of $\pm 40°$ with a six-times difference between their reflectivity and one target with the same RCS as the stronger one in the two symmetric targets at an azimuth angle of 50° are simulated. The proposed approach is compared with the traditional DBF, DBS methods, and *UDFMBSC* as shown in Fig. 6.6. The DBS profile shows 4 symmetric targets. With the proposed method, the targets are estimated at the correct position. The two targets at 50° and 40° are separated and estimated at 49.7° and 39.2° due to the narrow DBS beam. The

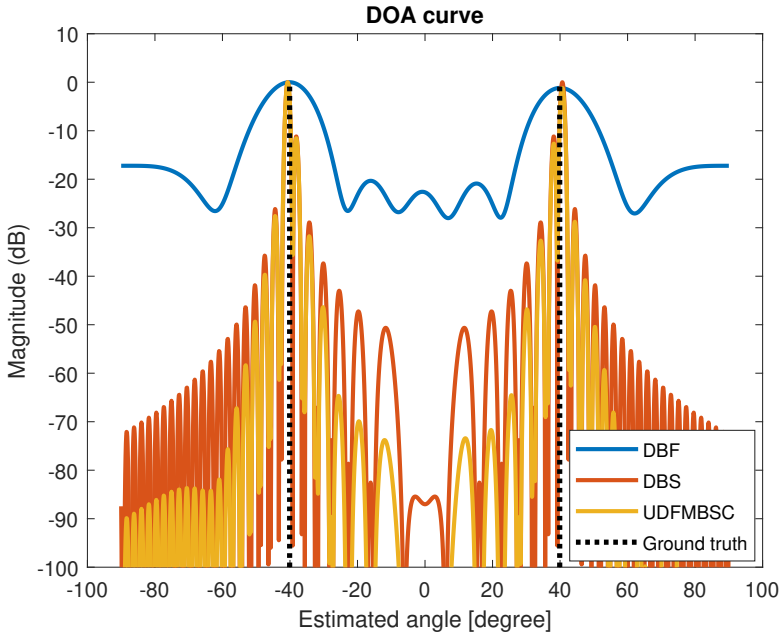

Figure 6.5: Simulated performance comparison with the conventional DBF, DBS and proposed UDFMBSC method. The two point targets are at -40° and 40° per ground truth lines.

proposed approach can successfully estimate the weaker target at -39.2°, whereas the *UDFMBSC* fails, proving the effectiveness of the adaptive threshold.

The second simulation is performed with the radar moving with velocity $[3,15]m/s$, i.e. with a component not in the forward-looking direction. The Doppler symmetric line will be located at approximately $\theta = 11.3°$. Two symmetric targets at an azimuth angle of 40° and 27.6° are simulated, as shown in Fig.6.7. The proposed *RUDAT* method successfully solves the ambiguity problem in this geometry, whereas the *UDFMBSC* fails.

6.4.3. COMPLEX EXTENDED TARGETS-'UDFMBSC' METHOD

To demonstrate the imaging capabilities of the proposed method beyond ideal point targets, simulated models of vehicles perceived as extended targets are used with the same setting as the complex car model in Section 4. Each car model is represented by 273 point scatterers generated randomly from the edges of the car, as shown in Fig. 4.12.

The first simulated scene is with the two static cars located symmetrically with respect to the broadside direction. Both cars are located at a 10-meter distance from the radar. The result is shown in Fig. 6.8. The DBF-based method can only distinguish the two targets without detailed information. In contrast, the DBS-based method provides more details but cannot determine whether the two targets are real or come from ambiguity. The UDFMBSC method can distinguish the two cars and provide more detailed information because of the resulting improvement in angular resolution, making it easier for subsequent processing stages based on these images, such as classification.

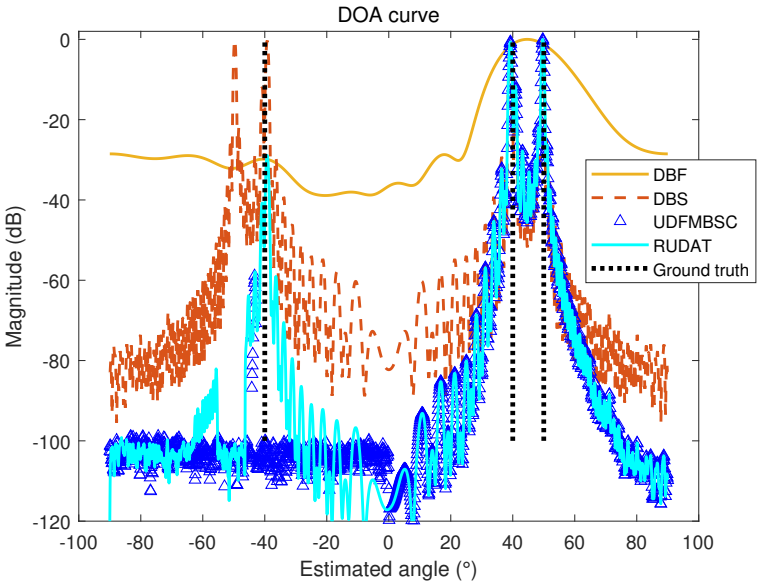

Figure 6.6: Simulated performance comparison between the conventional DBF, DBS, *UDFMBSC* and proposed *RUDAT* method for the first scenario.

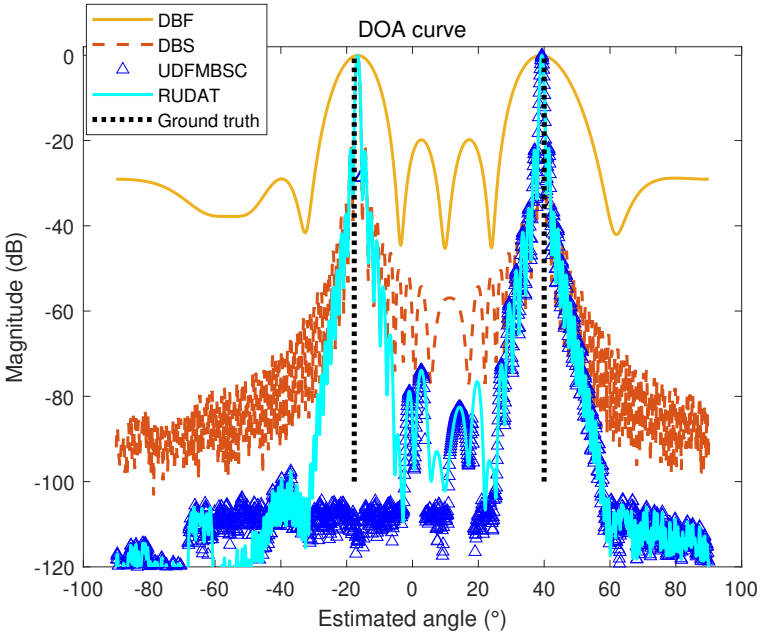

Figure 6.7: Simulated performance comparison between the conventional DBF, DBS, *UDFMBSC* and proposed *RUDAT* method for the second scenario.

The second simulated scene again includes two static cars, with spatial separation between them of $3m$. Also, the cars are located at a 10-meter distance from the radar, and the angle is approximately $-30°$. The DBF-based method cannot distinguish two targets because of poor angular resolution, while the DBS-based method can, but it will suffer from the ghost targets in its symmetric region. The proposed UDFMBSC method can separate two cars with more detailed information and solve the ambiguity problem.

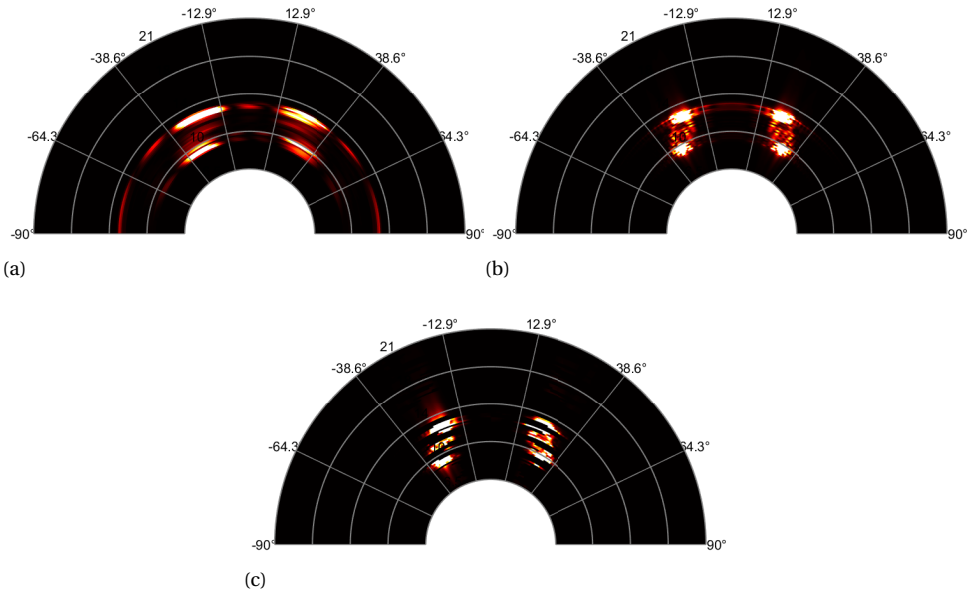

Figure 6.8: The resulting images for the two cars are symmetrically located with respect to the broadside when different DOA methods are applied. a) DBS-based method b) DBF-based method c) proposed UDFMBSC method.

To go beyond the simple visual inspection of images of extended targets, the image contrast metric is introduced in this work as discussed in Section. 4.4.2. The image contrast is defined as equation (4.21).

Also, more scatter points within the extended targets can be detected because of the improved angular resolution. Hence, the number of scatterers detected is also used to evaluate the results generated by different algorithms.

A Monte Carlo test is performed where two static cars are placed together in the scene with a spatial separation of $3m$. The centre position of the two cars is randomly selected in the different repetitions, with the range in the interval $[7.5m, 20m]$ and azimuth angle in the interval $[\pm 10°, \pm 45°]$. The resulting image contrasts from the range angle maps generated by different DOA algorithms are shown in Fig. 6.10. The number of detected scatter points in the scene is also given in Fig.6.11. It is shown that UDFMBSC obtains the highest value of the image contrast metric and can detect more scatter points, providing better separation capability and resolution for the considered extended targets. It should be noted that UDFMBSC yields almost the same results as DBS because the evaluations

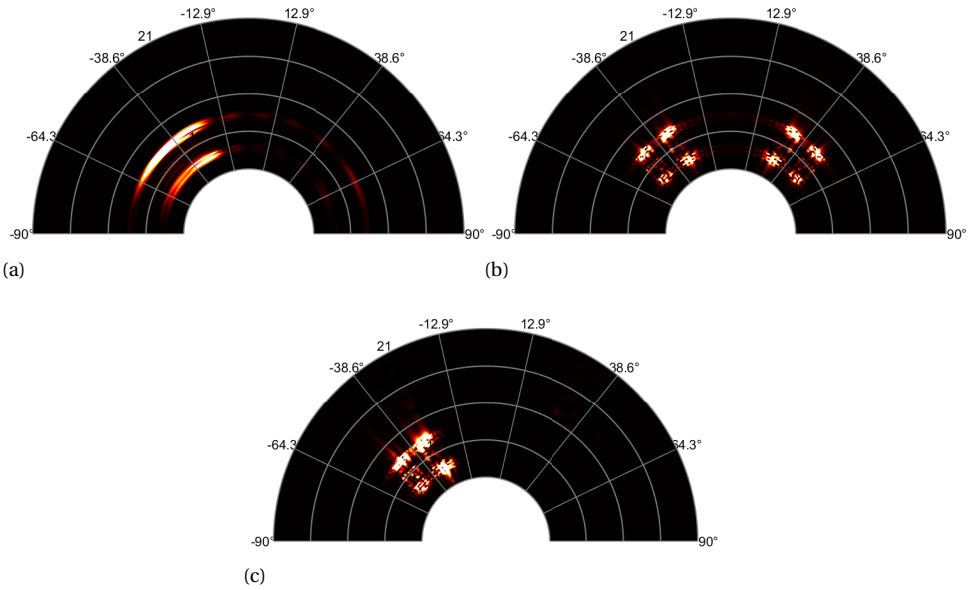

Figure 6.9: The resulting images for the two cars located close to each other when different DOA methods are applied. a) DBS-based method b) DBF-based method c)proposed UDFMBSC method.

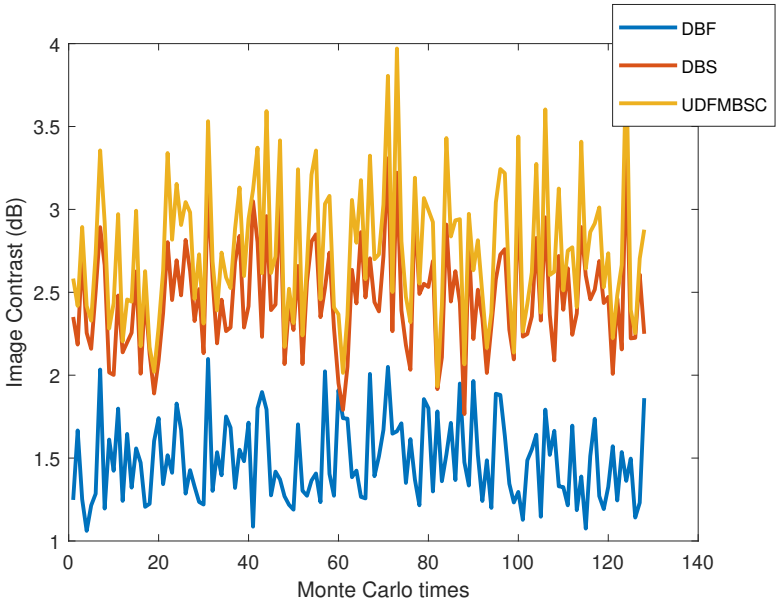

Figure 6.10: The image contrast metric as a function of different Monte Carlo tests for different DOA algorithms.

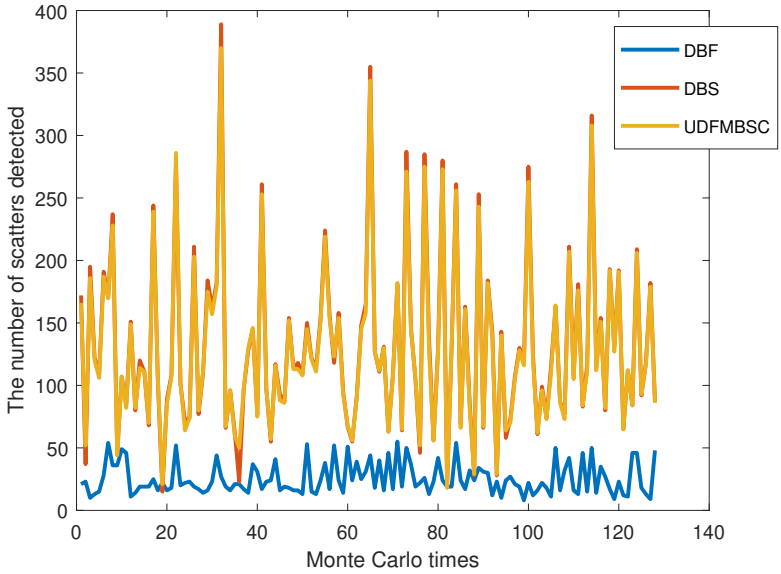

Figure 6.11: The number of scatter points detected within the extended targets' region as a function of different Monte Carlo tests for different DOA algorithms.

in this test are only calculated with respect to the ground truth value, so the detrimental problem of ambiguity is not considered here. With UDFMBSC, the image contrast is higher than with DBF, meaning the proposed methods can get better imaging results.

6.4.4. COMPLEX EXTENDED TARGETS-'RUDAT' METHOD

The simulated radar is now moving at $[3,15]m/s$ with four static car models located at a 10 m range from the radar. The four cars are divided into two groups located at an azimuth angle of 48.6° & -26°, symmetrically with respect to the motion trajectory at $\theta = 11.3^\circ$. The two cars in each group are separated by $3m$, and the group on the right-hand side is three times weaker than the other regarding reflectivity. The result is shown in Fig. 6.12. The DBF-based and DBS-based methods show the same problem as in Fig. 6.8. However, the *UDFMBSC* method fails as expected. In contrast, the *RUDAT* successfully separates the four cars in this challenging situation, i.e. non-ideal forward movement of the radar and diverse targets' reflectivity. It also provides more detailed images, simplifying subsequent processing stages such as classification that may be used.

6.4.5. EXPERIMENTAL RESULTS

The proposed approach is verified by experimental data. The radar used is the TI IWR6843ISK radar, shown in Fig. 4.15. The radar is the same one as in the Chapter.3 The parameters of this radar system are shown in Table. 6.2. Two transmit and four receive antennas are used for azimuth angle estimation during the measurement, and the spacing between adjacent receive antennas is half of the wavelength. The radar is installed on a moving platform, and the experimental measurement campaign was performed in the anechoic

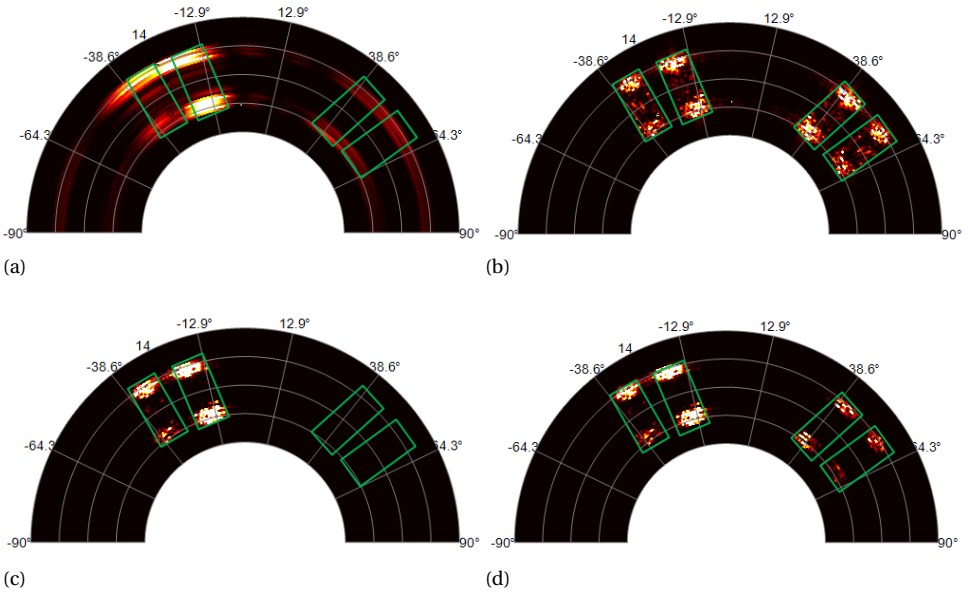

Figure 6.12: Simulated images for different DOA methods of 4 cars symmetrically located with respect to the movement of the radar. a) DBF-based method b) DBS-based method c) *UDFMBSC*. d) *RUDAT*

.

chamber at the Delft University of Technology (TU Delft). The experimental scene is shown in Fig. 6.13.

Table 6.2: The chosen radar parameters for the experimental verification

Parameters	Value
Central Frequency (GHz)	60
Slope (MHz/us)	10
Sampling Rate (Msps)	2.95
Bandwidth (GHz)	4
Number of chirps in snapshot	128
PRI(us)	420

Because of the limitations of the experimental moving platform, the radar speed is set at $v_y = 0.4m/s$. The PRI was set as large as possible within the radar limitations to have its best Doppler resolution at the cost of poor range resolution. Because the movement of the radar is limited, the improvement in the performance of the DBS over DBF is not shown here, but this has been demonstrated in [107, 109, 112–114]. The experiment results for the three corner reflectors with different processing methods are shown in Fig. 6.14. One can see that the two symmetric targets are well imaged, and the third target is unambiguously imaged with the UDFMBSC method, whereas the DBF has a wide main

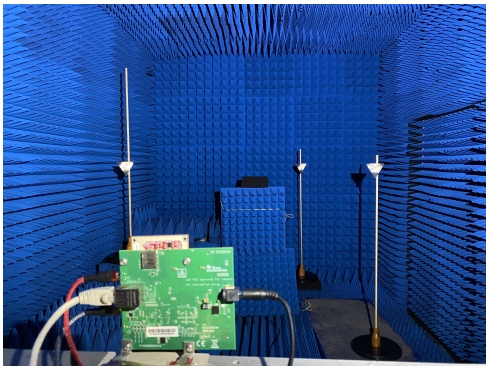

Figure 6.13: The experimental scene in the MS3 group's anechoic chamber with three corner reflectors; two are symmetric with respect to the radar.

lobe because of its poor angle resolution, and the DBS is ambiguous in the left/right direction. The angle profile of the two symmetric targets' range bin is also given in Fig.6.15.

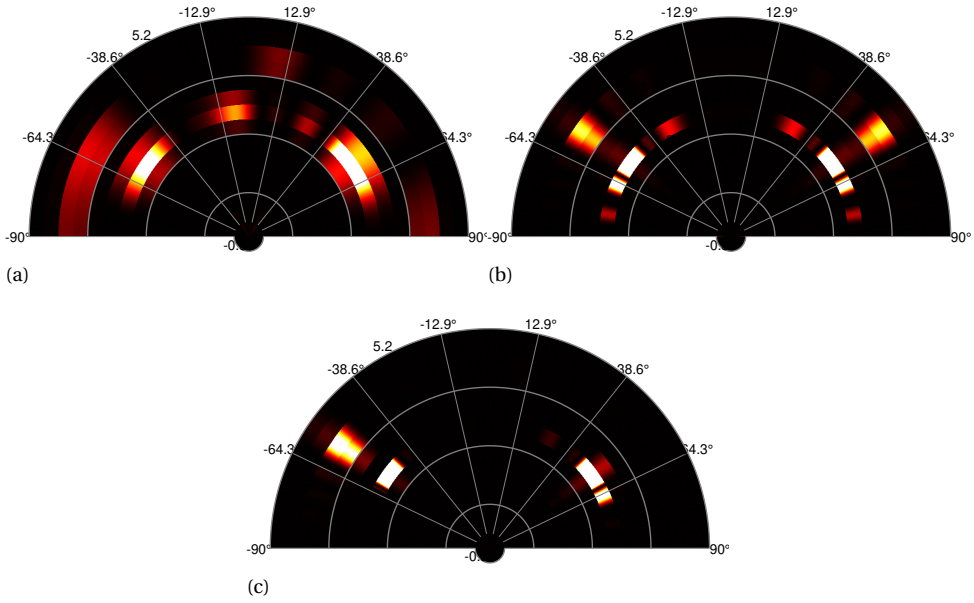

Figure 6.14: The experimental results for three corner reflectors. a) DBS-based method b) DBF-based method c) proposed UDFMBSC method.

Another frame's data is selected to prove the robustness of 'RUDAT' compared with 'UDFMBSC', as shown in Fig. 6.16. As the platform moves, the reflectivity from the three corner reflectors varies according to the different looking angles. The closer targets on the right side cannot be detected with 'UDFMBSC' but are resolved by the 'RUDAT', prov-

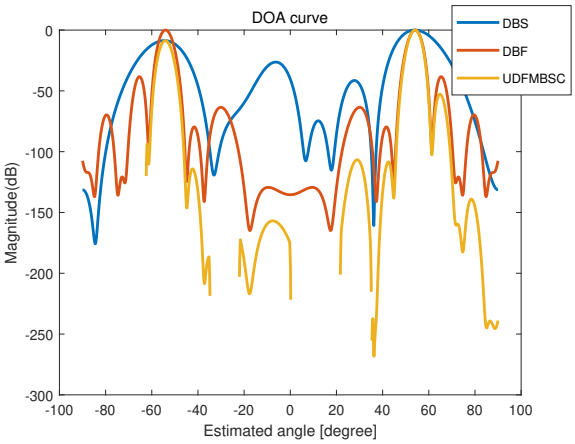

Figure 6.15: The DOA curve of the two symmetric targets in the experimental test under different methods.

ing the algorithm's performance in tackling the diverse targets.

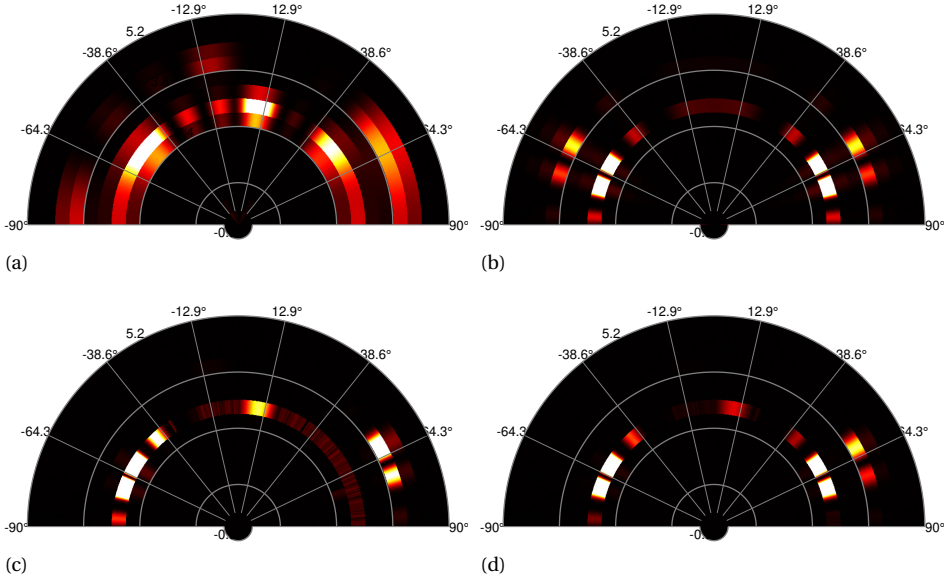

Figure 6.16: Imaging results for different DOA methods of experimental data. a) DBF-based method b) DBS-based method c) *UDFMBSC*. d) *RUDAT*

6.5. CONCLUSION

In this chapter, an 'unambiguous Doppler-based forward-looking multiple-input multiple-output radar beam sharpening scan' (UDFMBSC) algorithm is proposed, using MIMO array processing in combination with the Doppler beam sharpening. Azimuthal resolution improvement thanks to the Doppler beam sharpening has been demonstrated. Furthermore, the Doppler ambiguity has been solved for the first time, making it possible to use the Doppler beam sharpening to enhance the resolution for forward-looking radar without a high computational cost. Considering the potential cross-forward movement and forward velocity, the modified steering Doppler vector is also defined to compensate for the resulting error.

To further cope with differences in reflectivity between targets and be robust to non-ideal vehicle movements, i.e. velocity components not in the forward-looking direction, a 'Robust Unambiguous DBS with Adaptive Threshold' (*RUDAT*) algorithm is proposed. For a target at the angle of arrival of 40 degrees from the trajectory with 10m/s, the algorithm improves the azimuthal resolution of 8 elements' MIMO 6 times.

The proposed method has been verified for simulated point-like and extended targets, as well as on experimental data from a radar sensor, showing that UDFMBSC achieves better angular estimation than conventional DBS and DBF. It is worth noting that the proposed approach does not need any prior information on the environment, the number of targets, and their approximate position. The proposed approach is easier to apply in automotive applications in varying scenarios. Furthermore, the method relaxes the requirement of the number of antennas in the azimuth dimension, making it possible to use a larger array for elevation angle estimation. However, a limitation of the approach is that the target's movement will affect the DBS algorithm and degrade its performance, thus also influencing the performance of the proposed method. Also, beyond the ambiguity addressed in this manuscript, the forward-looking DBF method has the limitation of the blind zone problem, which needs to be addressed in future work.

7

3D Robust Doppler Beam Sharpening Algorithm for Forward-looking MIMO Radar

The ambiguity problem of targets in Doppler beam sharpening with forward-looking radar is considered. The RUDAT is extended to the 3D imaging algorithm after solving the coupling between the azimuth and elevation angle estimation and the ambiguity problem of the Doppler beam sharpening. The performance has been studied in simulations, and possible limitations have been discussed. In addition, the method has been verified experimentally with point-like and extended targets to show the robustness of the whole processing flowchart. The proposed method's performance is compared to existing approaches using simulated data with point-like and extended targets. The method is successfully verified using experimental data.

Parts of this chapter have been published in:

S. Yuan, F. Fioranelli and A. G. Yarovoy, "3DRUDAT: 3D Robust Unambiguous Doppler Beam Sharpening Using Adaptive Threshold for Forward-Looking Region," in IEEE Transactions on Radar Systems, vol. 2, pp. 138-153, 2024

7.1. INTRODUCTION

As discussed in 4, radar will play a more important role with 3D imaging ability in the future. The quality of 3D imaging will highly rely on the radar's resolution. Better resolution can provide a denser point cloud after detection, which will benefit later tracking, classification, and data association applications. The improvement of angular resolution by using DBS for forward-looking has been proved in 5. Extending the proposed RUDAT in the previous chapter to 3D imaging is important. This further explores the radar's 3D imaging ability, achieving high angular resolution algorithms.

However, to our knowledge, no 3D high-resolution imaging has been proposed, including the elevation dimension. Based on the previous study, a RUDAT was extended to a 3D imaging algorithm in this chapter, simultaneously solving the robust ambiguity problem for forward-looking Doppler and the coupling between elevation and azimuth angle problem . Furthermore, its performance is analyzed for ideal point targets and extended targets in simulations and real datasets.

The main contributions of the paper are listed as follows:

1. A 3D imaging using Doppler beam sharpening for achieving high angular resolution is proposed in this paper.

2. The ambiguity problem for Doppler beam sharpening in the robust vehicle's trajectory in the forward-looking region is solved by combining the MIMO processing.

3. The coupling between the elevation and the azimuth in the Doppler beam sharpening is addressed by processing the algorithm in both elevation and azimuth direction.

4. The voxelization accuracy and the image contrast are proposed to evaluate the general 3D imaging results.

The rest of this paper is organized as follows. In Section 7.2, the DBS algorithm for 3D imaging is provided. The problem formulation and the proposed method are demonstrated in Section 7.3. The results for simulated ideal point targets, simulated complex extended targets and experimental data, plus a discussion about the resolution improvement, are provided in Section 7.4. Finally, Section 7.5 concludes the paper.

7.2. DOA ESTIMATION

The DOA algorithm for forward-looking region is discussed in Section. 6.2. Here, the DBS is formulated for 3D context as well. The signal model in equation (6.4) for DBS becomes:

$$\mathbf{X}^H = \sum_{m=1}^{M} \mathbf{a}_{d_m} \mathbf{S}_t + \mathbf{N} \in \mathbb{C}^{L_d \times N_a N_e} \tag{7.1}$$

Assuming that all the targets are static in the radar field of view, the maximum Doppler will be no larger than the one corresponding to the vehicle's speed v_0. So, for Doppler beam sharpening, we introduce the steering of the Doppler vector:

$$\begin{aligned} \mathbf{a_d}(\theta,\phi) &= \mathbf{a_{d_m}} = [1, e^{-j2\pi f_d(1,m)T}, ..., e^{-j2\pi f_d(p,m)T} ... e^{-j2\pi f_d(L_d-1,m)T}]^T \\ f_d(p,m) &= \frac{2p(v_y \cos\theta_m \cos\phi_m + v_x \sin\theta_m \cos\phi_m + v_z \sin\phi_m)}{\lambda} \end{aligned} \tag{7.2}$$

The DBS algorithm can also provide the DOA estimation, and the weight vector $\mathbf{w}_{DBS}$ has the same form as (6.6).

The power of the weighted output of DBS is:

$$\begin{aligned} P_{DBS}(\theta,\phi) &= E[\left|\mathbf{w}_{DBS}^H \mathbf{X^H}\right|^2] \\ &= \frac{\mathbf{a_d}^H(\theta,\phi) R_{\mathbf{X^H X^H}} \mathbf{a_d}(\theta,\phi)}{\mathbf{a_d}^H(\theta,\phi)\mathbf{a_d}(\theta,\phi)} \end{aligned} \tag{7.3}$$

$R_{\mathbf{X^H X^H}} = E\left[\mathbf{X}\mathbf{X}^H\right]$ is the autocorrelation matrix of $\mathbf{X^H}$.

7.3. PROBLEM FORMULATION AND THE PROPOSED METHOD

7.3.1. PROBLEM FORMULATION

Automotive radar equipped with 3D high-resolution imaging ability will become one of the primary sensors in the autonomous vehicle industry. The Doppler beam is essentially narrower than the MIMO array beam in most of the area; thus, the Doppler beam sharpening can improve angular resolution in a large part of the field of view [69], which will be the strongest supportive algorithm in the future.

However, there are several problems when implementing Doppler beam sharpening in the forward region for 3D imaging. As the introduction mentions, this chapter focuses on the ambiguity problem instead of the blind zone problem. The ambiguity arises from the inherent geometry of the forward-looking radar. When the vehicle is moving toward the two static targets, both will appear symmetric concerning the trajectory of the radar, and they will experience the same Doppler velocity because of the vehicle's movement. Furthermore, the coupling between azimuth and elevation problems was raised when Doppler frequency was projected to the spatial domain, leading to the coupling between elevation and azimuth. These two factors make targets indistinguishable using Doppler beam sharpening for 3D imaging. One schematic of the ambiguity and coupling problem is shown in Fig. 7.1.

7.3.2. PROPOSED 3D DOPPLER BEAM SHARPENING

Our work in [119] has made the previous UDFMBSC[43] algorithm more robust to irregular trajectories in 2D and the diversity of targets' reflectivity. Specifically, the problem of ambiguous symmetric targets for non-ideal forward-looking vehicle trajectories was addressed in 2D via additional phase shift compensation. Targets with different reflectivity were retrieved using an adaptive threshold instead of a simpler peak search.

In this chapter, the novel *3DRUDAT* algorithm is proposed to tackle the problem of 3D imaging, which not only addresses the issue of ambiguity for forward-looking automotive radar but also solves the elevation-azimuth coupling problem with the Doppler frequency. The algorithm implements two consecutive filtering operations in elevation

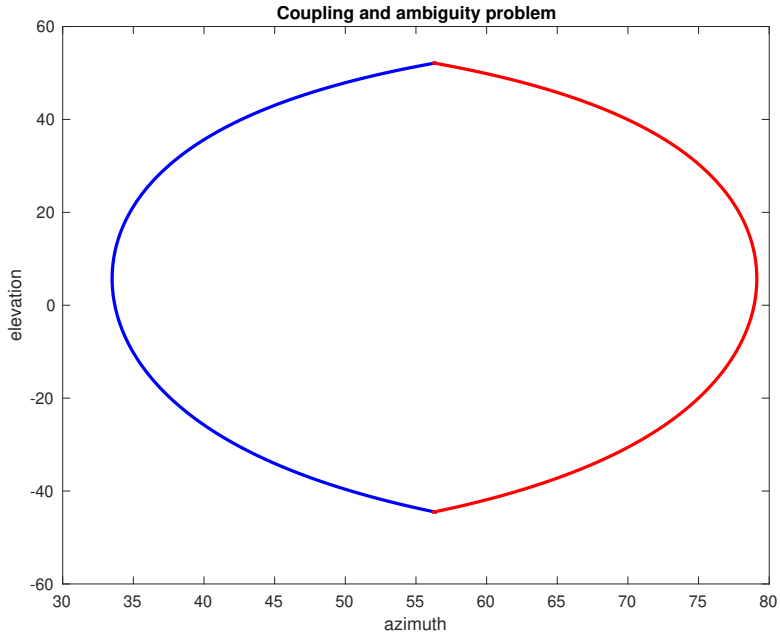

Figure 7.1: The coupling between the elevation and azimuth and the ambiguity problem to the trajectory. The blue and red curve indicates the ambiguity for both sides, while the curve itself indicates the coupling problem.

and azimuth. The ambiguity concerning the radar's trajectory is then solved with the MIMO processing in the azimuth array. At the same time, the coupling problem is addressed by using the MIMO processing in the elevation array.

First, considering that the vehicle is moving with speed $[v_x, v_y, v_z]$, a target with Doppler speed v_r is detected, and the possible positions after Doppler beam sharpening will be a group of (θ, ϕ) angles, satisfying the following equation (7.4). It should be noted that an example of the possible positions satisfying this equation in the azimuth-elevation plane $P_{DBS}(\theta, \phi)$ was shown in the sketch in Fig.7.1.

$$v_r = v_x \sin\theta \cos\phi + v_y \cos\theta \cos\phi + v_z \sin\phi \tag{7.4}$$

The first step of the proposed algorithm is to detect the target in a range bin. Then, for this range bin, the elevation angle profile $P_{DBFe}(\phi)$ and the coupled elevation-azimuth image $P_{DBFa}(\theta, \phi)$ will be obtained with the MIMO DBF algorithm. Basically, the $P_{DBFe}(\phi)$ will be obtained by 1D DBF on the selected elevation channels, while the $P_{DBFa}(\theta, \phi)$ will be obtained with the selected azimuth channels with an extra elevation term $\cos\phi$ in the 2D DBF steering vector.

Next, using DBS, every pixel of the curve in the azimuth-elevation plane $P_{DBS}(\theta, \phi)$ could be the candidate angles of a target; hence, every azimuth & elevation signal extracted from $P_{DBS}(\theta, \phi)$ will be processed. The corresponding Doppler velocity v_r can

be expressed as:

$$v_r = \sqrt{(v_x^2 + v_y^2)\cos^2(\theta - \theta_c) + v_z^2}\cos(\phi - \phi_c) \tag{7.5}$$

$\theta_c = \frac{v_x}{v_y}$ and $\phi_c = \frac{v_z}{(v_x^2+v_y^2)\cos^2(\theta-\theta_c)}$ are the azimuth and elevation directions of the trajectory, respectively. It should be noted that due to the coupling, the elevation direction will change according to different azimuth angles.

Considering a target's position with azimuth and elevation $[\theta_a - \theta_c, \phi_a - \phi_c]$ in the azimuth-elevation plane, the possible coupling position in the elevation signal $P_{DBS}(\theta_a - \theta_c, \phi^*)$ will be $-\phi_a - \phi_c$, and the possible ambiguous position in the azimuth signal $P_{DBS}(\theta^*, \phi_a - \phi_c)$ will be $-\theta_a - \theta_c$. θ^* and ϕ^* denote all the possible angles in azimuth and elevation when fixing the other angle. The Doppler cell index related to the target angular position $[\theta_a - \theta_c, \phi_a - \phi_c]$ is computed as:

$$l_{Do} = \frac{2v_r N_d T c}{\lambda} \tag{7.6}$$

where N_d is the number of chirps used for Doppler processing.

The angle vector of this Doppler cell can be obtained from the DAT defined in (2.20), and $\mathbf{X}_a(i, l_{Do})$ for azimuth and $\mathbf{X}_e(j, l_{Do})$ for elevation will be extracted separately for further processing. The phase difference of the antenna vector from those possible angular positions will follow the format of $\beta(\theta) = \frac{d\sin(\theta-\theta_c)}{\lambda}$ and $\beta(\phi) = \frac{d\sin(\phi-\phi_c)}{\lambda}$. An extra shift is implemented first to obtain the odd functions $\delta(\theta)$ and $\delta(\phi)$ as an essential step to solve the ambiguity. These shifts are implemented as follows:

$$\begin{aligned}
\delta(\theta) &= \beta(\theta) + \frac{d\cos\theta\sin\theta_c}{\lambda} = \frac{d\sin\theta\cos\theta_c}{\lambda} = -\delta(-\theta) \\
\delta(\phi) &= \beta(\phi) + \frac{d\cos\phi\sin\phi_c}{\lambda} = \frac{d\sin\phi\cos\phi_c}{\lambda} = -\delta(-\phi)
\end{aligned} \tag{7.7}$$

Specifically, the resulting phase term $\delta(\theta) - \beta(\theta)$ is implemented on the Fourier transform $X_a(f)$ of the azimuth angle vector $\mathbf{X}_a(i, l_{Do})$ at the selected Doppler index l_{Do} as a compensation for the irregular trajectory direction. Similarly, the resulting term $\delta(\phi) - \beta(\phi)$ is implemented on the Fourier transform $X_e(f)$ of the elevation angle vector $\mathbf{X}_e(j, l_{Do})$ at the selected Doppler index l_{Do}.

Taking $X_a(f)$ as an example, its auto-convolution $\chi_a(\Omega)$ will satisfy the following equation:

$$\chi_a(\Omega) = \sum X_a(f + \delta(\theta) - \beta(\theta)) X_a(\Omega - (f + \delta(\theta) - \beta(\theta))) \tag{7.8}$$

With the applied shifts, it is noted that the auto-convolution of the azimuth signal is different depending on the number of targets in the ambiguous positions. For the one target case, the auto-convolution $\chi_{a1}(\Omega, \theta)$ of the azimuth signal $X_a(f)$ can be written as:

$$\chi_{a1}(\Omega,\theta) = S_{o_1}(\Omega,\delta(\theta)) = \exp[j\frac{\pi N_a}{2}(-\Omega+2\delta(\theta))] \\ \text{sinc}(\frac{N_a(-\Omega+2\delta(\theta))}{4}) a_{o_1}^2 \pi^2 N_a \tag{7.9}$$

where a_{o_1} is the reflectivity of target o_1, N_a is the number of antennas for azimuth processing, and Ω is the sampling index in the signal.

Correspondingly, the auto-convolution $\chi_{a2}(\Omega,\theta)$ for the two targets' case will be:

$$\chi_{a2}(\Omega,\theta) = S_1(\Omega,\delta(\theta)) + S_2(\Omega,\delta(-\theta)) \\ + 2a_{o_1}a_{o_2}\pi^2 N_a \text{sinc}(\frac{N_a(\Omega)}{4}) \exp[j\frac{\pi N_a}{2}(\Omega)] \tag{7.10}$$

It is noted that for both cases, the value of $\chi_a^{-1}(\max(\chi_a(\Omega))$ will be $2\delta(-\theta)$, $2\delta(\theta)$, or $\frac{M_\Omega}{2}$ depending on the reflectivity of the targets, where $\frac{M_\Omega}{2}$ denotes the middle position index of the $\chi_a(\Omega)$. Each of these values is proportional to $\pi^2 N_a a_{o_1}^2$, $\pi^2 N_a a_{o_2}^2$ or $2a_{o_1}a_{o_2}\pi^2 N_a$, respectively.

An adaptive threshold-based criterion is then set for the proposed method as follows. First, the threshold is defined as:

$$Tr_a = \chi_a(\frac{M_\Omega}{2}) - \sqrt{\chi_a(\Omega_m)\chi_a(M_\Omega-\Omega_m)} \tag{7.11}$$

where M_Ω denotes the total sampling number of $\chi_a(\Omega)$, and $\Omega_m = \chi_a^{-1}(\max(\chi_a(\Omega)))$ is the maximum position of $\chi_a(\Omega)$. If $Tr_a \geq 0$, there will be two targets in the selected Doppler cell; otherwise, there is only one target.

The elevation signal has the same auto-convolution property as the azimuth. The aforementioned computations with auto-convolution $\chi(\Omega)$ are performed for every Doppler frequency, and the operation with thresholds Tr_e and Tr_a are applied for both elevation and azimuth signals to determine whether there are one or two targets in this Doppler cell.

If there is one target, the two coupled or ambiguous positions from the MIMO DBF angular profile will be compared to obtain the final position, as follows:

$$\text{sign}(\phi) = \begin{cases} 1 & P_{DBFe}(\phi) \geq P_{DBFe}(2\phi_c - \phi) \\ 0 & P_{DBFe}(\phi) < P_{DBFe}(2\phi_c - \phi) \end{cases} \tag{7.12}$$

$$\text{sign}(\theta) = \begin{cases} 1 & P_{DBFa}(\theta,\phi) \geq P_{DBFa}(2\theta_c - \theta,\phi) \\ 0 & P_{DBFa}(\theta,\phi) < P_{DBFa}(2\theta_c - \theta,\phi) \end{cases} \tag{7.13}$$

Then the value from equation (7.12) and (7.13) will be multiplied with the value from the normalized elevation profile $P_{DBFe}(\phi)$, the normalized coupled elevation-azimuth image $P_{DBFa}(\theta,\phi)$ and each pixel from the Doppler beam sharpening image $P_{DBS}(\theta,\phi)$ to derive the decoupled and unambiguous image $P_{ud}(\theta,\phi)$.

If there are two targets, the normalized MIMO DBF angular profile value in both directions will be multiplied directly by the Doppler beam sharpening image. It is worth

mentioning that for no target case or those regions whose θ or ϕ do not correspond to a real target, the multiplication operation will decrease the resulting energy significantly, as the MIMO DBF processing does not focus those regions.

Moreover, as the proposed method needs consecutive processes on elevation and azimuth signal, the algorithm performs the operation on elevation first to get the elevation uncoupled image $P(\theta,\phi)$. The operation on azimuth is then implemented on $P(\theta,\phi)$ to derive the final decoupled and unambiguous image $P_{ud}(\theta,\phi)$.

Based on the above theoretical analysis, the proposed algorithm is summarized as pseudocode shown in Algorithm 8.

Algorithm 8: Proposed *3DRUDAT* algorithm

Perform range estimation after 2D FFT on fast & slow time.
Then, for every range bin, select the azimuth-Doppler matrix $\mathbf{X}_a(i,l)$; the elevation-Doppler matrix $\mathbf{X}_e(j,l)$; the corresponding coupled elevation-azimuth image from MIMO DBF $P_{DBFa}(\theta,\phi)$ and elevation profile $P_{DBFe}(\phi)$; and the image from conventional DBS $P_{DBS}(\theta,\phi)$.
for θ in $[-\frac{\pi}{2},\frac{\pi}{2}]$ do:
  for ϕ in $[-\frac{\pi}{2},\frac{\pi}{2}]$ do:
    Compute the Doppler index l_{Do} in (7.6) and compute the Fourier transform $X_e(f)$ of the selected elevation angle vector $\mathbf{X}_e(j,l_{Do})$. Then compute the auto-convolution as follows:
    $\chi_e(\Omega)=\sum X(f+\delta(\phi)-\beta(\phi))X(\Omega-(f+\delta(\phi)-\beta(\phi)))$
    if $Tr_e \geq 0$
    $P(\theta,\phi)=P_{DBFe}(\phi)/\max(P_{DBFe}(\phi)\times P_{DBS}(\theta,\phi)$
    else
    Compute sign(ϕ) according to equation (7.12)
    $P(\theta,\phi)=P_{DBFe}(\phi)/\max(P_{DBFe}(\phi))\times P_{DBS}(\theta,\phi)\text{sign}(\phi)$
    end
    For the same Doppler index l_{Do} compute the Fourier transform $X_a(f)$ of the selected elevation angle vector $\mathbf{X}_a(i,l_{Do})$. Then compute the auto-convolution as:
    $\chi_a(\Omega)=\sum X(f+\delta(\theta)-\beta(\theta))X(\Omega-(f+\delta(\theta)-\beta(\theta)))$
    if $Tr_a \geq 0$
    $P_{ud}(\theta,\phi)=P_{DBFa}(\theta,\phi)/\max(P_{DBFa}(\theta,\phi)\times P(\theta,\phi)$
    else
    Compute sign(θ) according to equation (7.13)
    $P_{ud}(\theta,\phi)=P_{DBFa}(\theta,\phi)/\max(P_{DBFa}(\theta,\phi))\times P(\theta,\phi)\text{sign}(\theta)$
    end
  endfor
endfor
The unambiguous angle profile $P_{ud}(\theta,\phi)$ is finally obtained.

The 3DRUDAT method will be implemented over all range bins to get the azimuth-elevation-range map.

7.4. RESULTS AND DISCUSSION

In this section, the effectiveness of the proposed method is showcased through the utilization of simulated ideal point targets, simulated complex extended targets, and experimental data. Multiple evaluation metrics, i.e., the image contrast and voxelization accuracy, have been devised to establish the superiority of the proposed method and improve its resolution.

7.4.1. SIMULATED AND EXPERIMENTAL RESULTS

NUMERICAL SIMULATIONS

We employed a simulated 8×8 phased radar system for DOA estimation in both azimuth and elevation directions to generate the 3D images. The radar operates at 77GHz as commercial automotive radars. The radar parameters are specified as follows: the starting frequency of the FMCW chirp f_0 is 77 GHz, the chirp bandwidth B is 1 GHz, the chirp duration T_c is 16 μs, the sampling rate f_s is 64 Msps, and L = 512 chirps are processed in each frame. The MIMO antenna on the forward-looking radar is located at the coordinate centre.

For the initial simulation experiments, we considered a single point target situated at a range of 10 m, with an azimuth angle of $-20°$ and an elevation angle of $30°$. The results are shown in Fig. 7.2. To examine the imaging performance within the [-20,0] dB range, three distinct methods were utilized: beamscan (denoted by DBF, Digital Beam Forming), conventional Doppler beam sharpening (DBS), and the proposed method '*3DRUDAT*'. The resulting azimuth-elevation images, denoted as (a), (b), and (c), respectively, were generated for the range bin containing the target. The target's position is indicated by a white box, and the sub-figures in (a) and (c) provide enlarged views for more detailed information. Notably, with the beamscan method (a) and 3DRUDAT (c), the target appears well-focused, while conventional DBS yields a circular shape due to coupling and ambiguity problems, as previously discussed. Fig. 7.2 (d) and (e) display the azimuth and elevation profiles of the target, respectively. The Doppler-based method exhibits a narrower beam than the general DBF, resulting in improved angle resolution in both azimuth and elevation angles.

In the second simulation, four point targets were considered, as illustrated in Fig. 7.3, using the same parameters as the simulation for a single point target. The first row of the figure presents the four closely spaced targets at azimuth angles of $-30°$, $-30°$, $-45°$, and $-45°$, and elevation angles of $-20°$, $-35°$, $-20°$, and $-35°$, respectively. This arrangement aims to demonstrate the effectiveness of the proposed method in terms of angle resolution. White boxes denote the ground truth positions of the four targets and are also zoomed in subchapter-7/figures (a) and (c). Notably, the Doppler sharpening technique successfully generates four distinct spatial circles in both the azimuth and elevation planes. On the other hand, the MIMO beamscan fails to separate the four targets due to its limited resolution. In contrast, the proposed method effectively separates the targets with acceptable errors, thus demonstrating improved resolution capability.

In the second row of Fig. 7.3, another set of four targets is presented, each having different reflectivity. The targets are located at azimuth angles of $-20°$, $56.9°$, $-20°$, and $56.9°$, and elevation angles of $-20°$, $-20°$, $55.7°$, and $55.7°$. Importantly, these four targets possess the same Doppler frequency, resulting in a circular pattern in the Doppler

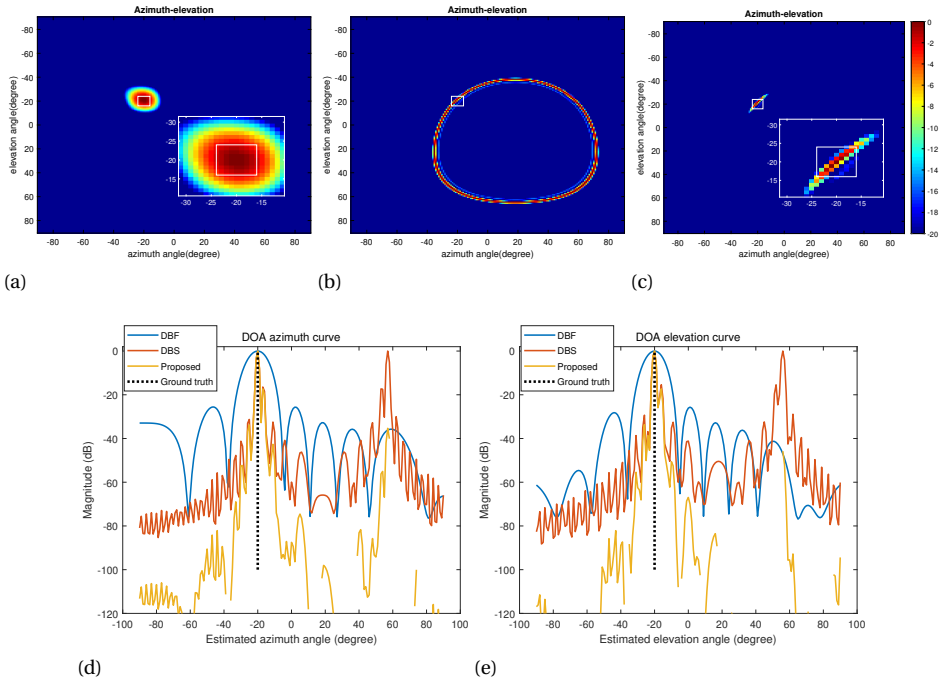

Figure 7.2: The simulation results for one point target: (a) the MIMO beamscan image; (b) the conventional Doppler beam sharpening image; (c) the proposed 3DRUDAT image; (d) azimuth profile with three different methods including ground truth marked with white box; (e) elevation profile with three different methods including ground truth marked with white box. The sub-figures in white in (a) and (c) provide enlarged/zoomed views for more detailed information.

beam sharpening approach. The imaging results obtained using different algorithms are displayed in the second row of the figure, highlighting the effectiveness of the proposed method in resolving coupling and ambiguity issues in DBS. In the MIMO beamscan image (d), the targets with different energy distributions are focused with varying power. The proposed method (f) successfully addresses the coupling issue, resulting in a focused circle.

In order to compare the improvement achieved in different spatial positions, we simulated four closely spaced point targets located at 10 meters. These targets were positioned with different combinations of azimuth and elevation angles, as presented in Table 7.1. The performance of different methods in resolving these targets was evaluated and illustrated in Fig. 7.4. Under the proposed method, the four targets are well separated, showcasing the improved angle resolution. However, in MIMO processing, the targets appear merged due to the limited angle resolution. Notably, it is observed that the targets located further away from the symmetric point, which is the middle point of the circle in Doppler beam sharpening, exhibit greater resolution improvement. This observation will be discussed in more detail in the subsequent discussion section.

In terms of computational complexity, Monte Carlo tests were conducted with ran-

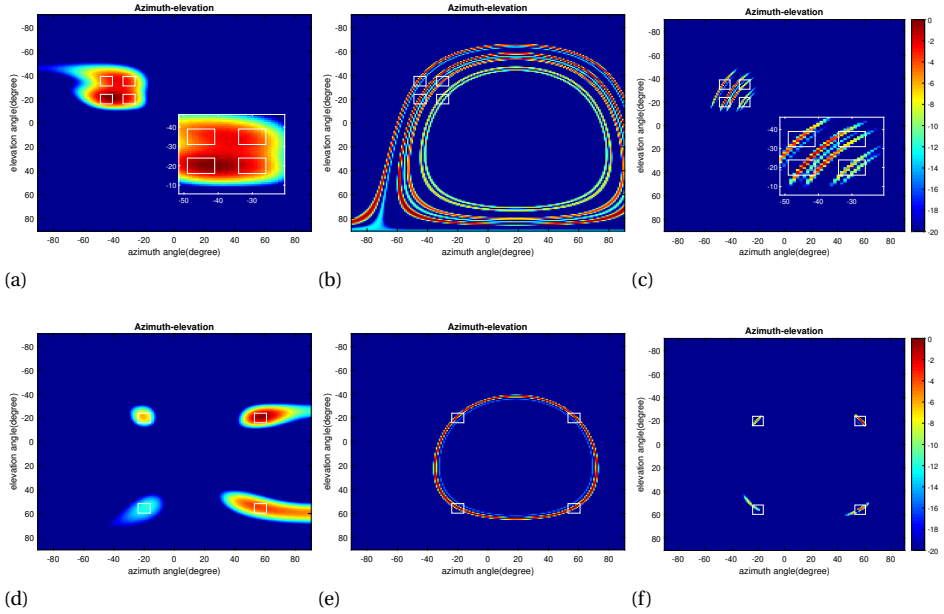

Figure 7.3: The simulation results for four point targets. (a), (b) and (c) are four closed targets under MIMO beamscan, conventional Doppler beam sharpening, and 3DRUDAT, respectively. (d), (e) and (f) are four coupling and ambiguous targets under MIMO beamscan, conventional Doppler beam sharpening, and 3DRUDAT, respectively.

7

Table 7.1: The Targets' positions used in simulation

Row	Azimuth Angle	Elevation Angle
Row 1	$[-60°, -60°, -45°, -45°]$	$[-20°, -35°, -20°, -35°]$
Row 2	$[-30°, -30°, -45°, -45°]$	$[-50°, -35°, -50°, -35°]$
Row 3	$[-60°, -60°, -45°, -45°]$	$[-50°, -35°, -50°, -35°]$

domly positioned targets to estimate the average time required to compute the azimuth-elevation image. These tests were performed using MATLAB on a standard desktop computer, and 100 repetitions were considered for each algorithm under evaluation. Specifically, the original MIMO beamscan algorithm exhibited a computation time of $0.35s$, whereas the proposed method took an average of $7.46s$. The increased computation time in the proposed method is attributed to the need to search each possible direction to determine the target, which results in a heavier computational load. However, it is important to note that this increased computation is necessary to achieve the enhanced resolution provided by the proposed method. Furthermore, it is worth mentioning that the time cost can be mitigated to some extent through parallel computing techniques, which can distribute the computational workload across multiple processors or cores, thus potentially reducing the overall processing time.

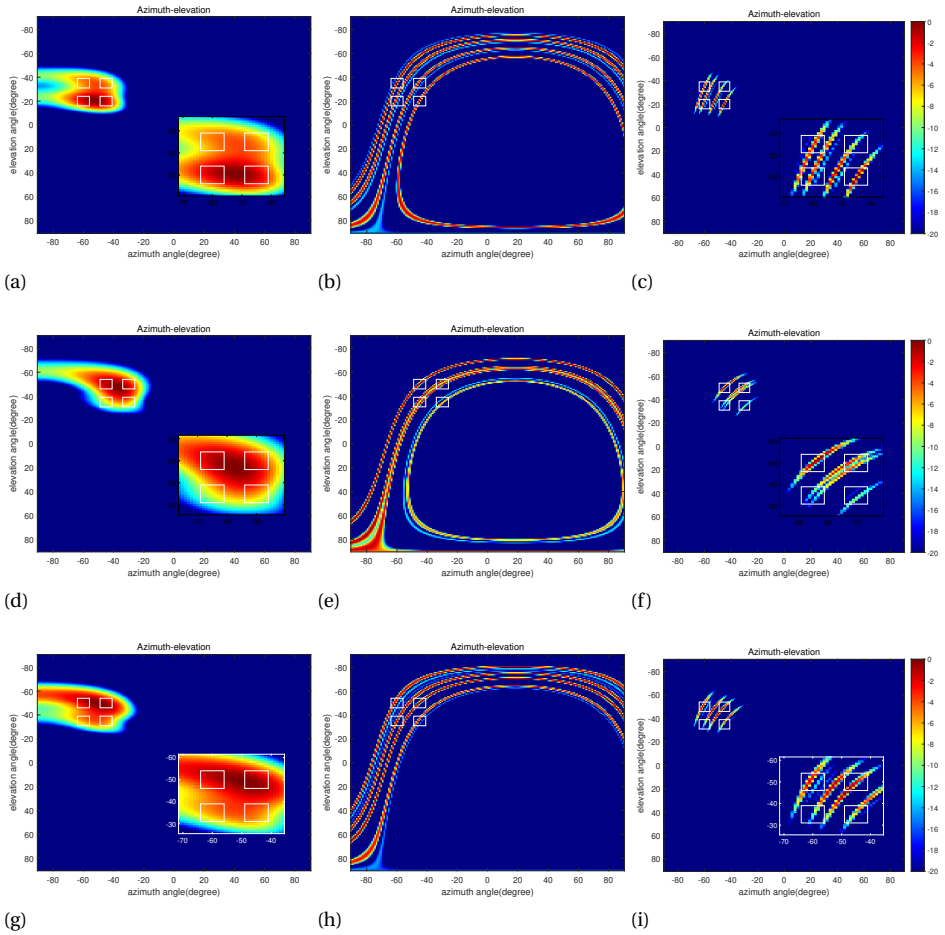

Figure 7.4: The simulation results for four closed point targets at different positions. The first row (a), (b), and(c) are images using different methods for four targets with larger azimuth angles but the same elevation angle compared with the setting in Fig. 7.3. The second row (d), (e), and(f) are images using different methods for four targets with the same azimuth angle but a larger elevation angle, while the third row (g), (h), and (i) are images using different methods for four targets with the larger azimuth angle and the larger elevation angle.

Simulated models of various 3D objects are utilized as extended targets to showcase the proposed method's imaging capabilities beyond ideal point targets. These 3D objects, namely the bridge, the Ferrari car, and the working man, are generated as CAD models, shown in Fig. 7.5. All the points comprising the surface of each CAD model are used as scatterers within the radar field of view. The bridge contains 13647 points; the working man contains 35612 points, and the Ferrari contains 61064 scattering points for radar simulation. It is important to note that the scatterers in the CAD models do not aim to precisely mimic electromagnetic scattering from the actual objects. Rather, they represent the object's body, with denser scatterers providing a more detailed struc-

(a) (b) (c)

Figure 7.5: The different objects from the CAD model for the extended targets' simulation. (a) is the bridge, (b) is the Ferrari car, and (c) is the working man holding his hand.

ture. To simplify subsequent analysis, certain factors are not considered, such as the multipath propagation of electromagnetic waves due to reflection from the road and the mutual occlusion of scatterers. These simplifications do not restrict the generality of the proposed imaging approach [97].

The amplitudes of all scatterers are drawn from a uniform distribution, $\alpha_o \sim \mathscr{U}(0.5,1)$. According to the Swerling model III, the amplitude can be treated as constant during one coherent processing interval. The scatterers are assumed to be isotropic and provide a constant amplitude and phase of the scattered field during the processing period, as described in [61].

The amplitudes of all scatterers are drawn from a uniform distribution, $\alpha_o \sim \mathscr{U}(0.5,1)$, satisfying the Swerling model III, same as the complex car model of Fig. 4.12 in Section 4.4. Using (2.16), the de-chirped signal for the scatterers representing the different targets can be simulated manually.

This simulation uses a general phased radar system with an 8×8 array for imaging, following the same setup as the ideal point targets. Due to the ambiguity and coupling issues in conventional Doppler beam sharpening, the corresponding images under Doppler beam sharpening are not compared.

All scatterers in the simulation have the same view direction, and the radar images are projected to the Cartesian coordinate using interpolation for comparison. The first column of Fig. 7.6 (a), (d), and (g) shows the scatterers with their respective densities. The MIMO beamscan results are displayed in the second column, Fig. 7.6 (b), (e), and (h), while the proposed method is shown in the third column, Fig. 7.6 (c), (f), and (i). Upon visual inspection, it can be observed that the proposed method provides more accurate target contours and detailed target information than MIMO processing. For instance, in the case of the bridge hole (with a height of 3.2 meters), the proposed method estimates the height information more accurately (around 3 meters) compared to MIMO processing (around 2.2 meters). This indicates that the proposed method can assist a driving vehicle in determining potential collisions with high targets in the front view. Similarly, for the Ferrari car (with dimensions of 3×2.5 meters), the proposed method preserves the car's shape in the bird's-eye view better than MIMO processing. This improvement is even more evident in the image of the working man, where the proposed method captures fine details such as the man's arm, while MIMO processing only pro-

duces large peaks. These observations are based on a simple visual inspection of the images generated from the 3D model objects. Two additional evaluation metrics are introduced to further evaluate the performance: voxelization accuracy and image contrast.

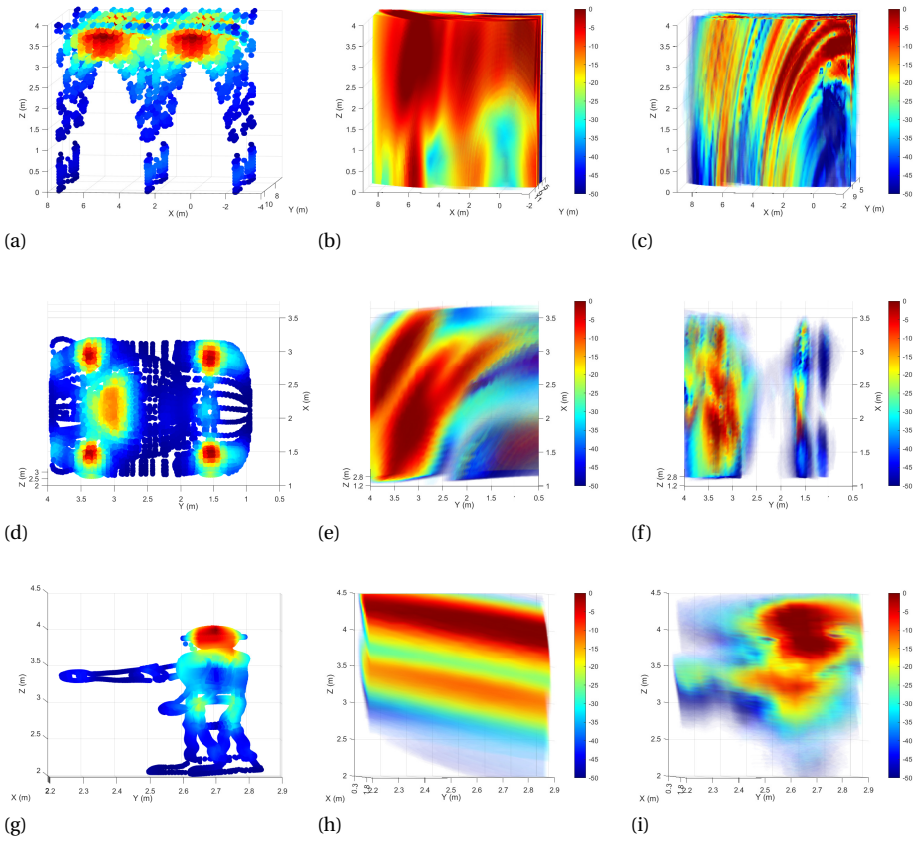

Figure 7.6: The 3D imaging results for different objects. The first row (a), (b), and(c) are images using different methods for the bridge model. The second row (d), (e), and(f) are images using different methods for the Ferrari car, while the third row (g), (h), and (i) are images using different methods for the working man model.

For voxelization, the cells in each range-elevation-azimuth tensor with intensity above +20 dB are considered to be detected to provide the target's position information. According to Section. 5.4.1 and (5.12), the results are shown in Table. 7.2. The proposed method is considered a better imaging approach with a higher F-score. The proposed one achieves significant improvement in precision and accuracy in almost every target, whereas the precision for the bridge is marginally improved because some of the objects are in the blind zone of the Doppler beam sharpening area. However, the AUC MIMO are slightly better for the bridge and the Ferrari. This is reasonable because the total number of detected points for the proposed method is much smaller than that for the MIMO beamscan, leading to lower sensitivity results. The proposed one is better imaging than

the MIMO beamscan with higher resolution.

Table 7.2: The evaluation results for the voxelization

Evaluation matrix	Target Type	MIMO	Proposed
Accuracy	Bridge	74.89	93.13
	Ferrari	89.51	96.94
	Working man	71.14	95.68
Precision	Bridge	1.46	2.96
	Ferrari	7.67	36.28
	Working man	1.82	10.09
AUC	Bridge	54.28	51.56
	Ferrari	57.8	54.23
	Working man	49.75	50.11
F-score	Bridge	2.76	5.10
	Ferrari	11.25	19.87
	Working man	3.28	12.2

The image contrast metric shows the differences in the intensity of each pixel of the image or signal as discussed in 4. The image contrast is defined as 4.21. In this case, each slice of the 3D radar images, i.e., the azimuth elevation, the range azimuth, and the range elevation, are evaluated by image contrast. The results are shown in Table .7.3. The proposed method obtains around twice the image contrast in every slice of the 3D imaging for all different objects.

EXPERIMENTAL DATA

The proposed algorithm was tested using the dataset collected in [120]. This dataset includes measurements from various sensors, including a single chip Radar from Texas Instruments (TI), a Cascaded Radar from TI, Lidar data, and IMU data. The sensor rig used to collect this dataset is depicted in Figure 7.7.

The proposed method was verified using data obtained from the TI IWR6843ISK radar, which operates at a central frequency of 77 GHz. The radar system has a range resolution of 0.125 meters, a maximum range detection of 12 meters, a Doppler resolution of 0.04 m/s, and a maximum Doppler velocity of 2.56 m/s. During the measurements, two transmitters were used for azimuth and one transmitter for elevation, along with four receive antennas. The dataset includes two different scenarios: one outdoor and one indoor. The outdoor scenario, called the Boulder Creek Path sequences, involves the sensor rig moving rapidly through an outdoor environment with dynamic obstacles such as pedestrians, cyclists, and road vehicles. The indoor scenario, named the Engineering Center (EC) hallways sequences, was captured in an indoor built environment. Two examples of these scenarios are shown in Figure 7.8. The dataset does not provide any camera information, and the Lidar data has a range limitation from 0 to 100 meters, which is not compatible with the radar's settings of 12 meters. Therefore, a direct comparison between the radar and Lidar point clouds is not feasible. The 3D images obtained from MIMO processing and the 3DRUDAT method are compared to evaluate the proposed method, as shown in Figure 7.9. In the indoor scenario (Fig. 7.9 (c) and (d)),

Table 7.3: The evaluation results for the image contrast

Target Types	**Method**	Image type	Image contrast
Bridge	MIMO	Range-azimuth	1.8139
		Range-elevation	1.8515
		Azimuth-elevation	1.2308
	Proposed	Range-azimuth	3.9848
		Range-elevation	3.5394
		Azimuth-elevation	2.1847
Ferrari	MIMO	Range-azimuth	3.0321
		Range-elevation	3.0531
		Azimuth-elevation	1.3372
	Proposed	Range-azimuth	7.5089
		Range-elevation	7.4599
		Azimuth-elevation	2.8927
Working man	MIMO	Range-azimuth	1.9652
		Range-elevation	2.1835
		Azimuth-elevation	0.6604
	Proposed	Range-azimuth	4.7425
		Range-elevation	7.1815
		Azimuth-elevation	1.8831

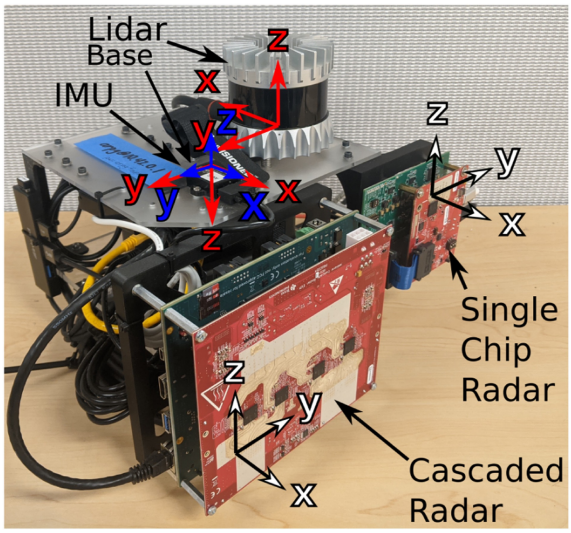

Figure 7.7: The sensor rig used to collect the dataset in [120].

the maximum X and Y ranges are set within 4 meters to accommodate the limited space of the indoor environment.

The comparison between the MIMO processing and the 3DRUDAT method shows that the targets are more focused and well-defined in the 3DRUDAT images. This is due

(a)

(b)

Figure 7.8: The scenario selected from the dataset in [120]. (a) scenarios 1: Boulder Creek Path, (b) scenarios 2: engineering center hallway.

to the narrow beam formed by the Doppler beam sharpening, which enhances the resolution and improves the imaging quality. Furthermore, it is important to consider the velocities associated with each scenario. The velocities for the targets in the engineering centre hallway are in the range of $[-1.3464, -0.0853, -0.078]$ m/s, while for the Boulder Creek Path, the velocities are $[-0.2462, 6.4590, 0.0612]$ m/s. These velocities limit the extent of resolution improvement achievable in the images. Additionally, it is observed that some targets appear in the 3DRUDAT images that are not present in the MIMO DBF images. This occurrence is more frequent in the Boulder Creek Path scenarios. This difference is because certain targets in the Boulder Creek Path scenario, such as pedestrians and road vehicles, are in motion, which introduces additional Doppler components. These extra components can degrade the proposed method's performance and lead to

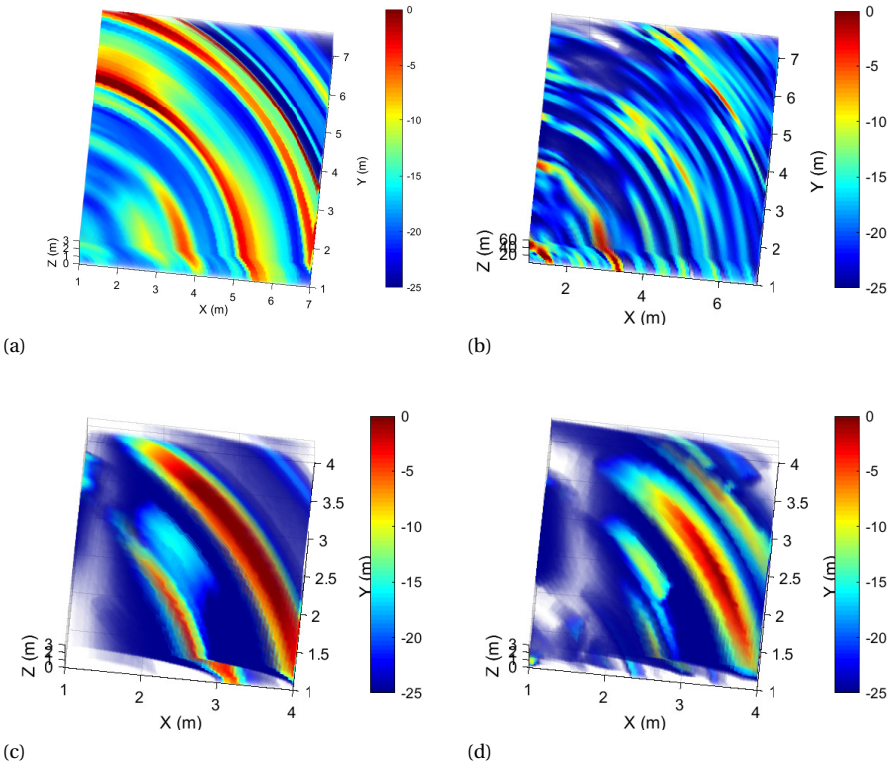

Figure 7.9: The 3D image results for two scenarios of the experimental data from the dataset in [120]. (a) and (b) are the data of scenarios 1 under MIMO beamscan and 3DRUDAT, respectively. (c) and (d) are the data of scenarios 2 under MIMO beamscan and 3DRUDAT, respectively

unmatched targets' appearance. In contrast, the targets in the engineering centre hallway scenarios are static, resulting in a better match between the two methods.

7.4.2. THE DISCUSSION OF ANGULAR RESOLUTION

MIMO ARRAY

To satisfy no ambiguity within the field of view $[-90°, 90°]$, the spatial difference between adjacent sampling points (i.e., MIMO antennas) should be $\lambda/2$.

Under such circumstances, let us assume that two targets are located at $\theta + \Delta\theta$ and θ. To resolve the two targets, the angle resolution $\Delta\theta$ should satisfy:

$$\begin{aligned} &\frac{2\pi d}{\lambda}(\sin(\theta+\Delta\theta)-\sin\theta)\cos\phi > \frac{2\pi}{N_a} \\ &\Rightarrow \Delta\theta_a > \frac{\lambda}{N_a d\cos\theta\cos\phi} \end{aligned} \tag{7.14}$$

where N_a is the number of spatial sampling points for azimuth estimation.

$$\begin{aligned} &\frac{2\pi d}{\lambda}\left(\sin(\phi+\Delta\phi)-\sin\phi\right)>\frac{2\pi}{N_e} \\ &\Rightarrow \Delta\phi_e>\frac{\lambda}{N_e d\cos\phi} \end{aligned} \tag{7.15}$$

where N_e is the number of spatial sampling points for elevation estimation.

DOPPLER BEAM SHARPENING

For a forward-looking radar borne on a vehicle moving at speed $[v_x, v_y, v_z]]$ in the forward direction, the instantaneous Doppler of a static target located at $[\theta, \phi]$ will be:

$$f_d=\frac{2(v_y\cos\theta\cos\phi+v_x\sin\theta\cos\phi+v_z\sin\phi)}{\lambda} \tag{7.16}$$

where λ is the wavelength of the radar signal.

Then, in order to resolve two closed targets using Doppler beam sharpening, neglecting the shrink of the unambiguous angle region because of the elevation angle, the following equation in azimuth and elevation should be satisfied:

$$\begin{aligned} &\frac{4\pi f_0 T\cos\phi}{c}(v_y\left(\cos(\theta+\Delta\theta)-\cos\theta\right) \\ &+v_x\left(\sin(\theta+\Delta\theta)-\sin\theta\right))>\frac{2\pi}{N_d} \\ &\Rightarrow \Delta\theta_d>\frac{\lambda}{2N_d T\cos\phi\left(v_y\sin\theta+v_x\cos\theta\right)} \end{aligned} \tag{7.17}$$

$$\begin{aligned} &\frac{4\pi f_0 T}{c}((v_y\cos\theta+v_x\sin\theta)\left(\cos(\phi+\Delta\phi)-\cos\phi\right) \\ &+v_z\left(\sin(\phi+\Delta\phi)-\sin\phi\right))>\frac{2\pi}{N_d} \\ &\Rightarrow \Delta\phi_d>\frac{\lambda}{2N_d T\left((v_x\sin\theta+v_y\cos\theta)\sin\phi+v_z\cos\phi\right)} \end{aligned} \tag{7.18}$$

where N_d is the number of chirps used for Doppler estimation, which is limited by the coherent processing time.

Also, it is clear that when the targets are close to the trajectory, i.e. θ close to $atan(\frac{v_x}{v_y})$, or the targets' elevation angle close to $\pi/2$, the resolution for azimuth will tend to infinity, causing the blind zone problem. And when targets close to the trajectory, i.e. ϕ close to $atan(\frac{v_z}{v_x\sin\theta+v_y\cos\theta})$, the resolution for elevation will tend to infinity, causing the blind zone problem too.

Compared with the two resolution equations (7.14,7.15) and (7.17,7.18), one can easily see that the angular resolution of the MIMO array decreases when the look angle of

the region becomes larger, while the Doppler has an inverse behaviour. With typical values in current automotive radar, specifically, the chirp duration of $100us$ and 256 chirps for Doppler estimation, even if influenced by the impact of the angle θ, most of the time, the Doppler can still provide better resolution capability if the ego-vehicle moves faster than $0.5m/s$. The resolution improvement for azimuth DOA is given in [42] and here is modified for 3D imaging when radar is moving at $[v_x, v_y, v_z]$ as:

$$n_a = \frac{2N_d T v_y}{N_a d} \tan(\theta)\cos(\phi) + \frac{2N_d T v_x}{N_a d} \cos(\phi) \tag{7.19}$$

$$n_e = \frac{2N_d T (v_y \cos(\theta) + v_x \sin(\theta))}{N_e d} \tan(\phi) + \frac{2N_d T v_z}{N_e d} \tag{7.20}$$

where n_a n_e is the resolution improvement terms for azimuth DOA and elevation DOA, respectively, N_d is the number of slow times used for DBS, N_e and N_a are the number of antenna elements used for DBF in azimuth and elevation, T is the pulse repetition time, θ and ϕ is the targets' position in azimuth and elevation.

7.5. CONCLUSION

In this chapter, we have proposed a novel high-resolution imaging algorithm using MIMO array processing in combination with the Doppler beam sharpening called 3D robust unambiguous Doppler beam sharpening using adaptive threshold (3DRUDAT). Thanks to the Doppler beam sharpening, the resolution improvement in both elevation and azimuth domain has been demonstrated, leading to a two times higher image contrast evaluation metric. The ambiguity problem for the forward-looking Doppler beam sharpening and the coupling problem between the elevation and azimuth angle in 3D imaging are jointly addressed, making it possible to use the Doppler beam sharpening to enhance the resolution for forward-looking radar with a decent computational cost. The diversity of the targets' reflectivity and the robustness of the trajectory directions are also tackled using adaptive threshold and extra phase shift.

The proposed method has been verified for simulated point-like and extended targets, as well as experimental data from the dataset [120], showing that 3DRUDAT achieves better angular estimation than conventional DBS and DBF. It is worth noting that the proposed approach does not need any prior information on the environment, the number of targets, and their approximate position. The proposed approach is easier to apply in automotive applications in varying scenarios. However, the proposed method takes 18 times longer than the conventional imaging method, but this increased computation is necessary to achieve the enhanced resolution provided by the proposed method.

8

JOINT EGO-MOTION ESTIMATION AND HIGH-RESOLUTION IMAGING ALGORITHM

The problem of joint ego-motion estimation and 3D imaging in automotive MIMO radar has been studied. Radar is in two different installations, side-looking and forward-looking, in consideration. The problem is addressed by the proposed overall processing flowchart. Simulations and the experimental data prove the effectiveness of the proposed pipeline.

Parts of this chapter are to be published in:

S. Yuan, F. Fioranelli, and A. Yarovoy, "Joint ego-motion estimation and 3D imaging for forward-looking region using automotive radar " IET international radar conference, Chongqing, China, 2023.

8.1. INTRODUCTION

In this thesis, Chapter. 3 proposed a novel 3D ego-motion estimation method, which can provide accurate ego-motion estimation. From chapter 4, different high-resolution algorithms for different radar installations were proposed based on the motion information, assumed as prior information. This prior information can be obtained with the 3D ego-motion estimation. Thus, this chapter proposed different processing flowcharts for different applications, jointly solving the ego-motion estimation and imaging problem together from the radar raw signal.

8.1.1. PROBLEM FORMULATION

Many of the presently available high-resolution imaging algorithms reliant on motion information encounter a significant challenge: the insufficient precision of the motion estimation. This motion-related data typically originates from sensors other than radar, and the lack of synchronization among these sensors introduces errors that lead to degradation in the overall performance. This adverse impact is particularly pronounced in high-frequency signals. The temporal synchronization issue can be avoided by imaging solely based on radar data, eliminating the introduction of supplementary errors.

At the same time, considerable attention is directed toward the forward-looking region in the context of automotive vehicles. However, the imaging range of forward-looking DBS and 3D imaging algorithms is limited. Consequently, developing a high-resolution 3D imaging approach that jointly combines the motion information derived from raw radar signals will bring substantial benefits to this application.

The side-looking radar is welcomed for automotive radar mapping applications. This context has a limited 3D imaging algorithm similar to the forward-looking region. One processing pipeline could jointly combine the motion information derived from raw radar signals, and 3D side-looking imaging is urgently needed for the current industry.

8.2. PROPOSED PIPELINE

To address the challenge of jointly addressing ego-motion estimation and achieving high-resolution 3D imaging using Doppler beam sharpening, a new processing pipeline has been proposed, illustrated in Figure 8.1. This pipeline contains a sequence of crucial steps described in this section.

The algorithm begins with the reception of the radar raw dechirped signal $z(i, j, l, k)$ in equation (2.16), which then undergoes range Fast Fourier Transform (FFT) processing to yield the range profile. Subsequently, Doppler FFT is employed to extract the range-Doppler spectrum $z^{i,j}(m, n)$ where m and n are the indices of the frequency in range and Doppler domain, followed by the application of the Cell Averaging 2D Constant False Alarm Rate (CA-2D CFAR) detector to identify targets. The signals in the detected cells then contribute to ego-motion estimation in Section. 3, yielding translational velocities $[v_x, v_y, v_z]$ across the three spatial dimensions. The range indices and the corresponding signal data, are conveyed to the MIMO processing stage, yielding poor-resolution azimuth-elevation imaging results. Also, the estimated velocities are combined with the same signals used in the MIMO processing to perform Doppler beam sharpening. This obtains data with coupling and ambiguous azimuth-elevation. The information from

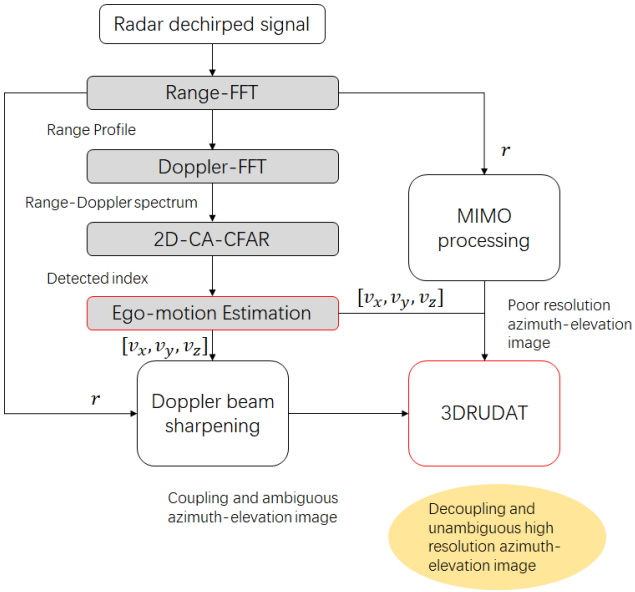

Figure 8.1: The proposed processing pipeline for the joint ego-motion estimation and 3D Doppler beam sharpening imaging problem.

the above processes is finally channelled into a 3D imaging algorithm [43] to generate the ultimate results.

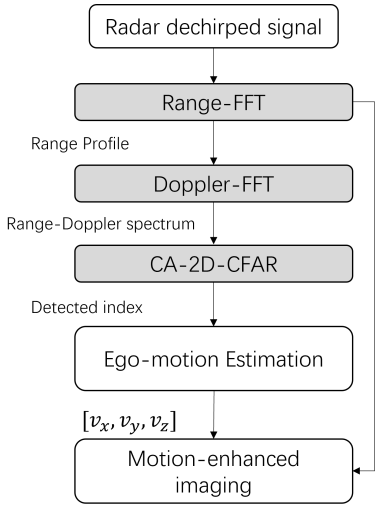

Figure 8.2: The proposed processing pipeline for the joint ego-motion estimation and 3D motion-enhanced imaging problem.

Similarly, as the processing pipeline shown in Fig. 8.1, starting from 3D ego-motion

estimation, the estimated velocities are directly used for motion-enhanced snapshots generation. The corresponding steering vector is also compensated with the calculated phase from the estimated velocities. The 3d high-resolution images will be obtained after the whole processing.

This comprehensive processing pipeline thus offers a systematic approach to addressing the joint problem of ego-motion estimation and high-resolution 3D imaging for different radar installations, equipping automotive radar with diverse applications.

8.3. RESULTS

Several results based on simulations are presented in this section to show the effectiveness of the proposed methods.

We employed an 8×8 phased radar system for DOA estimation in both azimuth and elevation directions to generate the 3D images, which already have a better resolution ability than commercial automotive radar. The radar parameters are specified as follows: the starting frequency of the FMCW chirp f_0 is 77 GHz, the chirp bandwidth B is 1 GHz, the chirp duration T_c is 16 μs, the sampling rate f_s is 64 Msps, and L = 512 chirps are processed in each frame. The MIMO antenna on the forward-looking radar is located at the coordinate centre.

A typical automotive vehicle's object, a car, is chosen as the target, the same as the car model in Section. 7.4.

Figure 8.3: The Ferrari car target derived from CAD models for the extended targets' simulation.

A typical scenario with two cars parking in parallel with an interval of 0.5m between each other is simulated here. One car is slightly behind the other car by 0.5 m. The two cars have the same scatterers' distributions but different positions, containing 20000 scattering points.

8.3.1. EGO-MOTION ESTIMATION

A simulation involving 50 frames with linearly changing velocities was conducted to assess the efficacy of the ego-motion estimation outcomes while keeping the same set of targets. The outcomes are graphically represented in Figure 8.5. Notably, the results for all three directions closely align with the ground truth values, providing robust evidence of the effectiveness of the ego-motion estimation algorithm. The root-mean-square error (RMSE) is calculated for each of the three directions to quantify this performance.

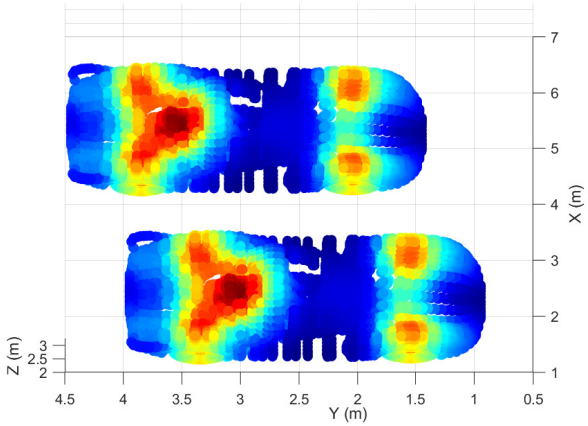

Figure 8.4: The simulated scenario with two cars that are parking.

Specifically, the mean RMSE values are achieved as follows: 0.1792 m/s for the X direction, 0.2574 m/s for the Y direction, and 0.2037 m/s for the Z direction.

8.3.2. IMAGING RESULTS OF JOINT PROCESSING FOR FORWARD-LOOKING APPLICATION

The 3D imaging results are showcased from an overhead perspective, simulating a bird's-eye view. The radar images are projected onto Cartesian coordinates using cubic interpolation to facilitate direct comparison. For accuracy, the frequency zero padding algorithm is not used to prevent generating artificial data points. The presented visualization, illustrated in Fig. 8.6, depicts the 3D imaging outcomes obtained through the conventional MIMO processing and our proposed pipeline. Conventional MIMO processing yields considerable energy distribution blocks, while the proposed method delineates the energy distributions originating from the two cars more clearly. Notably, the proposed methodology enables us to perceive the car shapes compared to the conventional MIMO processing. The superior performance of the proposed method is highlighted by its capacity to distinctly capture two better-defined car contours, thereby enhancing the overall precision of the imaging results.

Furthermore, images from the same simulation but captured from diverse viewing perspectives are depicted in Fig. 8.7. The ground truth is reconstructed, aligning its density with the viewpoint, as illustrated in sub-figure (a). This figure strongly highlights the ability of three-dimensional imaging. Notably, in this comparative analysis, our proposed method distinguishes itself by rendering more defined contours in contrast to the conventional MIMO processing. The proposed approach shows better internal details within the images, evidenced by a heightened energy distribution similar to the ground truth. To facilitate a more comprehensive performance assessment, two additional quantitative evaluation metrics are performed here, as in chapter 5, voxelization accuracy and image contrast.

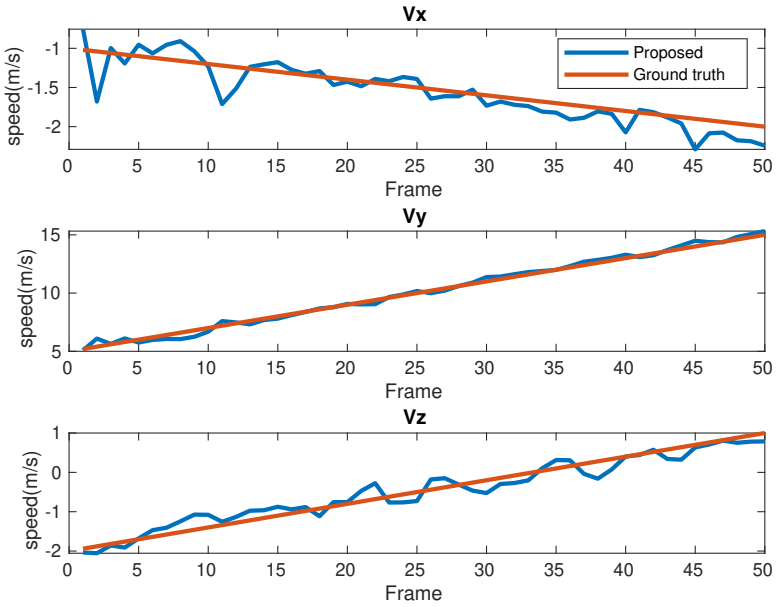

Figure 8.5: The ego-motion estimation in three directions, comparing ground-truth and proposed estimation.

The results of voxelization accuracy are presented in Table 8.1. The proposed method emerges as a superior imaging technique, as evidenced by its elevated F-score. The precision and accuracy have been improved a lot by the proposed method. However, it is noteworthy that the Area Under the Curve (AUC) for MIMO slightly outperforms the proposed method. This discrepancy is attributed to the fact that the total count of detected points for the proposed approach is considerably smaller than that achieved through conventional MIMO processing, leading to comparatively lower sensitivity outcomes.

Table 8.1: The quantitative evaluation metrics after the voxelisation process for extended targets

Evaluation matrix	MIMO	Proposed
Accuracy	96.74	99.39
Precision	2.36	8.18
AUC	61.26	60.24
F-score	4.30	11.96

In this case, each slice derived from the 3D radar images, projected onto distinct 2D planes such as azimuth-elevation, range-azimuth, and range-elevation planes, undergoes assessment through the computation of image contrast. Subsequently, the outcomes from these assessments for every slice are combined via averaging, yielding the ultimate evaluation metric. These consolidated results are presented in Table 8.2. Remarkably, the proposed methodology consistently yields a nearly twofold increase in

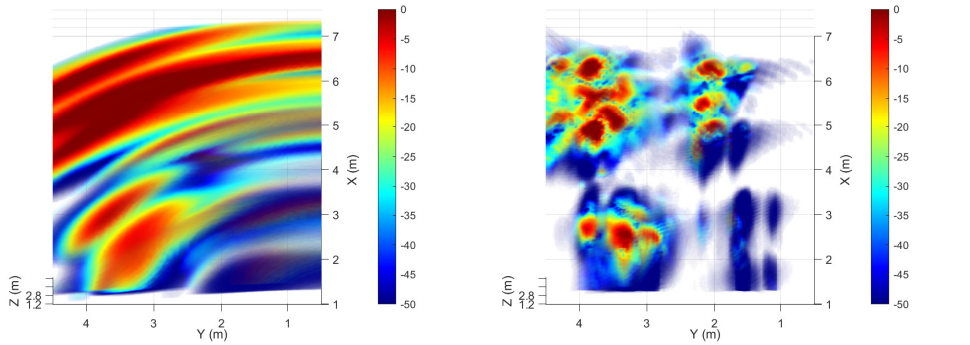

(a) (b)

Figure 8.6: 3D imaging results for the Ferrari car shown in Fig.8.4 using different methods. (a) Conventional MIMO processing. (b) Proposed processing pipeline.

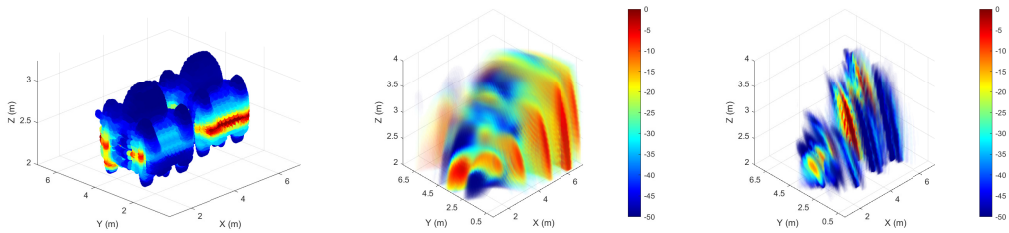

(a) (b) (c)

Figure 8.7: 3D imaging results for the same scenario shown in Fig.8.4 in a different view angle. (a) Ground truth with corresponding density, (b) Conventional MIMO processing, and (c) Proposed processing pipeline.

image contrast across all slices of the 3D imaging. The calculated dynamic range ratio, quantified at 1.1833, serves as an indicative measure affirming the similarity between the dynamic range achieved through the proposed method and the conventional MIMO approach. Consequently, the advancement in image contrast stems from the refinement in image resolution facilitated by our innovative methodology.

8.3.3. IMAGING RESULTS OF JOINT PROCESSING FOR SIDE-LOOKING APPLICATION

The same Ferrari car models are parking close to each other in the radar field of view. The radar is moving with the vehicle at a speed of 15m/s. The presented visualization, illustrated in Fig. 8.8, depicts the targets and 3D imaging outcomes obtained through conventional MIMO processing and joint processing for 3d ego-motion estimation and motion-enhanced imaging pipeline. Also, images from the same simulation but captured from diverse viewing perspectives are depicted in Fig. 8.9. The proposed pipeline

Table 8.2: The image contrast values of different types of images using different methods.

Image types	MIMO	Proposed
Range-azimuth	2.9610	8.5463
Range-elevation	3.0505	8.5204
Azimuth-elevation	1.7038	3.8260

provides clear visual results compared with the conventional one in both observation perspectives. The numerical evaluations are also given in the following chapter.

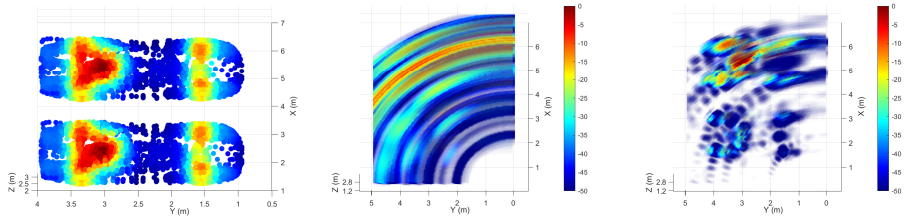

(a) (b) (c)

Figure 8.8: 3D imaging results for the Ferrari car shown in Fig.8.4 using different methods. (a) Conventional MIMO processing. (b) Proposed processing pipeline.

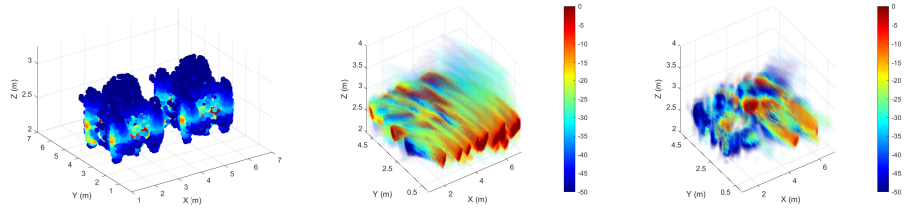

(a) (b) (c)

Figure 8.9: 3D imaging results for the same scenario shown in Fig.8.4 in a different view angle. (a) Ground truth with corresponding density, (b) Conventional MIMO processing, and (c) Proposed processing pipeline.

The results achieved the expected performance improvement, the same for the forward-looking one. The proposed one achieves a better F2 score than the conventional one, and the proposed methodology also yields a nearly twofold increase in image contrast across all slices of the 3D imaging. Differently, The calculated dynamic range ratio, quantified at 8.23, is contributed by the coherent summarization of the target's information with more data, also leading to the improvement of the SNR.

Table 8.3: The quantitative evaluation metrics after the voxelisation process for extended targets

Evaluation matrix	MIMO	Proposed
Accuracy	97.83	99.69
Precision	2.00	8.82
AUC	60.89	59.71
F-score	3.67	12.35

Table 8.4: The image contrast values of different types of images using different methods.

Image types	MIMO	Proposed
Range-azimuth	3.6259	7.4259
Range-elevation	5.2556	10.455
Azimuth-elevation	3.0712	7.3228

8.4. CONCLUSION

This chapter introduces novel processing pipelines that simultaneously tackle the challenges of ego-motion estimation and 3D imaging for both forward-looking and side-looking region applications. The pipelines integrate a 3D ego-motion estimation algorithm from radar raw signal, serving as a foundation for motion information extraction, followed by 3D high-resolution algorithms for forward-looking region and side-looking regions.

The effectiveness of the proposed pipeline is verified through a comprehensive analysis of both ego-motion estimation and imaging results. The pipelines' capabilities are validated using realistic 3D extended target models. Notably, the imaging aspect of the approach demonstrates a remarkable twofold enhancement in image contrast. The proposed methodologies do not require prior information about the environment, the number of targets, or their approximate positions. The image contrast has improved twice, and the F-score has increased approximately three times with the proposed pipeline compared with the conventional method.

9

HIGH-RESOLUTION IMAGING ALGORITHMS FOR AUTOMOTIVE RADAR: CHALLENGES IN REAL DRIVING SCENARIOS

The role of radar for building situation awareness in (semi-)autonomous vehicles is severely restricted by its low angular resolution. The physical size of the radar, which determines its antenna aperture size and thus the radar angular resolution, is often a subject of stringent limitations to physically fit the system in the vehicles. Multiple Input Multiple Output (MIMO) systems are used to increase the achievable angular resolution, and these are often combined in the literature with algorithms inspired by Synthetic Aperture Radar (SAR) techniques that exploit the vehicle's velocity for finer resolution. Some of the most common approaches are reviewed, in this context, with a specific focus on challenges for the implementation on data collected in real driving scenarios. Key experimental results using representative algorithms and driving data collected in the city of Delft, the Netherlands, are presented and discussed.

Parts of this chapter are supposed to be published in

S. Yuan, F. Fioranelli and A. Yarovoy, "High-resolution imaging algorithms for automotive radar: challenges in real driving scenarios", IEEE Aerospace and Electronic Systems Magazine. (Submitted)

S. Yuan, F. Fioranelli and A. Yarovoy, "Speeding up imaging over BP for automotive radar: High-resolution algorithm with multi-frame data" 2024 21th European Radar Conference (EuRAD), Paris, France.

9.1. INTRODUCTION

Significant research effort is ongoing to propose array designs and algorithms to improve angular resolution, but, to the best of our knowledge, such approaches are not always evaluated in real driving scenarios with multiple extended targets and considerable clutter in the scene of interest. Therefore, this chapter aims to first review some of the most recent approaches for high-resolution imaging in automotive radar and then discuss important insights and open challenges for their practical implementation. Specifically, data collected in the city of Delft, the Netherlands, with a vehicle equipped with both front-looking and side-looking radars, will be used to showcase performances for the different algorithms.

9.2. EXPERIMENT DESCRIPTION

The radar sensors used in this data collection are the Texas Instrument MMWCAS-RF-EVM cascade radar systems, shown in Chapter. 5 Fig. 5.11. GPS, IMU, Lidar and GoPro cameras are also installed on the vehicle used for the data collection, as shown in Fig. 9.1. These sensors can provide vital information in terms of ground truth for validation of radar-only algorithms, as well as offer opportunities to develop suitable data fusion techniques at a later processing stage. Specifically, the LiDAR sensor is the Robosense Ruby Plus Upgraded 128-beam, customized for L4 autonomous vehicle commercial operations, mounted on the top of the vehicle, operating at 10 Hz. This provides a maximum 250m observation range with 0.02m precision. The vertical field is within $[-25°, 25°]$, with up to 0.1° resolution, while the horizontal field is 360° with 0.2° resolution. Odometry information is provided by a filtered combination of several inputs: RTK GPS, IMU, and wheel odometry, with a frame rate of around 30 Hz. GPS is the industry standard GNSS/INS for ADAS and autonomous vehicle testing, RT3000 v3. Notably, as shown in Fig. 9.1(b), two radar sensors have been used, one for the front-looking region and one for the side-looking region concerning the driving trajectory.

9.2.1. RADAR WAVEFORM PARAMETERS

A crucial step of the experimental planning consists of the design of the radar waveform and its parameters. Specifically, four operational requirements, namely, maximum measurable range, maximum measurable Doppler, range resolution, and Doppler resolution, play an important role in the waveform design and the subsequent sensing capabilities[6, 121, 122]. The maximum range is determined as:

$$r_{max} = \frac{F_s c}{2\mu} \tag{9.1}$$

where F_s is the sampling frequency for the fast time, c is the speed of light, μ is the sweeping slope of the chirp modulation equal to the ratio of the chirp bandwidth B and duration of the chirp.

The maximum Doppler is determined as:

$$v_{max} = \frac{\lambda}{4T} \tag{9.2}$$

(a)

(b)

Figure 9.1: The vehicle used for data collection with multi-sensors mounted.

where λ is the wavelength of the radar signal, T_c is the PRI for the chirps.

The range resolution is determined as follows:

$$r_{res} = \frac{c}{2B} \tag{9.3}$$

where B is the bandwidth of the FMCW chirp.

The Doppler resolution is determined as:

$$v_{res} = \frac{\lambda}{2TL_d} \tag{9.4}$$

where L_d is the number of the chirps used for Doppler estimation.

Considering the required values for the aforementioned quantities, suitable waveform parameters (some shown in Fig. 9.2) can be set on the radar board. Specifically, these are the *start freq* which is the starting frequency of the chirp, the chirp slope μ, the *idle time* which is the time needed to reset the previous chirp, the *ADC start* which is the time for reaching the starting frequency of each chirp, the *sample frequency* in fast-time F_s, the *ramp end time* which is the time when the transmitter is off, and *adc samples* which is the number of samples per chirp. It should be noted that T_c denotes the whole chirp cycle time, including the idle time and ramp end time; the subtraction between the ramp end time and the ADC start time will determine the actual chirp duration. This highlights how it is important to pay attention to the inevitable idle times before and after the nominal chirp duration for the practical usage of this radar, an aspect that might be overlooked in purely theoretical studies.

An additional operational requirement for the radar is its angular resolution, which is calculated as:

$$a_{res} = \frac{\lambda}{Nd\cos(\theta)} \tag{9.5}$$

where λ is the wavelength of the radar signal, d is the distance between adjacent antenna elements for the ULA, θ is the azimuth angle from the boresight, N is the number of the channel elements in the formed MIMO ULA. To operate multiple channels orthogonally and thus increase the angular resolution, the chosen TI radar board offers time division multiplexing (TDM) and binary phase modulation (BPM) [123]. The TDM mode means that the transmitters will switch on one after the other to make the signals orthogonal in time dimensions, i.e., only one transmitter is active at any time. Compared with TDM, the BPM approach may suffer from imperfect orthogonality of the added phase modulations and degrade the radar detection performance. Thus, TDM access is commonly used for data collection with this radar board.

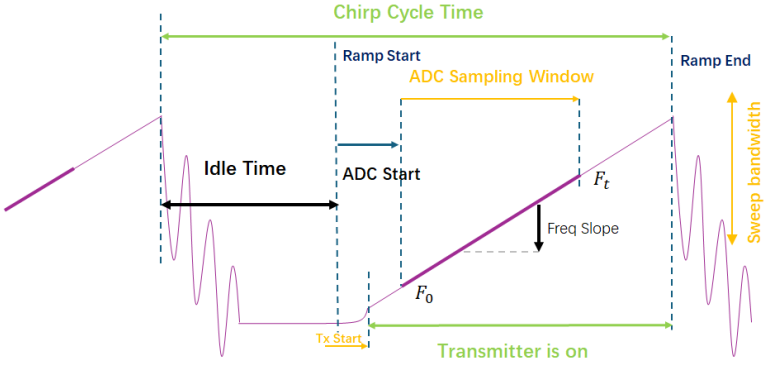

Figure 9.2: The parameters for the radar waveform design; figure inspired by the software used to configure the chosen radar by Texas Instrument [124].

9.3. EXPERIMENTAL RESULTS & DISCUSSION

9.3.1. RESULTS FOR IMAGING OF FORWARD-LOOKING DIRECTION

The radar waveform parameters for the forward-looking regions are designed based on the requirements mentioned in the previous section and reported in Table 9.1. With these waveform parameters, the maximum range is 60m, the range resolution is 0.23m, the maximum unambiguous velocity is 4.18 m/s, and the velocity resolution is 0.033 m/s. The angular resolution at boresight with full ULA formed is 1.3°.

Table 9.1: Radar parameters for the experimental data collection (front-looking region)

Radar parameters	**Symbol**	**Value**
Starting Frequency (GHz)	F_0	77
Slope (MHz/us)	μ	30
Sampling Rate (Msps)	F_s	12
Bandwidth (GHz)	B	0.64
Number of chirps	L_d	128
PRI (ms)	T	5.5
Number of ULA channels	N	86

In the following, some representative scenarios and results are presented and discussed. Fig. 9.3 and Fig. 9.4 present two different scenarios as seen by the camera and the LIDAR. The imagery in Fig. 9.3(a) from the camera offers an easy empirical interpretation of the scenario, with key targets such as a bus stop, rubbish bin, and display board marked in the corresponding figure; the same targets are also marked in the LIDAR image in Fig. 9.4(a). In Fig. 9.3(b), another scenario is shown with multiple posts and boards marked, where the poster is not visible because of the limited field of view of the camera. However, both targets are marked in the corresponding LIDAR image in Fig. 9.4(b).

Fig. 9.5 includes radar images for the first scenario shown in both Fig. 9.3(a) and Fig. 9.4(a) using a different number of channels for DOA and imaging algorithms. Fig. 9.5(a) uses 86 channel elements, equivalent to all those available in the chosen radar sensor. This offers a good spatial resolution of 0.6° at boresight. However, the practical utilization of such a large aperture is unfeasible in realistic vehicles. Additionally, the TDM approach necessary to operate the 4 independent MIMO radar chips together will further limit the unambiguous estimation of target velocities since the T_c in equation (9.2) need to multiply the number of transmitters used. Thus, in Fig. 9.5(b)-(c), the results are based on only 8 channel elements, which is much easier to achieve for practical automotive radar systems. Fig. 9.5(b) is generated using a conventional imaging approach and provides rough information on the bus stop and rubbish bin targets, making it not straightforward to interpret. With the *3DRUDAT* imaging algorithm proposed in [104], a higher resolution image can be obtained while still keeping the number of channel elements to 8.

Notably, several objects in the scene can be distinguished in the image, whereas they tend to form a broader, uniform signature in the image generated by the conventional imaging algorithm. To provide a quantitative observation, the side lobe level for the bus

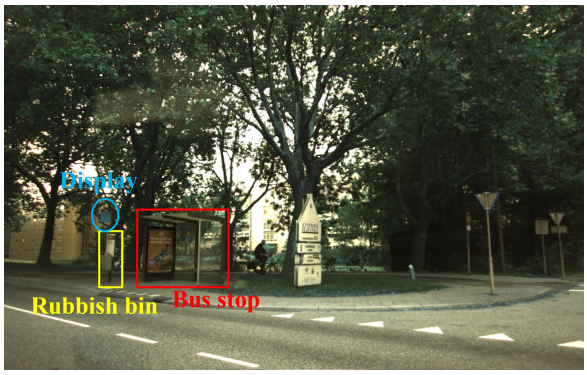

(a)

(b)

Figure 9.3: The optical image from the forward-looking camera.

stop target in Fig. 9.5(b) is measured at -2.3 dB, while in Fig. 9.5(a), this improves to approximately -20 dB. This improvement in side lobe level is attributed to the accumulated energy from the targets themselves when using more antenna elements, resulting in an improved SNR. In the case of the proposed method, which enhances SNR through the multiplication of results from Doppler beam sharpening (DBS) and beamforming, the side lobe level in Fig. 9.5(c) is notably low at -30 dB.

The radar-based results presented in Fig. 9.6 for the second scenario shown in both Fig. 9.3(b) and Fig. 9.4(b) provide similar trends to compare the different imaging algorithms. The multiple poles and boards and the poster targets appear to be well-focused and with more detail in Fig. 9.6(c), compared with the image generated by the conventional MIMO digital beamforming (DBF) in Fig.9.6(b). Both sub-figures are generated using only eight channel elements. Remarkably, the *3DRUDAT* imaging algorithm appears to also outperform the conventional MIMO DBF imaging using the larger aperture array, with results shown in Fig.9.6(a) with all the posts well focused with much narrower main lobe beam.

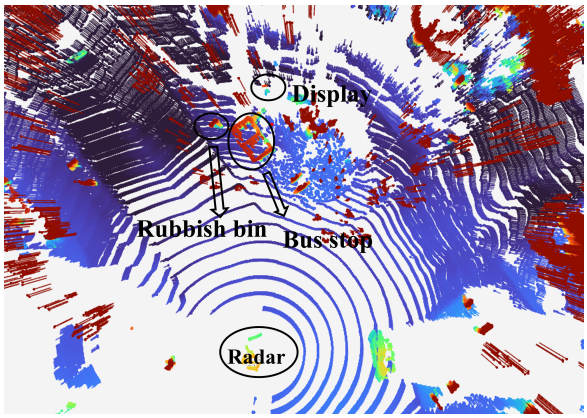

(a)

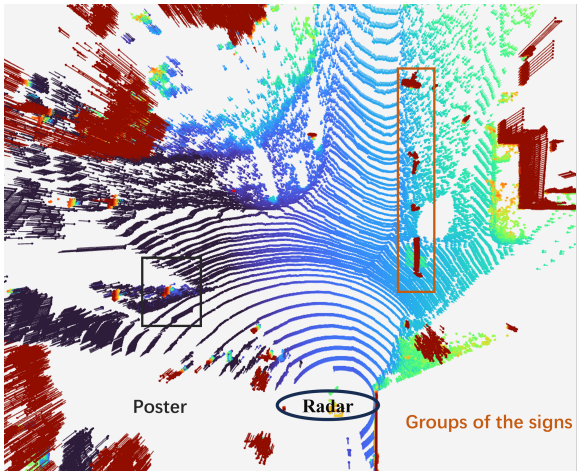

(b)

Figure 9.4: The image from Lidar data.

9.3.2. RESULTS FOR IMAGING OF SIDE-LOOKING DIRECTION

The radar waveform parameters for the side-looking region are reported in Table 9.2. With this waveform designed for a side-looking geometry, the maximum range is 30m, the range resolution is 0.12m, the maximum unambiguous velocity is 2.1 m/s, and the velocity resolution is 0.016 m/s.

The radar is installed on the side of the vehicle. The BP algorithm can provide robust high-resolution images in a 2D plane for the side-looking region. However, since it accumulates multiple frame data for each grid cell to form an image, it is computationally expensive, limiting its real-time application. The motion-enhanced imaging algorithm provides a lower computational cost solution to 3D high-resolution imaging. However,

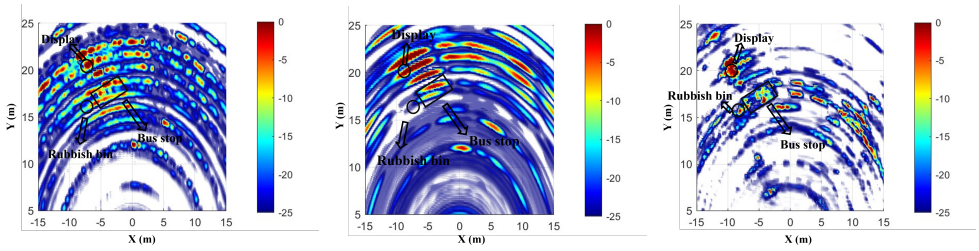

(a) (b) (c)

Figure 9.5: Radar images of scenarios 1 in Fig. 9.3 (a) and Fig. 9.4 (a). (a)The radar imaging results using all 86 elements. (b)The radar imaging results use only eight elements. (c) The imaging results using 8 elements with the proposed *3DRUDAT* algorithm.

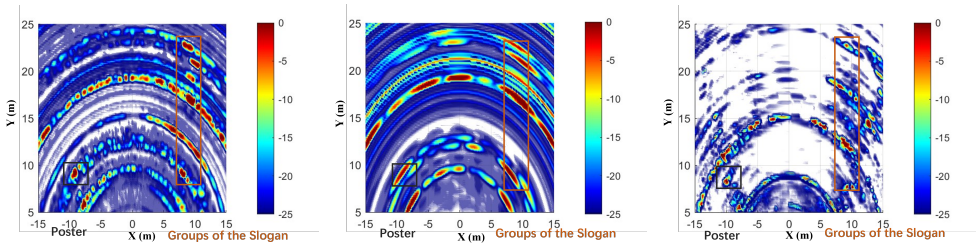

(a) (b) (c)

Figure 9.6: Radar images of scenarios 2 in Fig. 9.3 (b) and Fig. 9.4 (b). (a)The radar imaging results using all 86 elements. (b)The radar imaging results use only eight elements. (c) The imaging results using 8 elements with the proposed *3DRUDAT* algorithm.

Table 9.2: Radar parameters for the experimental data collection (side-looking region)

Radar parameters	**Symbol**	**Value**
Starting Frequency (GHz)	F_0	77
Slope (MHz/us)	μ	30
Sampling Rate (Msps)	F_s	6
Bandwidth (GHz)	B	1.28
Number of chirps	L_d	128
PRI (ms)	T	0.9
Number of ULA channels	N	86

as the vehicle's movement in one snapshot is limited, it is hard to interpret the environment with such little information.

The first step of BP [125] is to perform interpolated FFT along the dimension of the fast time to obtain a high-resolution range profile for each chirp. Then, the values of

the corresponding cells in the range profile are selected based on the distance from each grid cell to the radar. The extra phase term is compensated according to the distance for each signal, and the compensated results are accumulated to obtain the scattering information at the grid. The phase term is the compensated phase for each grid cell. After each cell is calculated, the BP results can be obtained.

Instead of the coherent summarization from multiple frame data, an efficient, high-resolution imaging algorithm is proposed to address this gap and improve imaging capabilities while maintaining computational efficiency. This uses weighted incoherent summation with multi-frame motion-enhanced imaging data. The grid cell is divided according to global coordinates at first. Then, each cell of the observation region will be contributed by every frame data containing the information of this cell using the vehicle motion. Specifically, the weight parameter is defined as:

$$w(x_o, y_o) = e^{-abs(\theta_o)} \tag{9.6}$$

where (x_o, y_o) is each discretized imaging grid cell, and θ_o is the azimuth angle for this cell.

This decreases with the direction of arrival angles; the farther from the broadside, the less weight. The weight parameter not only takes into consideration the fact that resolution is higher in the broadside view than in other directions but also provides different weight contributions among multi-frame data, i.e., for a given position in the observation region the frame data observing in the broadside needs to be trusted more with high weight. The flowchart of the proposed method compared with the conventional BP algorithm is shown in Fig.9.7.

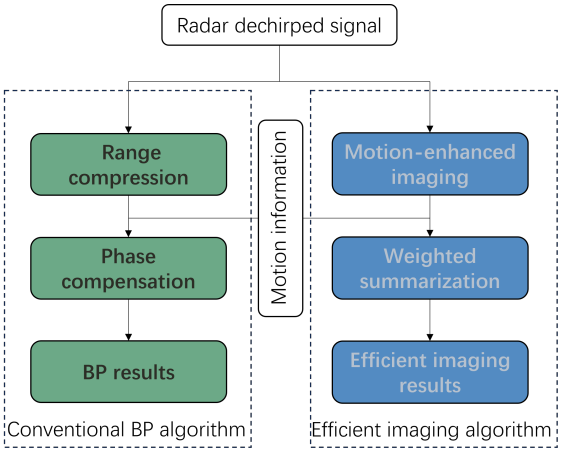

Figure 9.7: The proposed efficient imaging algorithm compared with conventional BP algorithm

In the following, figures of representative scenarios and results of radar-based imaging algorithms are presented and discussed. In Fig. 9.8(a), imagery from a GO-pro camera offers an easy visual interpretation of the scenario, with two parked cars and a building in the farther background region. The corresponding targets are also marked in the

Lidar image shown in Fig. 9.9(a). In Fig. 9.8(b), a scene from a parking lot in the TU Delft campus is shown with three parked vehicles highlighted in the foreground, whereas Fig. 9.9(b) shows the same scenario perceived by Lidar where even more cars are visible.

(a)

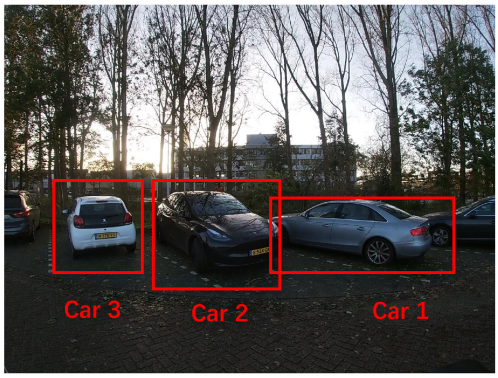

(b)

Figure 9.8: The optical image from the side-looking camera.

Fig. 9.10 includes radar images for the first scenario shown in Fig. 9.8(a) and Fig. 9.9(a). Fig.9.10 (a) is the result of conventional MIMO processing. Motivated by using a one-dimensional MIMO array in the elevation domain to alleviate the requirement for large radar apertures in-vehicle systems, the following processing is implemented with only one antenna in azimuth. Since only one antenna is used, there is no resolution in the azimuth direction. Fig. 9.10. (b) is the result of the imaging algorithm in [126], which uses one single frame data and 1D antenna array to generate 3D high-resolution imaging results. The two parked cars in the scene and the building in the background

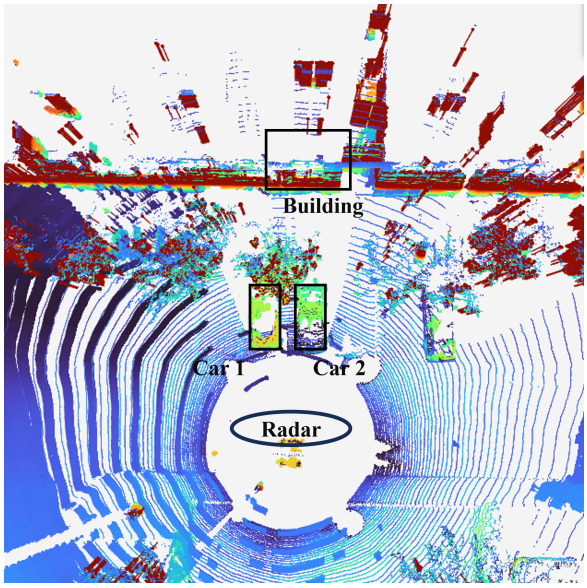

(a)

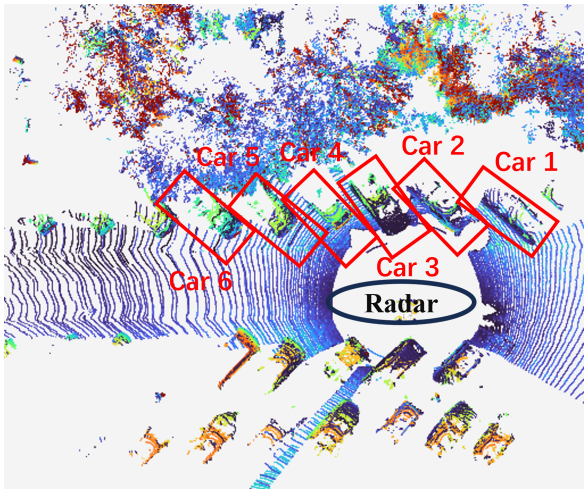

(b)

Figure 9.9: The image from Lidar data.

are well-focused in the image. However, with limited frame data, the results may still be challenging for interpretation and perception tasks. Fig.9.10(c) presents the result of the conventional BP imaging algorithm for the same scenario but using 49 frames of data. Since the BP algorithm is designed to work in a 2D plane, the images are without

elevation information. Fig.9.10(d) shows the image obtained by the imaging algorithm proposed in [127]. These results use only one antenna element but over 49 frames of data. The method incoherently sums the target information in the imaging field, leading to a three-times faster imaging algorithm than the conventional BP algorithm, easing its implementation in realistic contexts. The two cars are well separated, as in BP, and have more detailed information than when using only one frame of data.

Another example is presented in Fig. 9.11. The depicted scenario is the same as that shown in Fig. 9.8(b) with camera and Fig. 9.9(b) with Lidar. In Fig. 9.11(b), the three parked cars in the foreground are present in the image, but it is challenging to interpret the scene and the details of the targets. Similar to the scenario discussed in the previous example, all car targets appear to be better focused when using the conventional BP algorithm Fig.9.11(c) and the incoherent processing method of [127] with multiple frames data Fig.9.11(d). Specifically, in this example, 200 frames were considered, corresponding to the vehicle driving speed at 1m/s.

As no physical movement is present in the elevation dimension, the angular resolution will remain the same. The azimuth resolution improvement for DOA is approximated when the radar is moving at $[v_x, v_y, v_z]$ as:

$$n_a = \left\lfloor \frac{L_d}{\lfloor \frac{d}{2v_y T} \rfloor} \right\rfloor \frac{1}{N_a} + 1 \tag{9.7}$$

where $\lfloor\rfloor$ is the rounding operation, L_d is the total number of chirps in one snapshot, d is the distance between different receivers, T is the chirp duration, N_a is the number of antennas used for azimuth DOA estimation. It should be noted that $N_a = 1$ for Fig. 9.10 (a) and Fig. 9.11 (a) as only one azimuth antenna is used.

9.4. DISCUSSION

9.4.1. WAVEFORM PARAMETERS VS TDM

As mentioned, TDM is the most commonly used method to generate MIMO orthogonal signals for finer angular resolution. However, TDM will lead to problems in automotive scenarios. One of them is the decrease of the maximum measurable velocity, as this parameter, as defined in equation (9.2), is determined by the pulse repetition time. For TDM, this time is linearly positively correlated to the number of transmitters, i.e., the more transmitters need to be switched on/off one after the other, the longer that effective repetition time will be.

Orthogonal Frequency Division Multiplexing in MIMO waveform can potentially avoid the disadvantage of TDM. Different code families, namely random, Gold, zero correlation zone (ZCZ) and Kasami codes [128] are optimized for periodic auto-correlation properties. However, they still exhibit reasonable a-periodic auto-correlation properties, which means that the orthogonality cannot be achieved perfectly. This will increase the side lobes and worsen the beam pattern for the MIMO radar system, thus degrading the performance of DOA estimation. Ongoing research focuses on advanced signal processing methods to address the shrinking range of the unambiguous, measurable velocity by using all the transmitted signals in TDM or designing better-coded waveforms for different transmitters to achieve orthogonality.

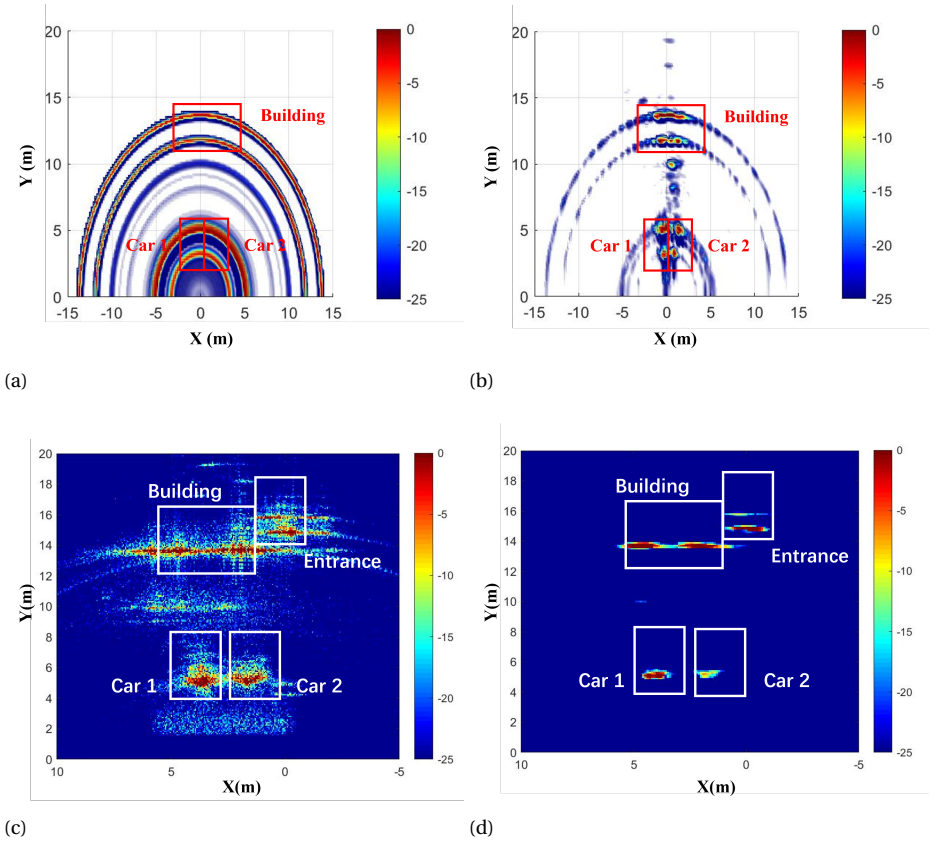

Figure 9.10: Radar images of scenarios 1in Fig. 9.8 (a) and Fig. 9.9 (a). (a) The radar imaging results of conventional MIMO processing. (b)The radar 3D imaging results using a 1D array of one frame data with the [126] algorithm. (c)The radar 2D imaging results using the BP algorithm of 200 frame data. (d) The imaging results of 200 frame data using the first element in the 1D array with the *yuan2024eurada* algorithm.

9

9.4.2. CALIBRATION WITH OTHER SENSORS

Calibrating the radar includes two tasks: one is for time synchronization, and another is for spatial alignment via coordinate transformation. For time synchronization, in this data collection, all the sensors' timing information was stored in the robot operating system (ROS) framework, except for the radar timing. To address this, the timestamp information is calculated and saved based on the starting recorded time in the radar files and the chosen pulse repetition time. As the updating rate is different for all sensors, the radar timestamps are taken as a reference, and all other sensor data are sampled at the closest position with respect to the radar timestamps.

Regarding spatial alignment, extrinsic transformations between sensors are formulated relative to the body coordinate frame. Extrinsic sensor calibration can be split into two procedures. First, a relative calibration procedure estimates the sensor's poses rel-

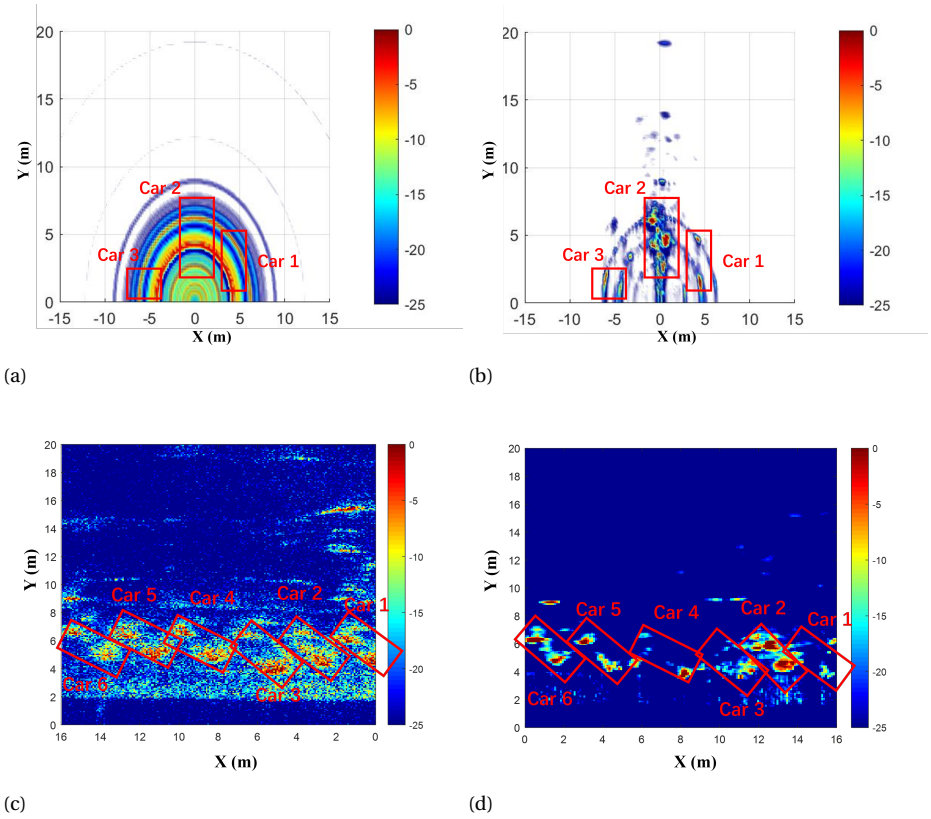

Figure 9.11: Radar images of scenarios 1in Fig. 9.8 (b) and Fig. 9.9 (b). (a) The radar imaging results of conventional MIMO processing. (b)The radar 3D imaging results using a 1D array of one frame data with the [126] algorithm. (c)The radar 2D imaging results using the BP algorithm of 200 frame data. (d) The imaging results of 200 frame data using the first element in the 1D array with the *yuan2024eurada* algorithm.

ative to all other sensors. Second, an absolute calibration procedure estimates sensor poses concerning the body coordinate frame of the sensor platform. The calibration of all the sensors except for radar is implemented according to the framework of [129]. The radar board is first installed at measured horizontal and vertical distances to the system in the forward-looking and side-looking regions. Then, the extrinsic transformations for the lidar and radar sensors are manually refined and adjusted using a test measurement with a corner reflector. This is an easy target to see with both lidar and radar, and the related point clouds from the two sensors are manually aligned to be as overlapped as possible as part of this spatial calibration. It is assumed that the extrinsic transformations do not change appreciably between different runs, so only one set of them is needed.

Besides the calibration with other sensors, for the chosen model of cascaded radar board, an inter-channel mismatch calibration is also required to account for frequency,

phase and amplitude mismatch across one single radar chip considered the master, and the other three chips considered the slaves. This calibration is a one-time bore-sight process using a corner reflector at about 5m and TDM MIMO configuration. The specific steps of the processing are detailed in [130].

9.4.3. INFLUENCE OF MOVING TARGETS

This challenge arises from the movement of targets in the scene. As motion-based high-resolution imaging algorithms are typically based on the relationship between the Doppler and the angle of targets, the presence of non-static targets will degrade their performance. Furthermore, the targets' movement will accumulate more errors when utilizing multiple frames in the imaging algorithm. To mitigate this effect, static and moving targets must be distinguished and processed using different techniques. Auto-focusing algorithms to estimate the target's movement and compensate for this during the imaging processing can be an interesting avenue of research in this context.

9.4.4. EFFECT OF DRIVING VELOCITY

Motion-based high-resolution imaging algorithms are based on the platform's movement. Depending on the specific implementation of these algorithms, different requirements on the driving velocities that are most suitable to obtain good images will follow. Specifically, algorithms for forward-looking regions such as [43, 69, 104, 131] are based on the Doppler profile, which means that the maximum velocity of the targets induced by the motion of the vehicle should be within the maximum unambiguous Doppler as in equation (9.2).

The algorithm for side-looking regions such as [132, 133] requires enough movement to physically expand the aperture during the frame period, which determines a lower driving velocity bound. Moreover, the generated additional motion-enhanced snapshots need to maintain coherence with the existing data from the physical MIMO array; this determines an upper bound of the driving velocity. Both lower and upper values are highly related to the vehicle speed and the duration of the radar chirp, as in:

$$V \in [\frac{d}{4L_d T}, \frac{d}{2T}] \tag{9.8}$$

where V is the driving velocity and d is typically assumed to be half wavelength.

9.5. CONCLUSIONS

In this chapter, an overview of existing resolution-enhancing approaches is provided. Despite their large variety, high computational costs and the complex nature of the scene, including clutter, limit their practical usage. At the same time, high-resolution imaging algorithms that exploit the movement of the vehicle have large potential, which has been demonstrated with examples for both the forward-looking regions and the side-looking regions. The forward-looking region can be used for bridge height estimation, obstacle avoidance, and adaptive cruise control, while the side-looking regions are mainly used for radar mapping. Experimental data collected in real driving scenarios in the city of Delft, the Netherlands, have been used to showcase the performances of the algorithms.

Specifically, it has been validated how some of these algorithms improve the angular resolution to estimate targets' positions and, consequently, the quality of the obtained images. In the analysis part, some important practical aspects for the implementation and applicability of imaging algorithms in realistic driving scenarios have also been listed and discussed. These are important to consider when moving from simulations of relatively simple scenes to practical automotive radar scenarios.

10

CONCLUSIONS

10.1. MAJOR RESULTS AND NOVEL CONTRIBUTIONS

The work described in this dissertation addresses some of the problems and challenges of automotive radar imaging, especially how to estimate the motion information of a vehicle using only radar and how to exploit this for better sensing ability. To solve these challenges, several novel algorithms have been developed, tested intensively in simulations, and verified using real-world experimental data. The algorithms proposed in this thesis are verified in improving the high-angular resolution and 3D imaging capability, meaning automotive radar can provide denser point clouds and sharper target contour information for different applications with the proposed approaches.

The major results of this PhD research are discussed in the following points.

- *3D Ego-motion estimation algorithm (Chapter 3)*

  The state-of-the-art algorithms for ego-motion estimation are based on radar point clouds, which are generated after several data processing steps. At least one coherent processing interval, i.e. one frame, is required to create such point clouds, which limits the possible update rate. Moreover, point clouds may not necessarily be coherent from frame to frame due to the scintillating scattering behaviour of extended targets at mm-wave frequencies, and they can be polluted by clutter and external interference. To address these challenges, it is proposed to perform ego-motion estimation using a lower signal level (i.e., the radar base-band signal before range-Doppler processing), which is beneficial for two reasons. Firstly, the ego-motion estimation can be performed fast, within one frame or even from chirp to chirp. Secondly, it will be easier to combine algorithms implemented directly on the signal level for ego-motion estimation with other algorithms to improve performances for other tasks, such as high-resolution imaging and target classification. **This thesis is the first to propose a novel 3D full ego-motion estimation algorithm working with radar raw signal at its input (i.e., the radar base-band signal before FFTs).** The proposed method first estimates the targets' positions and then uses their phase information from different times instances to determine the vehicle ego-motion through an optimization process. A detailed analysis of the proposed method performance is provided based on numerical simulations with point targets and realistic scenes reconstructed from the public *RadarScenes* dataset in [15]. The proposed method achieves at least five times higher accuracy than the state-of-the-art algorithm in realistic scenes.

- *2D Motion enhanced imaging algorithm for side-looking radar (Chapter 4)*

  As the ego-motion of the vehicle is known, this information can be used to improve recognition of the environment via imaging algorithms. Most of the algorithms inspired by synthetic aperture radar approaches are always computationally intensive and do not consider the arbitrary reset time between frames that is always present in real automotive radars. **This thesis proposes a novel formulation of the antenna array aperture extension using motion-enhanced snapshots that are generated by exploiting the vehicle's movement.** The array response at a specific time instance with data obtained at all the virtual receivers and corresponding to the same range-Doppler bin is defined as the array snapshot. This

new formulation includes a novel expression for the steering vectors to compensate for the error from the complex motion of the vehicle, a formulation with lower computational load via an approximation in the time tag, and a signal model accounting for the variable time interval for the data acquisition periods. The performance of the proposed method is analyzed in terms of its accuracy and probability of resolution. Azimuthal resolution improvement of approximately three times compared to existing methods has been demonstrated. A detailed analysis of the impact of forward and cross-forward velocity estimation errors on the performance of the direction-of-arrival method has been performed. Both simulated data from point-like and complex extended targets and experimental data have been used in the method performance analysis. The results show that the current MIMO system can achieve better resolution and accuracy in DOA estimation with motion-enhanced snapshots.

- *3D Motion enhanced imaging algorithm for side-looking radar (Chapter 5)*

  Side-looking automotive radar can provide more detailed information about the environment around the vehicle and is commonly used for mapping applications. Extended from Chapter 4, a 3D motion-enhanced imaging algorithm for side-looking radar is formulated in this thesis. **The proposed method is the first 3D imaging algorithm using only a 1D array in the literature for automotive Frequency-Modulated Continuous Wave (FMCW) radar.** First, it transposes the conventional automotive radar antenna array to get a better resolution in elevation. Then, the motion-enhanced snapshots are introduced to boost the resolution in azimuth. This tackles the imaging problem in the 3D domain of range-azimuth-elevation with a higher resolution in both directions compared with the state-of-the-art algorithms. The proposed method offers more degrees of freedom and achieves a better signal-to-noise ratio than conventional MIMO processing. The performance of the proposed method is thoroughly analyzed for ideal point targets and extended targets in simulations. Metrics based on voxelization accuracy and image contrast are proposed to evaluate quantitatively the 3D imaging results for simulated results. The F2 score of voxelization accuracy increases three times, showing a good imaging sensor obtained with the proposed method.

- *2D Robust Doppler Beam Sharpening Algorithm for Forward-looking MIMO Radar (Chapter 6)*

  The forward-looking region is very relevant for automotive vehicles. Most available approaches do not consider the ambiguity problem in the case of the forward-looking radar. **This thesis is the first to solve the ambiguity in Doppler beam sharpening for forward-looking multi-input-multi-output (MIMO) radar.** An unambiguous Doppler-based forward-looking multiple-input multiple-output radar beam sharpening scan (*UDFMBSC*) method is proposed by combining Doppler beam sharpening and MIMO array processing to solve the ambiguity problem of symmetric targets in forward-looking automotive radar. To further make UDFMBSC robust, Robust, Unambiguous DBS using Adaptive Threshold (RUDAT) is proposed, considering the diversity of target reflectivity and robust vehicle movement. The

proposed methods have been verified for simulated point-like and extended targets, as well as experimental data from a radar sensor, showing that the proposed methods address the ambiguity problem of conventional Doppler beam sharpening (DBS) and provide six times higher angular estimation than Digital Beam Forming (DBF). The proposed method does not require any prior information on the environment, the number of targets and their locations. The method is computationally efficient and can be implemented easily in current radar sensors.

- *3D Robust Doppler Beam Sharpening Algorithm for Forward-looking MIMO Radar (Chapter 7)*

  Currently, no 3D DBS imaging algorithm addresses the elevation and azimuth dimensions. Going beyond Chapter 6, in this thesis **a novel approach named *3DRUDAT* ('3D Robust Unambiguous DBS using Adaptive Threshold') is formulated.** This tackles the imaging problem in the 3D domain of range-azimuth-elevation by solving the coupling between elevation and azimuth angle and addresses the ambiguity problem in the forward-looking region of Doppler beam sharpening. The performance of the proposed method is thoroughly analyzed for ideal point targets and extended targets in simulations, as well as with experimental data from a public dataset. Metrics based on voxelization accuracy and image contrast are proposed to quantitatively evaluate the 3D imaging results for simulated and experimental data. The image contrast metric in each slice of 3D imaging results doubled, meaning better image quality and higher resolution images are obtained with the proposed method.

- *Joint ego-motion estimation and high-resolution imaging algorithm (Chapter 8)*

  Based on the proposed 3D ego-motion estimation algorithm in Chapter 3 and 3D high-resolution imaging algorithm in Chapter 5 and Chapter 7, **a joint ego-motion estimation and 3D imaging algorithm processing chain is proposed**. Specifically, this thesis proposes the idea of combining the ego-motion estimation algorithm with two 3D imaging algorithms for both the side-looking region and the forward-looking region. A detailed analysis of the method's performance and limitations is performed based on numerical simulations.

- *Verification in realistic driving scenarios (Chapter 9)*

  An experimental platform with multiple sensors mounted on the car is set up. The specific waveform for verifying different proposed methods is designed. The data is collected during actual driving scenarios in the city of Delft. **A fast, high-resolution imaging algorithm is proposed by incoherently accumulating the images from multiple frames' data in the radar field of view.** The method is three times faster than the conventional back-projection algorithm, a benchmark algorithm using multiple frame data, making it easier to implement in real-time applications. Using multiple data, the algorithm breaks the limitation of the method proposed in Chapter 5 with limited data, providing better sensing ability of the environment.

10.2. RECOMMENDATIONS FOR FUTURE WORK

The following recommendations are intended as possible starting points for further research:

- *Further improvement of ego-motion estimation.* To address the performance degradation with an increasing ratio of moving to static targets, a possible solution would be the introduction of a threshold to distinguish moving vs static targets and only use the static targets' information for ego-velocity estimation. In this way, the computation complexity of the method may also be reduced by considering fewer targets in the optimization stage presented in Chapter 3. To address the potential issue of ambiguous velocity values for high speed, frequency division multiple (FDM), code division multiple (CDM) or other Doppler velocity dealiasing techniques [134–136] to expand the unambiguous velocity range can also be implemented in the processing chain. To apply the proposed method in forward-looking radar configuration, the problem of ambiguity in Doppler velocity will need to be solved to help better separate ambiguous targets in individual range-Doppler bins.

- *The improvement of 3D Motion enhanced imaging algorithm for side-looking radar 5.* A potential limitation of the algorithm is that the movement of the targets in the scenarios might lead to a loss of focus and degrading performance. Potential improvements include the auto-focusing algorithm in SAR applications. With multiple radars observing different directions, the motion pattern of the targets will be different; such information could also be used for a better mapping algorithm. The potential 6D radar system can be obtained, i.e., the target's position can be retrieved from range azimuth and elevation angle, and the 3D movement of the targets can be obtained by labelling the moving targets and different measures of Doppler velocity.

- *The improvement of 3DRUDAT.* To address the blind zone issue of forward-looking SAR in Chapters 6 and 7, the fusion of motion-based high-resolution images and other high-resolution images generated from other advanced signal processing way could be a potential solution. Also, multi-radars installed on different vehicle positions can be exploited to further improve the 3D imaging resolution since they will provide the depth information of extended target information from different-looking angles. To solve the ambiguity problem, the current algorithm could combine other approaches, including compressed sensing, probability grid generation, and neural networks instead of classical MIMO processing in this thesis.

- *The improvement of the joint ego-motion estimation and high-resolution imaging algorithm.* The forward-looking SAR algorithm requires a high positioning accuracy, provided by the newly designed ego-motion estimation. However, instead of simply integrating two processes consecutively, the similar information sharing between two blocks will further improve both performances, e.g., the optimization of angle information of targets in ego-motion estimation could share and combine with the angle information with the MIMO processing in 3D forward-looking SAR processing.

- *The improvement of the real data processing.* The time division multiple access (TDMA) modulations will limit the maximum Doppler range, further influencing Doppler processing and the Doppler beam sharpening. This is even worse when using a typical cascaded TI board [124] since more transmitters are divided in the time axis. A new signal processing is needed to address this non-periodical sampling problem, i.e. parametric semianalytical model or non-parametric model-based approaches. The current commercial radar board only have a limited antenna in the 2D antenna-formed array [124]. Thus, the grating lobe from the 2D DOA estimation will decrease the accuracy of the DOA estimation.

A

SIMULATOR DESIGNED FOR THE WHOLE THESIS

A.1. INTRODUCTION

Facing inadequate measurement and lack of experimental data, simulation is always regarded as a strong supplementary data source for research. Simulation plays an important role in the radar field before being applied to the practice, and great progress has been made in the past years[137]. The revolutionary development in computation power made it possible to model radar signals as realistically as possible since the complex electromagnetic wave propagation could be calculated with exact solvers and/or with the ray tracing method. Specifically, full-wave simulation, using the moment method (MoM)[138], finite element method (FEM)[139], and finite-difference time-domain method (FDTD)[140], implements and solves the complete Maxwell equations' set during wave propagation, and can provide high-accuracy simulated data. However, they require relatively heavy computation, which increases with larger scenes and higher operation frequencies, such as the mm-wave band occupied by automotive radar. Hence, in this appendix, a computationally efficient simulator that considers the easy ray tracing method was built and designed to verify the performance of the proposed algorithms in this thesis.

A.2. SIMULATOR STRUCTURE

As the basis for the radar signal simulation, the structure design of the radar system plays an important role in the simulation of the radar signal. The flowchart of the simulation

Parts of this appendix are co-developed with co-supervised Master student Yongdian Sun in the MS3 group.

Parts of this appendix are published in Sun, Y., 2023. An FMCW MIMO Automotive Radar Signal Simulator For Realistic Extended Targets. http://resolver.tudelft.nl/uuid:294cb65b-7ca4-4770-8679-5e84d855962d

in this thesis is shown in Fig. A.1. A realistic target model based on detailed CAD models widely used in industrial design is proposed. Based on the CAD models, the grid of scattering points for the radar signals is generated. The CAD model is converted to the point cloud containing the position information of the scatters. It is important to note that the scatterers in the CAD models do not aim to precisely mimic electromagnetic scattering behaviour from the actual objects. Rather, they serve as a representation of the object's body shape and extent. Depending on the CAD source and the target's shape and complexity, the total number and distribution of extracted point scatters can differ; therefore, pre-processing for scaling the target model is necessary to get an acceptable target size for the considered scattering points.

Different applications may require different target information, i.e., the contour of the targets or the occlusion of the targets from different perspectives. Thus, the occlusion ability is defined as a parameter in the simulator for users' preferences. The hidden part is still visible in the radar simulator for evaluating the high-angular resolution algorithm, showing the similarity between the radar image and the ground truth. For classification applications, the hidden algorithm is necessary for realistic testing. The hidden point removal algorithm [141] could be applied to estimate the hidden points concerning the radar line-of-sight.

Then, the radar and target motion models are designed to describe the three-dimensional translational and rotational movement, respectively. The changes by the movement, i.e. range, velocity, and angle positions, are updated frame by frame. Finally, the maximum detection range in 3D spatial coordinates is calculated based on the radar setting. In the end, the reflected signal is generated for only the observed point scatterers using the defined signal model for different radar installations, i.e., side-looking or forward-looking. The frame loop will be performed until the required number of frames is generated.

A.2.1. RADAR SIGNAL MODEL

FMCW MIMO radar model is used in this thesis and has been selected as the radar model in this simulator, as it is the main type of radar employed in state-of-the-art automotive applications.

In real radar data measurement, the radar received signals are collected beats by beats, also known as frames by frames, wherein each beat/frame, several chirps signals are generated based on different radar settings. Therefore, in simulation, the total number of chirps in the frame needs to be determined in advance with the mathematical expression shown below, where F_n represents the total number of chirps in the frame, $T_{observation}$ refers to the total observation time for the simulation, N_{chirp} and T is related to the radar waveform setting of chirp number and pulse repetition interval for signal generation. Considering the uneven case during the calculation, the rounding ceiling function is added to generate a correct integer number of chirps per frame.

$$F_n = \lceil \frac{T_{observation}}{N_{chirp} * T} \rceil \tag{A.1}$$

The radar signal model can be derived from equation (2.16) as:

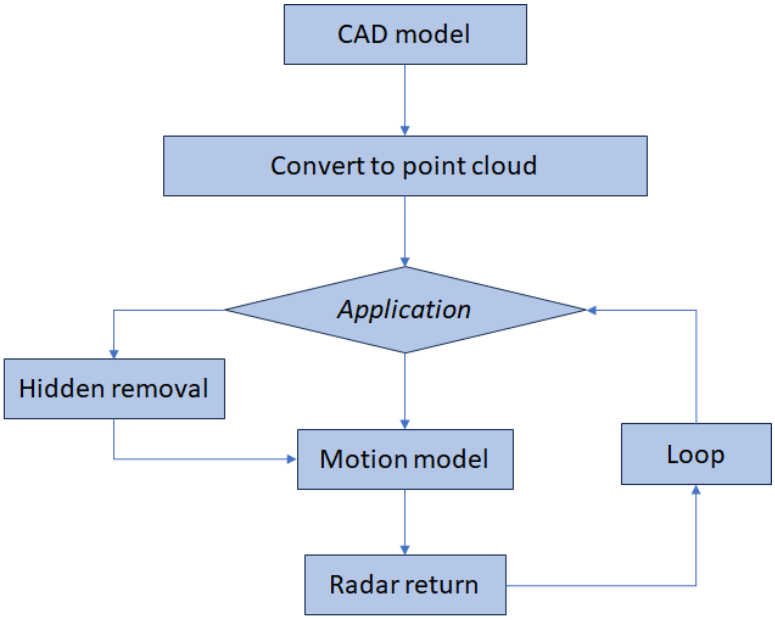

Figure A.1: Flow chart of simulation method used

$$\begin{aligned}\hat{z}_i(l,b,p,q) =& \alpha_i * \exp(j2\pi(a(\theta_i,\phi_i)p)) * \exp(j2\pi(e(\phi_i)q)) \\ & * \exp(j2\pi(f_d(v_i)l)) * \exp(j2\pi(f_r(R_i)b))\end{aligned} \tag{A.2}$$

where

$$a(\theta_i,\phi_i) = f_0\frac{d}{c}(\sin\theta_i\cos\phi_i), e(\phi_i) = f_0\frac{d}{c}(\sin\phi_i), f_d(v_i) = -f_0\frac{2v_i}{c}, f_r(R_i) = -\frac{\mu 2R_i}{cf_s}$$

The signal model could be written as:

$$\hat{z}_i = \alpha_i \mathbf{a}(\theta_i,\phi_i) \circ \mathbf{e}(\phi_i)\mathbf{f_d}(v_i) \circ \mathbf{f_r}(R_i) \tag{A.3}$$

where: $\circ$ is the outer production and

$$\begin{aligned}\mathbf{a}(\theta_i,\phi_i) &= [1, e^{j2\pi a(\theta_i,\phi_i)}, ..., e^{j2\pi a(\theta_i,\phi_i)(L-1)}]^T, \in \mathbb{C}^{L\times 1} \\ \mathbf{e}(\phi_i) &= [1, e^{j2\pi e(\phi_i)}, ..., e^{j2\pi a(\phi_i)(L-1)}]^T, \in \mathbb{C}^{L\times 1} \\ \mathbf{f_d}(v_i) &= [1, e^{j2\pi f_d(v_i)}, ..., e^{j2\pi f_d(v_i)(M-1)}]^T, \in \mathbb{C}^{M\times 1} \\ \mathbf{f_r}(R_i) &= [1, e^{j2\pi f_r(R_i)}, ..., e^{j2\pi f_r(R_i)(K-1)}]^T, \in \mathbb{C}^{K\times 1}\end{aligned}$$

For simplification of subsequent signal processing, the 4-dimension tensor has to be reshaped to the 3-dimensional tensor by stacking azimuth and elevation dimensions together as

$$\mathbf{Z}_i(l,b,pN_e+q) = \hat{z}_i(l,b,p,q) \tag{A.4}$$

Then, the radar data is reshaped into the radar cube matrix shown in Fig. A.2. In this project, one radar cube contains a single frame of simulated radar data, where three axes correspond to the fast-time (K), slow-time (L), and number of channels (P).

Therefore, the initial radar cube can be decomposed into three radar cube subsets that are only related to a single parameter with given values based on the above equation. Notably, the sub-cube should have the same size and origin as the original radar cube, and each sub-cube should be homologous on the dimension of the corresponding aforementioned vector. Then the received data of the f_nth frame in the presence of radar

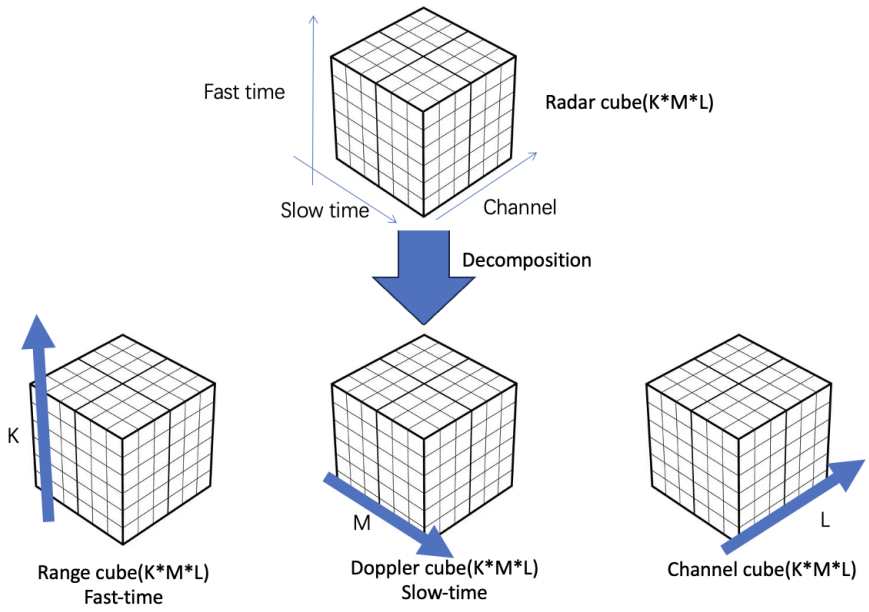

Figure A.2: Illustration of the radar cube and decomposition along specific directions with their meaning, namely fast-time, slow-time, and number of MIMO channels

LOS with the Gaussian noise N is written as

$$\mathbf{Z}^{(f_n)} = \sum_{i=1}^{I} \mathbf{X}_i + N \tag{A.5}$$

A.2.2. MOTION MODEL

With the derived signal model and target model given in the previous sections, to accurately describe the space information for point scatterers, a 3D coordinate system is established, shown in Fig.A.3 with an example of a single point target in the radar line-of-sight. To be more specific, the coordinate system is made of two parts, the world coordinates system, and the radar observation system, where the blue labels are related

to the parameter in the world coordinate system (XYZ-O) and black labels are related to the radar observation system (X'Y'Z'-O'). The world coordinate system (3D Cartesian co-

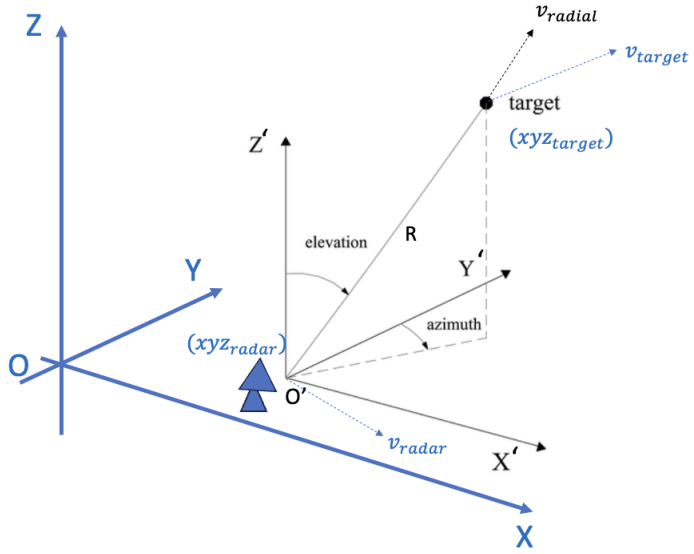

Figure A.3: World coordinate systems and radar observation

ordinate system) is the basis of the radar observation system, which is used to generate the radial velocity (v_{radial}), range (R), and azimuth angle (θ_i) used in equation (3.8).

With the known initial position of radar (xyz_{radar}) and single-point target (xyz_{target}), the range and azimuth angle between radar & target can be calculated with the below equation:

$$\begin{aligned} R &= ||xyz_{target} - xyz_{radar}|| \\ sin(\theta) &= (\frac{||x_{radar} - x_{target}||}{||xy_{radar} - xy_{target}||}) \end{aligned} \tag{A.6}$$

while the radial velocity (v_{radial}) can be calculated with projected v, the given velocity of radar (v_{radar}) and target (v_{target}) in world coordinates by using equation (3.13). However, to accurately describe the dynamic information of the target and the radar, the motion information is divided into two parts: translational motion and rotational motion.

Translational motion: Within the measurement time (t), the target position would be changed in the world coordinate system based on the below equation:

$$xyz_{translation}(t) = v_{translantion}(t) * t + xyz_{target}(t = 0) \tag{A.7}$$

Rotational motion: Compared with translational motion, rotational motion is more complex due to an extra rotation coordinate system involved. For simplification, the

A

sphere coordinate is introduced to define the rotational motion shown in Fig.A.4. With

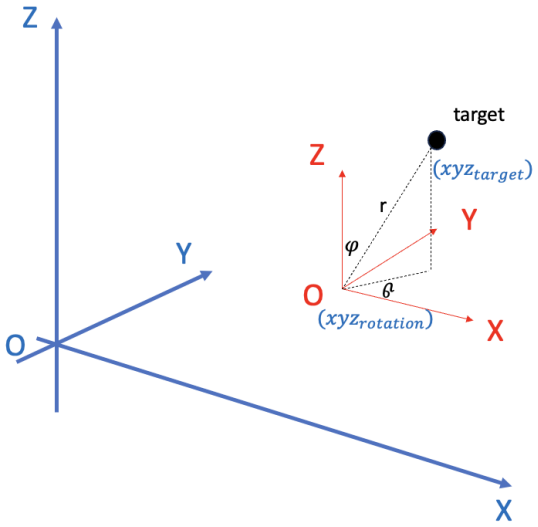

Figure A.4: Rotational motion coordinate system

set rotation centre $(xyz_{rotation})$, rotation direction (ϑ, φ), and rotation speed(ω), the target position can be calculated using the equations below:

$$\begin{aligned} xyz_r &= ||xyz_{target} - xyz_{rotation}|| \\ u_{xyz} &= [sin\varphi cos\vartheta, sin\varphi sin\vartheta, cos\varphi]^T \\ \theta_{rotation}(t) &= \omega * t \\ xyz_{afterrotation}(t) &= xyz_{target} + rm(t) * xyz_r \end{aligned} \tag{A.8}$$

where xyz_r refers to the target coordinate in the rotation coordinate system, u_{xyz} represents the unit rotation direction vector $(u_x^2 + u_y^2 + u_z^2 = 1)$ according to the Right-hand rule, and the rm is the rotation matrix defined as follows by substituting $\theta = \theta_{rotation}(t)$

$$rm(t) = \begin{bmatrix} cos\theta - u_x^2\,(1-cos\theta) & u_x\,u_y\,(1-cos\theta) - u_z\,sin\theta & u_x\,u_z\,(1-cos\theta) + u_y\,sin\theta \\ u_y\,u_x\,(1-cos\theta) + u_z\,sin\theta & cos\theta - u_y^2\,(1-cos\theta) & u_y\,u_z\,(1-cos\theta) - u_x\,sin\theta \\ u_z\,u_x\,(1-cos\theta) - u_y\,sin\theta & u_z\,u_y\,(1-cos\theta) + u_x\,sin\theta & cos\theta - u_z^2\,(1-cos\theta) \end{bmatrix} \tag{A.9}$$

Meanwhile, the instant linear velocity in the world coordinate system would be:

$$v_{linear}(t) = (\omega \dot{u}_{xyz}) \times rm(t) * xyz_r \tag{A.10}$$

where $(\omega \dot{u}_{xyz})$ is the angular velocity in vector form.

Therefore, for the single-point scatter shown in Fig. A.4, the instant position and radial velocity are the combined translational motion and rotational motion together shown in the equation below:

$$\begin{aligned} xyz_{target}(t) &= xyz_{translational}(t) + xyz_{afterrotation}(t) + xyz_{target}(t=0) \\ v_{radial}(t) &= v_{translation}(t) + v_{linear}(t) + v_{radial}(t=0) \end{aligned} \tag{A.11}$$

A.3. RESULTS OF THE SIMULATOR AND REAL EXPERIMENTS

To test the simulator's performance with the real experimental measurement, the targets in Fig. 4.12 are used here. Two cars with a width of 2.5m and a length of 5m are regarded as the targets in the radar field of view. The hidden removal operation is implemented realistically. The two cars in the experimental measurements are in optical images, Fig. 9.8 (a). The BP algorithm is used in real experiments and simulated data for comparisons.

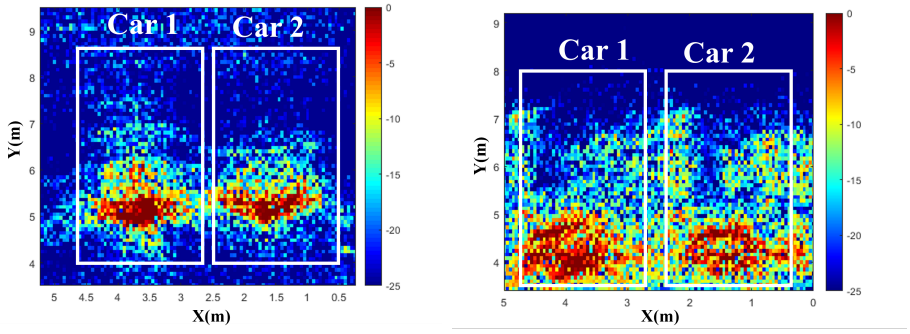

(a) (b)

Figure A.5: (a)The imaging results of the real car. (b) The imaging results of the simulated car.

The two cars are well focused, as shown in Fig. A.5 and have similarity in the contour between (a) and (b). Since the energy levels are highly related to the real reflectivity of the car, which is not considered in the simulator, thus the energy levels are not compared here. The imaging results prove the effectiveness of the simulator.

A.4. CONCLUSION

In this thesis, the simulator has been developed to provide an FMCW MIMO radar simulator for realistic extended targets under the balance between computation time and simulation accuracy. A Motion control system containing coordinate transform is built. The simulator is verified by the proposed algorithms in this thesis and can be utilized as a strong supplement for future radar signal processing algorithm developers.

BIBLIOGRAPHY

[1] I. Bilik, O. Longman, S. Villeval, and J. Tabrikian, "The rise of radar for autonomous vehicles: Signal processing solutions and future research directions," *IEEE Signal Processing Magazine*, vol. 36, no. 5, pp. 20–31, 2019.

[2] F. Engels, P. Heidenreich, A. M. Zoubir, F. K. Jondral, and M. Wintermantel, "Advances in automotive radar: A framework on computationally efficient high-resolution frequency estimation," *IEEE Signal Processing Magazine*, vol. 34, no. 2, pp. 36–46, 2017.

[3] S. H. Cen and P. Newman, "Precise ego-motion estimation with millimeter-wave radar under diverse and challenging conditions," in *2018 IEEE International Conference on Robotics and Automation (ICRA)*. IEEE, 2018, pp. 6045–6052.

[4] F. Roos, J. Bechter, C. Knill, B. Schweizer, and C. Waldschmidt, "Radar sensors for autonomous driving: Modulation schemes and interference mitigation," *IEEE Microwave Magazine*, vol. 20, no. 9, pp. 58–72, 2019.

[5] S. Sun, A. P. Petropulu, and H. V. Poor, "Mimo radar for advanced driver-assistance systems and autonomous driving: Advantages and challenges," *IEEE Signal Processing Magazine*, vol. 37, no. 4, pp. 98–117, 2020.

[6] F. Engels, P. Heidenreich, A. M. Zoubir, F. K. Jondral, and M. Wintermantel, "Advances in automotive radar: A framework on computationally efficient high-resolution frequency estimation," vol. 34, no. 2, pp. 36–46. [Online]. Available: http://ieeexplore.ieee.org/document/7870737/

[7] S. Chen, B. Liu, C. Feng, C. Vallespi-Gonzalez, and C. Wellington, "3d point cloud processing and learning for autonomous driving," *arXiv preprint arXiv:2003.00601*, 2020.

[8] A. Palffy, E. Pool, S. Baratam, J. F. Kooij, and D. M. Gavrila, "Multi-class road user detection with 3+ 1d radar in the view-of-delft dataset," *IEEE Robotics and Automation Letters*, vol. 7, no. 2, pp. 4961–4968, 2022.

[9] F. Ding, A. Palffy, D. M. Gavrila, and C. X. Lu, "Hidden gems: 4d radar scene flow learning using cross-modal supervision," in *Proceedings of the IEEE/CVF Conference on Computer Vision and Pattern Recognition*, 2023, pp. 9340–9349.

[10] P. Barton, "Digital beam forming for radar," *IEE Proceedings F (Communications, Radar and Signal Processing)*, vol. 127, pp. 266–277(11), August 1980.

[11] J. Capon, "High-resolution frequency-wavenumber spectrum analysis," *Proceedings of the IEEE*, vol. 57, no. 8, pp. 1408–1418, 1969.

[12] S. Xu, J. Wang, and A. Yarovoy, "Super resolution doa for fmcw automotive radar imaging," in *2018 IEEE Conference on Antenna Measurements & Applications (CAMA)*. IEEE, 2018, pp. 1–4.

[13] S. Xu and A. Yarovoy, "Joint doppler and doa estimation using 2d music in presence of phase residual," 10 2017, pp. 203–206.

[14] R. Roy and T. Kailath, "Esprit-estimation of signal parameters via rotational invariance techniques," *IEEE Transactions on Acoustics, Speech, and Signal Processing*, vol. 37, no. 7, pp. 984–995, 1989.

[15] O. Schumann, M. Hahn, N. Scheiner, F. Weishaupt, J. F. Tilly, J. Dickmann, and C. Wöhler, "Radarscenes: A real-world radar point cloud data set for automotive applications," in *2021 IEEE 24th International Conference on Information Fusion (FUSION)*. IEEE, 2021, pp. 1–8.

[16] S. M. Patole, M. Torlak, D. Wang, and M. Ali, "Automotive radars: A review of signal processing techniques," *IEEE Signal Processing Magazine*, vol. 34, no. 2, pp. 22–35, 2017.

[17] D. Johnson and D. Dudgeon, *Array Signal Processing: Concepts and Techniques*, 01 1993.

[18] R. H. Rasshofer and K. Gresser, "Automotive radar and lidar systems for next generation driver assistance functions," *Advances in Radio Science*, vol. 3, no. B. 4, pp. 205–209, 2005.

[19] P. Fritsche, B. Zeise, P. Hemme, and B. Wagner, "Fusion of radar, lidar and thermal information for hazard detection in low visibility environments," in *2017 IEEE International Symposium on Safety, Security and Rescue Robotics (SSRR)*. IEEE, 2017, pp. 96–101.

[20] J. Khalife and Z. M. Kassas, "Differential framework for submeter-accurate vehicular navigation with cellular signals," *IEEE Transactions on Intelligent Vehicles*, 2022.

[21] Y. Almalioglu, M. Turan, C. X. Lu, N. Trigoni, and A. Markham, "Milli-rio: Ego-motion estimation with low-cost millimetre-wave radar," *IEEE Sensors Journal*, vol. 21, no. 3, pp. 3314–3323, 2020.

[22] O. Bialer and I. Bilik, "Accurate self localization using automotive radar synthetic aperture radar," Oct. 15 2019, uS Patent 10,444,347.

[23] Y. Li, Y. Liu, Y. Wang, Y. Lin, and W. Shen, "The millimeter-wave radar slam assisted by the rcs feature of the target and imu," *Sensors*, vol. 20, no. 18, p. 5421, 2020.

[24] A. Kramer, C. Stahoviak, A. Santamaria-Navarro, A.-A. Agha-Mohammadi, and C. Heckman, "Radar-inertial ego-velocity estimation for visually degraded environments," in *2020 IEEE International Conference on Robotics and Automation (ICRA)*. IEEE, 2020, pp. 5739–5746.

[25] C. Doer and G. F. Trommer, "Radar visual inertial odometry and radar thermal inertial odometry: Robust navigation even in challenging visual conditions," in *2021 IEEE/RSJ International Conference on Intelligent Robots and Systems (IROS)*. IEEE, 2021, pp. 331–338.

[26] P. Wallrath and R. Herschel, "Egomotion estimation for a sensor platform by fusion of radar and imu data," in *2020 17th European Radar Conference (EuRAD)*. IEEE, 2021, pp. 314–317.

[27] D. Kellner, M. Barjenbruch, J. Klappstein, J. Dickmann, and K. Dietmayer, "Instantaneous ego-motion estimation using doppler radar," in *16th International IEEE Conference on Intelligent Transportation Systems (ITSC 2013)*. IEEE, 2013, pp. 869–874.

[28] ——, "Instantaneous ego-motion estimation using multiple doppler radars," in *2014 IEEE International Conference on Robotics and Automation (ICRA)*, 2014, pp. 1592–1597.

[29] M. Barjenbruch, D. Kellner, J. Klappstein, J. Dickmann, and K. Dietmayer, "Joint spatial-and doppler-based ego-motion estimation for automotive radars," in *2015 IEEE Intelligent Vehicles Symposium (IV)*. IEEE, 2015, pp. 839–844.

[30] M. Rapp, M. Barjenbruch, K. Dietmayer, M. Hahn, and J. Dickmann, "A fast probabilistic ego-motion estimation framework for radar," in *2015 European Conference on Mobile Robots (ECMR)*. IEEE, 2015, pp. 1–6.

[31] M. Rapp, M. Barjenbruch, M. Hahn, J. Dickmann, and K. Dietmayer, "Probabilistic ego-motion estimation using multiple automotive radar sensors," *Robotics and Autonomous Systems*, vol. 89, pp. 136–146, 2017.

[32] C. D. Monaco and S. N. Brennan, "Radarodo: Ego-motion estimation from doppler and spatial data in radar images," *IEEE Transactions on Intelligent Vehicles*, vol. 5, no. 3, pp. 475–484, 2020.

[33] K. Qian, Z. He, and X. Zhang, "3d point cloud generation with millimeter-wave radar," *Proceedings of the ACM on Interactive, Mobile, Wearable and Ubiquitous Technologies*, vol. 4, no. 4, pp. 1–23, 2020.

[34] P. Wallrath and R. Herschel, "Mimo radar based platform motion detection for radar imaging," in *2020 21st International Radar Symposium (IRS)*. IEEE, 2020, pp. 351–355.

[35] K. Haggag, S. Lange, T. Pfeifer, and P. Protzel, "A credible and robust approach to ego-motion estimation using an automotive radar," *IEEE Robotics and Automation Letters*, vol. 7, no. 3, pp. 6020–6027, 2022.

[36] A. Kingery and D. Song, "Improving ego-velocity estimation of low-cost doppler radars for vehicles," *IEEE Robotics and Automation Letters*, vol. 7, no. 4, pp. 9445–9452, 2022.

[37] M. Magnusson, A. Lilienthal, and T. Duckett, "Scan registration for autonomous mining vehicles using 3d-ndt," *Journal of Field Robotics*, vol. 24, no. 10, pp. 803–827, 2007.

[38] Y. S. Park, Y.-S. Shin, J. Kim, and A. Kim, "3d ego-motion estimation using low-cost mmwave radars via radar velocity factor for pose-graph slam," *IEEE Robotics and Automation Letters*, vol. 6, no. 4, pp. 7691–7698, 2021.

[39] S. Lim, J. Jung, S.-C. Kim, and S. Lee, "Radar-based ego-motion estimation of autonomous robot for simultaneous localization and mapping," *IEEE Sensors Journal*, vol. 21, no. 19, pp. 21 791–21 797, 2021.

[40] H.-W. Cho, S. Choi, Y.-R. Cho, and J. Kim, "Complex-valued channel attention and application in ego-velocity estimation with automotive radar," *IEEE Access*, vol. 9, pp. 17 717–17 727, 2021.

[41] K. Yeon, K. Min, J. Shin, M. Sunwoo, and M. Han, "Ego-vehicle speed prediction using a long short-term memory based recurrent neural network," *International Journal of Automotive Technology*, vol. 20, no. 4, pp. 713–722, 2019.

[42] S. Yuan, F. Fioranelli, and A. Yarovoy, "An approach for high-angular resolution implementation in moving automotive mimo radar," in *2021 18th European Radar Conference (EuRAD)*. IEEE, 2022, pp. 449–452.

[43] S. Yuan, P. Aubry, F. Fioranelli, and A. Yarovoy, "A novel approach to unambiguous doppler beam sharpening for forward-looking mimo radar," *IEEE Sensors Journal*, 2022.

[44] V. Milanés, S. E. Shladover, J. Spring, C. Nowakowski, H. Kawazoe, and M. Nakamura, "Cooperative adaptive cruise control in real traffic situations," *IEEE Transactions on intelligent transportation systems*, vol. 15, no. 1, pp. 296–305, 2013.

[45] M. Ibarra-Arenado, T. Tjahjadi, J. Pérez-Oria, S. Robla-Gómez, and A. Jiménez-Avello, "Shadow-based vehicle detection in urban traffic," *Sensors*, vol. 17, no. 5, p. 975, 2017.

[46] B. Zhu, S. Yan, J. Zhao, and W. Deng, "Personalized lane-change assistance system with driver behavior identification," *IEEE Transactions on Vehicular Technology*, vol. 67, no. 11, pp. 10 293–10 306, 2018.

[47] J. Hasch, "Driving towards 2020: Automotive radar technology trends," in *2015 IEEE MTT-S International Conference on Microwaves for Intelligent Mobility (ICMIM)*. IEEE, 2015, pp. 1–4.

[48] M. Gottinger, M. Hoffmann, M. Christmann, M. Schütz, F. Kirsch, P. Gulden, and M. Vossiek, "Coherent automotive radar networks: The next generation of radar-based imaging and mapping," *IEEE Journal of Microwaves*, vol. 1, no. 1, pp. 149–163, 2021.

[49] A. Farina and F. A. Studer, "A review of cfar detection techniques in radar systems," *Microwave Journal*, vol. 29, p. 115, 1986.

[50] C. Chen, C. He, C. Hu, H. Pei, and L. Jiao, "A deep neural network based on an attention mechanism for sar ship detection in multiscale and complex scenarios," *IEEE Access*, vol. 7, pp. 104 848–104 863, 2019.

[51] S. Khudoyarov, N. Kim, and J.-J. Lee, "Three-dimensional convolutional neural network–based underground object classification using three-dimensional ground penetrating radar data," *Structural Health Monitoring*, vol. 19, no. 6, pp. 1884–1893, 2020.

[52] M. Weiss, "Analysis of some modified cell-averaging cfar processors in multiple-target situations," *IEEE Transactions on Aerospace and Electronic Systems*, no. 1, pp. 102–114, 1982.

[53] K. S. Arun, T. S. Huang, and S. D. Blostein, "Least-squares fitting of two 3-d point sets," *IEEE Transactions on pattern analysis and machine intelligence*, no. 5, pp. 698–700, 1987.

[54] W. Kabsch, "A solution for the best rotation to relate two sets of vectors," *Acta Crystallographica Section A: Crystal Physics, Diffraction, Theoretical and General Crystallography*, vol. 32, no. 5, pp. 922–923, 1976.

[55] D. E. Goldberg, *Genetic Algorithms in Search, Optimization and Machine Learning*, 1st ed. USA: Addison-Wesley Longman Publishing Co., Inc., 1989.

[56] S. Kirkpatrick, C. D. Gelatt Jr, and M. P. Vecchi, "Optimization by simulated annealing," *science*, vol. 220, no. 4598, pp. 671–680, 1983.

[57] C. Audet and J. E. Dennis Jr, "Analysis of generalized pattern searches," *SIAM Journal on optimization*, vol. 13, no. 3, pp. 889–903, 2002.

[58] P. Vasant and N. Barsoum, "Hybrid pattern search and simulated annealing for fuzzy production planning problems," *Computers & Mathematics with Applications*, vol. 60, no. 4, pp. 1058–1067, 2010.

[59] R. Giubilato, S. Chiodini, M. Pertile, and S. Debei, "An evaluation of ros-compatible stereo visual slam methods on a nvidia jetson tx2," *Measurement*, vol. 140, pp. 161–170, 2019.

[60] M. Ester, H.-P. Kriegel, J. Sander, X. Xu *et al.*, "A density-based algorithm for discovering clusters in large spatial databases with noise." in *kdd*, vol. 96, no. 34, 1996, pp. 226–231.

[61] M. Andres, P. Feil, and W. Menzel, "3d-scattering center detection of automotive targets using 77 ghz uwb radar sensors," in *2012 6th European Conference on Antennas and Propagation (EUCAP)*. IEEE, 2012, pp. 3690–3693.

[62] J. Wang, P. Aubry, and A. Yarovoy, "3-d short-range imaging with irregular mimo arrays using nufft-based range migration algorithm," *IEEE Transactions on Geoscience and Remote Sensing*, vol. 58, no. 7, pp. 4730–4742, 2020.

[63] Y. K. Chan and V. C. Koo, "An introduction to synthetic aperture radar (sar)," *Progress In Electromagnetics Research*, vol. 2, pp. 27–60, 2008.

[64] E. Biglieri, R. Calderbank, A. Constantinides, A. Goldsmith, A. Paulraj, and H. V. Poor, *MIMO wireless communications*. Cambridge university press, 2007.

[65] W. Zhang, P. Wang, N. He, and Z. He, "Super resolution doa based on relative motion for fmcw automotive radar," *IEEE Transactions on Vehicular Technology*, vol. 69, no. 8, pp. 8698–8709, 2020.

[66] X. Gao, S. Roy, and G. Xing, "Mimo-sar: A hierarchical high-resolution imaging algorithm for fmcw automotive radar," *arXiv preprint arXiv:2101.09293*, 2021.

[67] H. Iqbal, A. Löffler, M. N. Mejdoub, D. Zimmermann, and F. Gruson, "Imaging radar for automated driving functions," *International Journal of Microwave and Wireless Technologies*, pp. 1–9, 2021.

[68] M. Manzoni, M. Rizzi, S. Tebaldini, A. V. Monti-Guarnieri, C. M. Prati, D. Tagliaferri, M. Nicoli, I. Russo, C. Mazzucco, S. D. Biarge *et al.*, "Residual motion compensation in automotive mimo sar imaging," *arXiv preprint arXiv:2110.14995*, 2021.

[69] S. L. Cassidy, S. Pooni, M. Cherniakov, E. G. Hoare, and M. S. Gashinova, "High resolution automotive imaging using mimo radar and doppler beam sharpening," *IEEE Transactions on Aerospace and Electronic Systems*, 2022.

[70] S. Xu, B. J. Kooij, and A. Yarovoy, "Joint doppler and doa estimation using (ultra-) wideband fmcw signals," *Signal Processing*, vol. 168, p. 107259, 2020.

[71] S. Xu and A. Yarovoy, "Joint features extraction for multiple moving targets using (ultra-) wideband fmcw signals in the presence of doppler ambiguity," *IEEE Transactions on Signal Processing*, vol. 68, pp. 6562–6577, 2020.

[72] M. L. L. de Oliveira and M. J. Bekooij, "Deep-mle: Fusion between a neural network and mle for a single snapshot doa estimation," in *ICASSP 2022-2022 IEEE International Conference on Acoustics, Speech and Signal Processing (ICASSP)*. IEEE, 2022, pp. 3673–3677.

[73] C. Liu, W. Feng, H. Li, and H. Zhu, "Single snapshot doa estimation based on spatial smoothing music and cnn," in *2021 IEEE International Conference on Signal Processing, Communications and Computing (ICSPCC)*. IEEE, 2021, pp. 1–5.

[74] M. L. L. de Oliveira and M. J. Bekooij, "Resnet applied for a single-snapshot doa estimation," in *2022 IEEE Radar Conference (RadarConf22)*. IEEE, 2022, pp. 1–6.

[75] I. Roldan, F. Fioranelli, and A. Yarovoy, "Enhancing angular resolution using neural networks in automotive radars," in *2021 18th European Radar Conference (EuRAD)*. IEEE, 2022, pp. 58–61.

[76] P. Hacker and B. Yang, "Single snapshot doa estimation," *Advances in Radio Science*, vol. 8, pp. 251–256, 2010. [Online]. Available: https://ars.copernicus.org/articles/8/251/2010/

[77] W. Liao and A. Fannjiang, "Music for single-snapshot spectral estimation: Stability and super-resolution," *Applied and Computational Harmonic Analysis*, vol. 40, no. 1, pp. 33–67, 2016.

[78] Y. Ma, Y. Zeng, and S. Sun, "A deep learning based super resolution doa estimator with single snapshot mimo radar data," *IEEE Transactions on Vehicular Technology*, vol. 71, no. 4, pp. 4142–4155, 2022.

[79] S. Fortunati, R. Grasso, F. Gini, M. S. Greco, and K. LePage, "Single-snapshot doa estimation by using compressed sensing," *EURASIP Journal on Advances in Signal Processing*, vol. 2014, no. 1, pp. 1–17, 2014.

[80] K. Srinivas, S. Ganguly, and P. Kishore Kumar, "Performance comparison of reconstruction algorithms in compressive sensing based single snapshot doa estimation," *IETE Journal of Research*, pp. 1–9, 2020.

[81] W. Roberts, P. Stoica, J. Li, T. Yardibi, and F. A. Sadjadi, "Iterative adaptive approaches to mimo radar imaging," *IEEE Journal of Selected Topics in Signal Processing*, vol. 4, no. 1, pp. 5–20, 2010.

[82] T. Yardibi, J. Li, P. Stoica, M. Xue, and A. B. Baggeroer, "Source localization and sensing: A nonparametric iterative adaptive approach based on weighted least squares," *IEEE Transactions on Aerospace and Electronic Systems*, vol. 46, no. 1, pp. 425–443, 2010.

[83] W. Wei, R. Liu, X. Yu, Q. Lu, G. Cui, X. Fang, and L. Zhang, "Doa estimation of distributed mmwave radar system via fast iterative adaptive approach," in *2021 International Conference on Control, Automation and Information Sciences (ICCAIS)*. IEEE, 2021, pp. 414–418.

[84] E. Aboutanios, A. Hassanien, M. G. Amin, and A. M. Zoubir, "Fast iterative interpolated beamforming for accurate single-snapshot doa estimation," *IEEE Geoscience and Remote Sensing Letters*, vol. 14, no. 4, pp. 574–578, 2017.

[85] Y. Fang, S. Zhu, C. Zeng, Y. Gao, and S. Li, "Doa estimations with limited snapshots based on improved rank-one correlation model in unknown nonuniform noise," *IEEE Transactions on Vehicular Technology*, vol. 70, no. 10, pp. 10 308–10 319, 2021.

[86] F. Roos, P. Hügler, L. L. T. Torres, C. Knill, J. Schlichenmaier, C. Vasanelli, N. Appenrodt, J. Dickmann, and C. Waldschmidt, "Compressed sensing based single snapshot doa estimation for sparse mimo radar arrays," in *2019 12th German Microwave Conference (GeMiC)*. IEEE, 2019, pp. 75–78.

[87] R. Cao, B. Liu, F. Gao, and X. Zhang, "A low-complex one-snapshot doa estimation algorithm with massive ula," *IEEE Communications Letters*, vol. 21, no. 5, pp. 1071–1074, 2017.

[88] G. Qin, M. G. Amin, and Y. D. Zhang, "Doa estimation exploiting sparse array motions," *IEEE Transactions on Signal Processing*, vol. 67, no. 11, pp. 3013–3027, 2019.

[89] S. Li and X.-P. Zhang, "A new approach to construct virtual array with increased degrees of freedom for moving sparse arrays," *IEEE Signal Processing Letters*, vol. 27, pp. 805–809, 2020.

[90] G. Kim, J. Mun, and J. Lee, "A peer-to-peer interference analysis for automotive chirp sequence radars," *IEEE Transactions on Vehicular Technology*, vol. 67, no. 9, pp. 8110–8117, 2018.

[91] A. Angelov, A. Robertson, R. Murray-Smith, and F. Fioranelli, "Practical classification of different moving targets using automotive radar and deep neural networks," *IET Radar, Sonar & Navigation*, vol. 12, no. 10, pp. 1082–1089, 2018.

[92] P. Bokare and A. Maurya, "Acceleration-deceleration behaviour of various vehicle types," *Transportation Research Procedia*, vol. 25, pp. 4733–4749, 2017, world Conference on Transport Research - WCTR 2016 Shanghai. 10-15 July 2016. [Online]. Available: https://www.sciencedirect.com/science/article/pii/S2352146517307937

[93] P. Stoica and A. Nehorai, "Music, maximum likelihood, and cramer-rao bound," *IEEE Transactions on Acoustics, speech, and signal processing*, vol. 37, no. 5, pp. 720–741, 1989.

[94] M. Grant and S. Boyd, "Graph implementations for nonsmooth convex programs," in *Recent Advances in Learning and Control*, ser. Lecture Notes in Control and Information Sciences, V. Blondel, S. Boyd, and H. Kimura, Eds. Springer-Verlag Limited, 2008, pp. 95–110, http://stanford.edu/~boyd/graph_dcp.html.

[95] G. A. Tyler and B. J. Thompson, "Fraunhofer holography applied to particle size analysis a reassessment," *Optica Acta: International Journal of Optics*, vol. 23, no. 9, pp. 685–700, 1976.

[96] S. J. Wright, *Primal-dual interior-point methods*. SIAM, 1997.

[97] S. Xu and A. Yarovoy, "Motion-based separation and imaging of closely spaced extended targets," *IEEE Sensors Journal*, vol. 20, no. 22, pp. 13 542–13 551, 2020.

[98] P. Swerling, "Probability of detection for fluctuating targets," *IRE Transactions on Information theory*, vol. 6, no. 2, pp. 269–308, 1960.

[99] T. Hermosilla, L. A. Ruiz, J. A. Recio, and J. Estornell, "Evaluation of automatic building detection approaches combining high resolution images and lidar data," *Remote Sensing*, vol. 3, no. 6, pp. 1188–1210, 2011. [Online]. Available: https://www.mdpi.com/2072-4292/3/6/1188

[100] M. Lasserre, S. Bidon, and F. Le Chevalier, "New sparse-promoting prior for the estimation of a radar scene with weak and strong targets," *IEEE Transactions on Signal Processing*, vol. 64, no. 17, pp. 4634–4643, 2016.

[101] S. Yuan, Z. Yu, C. Li, and S. Wang, "A novel sar sidelobe suppression method based on cnn," *IEEE Geoscience and Remote Sensing Letters*, vol. 18, no. 1, pp. 132–136, 2020.

[102] F. Berizzi and G. Corsini, "Autofocusing of inverse synthetic aperture radar images using contrast optimization," *IEEE Transactions on Aerospace and Electronic Systems*, vol. 32, no. 3, pp. 1185–1191, 1996.

[103] R. Prophet, A. Deligiannis, J.-C. Fuentes-Michel, I. Weber, and M. Vossiek, "Semantic segmentation on 3d occupancy grids for automotive radar," *IEEE Access*, vol. 8, pp. 197 917–197 930, 2020.

[104] S. Yuan, F. Fioranelli, and A. Yarovoy, "3drudat: 3d robust unambiguous doppler beam sharpening using adaptive threshold for forward-looking region," *IEEE Transactions on Radar Systems*, 2024.

[105] S. Patil and B. Ravi, "Voxel-based representation, display and thickness analysis of intricate shapes," in *Ninth International Conference on Computer Aided Design and Computer Graphics (CAD-CG'05)*, 2005, pp. 6 pp.–.

[106] M. Sokolova, N. Japkowicz, and S. Szpakowicz, "Beyond accuracy, f-score and roc: a family of discriminant measures for performance evaluation," in *Australasian joint conference on artificial intelligence*. Springer, 2006, pp. 1015–1021.

[107] L. Daniel, A. Stove, E. Hoare, D. Phippen, M. Cherniakov, B. Mulgrew, and M. Gashinova, "Application of doppler beam sharpening for azimuth refinement in prospective low-thz automotive radars," *IET Radar, Sonar & Navigation*, vol. 12, no. 10, pp. 1121–1130, 2018.

[108] C. A. Wiley, "Synthetic aperture radars," *IEEE Transactions on Aerospace and Electronic Systems*, no. 3, pp. 440–443, 1985.

[109] D. Mao, Y. Zhang, Y. Zhang, Y. Huang, and J. Yang, "Super-resolution doppler beam sharpening method using fast iterative adaptive approach-based spectral estimation," *Journal of Applied Remote Sensing*, vol. 12, no. 1, p. 015020, 2018.

[110] G. W. Stimson, *Introduction to airborne radar*. SciTech Publishing, Inc., 1998.

[111] D. Mao, Y. Zhang, Y. Zhang, Y. Huang, and J. Yang, "Doppler beam sharpening using estimated doppler centroid based on edge detection and fitting," *IEEE Access*, vol. 7, pp. 123 604–123 615, 2019.

[112] S. Chen, Y. Yuan, S. Zhang, H. Zhao, and Y. Chen, "A new imaging algorithm for forward-looking missile-borne bistatic sar," *IEEE Journal of Selected Topics in Applied Earth Observations and Remote Sensing*, vol. 9, no. 4, pp. 1543–1552, 2016.

[113] M. BAO, P. ZHOU, L. SHI *et al.*, "Study on deambiguity algorithm for double antenna forward looking missile borne sar," *Journal of Electronics Information Technology*, vol. 35, no. 12, pp. 2857–2862, 2013.

[114] M. Zhang, G. Liao, X. He, and S. Zhu, "Unambiguous forward-looking sar imaging on hsv-r using frequency diverse array," *Sensors*, vol. 20, no. 4, p. 1169, 2020.

[115] Y. Zhang, D. Mao, Y. Zhang, Y. Huang, and J. Yang, "Multi-beam doppler beam sharpening approach for airborne forward-looking radar imaging," in *2017 IEEE International Geoscience and Remote Sensing Symposium (IGARSS)*. IEEE, 2017, pp. 6142–6145.

[116] J. Lu, L. Zhang, P. Xie, Z. Meng, and Y. Cao, "High-resolution imaging of multi-channel forward-looking synthetic aperture radar under curve trajectory," *IEEE Access*, vol. 7, pp. 51 211–51 221, 2019.

[117] A. Albaba, A. Sakhnini, H. Sahli, and A. Bourdoux, "Forward-looking mimo-sar for enhanced angular resolution," in *2022 IEEE Radar Conference (RadarConf22)*. IEEE, 2022, pp. 1–6.

[118] A. Albaba, M. Bauduin, T. Verbelen, H. Sahli, and A. Bourdoux, "Forward-looking mimo-sar for enhanced radar imaging in autonomous mobile robots," *IEEE Access*, 2023.

[119] S. Yuan, F. Fioranelli, and A. Yarovoy, "An adaptive threshold-based unambiguous robust doppler beam sharpening algorithm for forward-looking mimo radar." Accepted for *European Radar Conference* 2023, Berlin, German.

[120] A. Kramer, K. Harlow, C. Williams, and C. Heckman, "Coloradar: The direct 3d millimeter wave radar dataset," *The International Journal of Robotics Research*, vol. 41, no. 4, pp. 351–360, 2022.

[121] G. Hakobyan and B. Yang, "High-performance automotive radar: A review of signal processing algorithms and modulation schemes," vol. 36, no. 5, pp. 32–44. [Online]. Available: https://ieeexplore.ieee.org/document/8828004/

[122] I. Bilik, O. Longman, S. Villeval, and J. Tabrikian, "The rise of radar for autonomous vehicles," p. 12.

[123] S. Rao. (2018) Mimo radar (rev. a) - texas instruments india application report. [Online]. Available: https://www.ti.com/lit/pdf/swra554

[124] T. I. Inc. (2019) Design guide: Tidep-01012—imaging radar using cascaded mmwave sensor reference design (rev. a). [Online]. Available: https://www.ti.com/lit/ug/tiduen5a/tiduen5a.pdf

[125] M. Hoffmann, T. Noegel, C. Schüßler, L. Schwenger, P. Gulden, D. Fey, and M. Vossiek, "Implementation of real-time automotive sar imaging," *arXiv preprint arXiv:2306.09784*, 2023.

[126] S. Yuan, S. Zhu, F. Fioranelli, and A. Yarovoy, "3-d ego-motion estimation using multi-channel fmcw radar," *IEEE Transactions on Radar Systems*, 2023.

[127] S. Yuan, F. Fioranelli, and A. Yarovoy, "Computationally efficient high-resolution imaging algorithm with multi-frame data for automotive radar," in *2024 21st European Radar Conference (EuRAD) (submitted)*.

[128] F. Uysal and S. Orru, "Phase-coded fmcw automotive radar: Application and challenges," in *2020 IEEE International Radar Conference (RADAR)*. IEEE, 2020, pp. 478–482.

[129] J. Domhof, J. F. Kooij, and D. M. Gavrila, "A joint extrinsic calibration tool for radar, camera and lidar," *IEEE Transactions on Intelligent Vehicles*, vol. 6, no. 3, pp. 571–582, 2021.

[130] T. I. Inc. (2020) mmwave studio cascade users guide 2. [Online]. Available: https://dr-download.ti.com/software-development/ide-configuration-compiler-or-debugger/MD-h04ItoajtS/02.01.00.00/mmwave_studio_cascade_user_guide.pdf

[131] S. Yuan, F. Fioranelli, and A. Yarovoy, "An adaptive threshold-based unambiguous robust doppler beam sharpening algorithm for forward-looking mimo radar," in *2023 20th European Radar Conference (EuRAD)*. IEEE, 2023, pp. 65–68.

[132] ——, "Vehicular motion-based doa estimation with a limited amount of snapshots for automotive mimo radar," *IEEE Transactions on Aerospace and Electronic Systems*, 2023.

[133] ——, "3d high-resolution imaging algorithm using 1d mimo array for autonomous driving application," 2024.

[134] T. Tang, C. Wu, and J. Elangage, "A signal processing algorithm of two-phase staggered pri and slow time signal integration for mti triangular fmcw multi-target tracking radars," *Sensors*, vol. 21, no. 7, p. 2296, 2021.

[135] V. Louf, A. Protat, R. C. Jackson, S. M. Collis, and J. Helmus, "Unravel: A robust modular velocity dealiasing technique for doppler radar," *Journal of Atmospheric and Oceanic Technology*, vol. 37, no. 5, pp. 741–758, 2020.

[136] M. Wüest, "Dealiasing wind information from doppler radar for operational use," Ph.D. dissertation, ETH Zurich, 2001.

[137] R. Weston, O. P. Jones, and I. Posner, "There and back again: Learning to simulate radar data for real-world applications," in *2021 IEEE International Conference on Robotics and Automation (ICRA)*, 2021, pp. 12 809–12 816.

[138] O. Chadebec, J.-L. Coulomb, and F. Janet, "A review of magnetostatic moment method," *IEEE Transactions on magnetics*, vol. 42, no. 4, pp. 515–520, 2006.

[139] O. C. Zienkiewicz, R. L. Taylor, and J. Z. Zhu, *The finite element method: its basis and fundamentals*. Elsevier, 2005.

[140] J. B. Schneider, "Understanding the finite-difference time-domain method," *School of electrical engineering and computer science Washington State University*, vol. 28, 2010.

[141] M. Moore, D. A. Robertson, and S. Rahman, "Simulating uav micro-doppler using dynamic point clouds," in *2022 IEEE Radar Conference (RadarConf22)*. IEEE, 2022, pp. 01–06.

ACKNOWLEDGEMENTS

This dissertation would not have been possible without the considerable support and guidance I received throughout my PhD journey.

First and foremost, I wish to express my deepest gratitude to my daily supervisor and promotor, Dr. Francesco Fioranelli. I am immensely thankful for the constant encouragement he provided during our numerous discussions over the years. His expertise and intuition were invaluable in helping me refine my research questions and methodology. Additionally, I greatly appreciated our personal conversations, through which we developed a meaningful connection.

I would also like to sincerely thank my promotor, Prof. DSc. Olexander Yarovyi, for granting me the opportunity to pursue my PhD within the MS3 group. It was his support that enabled me to embark on this journey in the first place. I am profoundly grateful for his prompt feedback, advice, and unwavering support whenever I faced challenges.

My heartfelt thanks extend to the other members of my doctoral committee for their time and effort in evaluating my thesis: Prof. R.F. Hanssen, Prof. D. Gavrila, Prof. K. Doris, Prof. M. Martorella, and Dr. R.F. Remis. A special thanks to Dr. Julian Kooij, who participated in my Go/No-Go meeting after the first year and provided invaluable feedback.

My sincere thanks also go to the MS3 support staff and secretaries, whose diligent assistance ensured the smooth progression of my research. In particular, I deeply appreciate the support provided by Esther de Klerk, Minke van der Put, Fred van der Zwan, Yun Lu, Peter Swart, and Pascal Aubry. Your contributions, though often behind the scenes, were essential to the success of my work.

I owe a debt of gratitude to my current and former office mates—Utku Kumbul, Tworit Dash, Feza Turgay Celik, and Dingyang Wang—for the moments of shared research and leisure that brightened my days in the Netherlands. To my colleagues, both past and present, who enriched my experience with informal yet profoundly insightful discussions by the coffee machine—Yanki Aslan, Oleg Krasnov, Nadia Haider, Max Schöpe, Hans Driessen, Jianping Wang, Nikita Petrov, Wietse Bouwmeester, Ronny Gündel, Nicolas Kruse, Berk Onat, Ignacio Roldan Montero, Simin Zhu, Rutkay Güneri, András Pálffy, Apostolos Pappas, Changxu Zhao, Stefano Chioccarello, Romain Vergez, Mareike Wendelmuth, Shengzhi Xu, Yongdian Sun, Yubin Zhao, Liyuan Ren, Xingzhuo Li, and Wenyi Lu—I thank you for reminding me that this journey was never a solitary one, and that the challenges we faced were shared.

In my first year, I was fortunate to find friends who stood by me through the trials of the COVID-19 lockdown. Xiaoyu Liu, Yigu Liu, Desong Du, Dinghao Wu, Cheng Chang, Zichao Li, Tianlong Jia, Zhenzhen Wu, Haiwei Xie, and Wenyi Lu, your companionship was the diamond during this journey during those trying times. I also hold dear the moments spent with Jun Wen, Yuqi Zhang, Xueting Liang, Junhan Wen, Wei Yuan, Zilong Zhao, Ruoyun Hu, Qisong Yang, and the enriching discussions with my friends Jiaoyue

Zhu, Ruihong Yin, Yiliu Chenran, Mengyuan Ma, Zhengxuan Liu, Ronghao Lin, Jinglin Geng, Changheng Li, Yubao Zhou, and Ke Xu. To my enduring friends in China, including Xinjian Ren, Shuyu Zhou, Zhexi Wang, Deqing Mao, Jindong Yu, Yukun Guo, Lujie Xue, Zheng Liang, and Hao Liang, your support has been a constant source of strength across the miles. I am also deeply grateful to my former teachers in China, Prof. Chunsheng Li and Prof. Ze Yu, whose guidance has left an indelible mark on my academic journey. Though I cannot name everyone, please know that I carry your kindness and support in my heart.

Above all, my deepest thanks belong to my family—my parents and my sister, Meng Yuan and Siheng Chen—whose unwavering love and support have been the bedrock upon which I have relied throughout these challenging years.

I am also profoundly grateful to the China Scholarship Council for their generous funding of my PhD studies. There are countless individuals who have touched my life during this journey, and while I cannot list each name, please know that my gratitude is boundless. Words alone cannot fully capture the depth of my appreciation.

About the Author

Sen Yuan was born in Yuncheng, Shanxi province, China, on April 27, 1998. After graduating from high school in Kangjie, Yuncheng, he started his bachelor's at Beihang University in 2013. He received a Bachelor of Engineering degree in electronic information engineering from Beihang University in 2017 and a master's degree in the speciality of signal processing from Beihang University in 2020 with Prof. C. Li and Prof. Z. Yu. He is currently pursuing a PhD degree in microwave sensing signals and systems with the Delft University of Technology, Delft, The Netherlands, in the MS3 section of the Department of Microelectronics. He was the recipient of the European Microwave Association Student Grant in 2021, 2022, 2023 and 2024.

He did an Internship with Tsinghua University, Beijing, about navigation with Dr. X. Chen in 2016. During his graduate education, he studied and became familiar with the SAR, including its satellite orbits, system design, and ground processing. In January 2021, he joined TU Delft. He works on millimetre radar signal processing in automotive applications.

LIST OF PUBLICATIONS

Journal

6. **S. Yuan**, F. Fioranelli, and A. Yarovoy, "High-resolution imaging algorithms for automotive radar: challenges in real driving scenarios", *IEEE Aerospace and Electronic Systems Magazine.*(submitted)

5. **S. Yuan**, F. Fioranelli, and A. Yarovoy, "3D high-resolution imaging algorithm using 1D MIMO array for autonomous driving application", *IEEE Transactions on Radar Systems.*(submitted)

4. **S. Yuan**, F. Fioranelli, and A. Yarovoy, "3DRUDAT: 3D robust unambiguous Doppler beam sharpening using adaptive threshold for forward-looking region", *IEEE Transactions on Radar Systems*, vol. 2, pp. 138-153, 2024.

3. **S. Yuan**, S. Zhu, F. Fioranelli, and A. Yarovoy, "3-D Ego-motion Estimation using Multi-channel FMCW Radar" *IEEE Transactions on Radar Systems*, vol. 1, pp. 368-381, 2023.

2. **S. Yuan**, F. Fioranelli, and A. Yarovoy, "Vehicular Motion-based DOA Estimation with a Limited Amount of Snapshots for Automotive MIMO Radar" *IEEE Transactions on Aerospace and Electronic Systems*, vol. 59, no. 6, pp. 7611-7625, Dec. 2023.

1. **S. Yuan**, P. Aubry, F. Fioranelli, and A. Yarovoy, "A Novel Approach to Unambiguous Doppler Beam Sharpening for Forward-Looking MIMO Radar" *IEEE Sensors Journal*, 2022, 22(23): 23494-23506.

Conference

9. **S. Yuan**, F. Fioranelli, and A. Yarovoy, "Speeding up imaging over BP for automotive radar: High-resolution algorithm with multi-frame data", *In 2024 European Radar Conference (EuRAD).* (accepted)

8. **S. Yuan**, D. Wang, F. Fioranelli, and A. Yarovoy, "Radar-assisted health monitoring of primates", *In 2024 European Radar Conference (EuRAD).* (accepted)

7. **S. Yuan**, F. Fioranelli, and A. Yarovoy, "Robust High-resolution Imaging with Unambiguous Doppler Beam Sharpening for Forward-looking Automotive Radar", *2024 IEEE INC-USNC-URSI Radio Science Meeting (Joint with AP-S Symposium)*, Florence, Italy, 2024, pp. 222-223.

6. **S. Yuan**, D. Wang, F. Fioranelli, and A. Yarovoy, "Improved Accuracy for 3D Ego-motion Estimation using Automotive FMCW MIMO radar. *2024 IEEE Radar Conference (RadarConf24)*.IEEE, 2024: 1-6.

5. **S. Yuan**, F. Fioranelli, and A. Yarovoy, 'Joint ego-motion estimation and 3D imaging for forward-looking region using automotive radar" *2023 IET international Radar conference.*

4. **S. Yuan**, F. Fioranelli, and A. Yarovoy, "An adaptive threshold-based unambiguous robust Doppler beam sharpening algorithm for forward-looking MIMO Radar" *2023 20 th European Radar Conference (EuRAD)*, IEEE, 2023: 1-4.

3. **S. Yuan**, F. Fioranelli, and A. Yarovoy, "Improved Direction Finding Accuracy for A Limited Number of Antenna Elements with Harmonic Characteristic Analysis" *2022 19 th European Radar Conference (EuRAD)*, IEEE, 2022: 1-4.

2. **S. Yuan**, F. Fioranelli, and A. Yarovoy, "An Approach for High-Angular Resolution Implementation in Moving Automotive MIMO Radar", *2021 18th European Radar Conference (EuRAD)*, IEEE, 2022: 449-452

1. U. Kumbul, N. Petrov, **S. Yuan**, Vaucher, C. S., and A. Yarovoy, "MIMO ambiguity functions of different codes with application to phase-coded FMCW radars" *International Conference on Radar Systems (RADAR 2022)*, 2022.